
Laser Interference Metallurgy of Metallic Surfaces for Tribological Applications

Doktorarbeit

zur Erlangung des Grades
des Doktors der Ingenieurwissenschaften
der Naturwissenschaftlich-Technischen Fakultät III
Chemie, Pharmazie, Bio- und Materialwissenschaft und Werkstofftechnik
der Universität des Saarlandes



VON

CARSTEN GACHOT

Saarbrücken

2012

Hiermit erkläre ich an Eides statt,
dass ich die vorliegende Arbeit selbst
und nur mit den angegebenen
Hilfsmitteln angefertigt habe.

Saarbrücken, June 2012

Dedicated to Rosa and Fabio!

... „It doesn't matter how beautiful your theory is, it doesn't matter how smart you are. If it doesn't agree with experiment, it's wrong .“

Richard P. Feynman

-
- Day of colloquium: 25.10.2012
 - First reviewer: Prof. Dr.-Ing. Frank Mücklich
 - Second reviewer: Prof. Dr. rer. nat. Martin H. Müser
 - Academic representative: Dr.-Ing. Michael Marx
 - Chairman of the colloquium: Prof. Dr. rer. nat. Wulff Possart

Contents

1. Reviewers	1
2. Acknowledgements	11
3. Introduction	14
3.1. How to influence tribological properties - A brief literature review	14
3.2. Aims and objectives	17
3.3. Thesis structure	18
I. Theory	19
4. Laser fundamentals	20
4.1. The laser concept	20
4.1.1. Absorption	20
4.1.2. Spontaneous emission	21
4.1.3. Stimulated emission	22
4.1.4. Population inversion	23
4.2. Fundamental properties of electromagnetic waves	26
4.2.1. Maxwell's equations in vacuum	26
4.2.2. Wave equations in free space	27
4.2.3. Energy transport by electromagnetic waves	27
4.2.4. Maxwell's equations in the presence of matter	28
4.3. The interaction of radiation with matter	29
4.3.1. Drude model of metals	29
4.3.2. Temperature dependence of reflectivity	32
4.3.3. Influence of surface roughness	34

4.3.4. Influence of the angle of incidence and the polarisation	35
4.4. Interference theory and design of periodic structures	37
4.4.1. The approximation of scalar waves	37
4.4.2. The vector character of electromagnetic fields	39
4.5. Thermal simulation	42
5. Dry friction and contact mechanics	44
5.1. The nature of friction	44
5.1.1. Amontons' laws	44
5.1.2. Bowden and Tabor's friction model	44
5.1.3. Tabor's junction growth model	45
5.1.4. The Prandtl-Tomlinson model	46
5.1.5. Structural lubricity and geometrical interlocking	48
5.1.6. Surface roughness parameters	52
5.2. Contact models	58
5.2.1. The Hertzian contact	60
5.2.2. The Greenwood-Williamson model	62
6. Lubricated friction	67
6.1. The role of lubricants	67
6.2. Lubrication regimes	67
6.3. The Stribeck curve	70
II. Experimental part	72
7. Experimental methods	73
7.1. Deposition of thin films	73
7.2. Laser interference structuring	74
7.3. Materials characterisation	76
7.3.1. Scanning electron and focused ion beam microscopy (SEM/FIB) .	76
7.3.2. Transmission electron microscopy (TEM)	77
7.3.3. Electron backscatter diffraction (EBSD)	77
7.3.4. Atom probe tomography (APT)	79
7.3.5. White light interferometry (WLI)	79

7.3.6. X-ray diffraction (XRD)	80
7.3.7. Tribometry	80
7.3.8. Nanoindentation	81
8. Results and discussion	83
8.1. Grain size architectures in metallic thin films	83
8.1.1. Introduction	83
8.1.2. Microstructural characterisation and modelling of laser-induced grain architectures	85
8.1.3. Laser processing and topographic analysis of Au thin films	104
8.1.4. Tribological properties	109
8.1.5. Contact modelling	123
8.2. Phase composites in TiAl multilayered films	129
8.2.1. Introduction	129
8.2.2. Topographic and microstructural analysis of TiAl multilayer	130
8.2.3. Thermal simulation	144
8.2.4. Tribological properties	150
8.3. Hierarchical surface structures by micro-coining and laser interference	157
8.3.1. Introduction	157
8.3.2. Tribological properties of laser-patterned aluminium surfaces	161
8.3.3. Combination of micro-coining and laser interference patterning - the influence of process sequence and coining geometry	165
8.3.4. Tribological properties of hierarchical surfaces under lubrication	172
8.4. Geometrical interlocking	174
8.4.1. Introduction	174
8.4.2. Topographic analysis of interlocking surfaces	174
8.4.3. Tribological properties	179
8.4.4. Microstructural and mechanical characterisation	184
 III. Summary and outlook	 188

Contents

IV. Appendix	A
Literature	B
Figures	M

1. Reviewers

- Day of colloquium: 25.10.2012
- First reviewer: Prof. Dr.-Ing. Frank Mücklich
- Second reviewer: Prof. Dr. rer. nat. Martin H. Müser
- Academic representative: Dr.-Ing. Michael Marx
- Chairman of the colloquium: Prof. Dr. rer. nat. Wulff Possart

Symbols

- A_c : real contact area
- A_n : nominal contact area
- A_{ul} : Einstein coefficient
- a : lattice constant
- α : absorption coefficient
- $\bar{\alpha}$: average absorption coefficient
- α_p : proportionality coefficient
- B : magnetic induction
- b : width
- b_m : molten width
- β : curvature radius of an asperity
- c : velocity of light in vacuum
- c_p : specific heat capacity
- χ_e : dielectric susceptibility
- χ_m : magnetic susceptibility
- \vec{D} : electric displacement vector
- d : structural depth
- d_f : film thickness

- ΔE_{diss} : dissipated energy
- ΔE_{ul} : energy difference between upper and lower level
- ΔH_{eff} : effective heat of formation
- $\Delta\nu$: spectral bandwidth
- δ : phase difference between electromagnetic waves
- \vec{E} : electric field strength
- E_l : energy of a lower level
- E_{total} : total energy flux
- E_u : energy of an upper level
- E_Y : Young's modulus
- E^* : reduced elastic modulus
- e : electron charge
- ϵ_0 : dielectric constant
- ϵ_1 : real part of the dielectric function
- ϵ_2 : imaginary part of the dielectric function
- ϵ_D : dielectric function
- ϵ_p : phase constant of an electromagnetic wave
- ϵ : strain
- η : dynamic viscosity
- F : laser fluence
- F_N : normal force
- F_R : friction force

- f_{ab} : cutting efficiency
- f_i : volume fraction
- f_m : molten fraction
- G : shear modulus
- g_l, g_u : degree of degeneracy for lower/upper level
- γ : surface energy
- γ_{damp} : damping coefficient
- \vec{H} : magnetic field strength
- H : Swedish height
- H_m : hardness
- h : surface height
- h_m : molten depth
- h_P : Planck's constant
- I_{peak} : peak intensity
- I_{total} : total intensity
- $I(z)$: Intensity along z-direction
- \vec{J} : current density vector
- \vec{J}_{cond} : conductive current density vector
- k : wave number
- k_B : Boltzmann's constant
- κ : extinction coefficient
- κ_{th} : thermal diffusivity

- L : Lorenz number
- L_s : sampling length
- l_c : coherence length
- l_D : thermal diffusion depth/length
- λ : wavelength
- λ_{adh} : Maugis adhesion parameter
- λ_p : plasma wavelength
- λ_{th} : thermal conductivity
- M_1, M_2 : bearing ratios for peak-to-core and core-to-valley transitions
- m_e : electron rest mass
- m^* : effective mass
- μ : friction coefficient
- μ_{adh} : Tabor adhesion parameter
- μ_1 : magnetic permeability
- N_e : electron density
- N_l, N_u : number of particles in the lower/upper level
- N_0 : initial number of asperities
- n : refractive index
- n_0 : initial number of excited particles
- n_l, n_u : population density lower/upper level
- ν : general frequency
- ν_k : kinematic viscosity

- ν_m : collision frequency
- ν_P : Poisson's constant
- ω : radiation frequency
- ω_p : plasma frequency
- ω_i : incident angle
- \vec{P} : polarisation vector
- P : power
- P_{peak} : peak pressure
- P_s : structural periodicity
- p_0 : Hertzian contact pressure
- \bar{p} : average contact pressure
- Φ : rotation angle
- $\Phi(z)$: Gaussian distribution function
- Ψ : plasticity index
- Q : laser heat source
- Q_m : melting heat
- R : radius
- R_a : arithmetic mean roughness
- R_{ku} : kurtosis
- R_p : reflectivity with parallel polarisation
- R_{pk} : reduced peak height
- R_s : reflectivity with perpendicular polarisation

- R_{sk} : skewness
- R_{vk} : reduced valley depth
- ρ : density
- ρ_c : charge density
- ρ_{ext} : external charge density
- \vec{S} : Poynting vector
- S_{rms} : root mean square slope
- σ : standard height deviation
- σ_e : electrical conductivity
- σ_{lu} : interaction cross-section
- σ_N : normal stress
- σ_0 : offset coefficient
- σ_y : yield strength
- T : temperature
- t : time
- t_b : bearing ratio
- t_p : laser pulse time
- τ_e : collision time
- τ_f : effective shear strength
- τ_{Gi} : information depth GI-XRD
- τ_p : laser pulse duration
- τ_s : shear stress

- τ_x, τ_y : shear stresses in x- and y-direction
- θ : diffraction angle
- θ_c : critical incident angle
- θ_i : incident angle
- U : relative sliding velocity
- u_e, u_m : electric and magnetic field energy
- V : volume
- V_0 : coupling strength
- V_s : surface potential
- v : velocity
- W : normal load (lubrication)
- W_V : wear volume
- x_{eq} : equilibrium position
- ξ_0 : dimensionless separation variable

Abbreviations

- *ADF*: Amplitude Density Function
- *APT*: Atom Probe Tomography
- *ASTM*: American Society for Testing and Materials
- *CI*: Confidence Index
- *EBSD*: Electron Backscatter Diffraction
- *EDS*: Energy Dispersive Spectroscopy
- *EHL*: Elasto-Hydrodynamic Lubrication
- *FDA*: Frequency Domain Analysis
- *FFT*: Fast Fourier Transformation
- *FIB*: Focused Ion Beam
- *GI – XRD*: Grazing Incidence-X-Ray Diffraction
- *HD*: Hydrodynamic Lubrication
- *IQ*: Image Quality
- *LIMET*: Laser Interference Metallurgy
- *LST*: Laser Surface Texturing
- *MEMS*: Micro-Electromechanical Systems
- *NI – SPM*: Nanoindenting-Scanning Probe Microscopy
- *PID*: Proportional-Integral-Differential

- *SAD*: Selected Area Diffraction
- *SCCM*: Standard Cubic Centimetre per Minute
- *SEM*: Scanning Electron Microscopy
- *SLG*: Super Lateral Growth
- *TEM*: Transmission Electron Microscopy
- *WLI*: White Light Interferometry
- *XPS*: X-Ray Photoelectron Spectroscopy
- *XRD*: X-Ray Diffraction

2. Acknowledgements

I would like to give profuse thanks to my supervisor Prof. Dr.-Ing. Frank Mücklich for giving me the opportunity to do this PhD thesis and of course for his continual guidance and support during my studies. Thank you Frank! A special mention is also made to my second supervisor Prof. Dr. rer. nat. Martin H. Müser who inspired me a lot!

Many thanks go to the German Research Foundation (DFG) and the Volkswagen Stiftung for financially supporting the research work finally leading to another DFG-funded project within the priority program SPP1551. Furthermore, I would like to thank my colleagues and friends Dr. Andrés Lasagni, Dr. Flavio Soldera and Dr. Afrooz Barnoush for their support and friendship.

A most deserved mention is made to my esteemed colleagues and friends Peter Leibenguth, Karsten Woll and Christian Selzner who have consistently been a source of inspiration for me when often faced with times of problems and PhD-related dilemmas! Thanks guys for a great time and many fruitful discussions during the last years with you.

An infinite thank you also goes to my friends Andreas Rosenkranz and Rodolphe Catrin for their friendship and for giving me the necessary motivation in troublesome times.

A mention to past and present members within our department is made. Benjamin Kelkel (section 7.1), Stefan Schommer (section 7.2), Bérenger Florence, Michael Hans, Christoph Pauly, Brice Raillard (section 7.3), Sebastian Slawik, Dominik Britz and Benjamin Bax are just a few names to whom I owe a great deal to. Special thanks also to Nicolas Souza for his help in proof reading of the thesis!

To my friends and family I give sincere thanks. My brother Jürgen and my two brothers-in-law Fiorenzo and Vito Bruno Bertucci for providing a most needed distraction at times.

And finally to my parents, my parents-in-law and of course my wife Rosa as well as my little son Fabio; the unconditional love and support that you have guaranteed me over the years has ensured that everything meaningful I have achieved, I owe to you.

Abstract

Tribological phenomena play a decisive role in diverse systems. For many years, researchers have sought to alleviate these problems and to understand their origin. There are many potential solutions to manipulate friction. In particular, the rapidly growing field of laser surface texturing has attracted a lot of attention in the last decades and shown to be an effective means of improving tribological properties.

A possible approach of laser surface texturing to scrutinise the effects of various pattern geometries and lateral feature sizes in one single laser shot is the so called Laser Interference Metallurgy (LIMET) which will be applied within this thesis.

The aim is to study the microstructural and topographic possibilities of LIMET concerning the tribological performance of laser-patterned thin film systems (Au and TiAl multilayer) and bulk aluminium as well as steel surfaces.

It will be shown that depending on the laser fluence for example, distinct grain size arrangements and intermetallic phase composites can be created with superior tribological properties compared to the unpatterned reference situation. Moreover, a successful process combination of micro-coining and LIMET will be presented with an enhanced oil retainment capability under lubrication. Finally, the results of laser-textured steel surfaces and their ability to geometrically interlock will be shown. Depending on the relative alignment between the textured sliding surfaces and the selected pattern line-spacing, the frictional response can be significantly influenced.

Most of the experimental results will be directly correlated to simulations in order to reveal the underlying phenomena.

Kurzfassung

Reibung spielt eine zentrale Rolle in vielen Bereichen. Insbesondere die Steuerung von Reibung ist dabei von enormer Bedeutung. Zur Minimierung von Reibung sind in den vergangenen Jahrzehnten bereits unzählige Methoden für trockene und geschmierte Bedingungen entwickelt worden. Besonders laserstrukturierte Oberflächen scheinen hierbei vielversprechend für tribologische Anwendungen zu sein.

Ein Ansatz, mikrostrukturell und topographisch maßgeschneiderte Werkstoffe zu erzeugen, ist die Laserinterferenzmetallurgie (LIMET).

Das Ziel der vorliegenden Arbeit ist die Untersuchung der erzielbaren mikrostrukturellen und topographischen Effekte durch LIMET und deren Auswirkungen auf die tribologischen Eigenschaften von metallischen Schichtsystemen (Au und TiAl-Multilagen) sowie massiven Aluminium- und Stahloberflächen.

Hierbei wird gezeigt, dass es z.B. abhängig von der gewählten Fluenz möglich ist, Korngrößenarchitekturen oder intermetallische Phasenkomposite definiert zu erzeugen, deren Reibeigenschaften denen der unbehandelten Ausgangssituation überlegen sind. Des Weiteren wird die erfolgreiche Kombination des Mikroprägens mit der LIMET-Methode vorgestellt. Die Ergebnisse zeigen, dass insbesondere die Ölspeicherfähigkeit in den hierarchischen Kavitäten unter geschmierten Bedingungen deutlich gegenüber einer unstrukturierten Oberfläche gesteigert ist. Schließlich werden die tribologischen Auswirkungen von beidseitig strukturierten Stahloberflächen in Abhängigkeit von deren gegenseitiger Orientierung und den gewählten Strukturabständen näher untersucht. Je nach Ausrichtung und den genannten Strukturperiodizitäten lässt sich das Reibverhalten reproduzierbar in gewissen Grenzen manipulieren.

Die experimentellen Ergebnisse werden mit Simulationen verknüpft, um dadurch die Wirkmechanismen näher zu beleuchten.

3. Introduction

3.1. How to influence tribological properties - A brief literature review

Most machines contain components with loaded solid surfaces that rub together. The interaction of such surfaces produces friction and results in mechanical damage. Thus, tribological phenomena play a decisive role in diverse systems. For many years, researchers have sought to alleviate these problems and to understand their origin. In this context, the reduction of friction and wear is very often the primary focus. Nevertheless, there are many applications such as brake systems and clutches in which a controlled increase in friction is desired [1]. It is important to note that the friction coefficient μ , being the ratio between the friction and the applied normal force, does not represent an inherent materials property. Moreover, μ is determined by the respective tribological system which comprises for example the interacting materials, the surface roughnesses, the stress collective, the kinematics and the environmental conditions (e.g. temperature and relative humidity).

The early work of Bowden and Tabor [2] showed that one determinant aspect for friction is the interaction of asperities. Those asperities weld together and will be released after having reached a critical shear stress τ . According to this model, one possibility to influence frictional properties is based on tailoring the real contact area of the mating surfaces. Being able to control the frictional response of a tribological system on different scales is likely to be of utmost importance for the design of miniaturized applications e.g. micro-electromechanical systems (MEMS), positioning devices and bearings [3]. There are many potential solutions to manipulate friction by modifying the surface materials e.g. changing the design of the rubbing elements [4], using hard coatings like TiC, TiB₂ or (TiAl)N [5], multilayer coatings such as WC/DLC/WS₂ [6] [7], lubricants e.g. oils, greases, soft metals (In, Au or Sn) or DLC films [8] and finally by texturing

the mating surfaces [9]. In particular, the rapidly growing field of surface texturing has attracted a lot of attention in the last decades and has proven to be an effective means of improving tribological properties. Nowadays, numerous industrial texturing methods are able to modify the contacting surfaces. Basically, those methods can be separated into stochastic (e.g. shot blasting or electrical discharge texturing) and deterministic processes (e.g. electron or laser beam texturing) with regard to the resulting texture geometry [10]. Another semi-deterministic technique is the cylinder liner honing which is well established for the enhancement of tribological properties in combustion engines. The honing process is characterised by a superposition of rotational and vertical movements of the so called honed edges. Depending on the selected honing method, specific surface finishes with for example cross-hatch patterns can be generated providing an improved oil retainment capability thus leading to sufficient piston ring lubrication [10]. A further development of the aforementioned technique is the combination with a certain laser treatment named laser honing. Usually, a nanosecond-pulsed excimer laser is applied to irradiate a honed cylinder surface. Because of very short pulse durations in the order of several nanoseconds, residual adhesive particles are removed and a micro-flattening of the mechanically prepared surface takes place.

Laser surface texturing (LST) proved to be a very promising candidate because laser is a fast and environmental friendly tool offering short processing times [9]. Moreover, by a proper variation of the laser wavelength (from UV to IR laser light), the beam polarisation (linear-, circular- or elliptic-polarisation), the pulse duration (ranging from femto- to nanoseconds or even continuous mode) and finally by adjusting the energy density, different materials (e.g. metals, ceramics and polymers) can be processed. There are manifold applications of laser surface texturing under dry and lubricated sliding conditions. Since Hamilton et al. [11], it is well known that textured surfaces have an advantageous impact on sliding bodies under hydrodynamic lubrication. Furthermore, surface patterns are able to act as lubricant micro-reservoirs under boundary lubrication conditions and trap wear debris under dry sliding thus reducing abrasive wear and fretting fatigue [10][12][13].

Still, the optimum design parameters for an efficient surface pattern concerning for example the pattern geometry, the lateral feature sizes or area densities are still a matter of lively discussion in the surface texturing community. Most texturing experiments are based on a simple trial and error approach [14]. For lubricated conditions, many articles emphasise the importance of the dimple depth over diameter ratio h/d and the area

3. Introduction

density of the patterns [15][9][16]. In particular, dimples with a depth in the nanoscale seem to be effective in reducing friction at low speed and high load [15]. Wakuda et al. performed friction tests of line contacts between a steel cylinder and a Si₃N₄ ceramic plate. Results showed that dimples with diameters larger than the Hertzian contact width lead to lower coefficients of frictions under lubricated sliding [17]. According to Costa and Hutchings, textures with feature sizes much larger than the elastic contact width yield film thicknesses smaller than those for non-textured specimens [16].

Additionally, the area density of the patterns plays a decisive role in the effectiveness under hydrodynamic and mixed lubrication. Andersson et al. reported low coefficients of friction for laser textured steel surfaces under oscillating sliding conditions for low area densities ($\approx 8\%$) [18][14]. Furthermore, Wang et al. have provided a load-carrying capacity map for SiC thrust bearings under water lubrication. The maximum load-carrying capacity was achieved by dimples of around 350 μm in diameter, 3.2 μm in depth and with an area density of about 5% [15].

Finally, there is a direct correlation between the tribological performance and the texture geometry as well as the orientation. Nanbu et al. performed a virtual surface generation involving a numerical texturing process in order to study the effect of texture bottom shape under hydrodynamic conditions [19]. They could determine two hydrodynamically favourable pattern geometries enhancing lubricant film thickness, namely micro-step and wedge bearings. Moreover, Siripuram and Stephens conducted experiments with protruding and recessed asperities with different geometries e.g. circular, hexagonal and triangular shapes with regard to the influence on the friction coefficient and the leakage rate for seals. It could be shown that the friction coefficient μ is more or less insensitive to the geometry but sensitive to the size of the asperities. In contrast, the leakage rate is affected by both parameters leading to the best results for triangular shaped textures [20].

As far as dry friction is concerned, much less publications exist dealing with the potential benefits of texturing a surface. Most of the work is related to the already mentioned trapping of wear debris in order to avoid third body interactions or reducing stiction in magnetic storage disks [21][22][23][24][25]. He et al. used a micromolding technique to texture an elastomer substrate (PDMS-polydimethylsiloxane) and to study the influence of different pattern geometries on the frictional response. Moreover, Borghi et al. performed laser texturing on nitrided steel surfaces and could demonstrate a decrease in the coefficient of friction of about 10 % due to embedded wear particles in the produced

laser dimples [26]. In addition, Rapoport and co-workers showed the enhanced storing capability of laser-patterned steel surfaces for solid lubricants such as MoS₂ [23]. However, most of the research is directly linked to the aforementioned effects.

One possible approach of LST to scrutinise the effects of various pattern geometries and lateral feature sizes in one single laser shot in a systematic way is the so called *Laser Interference Metallurgy* (LIMET) which will be applied within this thesis. This technique utilises interfering laser beams from a solid state Nd: YAG laser, to create well-defined surface topographies with long-range order on the micron scale [27][28]. Moreover, due to a periodic laser intensity distribution and significant heating /cooling rates of up to 10¹⁰ K/s [29], metallurgical effects like melting, resolidification and the formation of intermetallic phases can be induced [30].

3.2. Aims and objectives

This particular study aims to elucidate the microstructural and topographic possibilities of LIMET by establishing a direct relation between their tribological effectiveness under mainly dry as well as, to a smaller extent, lubricated conditions. With this in mind, novel microstructural architectures e.g. long-range ordered grain size arrangements and intermetallic phase composites have been created by LIMET in Au and TiAl thin film model systems.

Additionally, bulk specimens made of aluminium and austenitic stainless steel have been laser textured using different pattern geometries and lateral feature sizes in order to investigate the influence of the interference parameters on the frictional response.

Parallel to the laser processing, the detailed microstructural characterisation of the as-patterned samples by high resolution microscopic methods such as scanning electron and focused ion beam microscopy, electron backscatter diffraction, transmission electron microscopy and finally atom probe tomography, was just as important.

Moreover, numerical simulations studying the spatial temperature distribution and the respective heating and cooling rates during the laser treatment are presented and linked to the characterisation of the microstructure. This should provide a comprehensive understanding of the mechanisms by which the different microstructures are induced and governed.

In this sense, tribological contact models will be used to explain the observed experi-

mental findings.

Another important part of the thesis is the study of a hierarchical patterning approach by combining micro-coining and LIMET which was part of a project funded by the Volkswagen foundation in the last years.

Finally, a well-defined topographic design of two metallic sliding surfaces by laser interference patterning and their ability to geometrically interlock shall be presented. The results highlight the feasibility of creating bespoke contacting surface geometries leading to tuneable frictional properties.

3.3. Thesis structure

The work described in this thesis can effectively be split into three main parts, following a brief introduction into previous efforts that have attempted to deal with the question of textured surfaces. A literature review will highlight the areas of research which have been crucial in determining the knowledge base thus far. Also, a theoretical part summarises the important aspects of the fundamental state of knowledge in the area of laser physics and tribology-related topics.

In the second part, the used experimental methodology will be briefly presented. The results are shown and discussed in the final portion of the thesis (chapter 7).

A final summary and conclusions are made in the third part as to the validity of the current findings.

Part I.

Theory

4. Laser fundamentals

4.1. The laser concept

Laser is an acronym derived from **L**ight **A**mplification by **S**timulated **E**mission of **R**adiation. Thermal radiators, such as the sun, emit light with different wavelengths in all directions, the individual photons having no defined relationship with one another. But because the laser is an oscillating amplifier of light, and because its output comprises photons that are identical in phase and direction, it is unique among other light sources. Some fundamental laser properties are coherence, monochromaticity and directionality. The power density, meaning the ratio between the output power and the irradiated area, can be as much as 10^{14} W/cm^2 [31], nearly seven orders of magnitude larger than that of the sun. In order to understand the basic principle of light amplification, it is important to introduce the concepts of absorption, spontaneous and stimulated emission, the latter being an important part of the laser acronym.

4.1.1. Absorption

Absorption takes place when an electromagnetic wave interacts with the electrons of an atom, for example. A precondition is that the wave fulfils the following equation: $\nu = \Delta E_{ul}/h$, with ν representing the frequency of the wave, ΔE_{ul} the energy difference between an upper and a lower energy level and finally h_P the so called Planck's constant with $h_P = 6.626 \cdot 10^{-34} \text{ Js}$. The respective atom is able to draw energy from the electromagnetic field and consequently to occupy a higher energy level with an energy $E_u = E_l + \Delta E_{ul}$. E_u and E_l are the energies of an upper and a lower level. The probability of this process is described by an effective interaction cross-section σ_{lu} . Figure 3.1 shows an infinitesimal volume of a medium with $V = Adz$. This volume should contain N_l particles with a cross-section σ_{lu} , assuming dz is small enough to avoid the overlapping of effective cross-sections within the volume V .

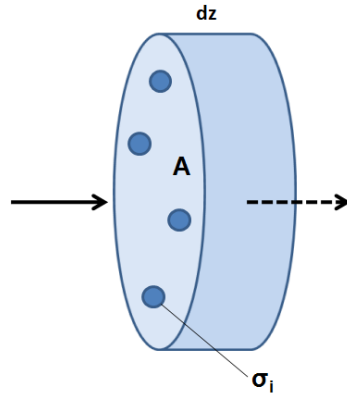


Figure 4.1.: Schematic description of an effective interaction cross section σ_{lu} regarding absorption of light.

Furthermore, a light beam shall cross the infinitesimal volume V in the z -direction, interacting with the effective cross-sections σ_{lu} of the particles. Aside the cross-section, the light beam is transmitted without perturbation. If $I(z)$ denotes the intensity of the incident beam travelling in the z -direction before crossing the volume, the latter absorbs a power $P = I(z) \cdot N_l \cdot \sigma_{lu}$. Hence, the power loss along the path dz can be expressed as [32]:

$$dP(z) = -I(z) \cdot N_l \cdot \sigma_{lu} = -I(z) \cdot n_l \cdot A \cdot dz \cdot \sigma_{lu}. \quad (4.1)$$

with n_l being the number of particles per unit volume. Using the relation $dI = dP/A$, equation 3.1 can be written as:

$$\frac{dI(z)}{dz} = -I(z) \cdot n_l \cdot \sigma_{lu}. \quad (4.2)$$

By integrating equation 3.2 and using the boundary condition: $I(z = 0) = I_0$, it follows:

$$I(z) = I_0 \cdot e^{-z \cdot n_l \cdot \sigma_{lu}}. \quad (4.3)$$

4.1.2. Spontaneous emission

When an atom is in an electronically excited state (figure 3.2), the probability that it will emit a photon returning to a lower energy level is determined by the *Einstein coefficient* A_{ul} for spontaneous emission. The transition rate for spontaneous emission is given by $A_{ul} \cdot n_0$ where n_0 denotes the initial number of excited particles. Consequently,

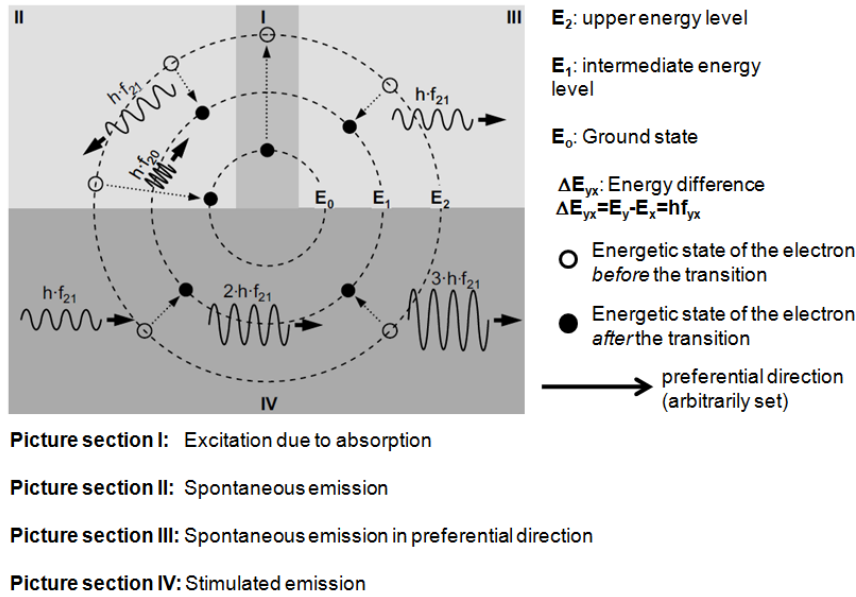


Figure 4.2.: Schematic summary of absorption, spontaneous and stimulated emission according to [33].

the initial density of excited states decreases at the following rate:

$$\frac{dn_0}{dt} = -A_{ul} \cdot n_0. \quad (4.4)$$

The decay rate can be expressed as:

$$n_0(t) = n_0(t=0) \cdot e^{-A_{ul} \cdot t}. \quad (4.5)$$

4.1.3. Stimulated emission

Stimulated emission can be observed during the interaction between a radiative field and electronically excited atoms. If the frequency of the radiation satisfies the resonance conditions $\nu = \Delta E_{ul}/h_P$, the atom will transfer the energy $\Delta E_{ul} = E_u - E_l$ to the electromagnetic wave thus lowering its energy state. During this process, the incoming electromagnetic wave is amplified. The probability rate of amplifying a quasi-monochromatic beam can also be expressed in terms of an effective cross-section. In contrast to absorption, the wave is amplified rather than attenuated. Thus, the rate is

given by:

$$\frac{dI(z)}{dz} = I(z) \cdot n_0 \cdot \sigma_{ul} \quad (4.6)$$

where σ_{ul} is the effective cross-section for stimulated emission.

4.1.4. Population inversion

So far, different effective cross-sections σ_{lu} and σ_{ul} have been introduced. Supposing thermodynamic equilibrium, the following relation between the two processes can be given:

$$g_l \cdot \sigma_{lu} = g_u \cdot \sigma_{ul} \quad (4.7)$$

where g_l and g_u represent the degree of degeneracy of an energy level which describes the number of quantum-mechanical states with the same energy. The next step is based on the derivation of an expression for a light beam crossing a medium containing *active* particles with population densities n_l and n_u . Considering absorption and stimulated emission, it follows:

$$\frac{dI}{dz} = I \cdot \sigma_{ul} \cdot \left(n_0 - \frac{g_u}{g_l} \cdot n_l \right). \quad (4.8)$$

Amplification only takes place, if the following condition is satisfied:

$$\left(n_0 - \frac{g_u}{g_l} \cdot n_l \right) > 0. \quad (4.9)$$

Without degenerated states ($g_u = g_l = 1$), the population inversion of the upper (excited) energy level must be higher than that of the lower level. When a material is at thermal equilibrium, the atoms follow a Boltzmann distribution of energy levels, with the most atoms in the ground state. Since the rate of absorption of all frequencies exceeds that of emission, the absorption coefficient at any frequency is positive:

$$\frac{n_u}{g_u} = \frac{n_l}{g_l} \cdot e^{\frac{-(E_u+E_l)}{k_B T}} \quad (4.10)$$

with n_u/g_u always smaller than n_l/g_l thus not fulfilling the population inversion. As a consequence, the system must be continuously supplied with energy in order to achieve population inversion. After having suspended the energy input, the population n_u converges towards the Boltzmann distribution. If enough light of frequency ν is supplied,

the populations can be shifted until $n_l = n_u$. Under those conditions the rates of absorption and stimulated emission are equal, and the absorption coefficient at frequency ν is zero. If the transition scheme is limited to two energy levels, population inversion is not possible [34]. However, if the transition scheme consists of three or even more energy levels, satisfying the condition mentioned in equation 3.9, population inversion can occur. Figure 3.3 displays a typical four-level laser transition scheme.

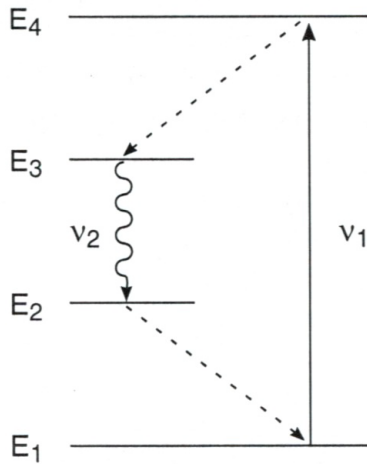


Figure 4.3.: A typical four-level laser transition scheme [34]

A photon of frequency ν_1 excites an atom from E_1 to E_4 . If the E_4 to E_3 transition probability is greater than that of E_4 to E_1 , and if E_4 is short lived, the atom will decay almost immediately to E_3 . If E_3 is metastable i.e. atoms that occupy it, have a relatively long lifetime, the population will grow rapidly as excited atoms cascade from above. The E_3 atom will eventually decay to E_2 , emitting a photon of frequency ν_2 . Finally, if E_2 is unstable, its atoms will rapidly return to the ground state, E_1 , keeping the population of E_2 small and reducing the rate of absorption of ν_2 . In this way, the population of E_3 is kept large and that of E_2 remains low, thus establishing a population inversion between E_3 and E_2 . Under these conditions, the absorption coefficient at ν_2 becomes negative. Light is amplified as it passes through the active laser medium.

4. Laser fundamentals

The used laser in this thesis is a Nd:YAG solid state pulsed laser with a four-level transition scheme. Figure 3.4 depicts the energy level diagram for a Nd:YAG laser source which is more complex than the previously discussed four-level scheme.

The physical properties of the neodymium-doped yttrium aluminum garnet (Nd:YAG)

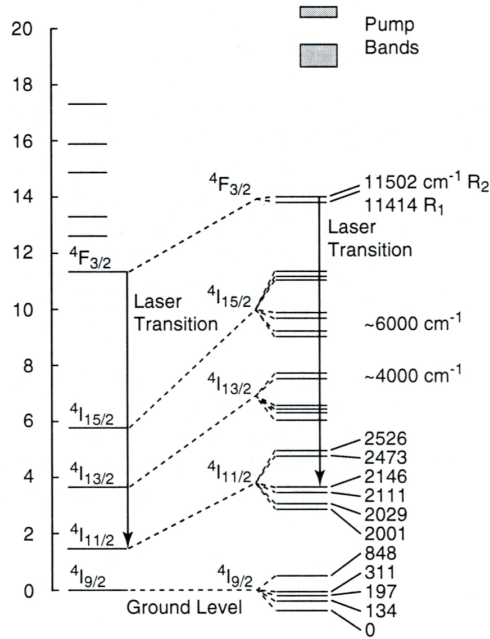


Figure 4.4.: Energy level diagram for a Nd:YAG solid state laser [34]

are the most intensively studied and best understood of all solid state laser media. The active medium is triply ionised neodymium, which is optically pumped by a flash lamp whose spectral range matches principle absorption bands in the red and infrared. The most probable lasing transition is to the ${}^4I_{11/2}$ state, emitting a photon at 1064 nm. Due to the absorption characteristics of the used materials in this thesis, mainly the third harmonic at 355 nm was applied for the experiments.

4.2. Fundamental properties of electromagnetic waves

4.2.1. Maxwell's equations in vacuum

All physical phenomena associated with the propagation of electromagnetic waves in different materials are mathematically described by a set of fundamental differential equations known as **Maxwell's Equations** [35]. In the case of vacuum, the four relevant equations are:

$$\nabla \times \vec{E}(\vec{r}, t) + \frac{1}{c} \frac{\partial \vec{B}(\vec{r}, t)}{\partial t} = 0. \quad (4.11)$$

This first equation is the so called **Faraday's law** of induction which describes how a time varying magnetic field induces an electric field. This aspect of electromagnetic induction is the basic principle for electric generators

$$\nabla \cdot \vec{B}(\vec{r}, t) = 0. \quad (4.12)$$

This equation refers to **Gauss's law of magnetism** postulating that there are no magnetic monopoles analogous to electric charges. Instead, the magnetic field due to a material is generated by dipoles

$$\nabla \times \vec{B}(\vec{r}, t) - \frac{1}{c} \frac{\partial \vec{E}(\vec{r}, t)}{\partial t} = \frac{4\pi}{c} \vec{J}(\vec{r}, t). \quad (4.13)$$

Ampère's law states that magnetic fields can be generated in two ways: (a) by electrical currents and (b) by time-varying electric fields

$$\nabla \cdot \vec{E}(\vec{r}, t) = 4\pi\rho(\vec{r}, t). \quad (4.14)$$

Finally, **Gauss's law in electrostatics** points out that electric fields can be traced back to electric charges. In this context, E and B are the electric field strength and the magnetic induction with $c = 2.99792458 \cdot 10^8 m/s$ the velocity of light in vacuum. The current density J and the charge density ρ used in this set of equations refer to the total magnitudes including both external and induced currents and charge densities. All quantities are assumed spatial- and time-dependent as indicated by (\vec{r}, t) [36].

4.2.2. Wave equations in free space

In the absence of free current and external charge ($J=0$ and $\rho = 0$), the combination of Faraday's induction law and Gauss's law for electrostatics yields:

$$\frac{1}{c} \frac{\partial}{\partial t} (\nabla \times \vec{B}) = \nabla^2 \vec{E}. \quad (4.15)$$

Using Ampère's law, the following relation for the electric field can be obtained:

$$\nabla^2 \vec{E} - \frac{1}{c^2} \frac{\partial^2 \vec{E}}{\partial t^2} = 0. \quad (4.16)$$

This is a wave equation in its simplest form without dissipation or other factors. One possible solution for this differential equation is given by a harmonic wave:

$$\vec{E}(\vec{r}, t) = E_0 \exp \{ i(\vec{k} \cdot \vec{r} - \omega t) \}. \quad (4.17)$$

Here, \vec{k} denotes the wave vector given by the relation $k = 2\pi/\lambda$. The corresponding wave equation for the \vec{B} -field can easily be derived from Maxwell's equations and has the same form as 3.16:

$$\nabla^2 \vec{B} - \frac{1}{c^2} \frac{\partial^2 \vec{B}}{\partial t^2} = 0. \quad (4.18)$$

The three vectors \vec{E} , \vec{B} and \vec{k} are perpendicular to one another.

4.2.3. Energy transport by electromagnetic waves

There is an energy associated with the generation of electric and magnetic fields. The time-average density of the electric field energy is $u_e = \frac{1}{4\pi} \langle \vec{E} \rangle_t^2$ and that of the magnetic field $u_m = \frac{1}{4\pi} \langle \vec{B} \rangle_t^2$. A travelling electromagnetic wave implies the transport of electromagnetic energy. There will be no energy dissipation as long as damping effects can be neglected. The energy density i.e. the energy per unit volume, associated with a harmonic wave is given as [36]:

$$u = \frac{1}{8\pi} E^2 + \frac{1}{8\pi} B^2. \quad (4.19)$$

In the case of $|E| = |B|$, it follows that $u_e = u_m$. The vector directed along the direction of propagation and describing the transported energy i.e. the flow of energy per unit area per unit time, is called **Poynting vector**:

$$\vec{S} = \frac{c}{4\pi} \vec{E} \times \vec{B} \quad (4.20)$$

with

$$\nabla \cdot \vec{S} = -\frac{\partial u}{\partial t}. \quad (4.21)$$

4.2.4. Maxwell's equations in the presence of matter

The presence of a medium in electric and magnetic fields may lead to electric dipoles and magnetic moments, polarization charges and induced currents. Clearly, the electric and magnetic fields will not be uniform within the material but rather fluctuate from point to point reflecting the periodicity of the atomic lattice. Said fields, however, differ from fields in vacuum. As a consequence, the electric displacement \vec{D} replaces the electric field strength \vec{E} , and the magnetic induction \vec{B} replaces the magnetic field strength \vec{H} , to account for the respective medium.

The electric field strength \vec{E} and the electric displacement \vec{D} are connected by the dielectric constant (or permittivity) ϵ_0 :

$$\vec{D} = \epsilon_0 \vec{E} = (1 + 4\pi \chi_e) \vec{E} = \vec{E} + 4\pi \vec{P} \quad (4.22)$$

where χ_e is the dielectric susceptibility and $\vec{P} = \chi_e \vec{E}$ is the dipole moment density or polarisation density. The dielectric constant ϵ_0 can be either positive or negative. Similarly, the magnetic field strength \vec{H} is connected to the magnetic induction \vec{B} by the permeability μ_1 :

$$\vec{B} = \mu_1 \vec{H} = (1 + 4\pi \chi_m) \vec{H} = \vec{H} + 4\pi \vec{M} \quad (4.23)$$

where χ_m is the magnetic susceptibility and $\vec{M} = \chi_m \vec{H}$ the magnetic moment density, or magnetisation. The quantities ϵ_0 , χ_e , μ_1 and χ_m which connect the fields are dimensionless. The magnetic susceptibility χ_m is typically four to five orders of magnitude smaller than the dielectric susceptibility χ_e (except in the case of ferromagnetism), which is of the order of unity. For this reason, the dia- and paramagnetic properties can, in

general, be neglected compared to the dielectric properties when electromagnetic waves pass through a medium. Based on these modifications, the Maxwell equations in the presence of matter can be reformulated:

$$\nabla \times \vec{E} + \frac{1}{c} \frac{\partial \vec{B}}{\partial t} = 0 \quad (4.24)$$

$$\nabla \cdot \vec{B} = 0 \quad (4.25)$$

$$\nabla \times \vec{H} - \frac{1}{c} \frac{\partial \vec{D}}{\partial t} = \frac{4\pi}{c} \vec{J}_{cond} \quad (4.26)$$

$$\nabla \cdot \vec{D} = 4\pi \rho_{ext} \quad (4.27)$$

where J_{cond} represents the conductive current density arising from the motion of electrons in the presence of an electric field and ρ_{ext} represents an external charge density.

4.3. The interaction of radiation with matter

4.3.1. Drude model of metals

The optical response of metals is mainly governed by conduction electrons. A basic property is their high reflectivity and accordingly low absorption. In contrast to atoms and molecules, absorption occurs continuously (from far infrared to ultraviolet light) rather than with discrete frequencies [37]. An explanation for the absorption of electromagnetic radiation and the related optical constants of metals is given by the modified *Drude theory* [38]. This theory describes the electrons of a metal as a free electron gas in a potential well. This model is preferably applicable to simple isotropic metals such as sodium and potassium and allows for the determination of the real refractive index n and the extinction coefficient κ based on the following hypotheses:

1. The electromagnetic wave only interacts with the free electrons.
2. The free electrons obey Ohm's law $\vec{J} = \sigma \vec{E}$.
3. All free electrons can be described by a uniform effective mass m^* and collision frequency ν_m .

Generally, the absorption in metallic materials for a given wavelength is mainly determined by four parameters:

- the optical constants of the material
- the surface roughness
- the chemical composition of the surface (e.g. oxide layers, adsorbates etc.)
- the temperature (which also influences the aforementioned parameters)

According to the degenerated electron gas, only electrons near the Fermi level, referred to as free electrons contribute to the optical properties. The dielectric function of a metal can be written as [37]:

$$\epsilon_{D,metal} = 1 + \omega_p^2 \cdot \frac{-\tau_e^2 + i\tau_e/\omega}{1 + \omega^2\tau_e^2} \quad (4.28)$$

where ω_p denotes the so called *plasma frequency*, τ_e the collision time and ω the frequency of the applied radiation. The plasma frequency is given by:

$$\omega_p = \sqrt{\frac{N_e \cdot e^2}{m_e \cdot \epsilon_0}} \quad (4.29)$$

where N_e represents the electron density (the number of free electrons per unit volume), e the electron charge ($e = 1.602 \cdot 10^{-19}$ C), m_e the free electron rest mass ($m_e = 9.108 \cdot 10^{-31}$ kg) and ϵ_0 the dielectric constant ($\epsilon_0 = 8.854 \cdot 10^{-12}$ C/Vm). In figure 3.5, the frequency dependence of the real and imaginary part of the complex dielectric function, the refractive index, the absorption and finally the reflectivity are displayed for $T = 298$ K, $\tau_e = 3.29 \cdot 10^{-14}$ s and $N_e = 5 \cdot 10^{28} m^{-3}$. At $\omega = \omega_p$, generally in the ultraviolet range for metals, the real part of the dielectric function ϵ_1 and the real refractive index n_1 vanish. The plasma frequency ω_p splits the frequency dependence of the reflectivity into two main regimes:

- Large R and small α for $\omega < \omega_p$
- Small R and α for $\omega > \omega_p$

As a consequence, the frequency ω or wavelength λ of the used laser system should be adjusted to values above ω_p or below λ_p in order to efficiently absorb energy for a subsequent laser treatment. Due to the fact that ω_p is in the UV range for most

metals, the third harmonic of the available Nd:YAG laser at 355 nm was chosen for the experiments in this thesis. In reality, the approximation of free electrons is influenced

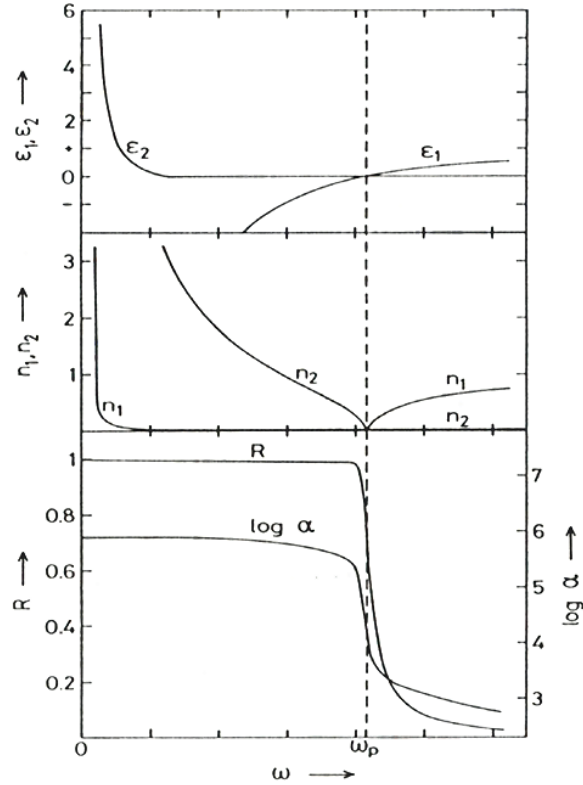


Figure 4.5.: Frequency dependence of the dielectric function ϵ_D , the refractive index n , the absorption coefficient α and the reflectivity R [37].

by various secondary effects such as inter- and intraband transitions. Figure 3.6 depicts the wavelength dependence of the reflectance R and the absorption coefficient α for gold and aluminium thin films. Some of the clearly visible oscillations can be attributed to interband transitions (e.g. at $0.83\ \mu\text{m}$ in Al). The figure reveals that the plasma frequency of Al is indeed in the vacuum UV range whereas ω_p of Au is stronger in the visible part of the spectrum. The relatively low plasma frequency of Au is caused by transitions from the d-band resulting in the typical yellow colour of gold. Apart from the frequency dependence, further factors such as temperature, surface roughness, incident angle and the polarisation of the incoming wave influence the reflectivity behaviour of a material.

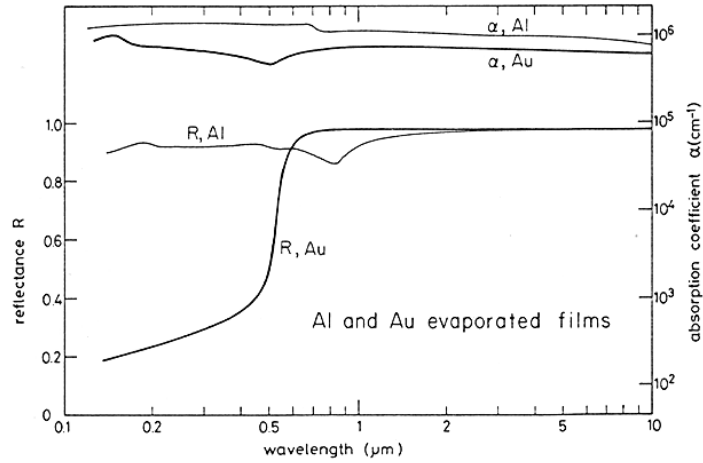


Figure 4.6.: Wavelength dependence of the reflectance R and the absorption coefficient α for gold and aluminium thin films [37].

4.3.2. Temperature dependence of reflectivity

The reflectivity of metals often drops at high temperatures and was already discussed in the early work of Boloshin [39]. The absorption of light initially occurs in the solid, molten or evaporated plasma states [40] of a metal. According to the Drude theory, the electron-phonon collision frequency is a decisive parameter when discussing the temperature influence. An increase in temperature leads to a rising phonon population and thus to an increased collision frequency [40]. This interrelation determines the optical properties of metals. The electron-phonon collision frequency can be derived from the empirical Wiedemann-Franz law describing that the ratio between thermal and electrical conductivity is proportional to the temperature:

$$\frac{\lambda_{th}}{\sigma_e} = \frac{\pi^2 k_B}{3 e} = LT \quad (4.30)$$

where λ_{th} represents the thermal and σ_e the electrical conductivity, k_B the Boltzmann constant with $k_B = 1.308 \cdot 10^{-23}$ J/K, e the electron charge and L the so called Lorenz number ranging between 2.1 and $2.9 \cdot 10^{-8}$ $W\Omega K^{-2}$ [41]. For identical relaxation times of thermal and electrical processes, the Lorenz number is independent of the collision time. The Lorenz number usually decreases with decreasing temperature. This can be explained by different average collision times of the thermal and electrical conductivity

[42]. The collision frequency can be expressed by:

$$\nu_m = \frac{e^2 N_e L T}{m_e \lambda_{th}}. \quad (4.31)$$

Summarising, it can be stated that the temperature dependence of the reflectivity and the electrical conductivity are the result of the same physical law. Figure 3.7 shows the reflectivity as a function of temperature for different metals. For the displayed metals,

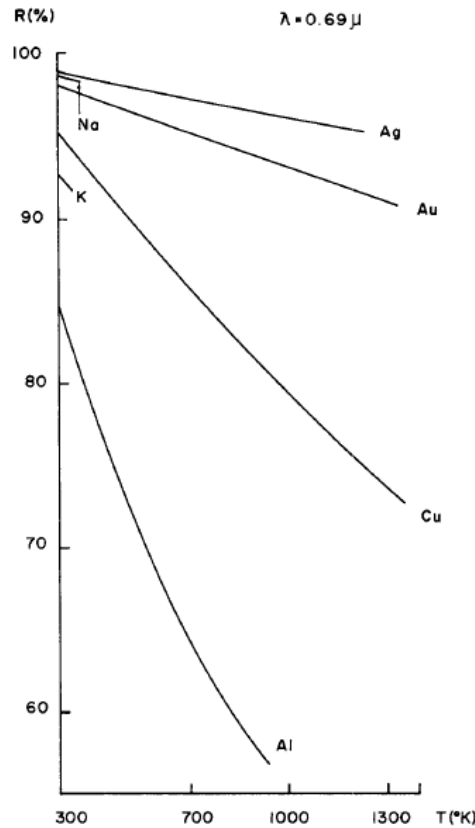


Figure 4.7.: Reflectivity versus temperature for different metallic surfaces [40].

the decrease in reflectivity can be significant. In the case of aluminium, R drops from 0.85 at 300 K to about 0.56 at about 1000 K. With regard to the following thermal simulations of laser irradiated aluminium specimens, this is an important aspect which must be kept in mind. Moreover, there seems to be a relation between the initial value of the reflectivity and the temperature sensitivity. Metals having a lower reflectivity at room temperature exhibit a stronger reduction of R with respect to the temperature.

4.3.3. Influence of surface roughness

Surface roughness plays a crucial role in the amount of laser energy being absorbed by a material. Basically, the problem may be divided into two regimes:

- $rms/\lambda \ll 1$ being the ratio of the root mean square roughness rms and the wavelength of the respective laser light. The rms value is defined as:

$$rms = \sqrt{\frac{1}{L} \int_0^L z^2 dx} \quad (4.32)$$

- $rms/\lambda \gg 1$

In the first case, the surface can be treated as ideally flat. In contrast, for $rms/\lambda \gg 1$ multiple reflections are produced on the rough surface thus increasing the absorption coefficient by up to an order of magnitude [43]. Ang et al. have developed a relatively simple model to demonstrate the influence of roughness on the absorption coefficient for the scenario $rms/\lambda \gg 1$ by introducing a distribution function of rectangular wells with heights h and widths w (see figure 3.8) and finally determining a cumulative absorption coefficient [43]. Figure 3.8 shows the position with the incident angle θ_i and the critical incident angle θ_c at which a photon is able to enter the rectangular well. The cumulative absorption coefficient was measured for different surface roughness values h_0/w_0 for two wavelengths. Figure 3.9 highlights the possibility of absorbing more laser energy by

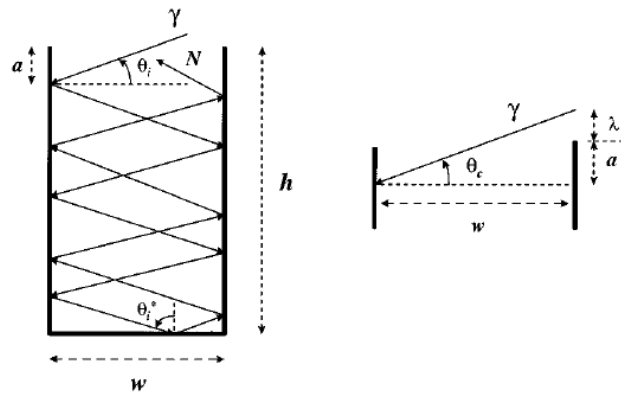


Figure 4.8.: Representation of surface roughness by rectangular shaped wells with height h and width w [43].

increasing the roughness parameter h_0/w_0 . The value $h_0/w_0 = 0$ denotes the original

flat surface with a fraction of absorption of about 0.01. In the case of UV light, raising the surface roughness can enhance the fraction of absorption by an order of magnitude. This shows the influence of surface roughness on the absorption or reflectivity characteristics.

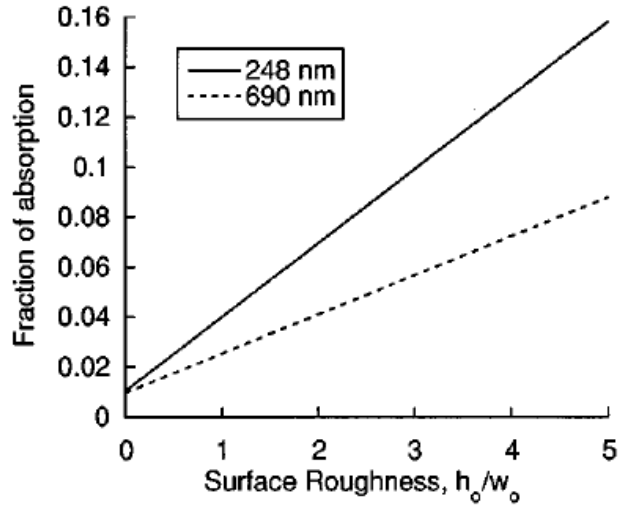


Figure 4.9.: Cumulative absorption coefficient versus surface roughness h_0/w_0 for two different wavelengths on a solid aluminium surface [43].

4.3.4. Influence of the angle of incidence and the polarisation

The reflectivity of a material varies with the incident angle of the beam and the respective polarisation. If the polarisation plane is in the plane of incidence, the beam is denoted as p-polarised. Otherwise, with the polarisation plane perpendicular to the incident plane, the beam is defined as s-polarised [31]. The reflectivities of parallelly and perpendicularly polarised beams can be derived from the general Fresnel formula:

$$R_p = \frac{[n - (1/\cos\theta)]^2 + \kappa^2}{[n + (1/\cos\theta)]^2 + \kappa^2} \quad (4.33)$$

$$R_s = \frac{(n - \cos\theta)^2 + \kappa^2}{(n + \cos\theta)^2 + \kappa^2} \quad (4.34)$$

where n is the real refractive index, κ the extinction coefficient and θ the incident angle.

For dielectric materials under normal incidence, R only depends on the refractive index simplifying the abovementioned equations:

$$R = \left(\frac{n - 1}{n + 1} \right)^2. \quad (4.35)$$

Figure 3.10 plots the reflectivity of steel as a function of incidence angle and beam polarisation. The reflectivity of a p-polarised ray exhibits a particularly strong sensitivity for different incident angles. For the experiments conducted within this thesis, the p-polarised state can be neglected given the s-polarisation of the Nd:YAG laser.

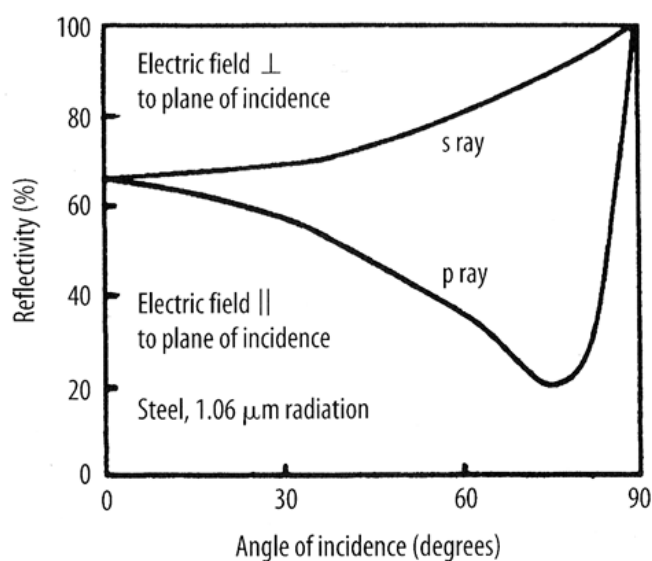


Figure 4.10.: Reflectivity of steel as a function of incidence angle and beam polarisation [31].

4.4. Interference theory and design of periodic structures

One of the most important parts of the theoretical framework of this thesis is the concept of interference and its application to the design of periodic structures in different metallic surfaces. Therefore, in the following chapter, the fundamental theoretical aspects of interfering waves will be explained. At first, a scalar approximation for the interference of two linearly polarised plane waves is given and subsequently extended to the interference of multiple beams. In conclusion, the vectorial properties of light will be added and the general expressions for two interfering beams will be derived. In this context, a case-by-case analysis is performed for constructive and destructive interferences.

4.4.1. The approximation of scalar waves

In addition to interference phenomena, the diffraction of light plays an important role. However, a clear distinction between diffraction and interference is difficult due to their relation. Diffraction through a single slit can be considered as the interference of a large number of partial waves reassembling into a new wavefront according to the well known *Huygens-Fresnel principle* [44]. The mathematical formulation of the diffraction theory always contains a propagating wave which is perturbed by an object such as a single slit with dimensions in the order of the wavelength. Consequently, the amplitude and phase of the wave will be changed. In some cases, an analytical solution for diffraction or interference problems is difficult because the exact geometry and dielectric properties of the object must be known and the interaction of the diffracted wave with the original wavefield should be implemented. Therefore, a more feasible approach is based on the assumption that the amplitude and phase of the wave can be described by scalar values. Polarisation effects should be neglected. This approach is called *scalar wave approximation*. First of all, the scalar approach shall be applied to the superposition of waves having the same frequency ν . The scalar wave equation can be expressed in Cartesian coordinates as [45]:

$$\frac{\partial^2 E}{\partial x^2} + \frac{\partial^2 E}{\partial y^2} + \frac{\partial^2 E}{\partial z^2} = \frac{1}{c^2} \frac{\partial^2 E}{\partial t^2}. \quad (4.36)$$

One possible solution to the wave equation is given by:

$$E(x, t) = E_0 \sin[\omega t - (kx + \epsilon_p)] \quad (4.37)$$

where ϵ_p represents the initial phase constant. Separating the spatial from the temporal part of the phase leads to: $\alpha(x, \epsilon_p) = -(kx + \epsilon_p)$. Let us define two waves with the same propagation velocity and frequency:

$$E_1 = E_{01} \sin(\omega t + \alpha_1) \quad (4.38)$$

and

$$E_2 = E_{02} \sin(\omega t + \alpha_2). \quad (4.39)$$

According to the superposition principle, $E_{total} = E_1 + E_2$. This results in:

$$E_{total} = E_{01}(\sin(\omega t)\cos(\alpha_1) + \cos(\omega t)\sin(\alpha_1)) + E_{02}(\sin(\omega t)\cos(\alpha_2) + \cos(\omega t)\sin(\alpha_2)). \quad (4.40)$$

Once the temporal parts are removed and addition theorems are applied, the amplitude becomes:

$$E_0^2 = E_{01}^2 + E_{02}^2 + 2E_{01}E_{02}\cos(\alpha_2 - \alpha_1) \quad (4.41)$$

and the phase:

$$\tan\alpha = \frac{E_{01}\sin(\alpha_1) + E_{02}\sin(\alpha_2)}{E_{01}\cos(\alpha_1) + E_{02}\cos(\alpha_2)}. \quad (4.42)$$

In conclusion, the total flux density E_{total} is not simply the sum of the partial flux densities. There is an additional term called the interference term $2E_{01}E_{02}\cos(\alpha_2 - \alpha_1)$. Here, the brackets $(\alpha_2 - \alpha_1)$ represent the phase difference δ between the interfering waves. For $\delta = 0, \pm 2\pi, \pm 4\pi, \dots$ the resulting amplitude is maximal (constructive interference) and for $\delta = \pm\pi, \pm 3\pi, \pm 5\pi, \dots$ it is minimal (destructive interference). The phase difference can be expressed by the difference of the initial phase constants $(\epsilon_1 - \epsilon_2)$ or the difference of the optical paths $(x_1 - x_2)$:

$$\delta = \frac{2\pi}{\lambda}(x_1 - x_2) + (\epsilon_1 - \epsilon_2). \quad (4.43)$$

Waves with a fixed relationship between the initial phase constants are by definition coherent.

Considering the interference of n coherent waves with a constant phase difference, the following general expression can be derived [45]:

$$E = \sum_{i=1}^N E_{0i} \cos(\alpha_i \pm \omega t) \quad (4.44)$$

and subsequently

$$E_0^2 = \sum_{i=1}^N E_{0i}^2 + 2 \sum_{j>1}^N \sum_{i=1}^N E_{0i} E_{0j}. \quad (4.45)$$

This is equivalent to:

$$E_0^2 = \left(\sum_{i=1}^N E_{0i} \right)^2. \quad (4.46)$$

If each amplitude E_{0i} is set to be E_{01} then the final result is [45]:

$$E_0^2 = (nE_{01})^2 = n^2 E_{01}^2 \quad (4.47)$$

where n is the number of interfering beams. So far, only the interference of waves having the same frequency or wavelength have been considered. In reality, most of the waves are not strictly monochromatic but quasi-monochromatic. Two plane waves propagating in the same direction but with different frequencies yields [45]:

$$E_1 = E_{01} \cos(k_1 x - \omega_1 t) \quad (4.48)$$

$$E_2 = E_{02} \cos(k_2 x - \omega_2 t) \quad (4.49)$$

$$\Rightarrow E_{total} = 2E_{01} \cos(k_m x - \omega_m t) \cos(\bar{k}x - \bar{\omega}t) \quad (4.50)$$

where \bar{k} and $\bar{\omega}$ are the average wave number and angular frequency. k_m and ω_m are the modulation wave number and angular frequency [45]. The resulting wave is a so called *beat* with a time-dependent amplitude (see figure 3.11).

4.4.2. The vector character of electromagnetic fields

In the beginning of this chapter, the scalar approximation was introduced with two interfering waves. Now, the vectorial properties of electromagnetic fields shall be introduced for a more general expression to be derived. First, several assumptions about the waves are necessary:

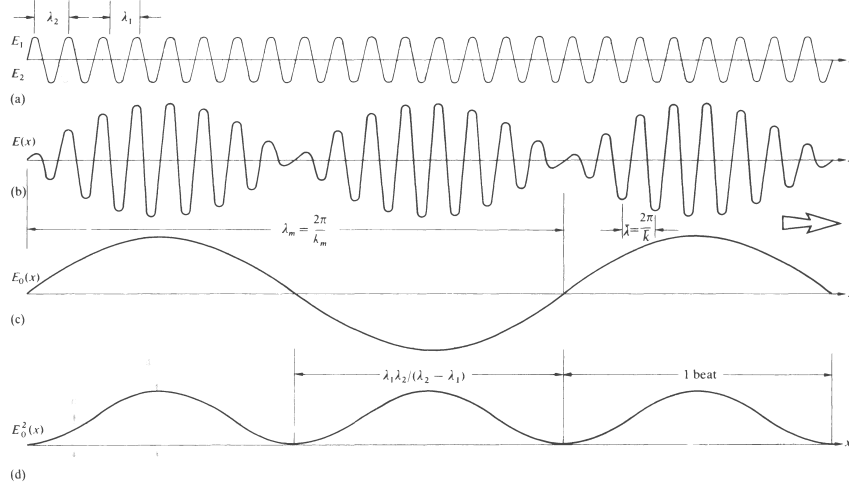


Figure 4.11.: Superposition of two harmonic waves having the same amplitude but different frequencies. The resulting wave is a beat [45].

1. The waves are monochromatic.
2. Only plane and linearly polarised waves should be considered.
3. The respective waves propagate in a homogeneous medium.

Waves of the following form should be regarded:

$$\vec{E}_1(\vec{r}, t) = \vec{E}_{01} \cos(\vec{k}_1 \vec{r} - \omega t + \epsilon_1) \quad (4.51)$$

$$\vec{E}_2(\vec{r}, t) = \vec{E}_{02} \cos(\vec{k}_2 \vec{r} - \omega t + \epsilon_2). \quad (4.52)$$

Superposition leads to:

$$\vec{E}_{total}^2 = \vec{E}_1^2 + \vec{E}_2^2 + 2\vec{E}_1 \vec{E}_2 \quad (4.53)$$

with an intensity:

$$I = I_1 + I_2 + I_{12}. \quad (4.54)$$

where $I_1 = \langle \vec{E}_1^2 \rangle_T$, $I_2 = \langle \vec{E}_2^2 \rangle_T$ and $I_{12} = 2 \langle \vec{E}_1 \vec{E}_2 \rangle_T$. The last expression for I_{12} is called *interference term*. The term in brackets expands to $\langle \vec{E}_1 \vec{E}_2 \rangle_T$ [45]:

$$\langle \vec{E}_1 \vec{E}_2 \rangle_T = 1/2 \vec{E}_{01} \vec{E}_{02} \cos(\vec{k}_1 \vec{r} + \epsilon_1 - \vec{k}_2 \vec{r} - \epsilon_2). \quad (4.55)$$

Thus, the interference term:

$$I_{12} = \vec{E}_{01}\vec{E}_{02}\cos\delta. \quad (4.56)$$

with a phase difference $\delta = (\vec{k}_1\vec{r} - \vec{k}_2\vec{r} + \epsilon_1 - \epsilon_2)$. For $\vec{E}_{01}\perp\vec{E}_{02}$ (and thus $\vec{E}_1\perp\vec{E}_2$), it follows $I_{12} = 0$ and $I = I_1 + I_2$. For E_{01} parallel to E_{02} , the interference term can be simplified to:

$$I_{12} = 2\sqrt{I_1I_2}\cos\delta \quad (4.57)$$

and thus a total intensity:

$$I_{total} = I_1 + I_2 + 2\sqrt{I_1I_2}\cos\delta. \quad (4.58)$$

Depending on the phase difference δ , the following case-by-case analysis can be obtained [45]:

1. For $\cos\delta = 1$, the maximum intensity I_{max} is achieved with $I_{max} = I_1 + I_2 + 2\sqrt{I_1I_2}$ for $\delta = 0, \pm 2\pi, \pm 4\pi, \dots$ which is named *complete constructive interference*.
2. If $0 < \cos\delta < 1$ then $I_1 + I_2 < I < I_{max}$ and the waves are out of phase but showing constructive interference.
3. For $\delta = \pi/2$ it follows $\cos\delta = 0$ and $I = I_1 + I_2$.
4. If $0 > \cos\delta > -1$ then $I_1 + I_2 > I > I_{min}$. This refers to *destructive interference*.
5. Minimum intensity is given for $\cos\delta = -1$ then $I_{min} = I_1 + I_2 - 2\sqrt{I_1I_2}$ with a phase shift of π . This is fulfilled for $\delta = \pm\pi, \pm 3\pi, \pm 5\pi, \dots$

Finally, assuming that $\vec{E}_{01} = \vec{E}_{02}$, then $I_1 = I_2 = I_0$ and the equation (3.58) for two interfering laser beams having the same amplitude takes the form:

$$I = 4I_0\cos^2\left(\frac{\delta}{2}\right) \quad (4.59)$$

for two interfering beams having the same amplitude. Varying the number of interfering (laser) beams, numerous pattern geometries are possible, ranging from e.g. line- (two beams) to dot-like (three beams) geometries, which can be seen in figure 3.12. The pictures on top show calculated intensity distributions for the aforementioned geometries. In the middle and in the last row, corresponding white light interferometric pictures as

well as scanning electron micrographs of real metallic surfaces after the laser interference patterning are presented.

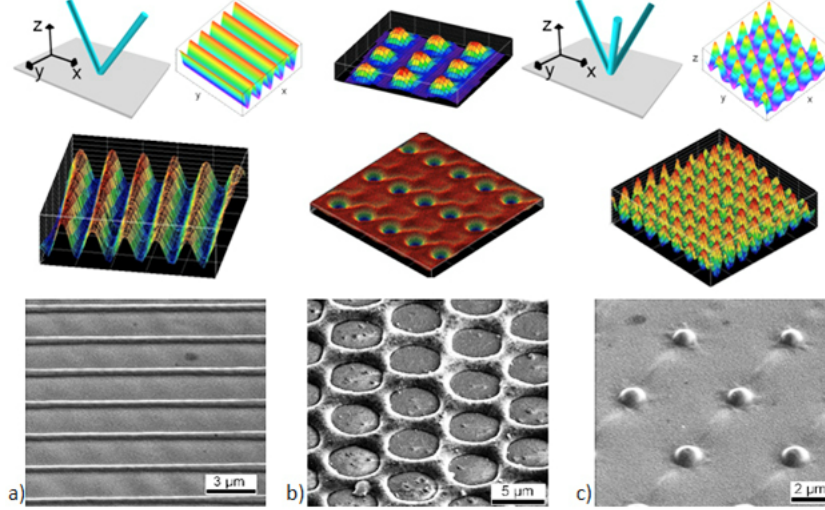


Figure 4.12.: Beam configuration and calculated intensity distribution (top), white light interferometry measurements (middle) and scanning electron micrographs (bottom) of the corresponding laser patterns on different material surfaces [46].

4.5. Thermal simulation

Thermal simulations were carried out using the *COMSOL Multiphysics* and *FlexPDE* software. For the Au, Pt and W thin films, the liquid and solid interphase during the resolidification process was simulated by *FlexPDE*. In addition, periodicity-dependent temperature distributions, heating/cooling rates and fractions of molten material were modelled for TiAl multilayer thin films by *COMSOL Multiphysics*. Finally, the thermal response of stainless steel surfaces and a geometry-dependent simulation of the heat input in the case of micro-coined aluminium specimens were performed by *COMSOL*. The simulation is generally based upon the heat diffusion equation [47]:

$$\rho c_p \frac{\partial T}{\partial t} - \nabla(\lambda_{th} \nabla T) = Q \quad (4.60)$$

where ρ denotes the density, c_p the specific heat capacity, λ_{th} the heat conductivity and Q the laser heat source. For the analysis, the following assumptions were made [48]:

- No radiation loss from the surface.
- Convection above the surface can be neglected.
- No convection occurs due to gravitational or electromagnetic effects during melting.
- The laser energy is considered as a sinusoidal function with a Gaussian distribution in time.
- The heat conduction includes solid/liquid and liquid/vapor transitions, considering the latent heat required to melt and vaporise metals.

The laser heat source $Q(x, z, t)$ at the position x , z and time t can be defined as:

$$Q(x, z, t) = FP(1 - R)I(x)I(z)I(t) + Q_m \quad (4.61)$$

whith F being the fluence (power density), P the structural periodicity, R the reflectivity of the surface, Q_m the melting heat and $I(x)$, $I(z)$ and $I(t)$ the spatial and temporal intensity functions:

$$I(x) = \frac{4}{P} \cos\left(\frac{\pi x}{P}\right)^2 \quad (4.62)$$

$$I(z) = \bar{\alpha} e^{-\bar{\alpha} z} \quad (4.63)$$

$$I(t) = \frac{1}{\sigma\sqrt{2\pi}} e^{-\frac{t-t_p}{2\sigma^2}} \quad (4.64)$$

with

$$\sigma = \frac{\tau_p}{2\sqrt{2\ln 2}} \quad (4.65)$$

and $\bar{\alpha}$ the average absorption coefficient, t_p the pulse time and τ_p the pulse duration. The first term in equation 3.61 represents the linearly normalised energy input. The melting heat Q_m could not be implemented in the simulation as released heat because the software is not capable of modelling phase transformations. In order to circumvent this problem, the specific heat capacity c_p is increased in a temperature range of 50 K by a factor of $\frac{Q_m}{50K}$ around the melting point. Finally, the expression $(1 - R)$ takes into account that due to reflectivity losses a certain fraction of the laser heat input does not contribute to the melting process.

5. Dry friction and contact mechanics

5.1. The nature of friction

5.1.1. Amontons' laws

In practice, engineering surfaces are not atomically smooth but rough. This means that the real contact area in dry and thin film, lubricated contacts is much less than the geometrical contact area, while the local pressures at the contact points are much higher than the average value. This, in turn, strongly influences the tribological performance of machine components, such as friction, wear and rolling contact fatigue. At first, the well known Amontons' laws of friction shall be recapitulated. Amontons studied sliding friction in dry systems in 1699 and found:

1. Friction is proportional to the applied load, $F_R = \mu F_N$ (Amontons' first law).
2. Friction is independent of the geometrical contact area, $F \neq f(A_n)$ (Amontons' second law).
3. Friction depends only very slightly on the sliding speed (Coulomb's first law).

5.1.2. Bowden and Tabor's friction model

In the 1940s, Bowden and Tabor developed an important friction model based on solid/solid adhesion. Adhesion of smooth surfaces implies that friction should rise with increasing contact surface area, in contrast to Amontons' second law. However, Bowden and Tabor realised that because all practical engineering surfaces are rough, the real area of contact is far less than the geometrical contact area, and is a function of the applied

load. According to their model, as rough surfaces approach, the initial contacting asperities deform plastically and adhere until the real area of contact, A_c , is just enough to support the load (see figure 4.1) [49]. For fully plastic deformation, the real area of

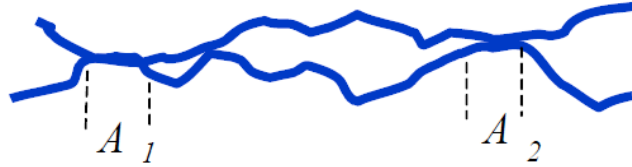


Figure 5.1.: Model of the real area of contact shown for two contacting asperities. A_1 and A_2 define the respective contact areas [49].

contact is proportional to the applied load:

$$F_N = A_c H_m \quad (5.1)$$

where H_m is the effective surface hardness. The force needed to shear these junctions will be proportional to the real area of contact [2]:

$$F_R = A_c \tau_f \quad (5.2)$$

with τ_f being the effective shear strength of the junctions. Therefore, assuming friction increases only from adhesion at contacting asperities, the friction coefficient μ is given by:

$$\mu = \frac{F_R}{F_N} = \frac{\tau_f}{H_m}. \quad (5.3)$$

This simple model explains Amontons' laws but predicts too low values of friction coefficient for clean metals (for metals, shear strength $\tau_f = 0.5 \cdot \sigma_y$, $H_m \approx 3 \cdot \sigma_y$, so μ should be $1/6$, whereas in practice, for clean metals, $\mu \approx 0.5$ to 2) [49].

5.1.3. Tabor's junction growth model

When asperities adhere and a shearing force is applied, the junctions can grow plastically, since both the normal load and the shear force will couple to produce deformation. This will result in an increase in the real area of contact and thus in the friction coefficient μ . Tabor used this to extend his simple model and thus explain the very high coefficients

of friction found with clean metal surfaces. The basic equation is:

$$\mu = \frac{1}{\delta^{1/2}(f^{-2} - 1)^{1/2}} \quad (5.4)$$

where $f = \tau_f/\sigma_y$ is the ratio of the film shear strength of the to the bulk yield strength, and δ a constant with a value of ≈ 9 . Assuming that the hardness can be expressed as $H_m \approx 3 \cdot \sigma_y$, this yields:

$$\mu = \frac{1}{((H_m/\tau_f)^2 - 9)^{1/2}}. \quad (5.5)$$

Equation 4.5 predicts values ranging from ones similar to the simple solution (see equation 4.4) for low ratios of τ_f/H_m , to much larger values for τ_f/H_m than 0.3, i.e. τ_f/σ_y approaching unity [50].

5.1.4. The Prandtl-Tomlinson model

The Prandtl-Tomlinson model for friction is a widely used generic model which describes many substantial effects of dry friction [51]. In his original work, Prandtl assumed that a surface atom of mass m is coupled by a harmonic spring with stiffness k to its equilibrium position in the lattice [52] (see figure 4.2).

Each surface atom perceives a periodic and conservative force F which is given by

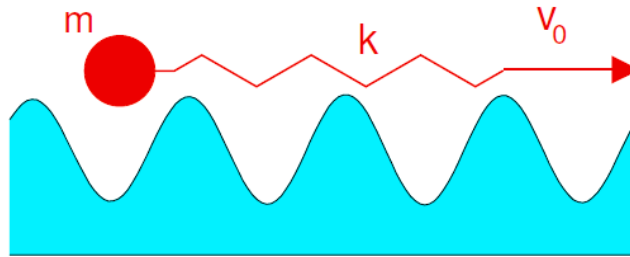


Figure 5.2.: Schematic representation of the one-dimensional Prandtl-Tomlinson model for elastic instabilities [51].

$F = -\nabla V_s$ with V_s being a surface potential of the form $V_s = V_0 \cos(2\pi x/a)$. In this case, V_0 has the coupling strength as a unit of energy, a is the respective lattice constant of the substrate and x is the current position of the surface atom. Additionally, the interaction of the surface atom with not explicitly considered phonons or other

elementary excitations should be integrated by the Stokes friction law [51]:

$$F_{Stokes} = -\gamma v \quad (5.6)$$

where γ denotes the damping coefficient. Based on that, a corresponding equation of motion for the surface atom can be formulated:

$$m\ddot{x} + \gamma\dot{x} = k(v_0t - x) + \frac{2\pi}{a}V_0\sin(2\pi x/a). \quad (5.7)$$

On the basis of the Prandtl-Tomlinson model, it is possible to derive Coulomb's law pointing out the independency of solid friction from sliding friction [53]. At first, let us consider a coupling k to an equilibrium position which is larger than a critical value indicated by k_{crit} representing the maximum curvature of the substrate potential. Consequently, there will always be one distinct equilibrium position x_{eq} . This leads to a linear relationship between the friction and v_0 for small values of v_0 .

On the other hand, if the coupling is relatively weak with regard to k_{crit} , then several mechanically stable positions are possible at certain instances of time as can be seen in figure 4.3:

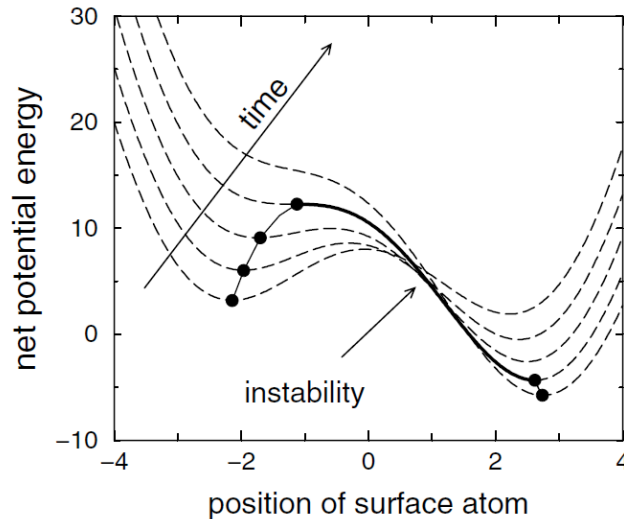


Figure 5.3.: Illustration of an instability in the Prandtl-Tomlinson model [51].

The time dependence of the combined substrate and spring potential reveals that mechanically stable positions disappear at a particular time due to the motion of the spring. The energy difference between the initial and the final position will be first of all transformed into kinetic energy and later on dissipated into the lattice. The energy loss ΔE_{diss} mainly depends on the frequency of the instabilities. Hence, ΔE_{diss} increases linearly with the displacement of the solids thus being independent of v_0 (Coulomb's law).

The Prandtl-Tomlinson approach is a minimalistic model incorporating the basic idea of Coulomb with certain limitations. Especially the choice of the surface potential as well as occurring plastic deformation can be critical. Nevertheless, it is a helpful tool of high clarity to combine a conservative periodic force and a velocity-dependent dissipative force acting on a solid [52].

5.1.5. Structural lubricity and geometrical interlocking

In the introduction, many different methods for modifying the frictional behaviour of contacting solids have already been presented. Apart from this approach, there is a state of vanishing friction called superlubricity or structural lubricity between two contacting bodies was first proposed by Hirano and Shinjo in the nineties [54]. A superlubric state is characterised by zero static friction meaning that the solids are able to slide without any resistance to motion. A one dimensional friction model shall be presented to describe this state (see figure 4.4) [55].

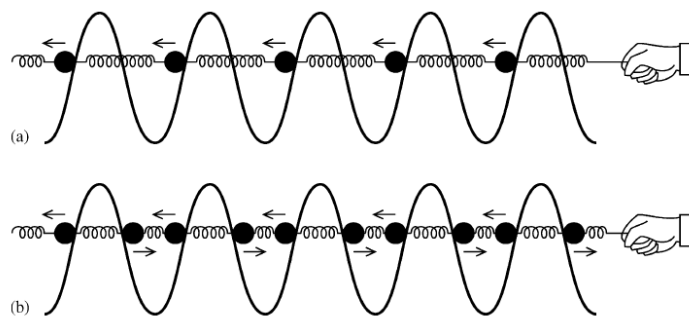


Figure 5.4.: One-dimensional friction model. In (a) friction is not zero and in (b) friction is reduced to zero. The arrows denote the directions of the resulting forces [55].

For reasons of simplicity, the atoms of one solid are connected by springs in one dimension experiencing the surface potential of another body. In the first case, the ratio of the lattice constants of the interacting solids should be a rational number. The solid will slide, if the atoms of the chain uniformly overcome the surface potential peak of the other body. The direction of the resulting force is opposite to the external pulling force. For a coordinated movement of the atoms, it is necessary for the external force to be larger than the total amount of the individual atomic contributions. Apart from that, if two solids have an irrational lattice constant ratio, the contact is incommensurate and the lateral forces systematically compensate each other thus leading to zero friction. At first, Hirano and Shinjo studied the frictional anisotropy of muscovite mica depending on the lattice misfit angle. They could show that in the case of incommensurate i.e. non-matching contacts the frictional force is significantly reduced compared to commensurate i.e. matching contacts.

Figure 4.5 shows the results of their experimental work in which the friction force is plotted versus the twist angle between the mating surfaces for different surface temperatures and relative water vapor pressures [54]. The measured friction force varies between 2.5 and $5.0 \cdot 10^{-4}$ N for $\theta = 0^\circ$ and $\theta = 90^\circ$ under a dry atmosphere and at a high surface temperature. The effect almost disappears, as soon as the relative vapor pressure increases and the surface temperature is decreased to room temperature. This can be mainly attributed to the influence of surface contaminations such as adsorbates, hydrocarbons and so on. He and Müser already pointed out the importance of clean surfaces as a prerequisite for superlubric conditions [56]. According to their work, adsorbed atoms of lubricants or contaminations can be preferentially found in regions of sufficient space between the contacting bodies thus leading to an interlocking of the respective surfaces. As a consequence, a characteristic slope with an angle α must be overcome to shift the solid relatively to the substrate. This mechanism is also valid for surfaces with different lattice constants (incommensurate contacts) [57].

Weakly bound adsorbed atoms have a decisive effect on the sliding process and may be able to raise frictional forces by rearranging themselves in corrugated potentials between the mating surfaces [58].

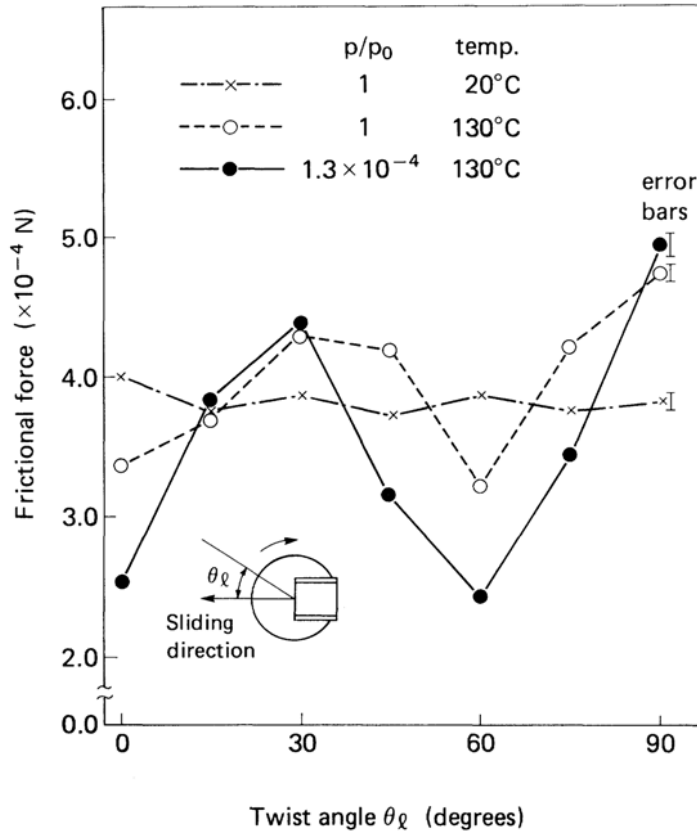


Figure 5.5.: Frictional force as a function of twist angle between two mating mica surfaces for different surface temperatures and relative water vapor pressures [54].

Recently, Dienwiebel et al. provided experimental evidence of superlubricity by studying the frictional behaviour of a graphite substrate and a graphite flake fixed to a tip of a frictional force microscope [59]. Figure 4.6 highlights the main results of said research. Depending on the rotation angle Φ , two different frictional force peaks are visible at about 60° from each other. This distance can be traced back to the hexagonal symmetry of graphite. The friction peaks denote the positions with perfect interlocking of the contacting surfaces. As a consequence the average friction forces are high. After having rotated the sample, the surfaces are no longer well aligned resulting in an incommensurate contact accompanied by nearly vanishing friction forces.

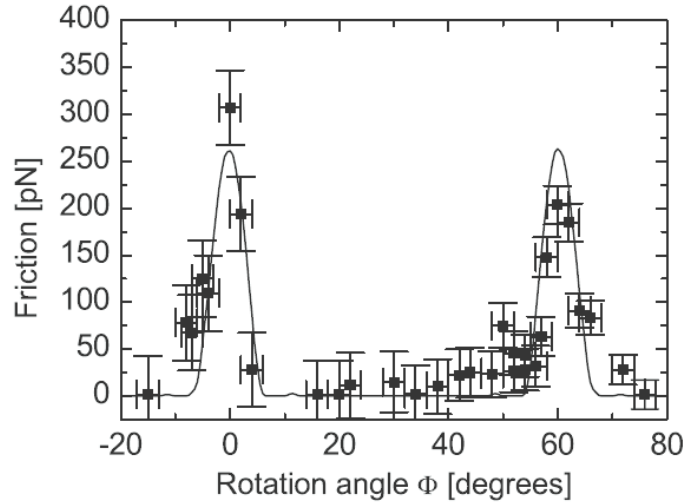


Figure 5.6.: Average friction force as a function of the rotation angle of a graphite specimen around an axis perpendicular to the surface. The plot fitting the data points is based on a simulation of a Tomlinson model for graphite [59].

Beyond the atomistic scale, Sondhauß et al. have demonstrated the influence of mesoscopically patterned contacts on frictional properties by using FIB [60]. Figure 4.7 summarises the experimental approach. Titanium spheres with fixed radii of 2.3 and 7.9 μm were mounted on the tip of a friction force microscope. Additionally, silicon substrates were FIB patterned with varying groove widths ranging from 500 to 3500 nm. Finally, it could be shown that for specific groove widths, a modification of the frictional forces is possible. This result is mainly driven by geometrical interlocking effects. In this sense, the term superlubricity would be misleading compared to other physically well known effects such as superconductivity and superfluidity. Strictly speaking, superlubricity or better said structural lubricity requires sufficiently flat specimens, clean and chemically inert surfaces and a moderate normal pressure in order to avoid plastic deformation [61]. Within this thesis, experimental results related to the geometrical interlocking of laser patterned surfaces will be presented and discussed. The main differences with the work of Sondhauß et al. are the patterning technique, the used materials (V2A-steel instead of silicon surfaces), the patterning of both interacting surfaces and the study of the influence of the relative specimen alignment for the as-patterned contacting surfaces.

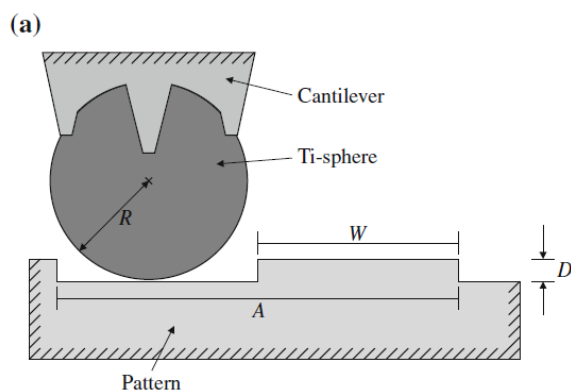


Figure 5.7.: Schematic overview of the measuring set up. A titanium sphere with fixed radius is mounted to a tip. Patterned silicon surfaces fabricated by FIB are used with different groove widths [60].

5.1.6. Surface roughness parameters

The surface topography and roughness have a decisive influence on friction and wear properties of contacting solids. It is well known that engineering surfaces are not ideally smooth but rather present roughness values on different scales ranging from the macroscopic to the microscopic level [62][63][64][65] (figure 4.8). For a detailed description of the original surface roughness and the as-patterned specimens, at least two parameters are necessary, one indicating the asperity height such as the arithmetic average height (R_a), the root mean square (rms) roughness or the Swedish height (H) and the other taking the distribution into account e.g. correlation length or peak density [49].

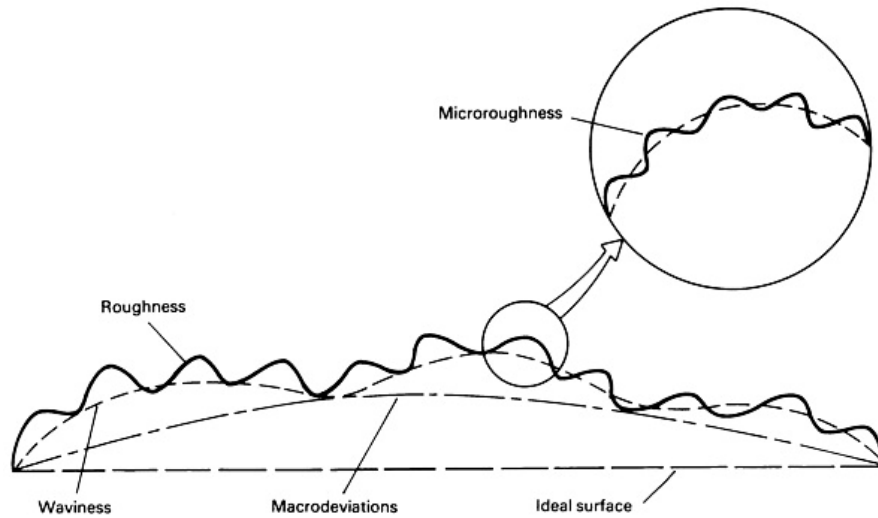


Figure 5.8.: Geometrical deviations of technical surfaces composed of roughness values on different scales [66].

Both the height and spatial structure of surfaces are better described by functions, such as the height distribution and the autocorrelation function or power spectrum. Within this thesis, respective surface parameters were recorded and analysed by white light interferometry based upon 3-D xyz-data of the surface. In order to get a representative value, a stitching over a complete laser spot was performed and the surface parameters were determined on this basis. It is important to note that because of the strong scale dependence of surface roughness, the values are directly related to the measurement scale and the sampling interval [67]. Sayles and Thomas could show that there is a linear relation between the rms value and the measured distance [68]. Furthermore, integral roughness parameters are very often not suitable to accurately describe surfaces. Two surfaces may have identical R_a values, yet show a completely different behaviour [67]. In this context, it is useful to study wavelength-dependent parameters and to consider the corresponding sampling interval [65][68]. Generally, at longer sampling lengths, imperfections of the specimen are included. In profilometry, this is controlled by selecting an adequate cut-off length, L (a filter to ignore wavelengths above a certain value).

In the following, several surface parameters which were used for the topography and roughness characterisation will be briefly introduced and discussed. At first, the rms value shall be defined. A major advantage of this parameter compared to the R_a value

is the more pronounced sensitivity for height deviations. The rms result describes the standard deviation of surface heights (depths) from a center line within a sampling length denoted by L (see figure 4.9).

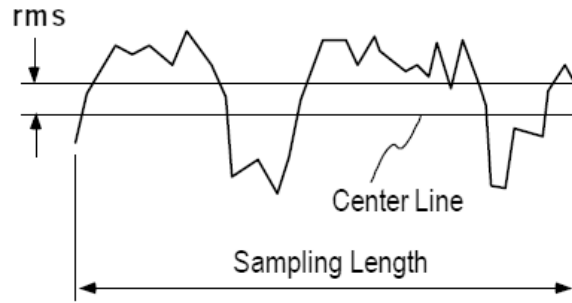


Figure 5.9.: Definition of the root mean square roughness value (rms) of a given cross-section profile plot within a sampling length L_s [69].

It is calculated by the following expression:

$$rms = \sqrt{\frac{1}{L} \int_0^L z^2 dx}. \quad (5.8)$$

Another adequate parameter to get a height information of a given profile is the so called *Swedish height* H . This value is less sensitive to specific surface peaks than the conventional peak to valley parameter. Figure 4.10 illustrates the parameter H .

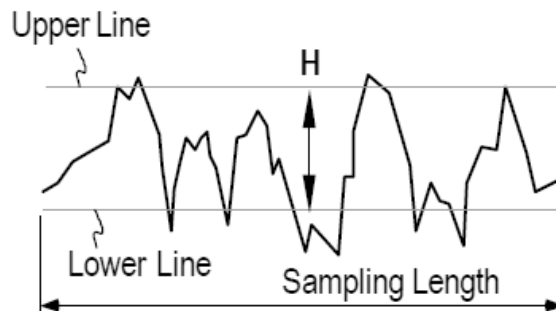


Figure 5.10.: Definition of the Swedish height H of a cross section profile [69].

The Swedish height denotes the distance of two reference lines within a cross section profile. The upper line is localized inside a profile exposing 5 % of the data points

whereas the lower line exposes 90 % of the data [69]. Apart from height parameters, the bearing capability of a given profile is characterised by bearing ratio or *Abbott-Firestone* plots. The bearing ratio t_b , which is usually expressed as a percentage, is the ratio of the bearing length at a particular depth. Generally, a reference line is drawn parallelly to the profile center intersecting the respective profile. Finally, the sum of the individual bearing lengths is related to the overall sampling length L_s (figure 4.11) [69].

$$t_b = \frac{1}{L_s} \sum_{i=1}^n l_i \quad (5.9)$$

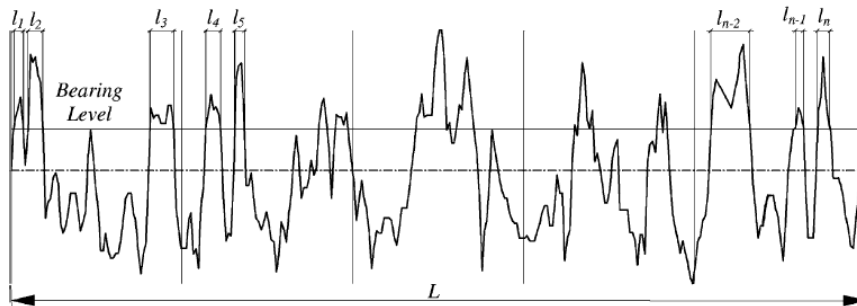


Figure 5.11.: Calculation of the bearing length t_b of a profile [70].

Consequently, the bearing ratio plot displays the bearing ratio t_b at different profile depths of the complete data matrix. This is shown in figure 4.12 for a corresponding surface profile.

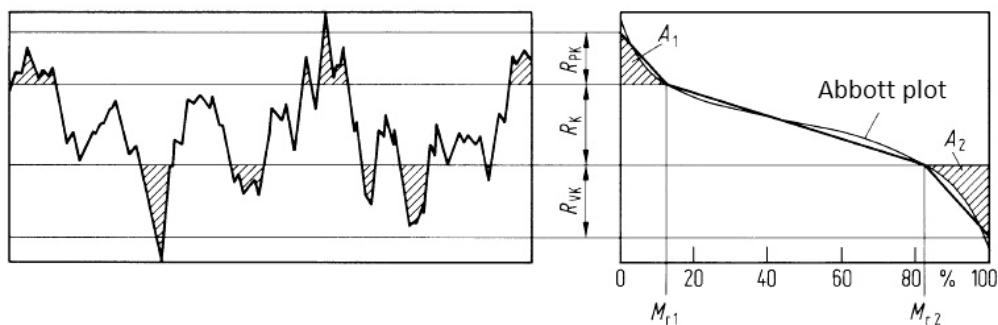


Figure 5.12.: Surface profile and resulting Abbott-Firestone plot with the belonging Abbott parameters [71].

Here, A_1 represents the quantity of solid heights, A_2 the quantity of solid valleys, R_k the core roughness depth, R_{vk} the reduced valley depth, R_{pk} the reduced peak height and finally M_{r1} and M_{r2} the bearing ratio at the peak-to-core and core-to-valley transition regions. The reduced peak height R_{pk} is mainly influencing the running-in regime whereas the reduced valley depth indicates the potential lubricant retainment capability. A more detailed overview of the Abbott parameters can be found in [72] and [73]. In particular, Bigerelle et al. show an interesting comparison between different surface profiles (e.g. sinusoidal, half-sinusoidal and peaked functions) and corresponding bearing ratio plots and Abbott parameters [73].

Based upon the bearing ratio plot, the *Amplitude Density Function* (ADF) can be derived showing the frequency distribution of the profile heights of a given surface profile. Moreover, four different spectral moments can be calculated related to the ADF. The first and second spectral moments are simply the arithmetic mean and root mean square roughnesses of a profile. The third spectral moment is denoted as the *skewness* R_{sk} . This parameter is determined by:

$$R_{sk} = \frac{1}{n(rms)^3} \left(\sum_{i=1}^n z_i^3 \right) \quad (5.10)$$

with n being the number of data points. More plateau-like surfaces are characterised by a negative skewness value typically ranging between -1.6 and -2.0 [69] having good bearing properties. In contrast, a positive skewness is an indicator for a more peaked surface (see figure 4.13).

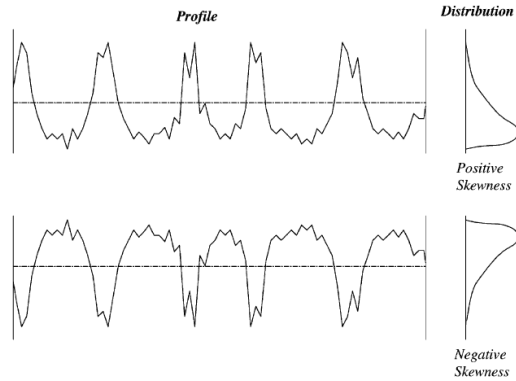


Figure 5.13.: Definition of skewness (R_{sk}) for more peaked surfaces (top) having a positive value and bearing surfaces (bottom) with a negative R_{sk} value. The ADF for the two cases is shown on the right [70].

Concluding, the fourth spectral moment is called *kurtosis* R_{ku} describing the sharpness of the amplitude density function. The kurtosis can be calculated by:

$$R_{ku} = \frac{1}{n(rms)^4} \left(\sum_{i=1}^n z_i^4 \right) \quad (5.11)$$

Surfaces with a kurtosis larger than 3 are defined as leptokurtoic and for values smaller than 3 platykurtoic.

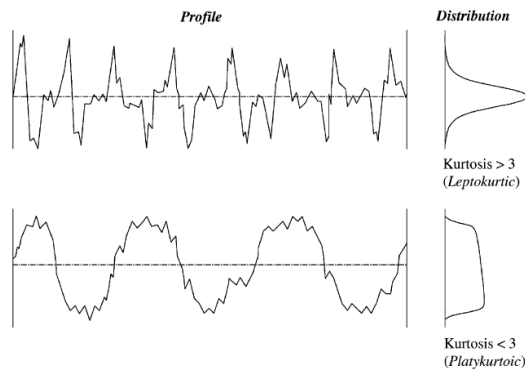


Figure 5.14.: Definition of the kurtosis (R_{ku}) and distinction between leptokurtoic and platykurtoic surfaces [70].

A perfectly random surface has a R_{ku} value of 3. The larger the distance from this value, the more repetitive a surface is (figure 4.14) [69].

5.2. Contact models

There has been an increasing interest in the modelling of contact and friction issues during the recent years [74]. The uncertainties involved in the representation of frictional interfaces now represent one of the most significant uncertainties in predicting the behaviour of mechanical systems. After advances in the mid-20th century, progress was more limited, but interest in the area of friction has recently seen a resurgence. This is partly due to improvements in measuring techniques, and partly as a result of improved computational tools. There is now a recognition of the importance of frictional contact in the behaviour of complex engineering systems. The remaining question is still dealing with the most accurate asperity contact theory between rubbing surfaces. There has been a lively debate about this topic for many years now and the contact mechanics community may be divided roughly in two groups, one favouring the so called multi-asperity theories based upon the early work of Greenwood and Williamson [75] and the other preferring Persson's contact theory [76]. Looking at relatively small loads, both theories generally predict a linear relationship between the real contact area and the applied normal load. According to Bowden and Tabor [2], contacting asperities are welded together and finally plastically deformed during a relative sliding motion. Assuming a constant yield stress, this results in a direct proportionality between the normal force and real area of contact. Despite that, it seems as if for many daily operating engineering components, the assumption of plastic asperity deformation cannot be maintained over the entire lifetime of machines. Instead, plastic deformation might occur in the very beginning. After having reached a steady-state, the load may be supported by elastic deformation of respective asperities forming individual contacts [77].

The multi-asperity contact theory is a generalised Hertzian approach taking into account e.g. the asperity curvature and the height distribution. The classical Greenwood and Williamson model considered a surface composed of identical spherical asperities with a random height distribution [75]. Thereafter, some modifications were performed by McCool thus leading to the Greenwood-McCool model. In this model, an elastic flat plane and a rigid counter body are in direct contact. The surface roughness of the respective counter body can be thought of as different spherical summits with the same curvature radius and a random height distribution. Additionally, it was assumed that the summits are distributed according to a Gaussian probability distribution with a standard deviation.

However, this assumption is not so strict because many technical surfaces are subject to normal distributions [78].

Apart from Greenwood and McCool, Bush, Gibson and Thomas developed a fundamental asperity contact theory, regarding paraboloidal asperity geometries and an elliptic contact without focussing on the asperity curvature radii [77]. Nevertheless, recent calculations of Carbone and Bottiglione revealed some errors related to load values [77]. Furthermore, Nayak and Thomas considered summits as rigid spherical asperities with a curvature equal to arithmetic mean curvature [79]. In 2006, Greenwood made some modifications to his previous theory by proposing a simplification of the work of Bush, Gibson and Thomas [80]. Within this modified theory, the asperity curvature is described by a geometric mean curvature of the surface. The major drawback of all multi-asperity models is that they only predict linearity between the applied normal load and the real contact area for very small loads. Under full contact conditions, there is also a strong deviation from linearity.

In contrast, Persson's model starts from full contact conditions rather than assuming that the real area of contact only represents a small part of the nominal area. Here, the contact between an elastic half-space and a rigid counter body is taken into consideration. An advantage of Persson's theory is that the model allows for very accurate results when the real contact area is up to 15 % of the nominal one [77][76].

However, some strong approximations are made within Persson's theory and by simple modifications of Greenwood's theory similar and reasonable results can be obtained [77]. So far, only non-adhesional contacts have been considered. At small scales and loads, the surface to bulk ratio becomes significant. Therefore, adhesion arising from attractive forces is generally not negligible [81]. Two limiting cases can be basically identified:

- Short-ranging surface forces compared to elastic deformations (e.g. compliant materials and strong adhesion-*Johnson-Kendall-Roberts* or JKR-theory)
- Long-ranging surface forces (e.g. stiff materials, weak adhesion forces-*Derjaguin-Müller-Toporov* or DMT-regime [81])

By introducing and defining a dimensionless parameter μ_{Adh} (*Tabor parameter*), the transition between the different regimes can be described quantitatively [82].

Maugis defined an equivalent transition parameter λ_{Adh} [83]. If λ_{Adh} is larger than 5, the Johnson-Kendall-Roberts model is used. On the other hand, if λ_{Adh} is smaller than 0.1, the Derjaguin-Müller-Toporov model is to be applied.

All values in between denote a transition between the JKR and DMT model [81]. In the case of surface roughness, it is well known that depending on the size of the contact, adhesion may only have a marginal influence. Popov showed for a contact between a rigid flat plane and a rigid rough surface having a characteristic height h and structural wavelength λ [84]:

$$h^2 < \frac{4\gamma\lambda}{G} \quad (5.12)$$

with γ being the surface energy in J/m² and G the shear modulus of the used material in GPa. Below a critical roughness value, the surface can be considered as ideally flat potentially leading to adhesion effects. In contrast, above a certain roughness, there will be only limiting contact points resulting in a significant decrease in adhesional contributions. Apart from h and λ , the adhesional part also depends on the surface energy and the shear modulus. For most metallic surfaces, the shear modulus is much larger than for rubber materials for example (with a typical shear modulus around 1 MPa) [84]. By using typical values for the structural height h , the wavelength or periodicity λ , surface energies and finally shear moduli of the laser patterned materials, equation 4.12 demonstrated that within this thesis, adhesion might not have a strong effect on the frictional experiments. After all, it is not aimed at identifying all frictional contributions and finally to predict the friction coefficient for the respective arrangements. Usually, adhesion should act in a similar way in the different measurement directions. In fact, direction-dependent measurements revealed large differences. Therefore, adhesion will not be further considered in the following discussion.

5.2.1. The Hertzian contact

Classical contact mechanics is undoubtedly connected to Heinrich Hertz. In 1882, Hertz analysed and finally solved the problem of two elastically contacting bodies with curved surfaces [85]. Originally, Hertz tried to understand how the optical properties of multiple, stacked lenses may change depending on the clamping forces holding the optics together. In the following, two elastic bodies forming a non-conformal contact shall be considered. In this context, the shape and size of the contact and pressure distribution are to be studied and the basic equations such as the Hertzian contact radius as a function of normal force as well as the pressure in the centre of the contact region shall be presented for point contacts.

At first, several assumptions with regard to the applicability of the Hertzian contact theory are necessary:

- surfaces are continuous (smooth) and non-conformal i.e. high local pressures within a small contact area typically in the case of point contacts,
- small strains and within the elastic limit,
- elastic deformation as for half space (or plane) thus $a \ll R$,
- the surfaces are frictionless,
- adhesional forces are to be neglected

The point contact which has to be solved is schematically represented in figure 4.15.

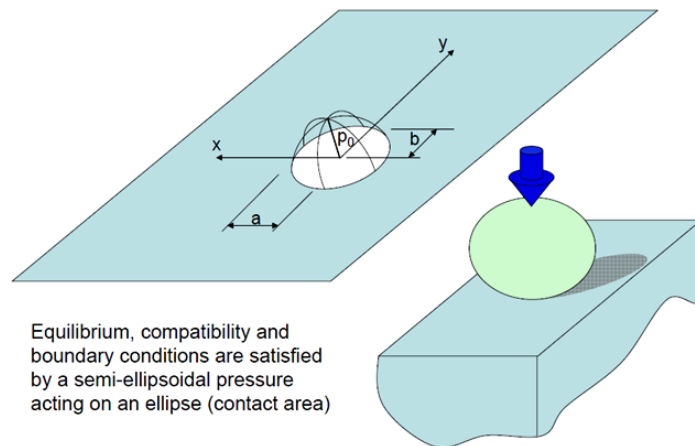


Figure 5.15.: Schematic overview of a Hertzian point contact with the respective dimensions and the maximum Hertzian contact pressure p_0 [49].

Looking at the contact in more detail (see figure 4.16), it is possible to determine the displacement $w(r)$ at a distance, r , from the normal force F_N :

$$w(r) = \frac{1 - \nu^2}{\pi E_Y} \frac{F_N}{r} \quad (5.13)$$

where ν_P is Poisson's ratio (typically 0.3 for metals) and E_Y the corresponding Young's modulus. Without further derivation, the following basic equations for the Hertzian

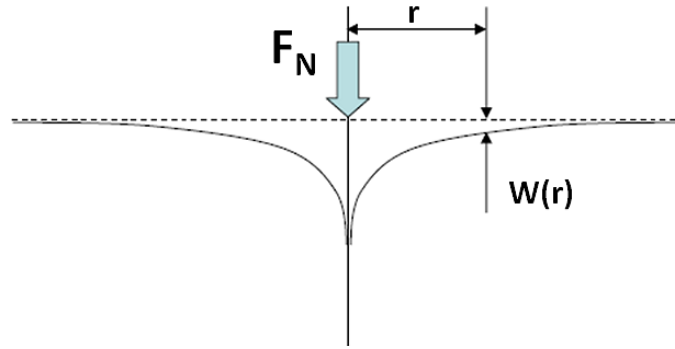


Figure 5.16.: Schematic figure of the point contact and the resulting vertical displacement $w(r)$ [49].

contact radius a , the maximum Hertzian contact pressure p_0 and the mean contact pressure \bar{p} for a point contact shall be summarised:

$$a = \left(\frac{3 F_N R}{4 E^*} \right)^{1/3} \quad (5.14)$$

with F_N the normal load, R the radius of the ball and E^* the reduced Young's modulus given by:

$$\frac{1}{E^*} = \left(\frac{1 - \nu_1^2}{E_{Y1}} + \frac{1 - \nu_2^2}{E_{Y2}} \right). \quad (5.15)$$

$$p_0 = \left(\frac{1}{\pi} \right) \left(\frac{6 F_N E^{*2}}{R^2} \right)^{1/3}. \quad (5.16)$$

$$\bar{p} = \frac{F_N}{\pi a^2} = 2/3 p_0. \quad (5.17)$$

5.2.2. The Greenwood-Williamson model

Bowden and Tabor's model explains Amontons' first two laws on the basis of a very small area of contact A_c , which is proportional to the applied load and independent of the geometrical area [2]. Since friction is proportional to this area, it is also proportional to the load. However, their model requires that the asperities be deformed plastically. In practice, some of the load will be supported by elastically deformed asperities. Amontons' law requires that the real area of contact also be proportional to the load in elastic contact. Archard, in 1957 [50] and subsequently Greenwood and Williamson in 1966,

verified that even for elastic asperity deformation, a statistically-distributed, rough surface will result in $A_c \propto F_N$ [75]. In particular, Greenwood and Williamson showed how the contact deformation depends on the topography of the surface, and established the criteria for differentiating surfaces with elastic and plastic contacts by introducing a so called *plasticity index* Ψ [75]. First of all, a relatively simple model shall be presented displaying a surface which is composed of spherical asperities having the same curvature radius and height (figure 4.17) [84]. The individual micro-contact area and thus

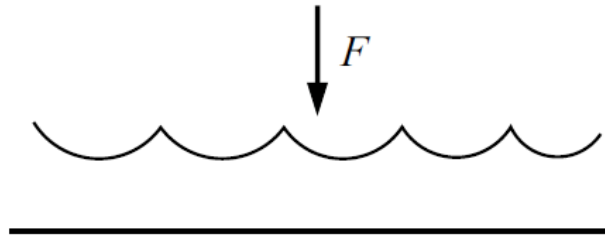


Figure 5.17.: Simplified model of a rough surface composed of spherical asperities with the same curvature radius and height.

the total area is given by $\Delta A \propto F^{2/3}$. In contrast, real surfaces are characterised by a stochastic roughness. According to Greenwood and Williamson's model, the stochastic surface roughness is approximated by spherical asperities with the same asperity curvature radius and stochastically distributed asperity heights around an average value. If the space between the contacting asperities is large enough, then the deformations will be independent from each other. The exact position of the asperities and thus the precise configuration of the surface are therefore irrelevant. The probability that a particular asperity has a height between z and $z + dz$ above a reference plane will be $\Phi(z)$ [84]. If the total number of asperities is N_0 , then the number of asperities in the interval $[z, z + dz]$ equals $N_0 \cdot \Phi(z)dz$. For many technical surfaces, a Gaussian height distribution can be presumed:

$$\Phi(z) = \left(\frac{1}{2\pi(rms)^2} \right)^{1/2} e^{\frac{-z^2}{2(rms)^2}} \quad (5.18)$$

where rms represents the root mean square height value given by $rms = \sqrt{\langle z^2 \rangle}$. Let us consider a contact between an elastic plane with the abovementioned roughness distribution and a rigid plane both having a distance h_0 from an average reference level

which represents the zero position of the z -axis (see figure 4.18). Neglecting the elastic

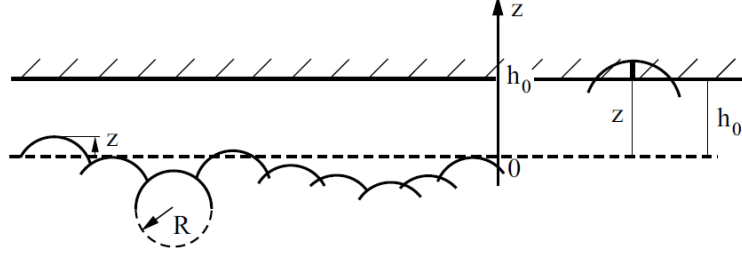


Figure 5.18.: Model of a stochastic surface according to Greenwood and Williamson [75] [84].

asperity interaction, all asperities with $z > h_0$ are in contact with the rigid plane. The compliance d of an individual asperity equals $d = z - h_0$. According to the Hertzian contact theory for a single contact, the contact area of an asperity is expressed by: $\Delta A = \pi a^2 = \pi \cdot d \cdot R = \pi(z - h_0)R$ and the individual force by:

$$\Delta F = \frac{4}{3}E^* \cdot R^{1/2} \cdot d^{3/2} = \frac{4}{3}E^* \cdot R^{1/2}(z - h_0) \quad (5.19)$$

The total number of asperities in contact, the total area of contact and the total normal load F_N can be determined by integrating over all contacting asperities from h_0 to infinity:

$$N = \int_{h_0}^{\infty} N_0 \Phi(z) dz \quad (5.20)$$

$$A = \int_{h_0}^{\infty} N_0 \Phi(z) \pi R (z - h_0) dz \quad (5.21)$$

$$F_N = \int_{h_0}^{\infty} N_0 \Phi(z) \frac{4}{3} E^* R^{1/2} (z - h_0)^{3/2} dz \quad (5.22)$$

By pressing the two bodies together, the values N , A and F_N increase exponentially as opposed to their respective ratios which only slightly change.

The average values for a single asperity may be expressed by:

$$\langle A \rangle = \frac{A}{N} = \frac{\int_{h_0}^{\infty} dz N_0 \Phi(z) \pi R (z - h_0)}{\int_{h_0}^{\infty} dz N_0 \Phi(z)} \quad (5.23)$$

Introducing a dimensionless variable $\xi = z/(rms)$ and $\xi_0 = h_0/(rms)$, one can obtain:

$$\langle A \rangle = \pi Rl \left[\frac{\int_{\xi_0}^{\infty} d\xi e^{(-\xi^2/2)} \cdot (\xi - \xi_0)}{\int_{\xi_0}^{\infty} d\xi e^{(-\xi^2/2)}} \right] \quad (5.24)$$

In figure 4.19 , the contact and average contact area are plotted as functions of the dimensionless separation variable ξ_0 . By changing the relative distance between the sur-

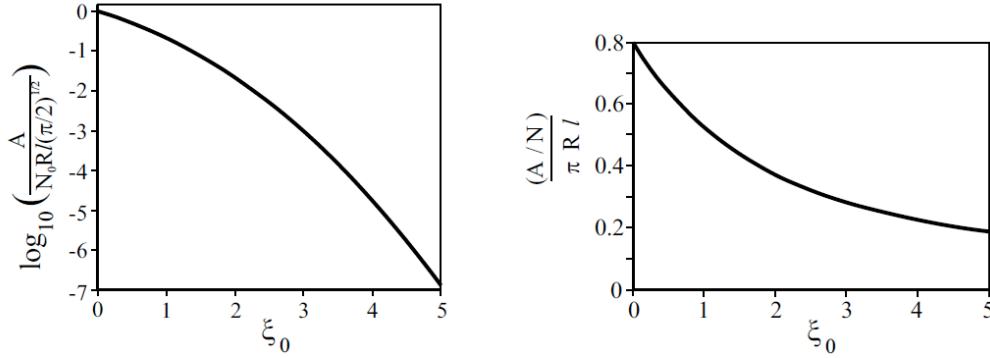


Figure 5.19.: Contact and average contact area as functions of the dimensionless variable ξ_0 [84].

faces from $\xi_0 = 0$ to 5, the contact area decreases by seven decimal orders of magnitude whereas the average contact area is only changed by less than a factor of three. The typical range of mean normal forces which correlates with a real contact area between 10^{-2} and 10^{-4} of the nominal area, results in a ξ_0 between 2.5 and 3.5 [84].

The ratio between the contact area A and the normal force F_N can be approximated by the following expression:

$$\frac{A}{F_N} \approx \left(\frac{R}{(rms)} \right)^{1/2} \cdot \frac{3.3}{E^*} \quad (5.25)$$

and consequently for the average pressure $\langle \sigma \rangle$:

$$\langle \sigma \rangle = \frac{F_N}{A} \approx 0.3 E^* \left(\frac{rms}{r} \right)^{1/2}. \quad (5.26)$$

The last equation can be slightly modified by taking into account the root mean square of the surface gradient ∇z :

$$\langle \sigma \rangle = \frac{F_N}{A} \approx 1/2 E^* \nabla z. \quad (5.27)$$

In order to distinguish between elastically or even plastically contacting asperities, it is

necessary to introduce a suitable parameter. As a plastic flow criterion, Tabor already suggested in 1951 [86] that the Hertzian pressure p_0 should reach $0.6 \cdot H_m$ where H_m is the hardness of the corresponding material. Plastic flow occurs internally, and is restricted by the adjacent elastic material.

Greenwood and Williamson defined a so called *Plasticity Index* Ψ which is given by:

$$\Psi = \frac{E^*}{H_m} \sqrt{\frac{\sigma}{\beta}} \quad (5.28)$$

with E^* being the reduced Young's modulus, H_m the hardness, σ the standard height deviation of the asperities and β the curvature radius of the respective asperities [75].

It combines the material and the topographic properties of the solids in contact.

Basically, the plasticity index merely determines the critical load at which the deformation changes from elastic to plastic. In practice, however Ψ entirely dominates the behaviour, and the load has only little effect [75].

In theory, Ψ can reach values up to infinity (typically from 0.1 to 100) [75]. It is only for a narrow range between 0.6 and 1.0 that the deformation mode is uncertain. When $\Psi < 0.6$ plastic contact can only be caused if the surfaces are forced together under very large nominal pressures. When $\Psi > 1.0$, plastic deformation will take place at even trivial pressures. In summary, the following distinction can be made with regard to Ψ :

- $\Psi < 0.6$: Insignificant plastic flow at any load (elastic behaviour)
- $0.6 < \Psi < 1.0$: Plastic flow depends on the load
- $\Psi > 1.0$: Plastic flow at trivial loads

6. Lubricated friction

In this last chapter of the theoretical part, a general overview about the fundamental aspects of lubricated sliding is presented. At first, the different lubrication regimes shall be explained and subsequently arranged within the Stribeck curve. To conclude the chapter, the elasto-hydrodynamic and fully hydrodynamic regime will be discussed in more detail.

6.1. The role of lubricants

Gases, liquids or solids (though most commonly they are hydrocarbon-based liquids such as mineral oil) may act as lubricants. Although the prime role of a lubricant is to reduce friction and wear, by separating the sliding surfaces as far as practicable, a lubricant may also have to:

- Cool the rubbing surfaces
- Remove debris
- Protect the surfaces from water
- Neutralise acid combustion products (e.g. in engines)

A lubricant must be able to maintain its properties intact for a reasonable length of time in the environment in which it is used. This may mean being resistant to oxidation, radiation, evaporation etc. and inert to metals and seals. Regular monitoring of the lubricant is a viable way of anticipating and preventing failure [49].

6.2. Lubrication regimes

Probably the most effective way of reducing friction and wear on sliding surfaces is to separate them completely with a thick film of a low shear strength material such as a

liquid or a gas. Ideally, this film should be thicker than the combined asperities on the two respective surfaces. There are a number of possibilities to form such a protective film known as regimes of lubrication [49].

1. Hydrodynamic lubrication (HD regime)
2. Hydrostatic lubrication
3. Elastohydrodynamic lubrication (EHL regime)
4. Boundary lubrication
5. Mixed lubrication
6. Solid lubrication

In the absence of any lubricating film, a dry contact is formed.

Hydrodynamic lubrication (1): In hydrodynamic lubrication the contact occurs such that the two sliding surfaces are nearly parallel but can form a shallow wedge, so that their relative motion drags (or entrains) lubricant in between them, forcing the lubricant to high pressures of up to 200 MPa, large enough to support external loads. The formed lubricant films are generally thicker than most combined engineering surface roughnesses with negligible solid/solid contact. Pressures encountered in hydrodynamic lubrication are not enough to significantly deform the sliding surfaces nor to increase the lubricant viscosity. A mathematical analysis is based on fluid flow, which yields the Reynolds equation. Typical hydrodynamic applications are thrust bearings, plane journal bearings, piston rings/liners and ice skates for example [49].

Hydrostatic lubrication (2): In hydrostatic lubrication the film thickness again fully separates the sliding partners however the contact is supplied by high pressure by an external source rather than by the relative motion of the two surfaces. This has the advantage over hydrodynamic lubrication that a gradual film collapse does not occur as the surfaces slow down. Another advantage is that low viscosity lubricants, such as air, can be applied rendering aerostatic bearings increasingly important [49].

Elastohydrodynamic lubrication (3): The EHL regime takes place within a point or line contact, focusing the load over a small contact area. Typical applications are

rolling element bearings and most gears. Concentrated or non-conformal contacts lead to high peak pressures of usually 2 GPa between the rubbing partners. Such pressures cannot be supported by a hydrodynamic film. In practice, lubricant films do form and have a thickness comparable to the surface roughness of normal gear and bearing materials. This is because the high pressure has two beneficial effects unaccounted for in classical hydrodynamics: elastic flattening appears and results in a locally conforming contact and the high pressure significantly raises the viscosity of the lubricant. Elastohydrodynamic lubrication is consequently studied using a combination of the Reynolds equation, elasticity theory and the lubricant viscosity-pressure equations [49].

Boundary lubrication (4): Boundary lubrication appears when there is insufficient hydrodynamic or elastohydrodynamic film to separate the surfaces but the lubricant interacts with the sliding surfaces to create a low shear strength chemical layer between the rubbing surfaces, generally only a few nanometers thick, but sufficient to reduce friction between colliding asperities. It is especially important in slowly moving contacts where thicker, hydrodynamic films cannot form, or, similarly at high temperatures, when the lubricant viscosity is very low. However it is also required in all transition phase contacts starting and stopping [49].

Mixed lubrication (5): At speeds just below those needed to give full hydrodynamic or elastohydrodynamic lubrication there are mixed hydrodynamic/boundary and EHL/boundary conditions. The summits of the asperities rub but most of the solid is separated by a lubricant film. This lubrication regime is very important since many machine components, such as piston ring/liners partially operate in mixed lubrication. Moreover, this regime is characterized by the occurrence of the most wear and friction [49].

Solid lubrication (6): In solid lubrication, the sliding contacting bodies are coated with a low shear strength solid material such as MoS₂ or PTFE. Typical coating thicknesses are 0.2 to 2 mm, on a steel substrate. Such systems have a finite lifetime but are relatively cheap and simple to use [49].

6.3. The Stribeck curve

The traditional concept of mixed lubrication originally has its source in the *Stribeck* or *Gumbel-Hersey* curves for friction of plain journal bearings. These show how friction varies with the parameter ($U\eta/W$) and thus with the hydrodynamic film thickness, where U denotes the relative velocity of the sliding bodies, η the dynamic viscosity of the used lubricant and W the normal load (see figure 5.1). As the film thickness is lowered, the friction rises from values characteristic of hydrodynamic lubrication to that of boundary lubrication. This transition stage is recognised to be the mixed lubrication region. The curve can be plotted with a linear abscissa, or with a logarithmic one to emphasise the boundary regime. Although the origins of mixed lubrication are quite clear, there is a limited possibility to model it. When the film thickness is in the vicinity of the surface roughness, a number of complicating factors arise. The presence of roughness starts to influence fluid entrainment and thus film formation. This means that the standard hydrodynamic and EHL film thickness equations collapse. Also, local pressure begins to cause asperity deformation, which means that the in-contact roughness becomes much less than the out-of-contact value. The asperity conjunctions themselves may also act as tiny elastohydrodynamic films.

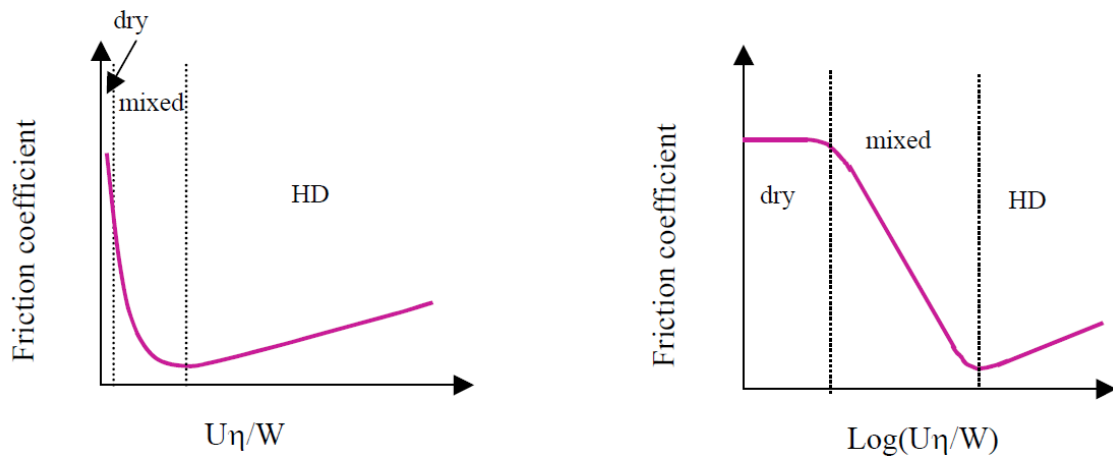


Figure 6.1.: Schematic Stribeck curve with linear (left) and logarithmic abscissa (right) [49].

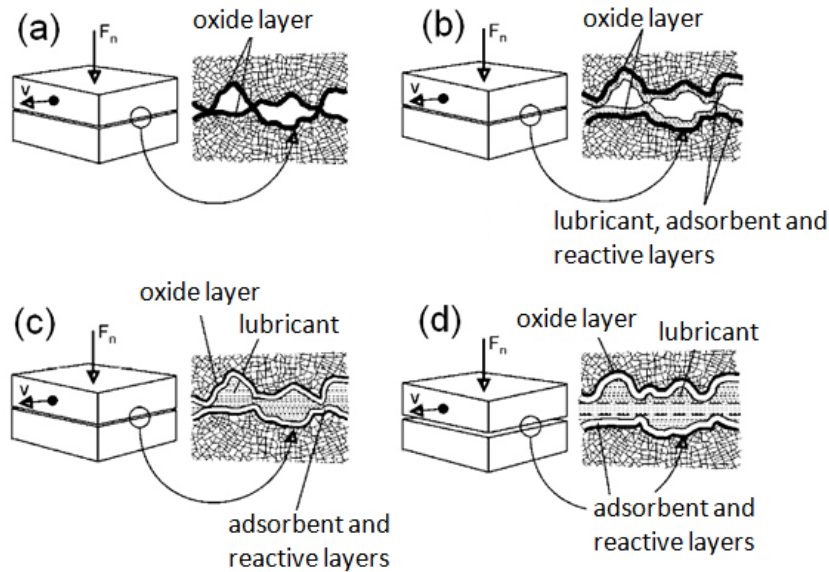


Figure 6.2.: Representation of the different friction regimes according to the Stribeck curve [87].

The different friction regimes within the Stribeck curve can be visualised with the help of the next figure. In figure 5.2a, the initial solid friction is displayed. Here, there is no permanent lubrication film to separate the sliding surfaces. Consequently, the asperities are in direct contact with each other, explaining the relatively high initial friction. The friction coefficient then drops due to the formation of friction reducing layers by physio- or chemisorption phenomena and finally by tribochemical reactions (see figure 5.2b). These layers may be composed of additives originating from the lubricant. This regime is accordingly named boundary lubrication. In figure 5.2c, the mixed lubrication regime is presented. The lubricant thickness is still insufficient to guarantee an effective separation of the mating surfaces. The loading is partially supported by the asperities and to some extent by the lubricant. Finally, the film thickness reaches a critical value thus completely separating the surfaces. The slight increase in μ can be traced back to a rising pressure within the lubricant (see figure 5.2d) [88]. 00

Part II.

Experimental part

7. Experimental methods

7.1. Deposition of thin films

Au thin films were electron beam evaporated on doubleside polished, (100)-oriented p-type silicon wafers from pellets with a purity of 99.95 % in standard equipment (*Balzers, PLS 570*). At a residual base pressure of less than $3.75 \cdot 10^{-7}$ Torr, the deposition process of both metal types is started and performed subsequently without breaking the vacuum to avoid oxidation effects. The Au top layers have a thickness of 300 nm. For the Pt samples, the Pt layer was synthesized by the same method with an emission current of 250 mA resulting in a growth rate of about 0.5 nm/s. The substrate material and the residual base pressure were the same as for Au. During deposition, none of the substrates were nominally heated and all substrates were placed on a rotary stage, ensuring improved homogeneity of the layer thickness within the samples and from sample to sample. Before irradiation, the 4 in wafer was diced into specimens of about $10 \times 10 \text{ mm}^2$ to fit into the experimental set-up and to ease the handling. For the deposition process of the W films, a magnetron sputter facility (*von Ardenne, PPS-A 200*) was employed using a sputter power of 500 W, an argon gas pressure of $2.25 \cdot 10^{-3}$ Torr, and a gas flow of 60 sccm on (100)-oriented silicon wafers. All the metallic top layers have a nominal thickness of about 300 nm. In order to improve the adhesion between the metallic top layers and the Si substrate, an intermediate Ti layer with a thickness of approximately 10 nm was used.

TiAl multilayer films were produced by magnetron sputtering (*von Ardenne, LS 730 C*) on doubleside polished, (100)-oriented p-type silicon wafers. In order to facilitate the sample handling, the wafer was diced into specimens of $2 \times 2 \text{ cm}^2$. The metallic film with a total thickness of around 300 nm consists of 14 Ti with 17 nm and 14 Al layers with 5 nm individual layer thickness. Due to its good adhesion to silicon, Ti was chosen as the primary layer. In addition to that, a 30 nm thick Ti layer was added as a top

layer because the material with the higher melting point must be on top to inhibit a topographic patterning. The deposition process with a power of 300 W was carried out in an argon atmosphere with a pressure of $3 \cdot 10^{-3}$ mbar and a gas flow of 80 sccm.

7.2. Laser interference structuring

A pulsed solid state Nd:YAG laser (*Spectra Physics, Quanta Ray Pro 290*) was used for the laser interference experiments. The fundamental wavelength of the laser is 1064 nm in the infrared range from which shorter wavelengths (532, 355 and 266 nm) can be provided by harmonic generation. Due to the absorption characteristics of the selected materials, the third harmonic at 355 nm was applied for the patterning. The repetition rate of the laser is 10 Hz with a pulse duration of 10 ns. Moreover, all the experiments were performed under ambient conditions. In order to obtain laser interference, a sufficiently large coherence length is necessary. Basically, the coherence length l_c is defined as the distance over which a fixed phase relationship between the waves is maintained. The coherence length can be expressed by:

$$l_c = \frac{c}{\Delta\nu} \quad (7.1)$$

where c depicts the velocity of light in free space and $\Delta\nu$ the spectral bandwidth. For the used solid state laser, the spectral bandwidth is specified to be 1 GHz which produces a coherence length of around one meter [46] [34]. Figure 6.1 shows the laser interference set up used for the experiments:

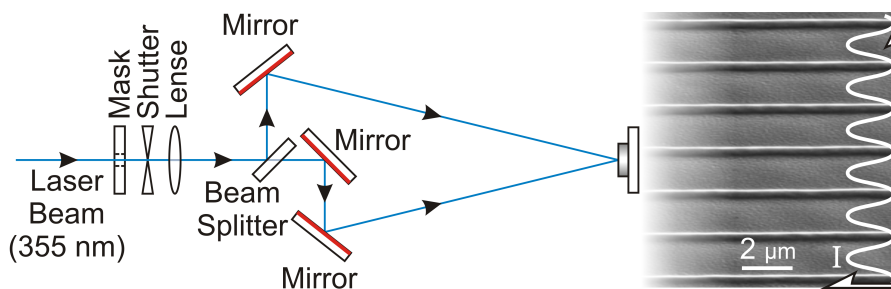


Figure 7.1.: Schematic drawing of the interference set up. The scanning electron micrograph shows a typical interference line-pattern made on stainless steel.

A primary laser beam ($\lambda = 355$ nm) with a circular beam cross-section having a diameter

7. Experimental methods

of 10 mm is split into two or more sub-beams in order to interfere with each other on the specimen surface. At first, the beam is shaped by a mask to create a quadratic spot with typical dimensions $1.5 \times 1.5 \text{ mm}^2$ on the sample surface. By utilising a mechanical shutter system (*Uniblitz Electronic VS25S2ZMO*), the number of pulses is adjustable by varying the delay and exposure time of the shutter. The power of each beam was measured by a power meter (*Gentec-eo, Solo 2*). After that, a lens with an anti-reflective coating is employed for a further variation of the spot size and the energy density on the sample surface. The intensity of each individual sub-beam can be controlled by suitable beam splitters. Finally, highly reflective mirrors are needed to deflect the individual beams onto the surface of the specimen in order to create the desired interference pattern.

7.3. Materials characterisation

7.3.1. Scanning electron and focused ion beam microscopy (SEM/FIB)

All specimens were studied by a high resolution scanning electron microscope (SEM) equipped with a field emission gun (*FEI, Strata DB 235*) at 5 kV acceleration voltage. Concerning the chemical analysis of the used materials, element mappings and line scans were conducted by energy dispersive spectroscopy (EDS) with an acceleration voltage of 15 kV using an EDAX instrument detector and EDAX Genesis software. In addition to that, focused ion beam microscopy (FIB) was used for cross-sections of the as-patterned specimens and for a detailed characterisation of wear tracks after tribological experiments. Moreover, FIB was applied to prepare thin foils for a subsequent localized cross-sectional study in a transmission electron microscope (TEM) (*JEOL 2010*). The general approach for the preparation of thin TEM foils is shown in figure 6.2:

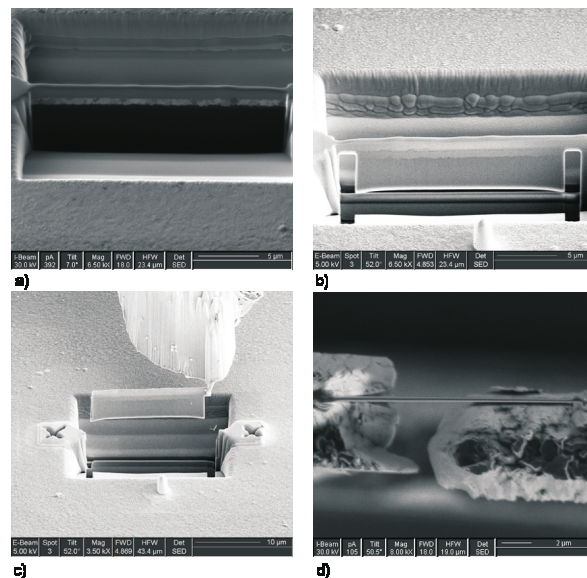


Figure 7.2.: General scheme for TEM foil preparation using FIB. Insets a) and b) show the coarse milling step with the nearly released foil. In c) the transfer of the foil to the TEM grid by the micromanipulator is displayed. Finally, d) shows the fixed foil at the TEM copper grid.

Initial milling down to a foil thickness of around 200 nm was performed utilising the TEM wizard provided by the microscope software and ion beam currents between 5000 and 300 pA. The lift-out of the foil was realized by a micromanipulator (*Kleindiek Instruments*) and the specimen was fixed to a copper TEM grid by a Pt complex. By a subsequent reduction of the ion beam current down to 30-50 pA, a final thinning step is performed with a resulting thickness ranging between 70-100 nm. In this range, the as-prepared foil has a suitable transmissivity for electrons and can be used for further studies in TEM.

7.3.2. Transmission electron microscopy (TEM)

TEM studies were carried out using a *JEOL 2010* facility at an operating voltage of 200 kV. Both, direct imaging scrutinising the microstructural aspects, and selected area diffracton (SAD) were applied to the specimens. Furthermore, EDS analyses (*Oxford ISIS*) were performed in order to elucidate the chemical information of the different phases.

7.3.3. Electron backscatter diffraction (EBSD)

For a detailed microstructural study of grain sizes and misorientations, electron backscatter diffraction (EBSD) was performed with regard to the as-patterned Au, Pt and W thin films.

EBSD dates back to the pioneering work of Venables, Harland and Dingley in 1984 [89][90]. A schematic set up of the measuring system and the technical realisation in a typical scanning electron microscope are displayed in figure 6.3.

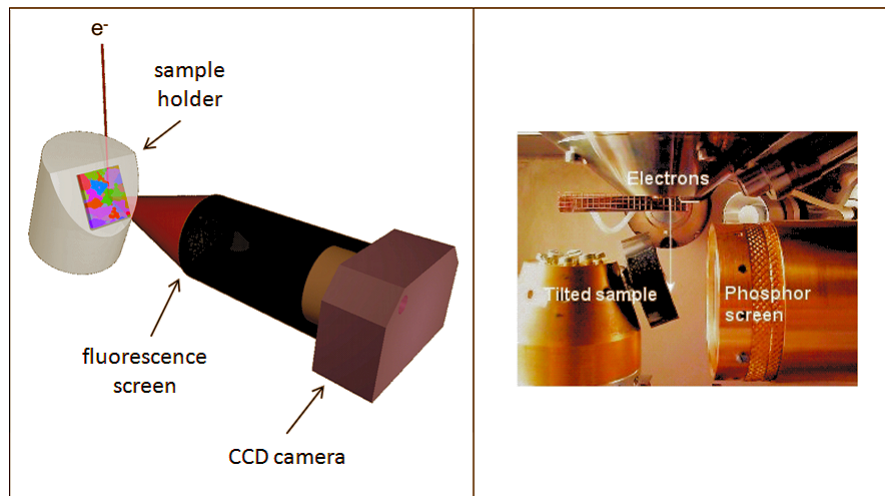


Figure 7.3.: Schematic overview of a typical EBSD measuring system consisting of sample holder, fluorescence screen and CCD camera (left picture) and the technical realisation in the SEM (right picture)

The specimen is mounted on a SEM sample stub, which is tilted by an angle of 45° . Moreover, the sample stage has an additional tilt of about 25° leading to a final tilt angle of 70° concerning the incident electron beam. The coefficient of backscattered electrons which describes the ratio between the current of backscattered electrons and the primary electron beam is a function of the incidence angle θ_i showing a maximum yield at about 70° . During the interaction of the primary electron beam with the material, those electrons are incoherently scattered in various directions. As a consequence, sufficient electrons are available in different directions due to excitation effects of atoms. This leads to the fact that some electrons are finally fulfilling Bragg's law thus being diffracted at specific lattice planes. The source of diffracted electrons is located between two lattice planes. According to that, two surfaces of Kossel cones arise. The typical Bragg angles are in the order of 0.5° . Hence, the point angle of the cones is nearly 180° resulting in widely-opened cones. The intersection of the cones with the fluorescence screen causes the well known *Kikuchi lines*. The angular distance equals $2\theta_B$ which is proportional to the lattice distance d . Finally, the surface quality is decisive for a successful EBSD study. The lateral resolution is in the order of 20-50 nm whereas the information depth approximately ranges between 10 and 150 nm. Therefore, EBSD is very sensitive to deformed layers or contaminations. Moreover, pronounced topographies can result in

shadowing effects leading to blurred Kikuchi patterns.

7.3.4. Atom probe tomography (APT)

The chemical composition of the intensity maximum and minimum positions for the TiAl multilayer samples as well as a zone localised in between was analysed by CAMECA (Mr. P. Clifton is kindly acknowledged) using 3D-Atom Probe (AP) Tomography (*CAMECA LA-WATAP and LEAP3000 XHR, formerly IMAGO*) in order to observe intermixing effects.

7.3.5. White light interferometry (WLI)

White light interferometry is a contactless method for height profile measurement. The measurement principle is based on classical *Michelson interferometry*. The used white light interferometer (WLI) is a *Zygo New View 7300* having a vertical resolution of about 0.1 nm and an objective-dependent lateral resolution ranging between 0.36 and 9.5 μm [69]. It is important to note that the vertical resolution is a theoretical value which is of course limited by the lateral resolution. Generally, the vertical resolution, depending on the measured surface, is in the range of 10 nm. The instrument uses a broad band white light source having the benefit of circumventing the 2π -ambiguity problem [91] and thus enhancing the resolution. Such a source is composed of a continuous band of wavelengths from which the phases of the individual spatial frequencies can be extracted. Figure 6.4 represents the basic set up of a conventional WLI.

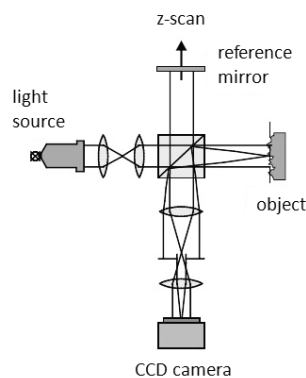


Figure 7.4.: Optical system for scanning white light interferometry [91].

First of all, the light is collimated into a parallel beam. With an appropriate beam splitter, the primary beam is splitted into two beams. One of the beams is directed to a reference mirror and the second towards the object. The reflected beams interfere with each other resulting in a typical interferogram. Moving the reference mirror in the z-direction leads to a variation of the light intensity on a recording screen following the coherence function of the white light source. The relation describing the dependence of the light intensity on the object position is called correlogram [92]. During the scanning process, interferograms are simultaneously recorded for each pixel within the respective field of view. Therefore, the intensity variation is measured for each pixel as a function of the scan position. By a *Frequency Domain Analysis* (FDA), the data are processed on the basis of a *Fast Fourier Transform* (FFT). In a final step, the surface is reconstructed according to the processed height data [91].

In this thesis, WLI is especially applied for the determination of topographic parameters such as periodicity, structural depth, rms value etc. after laser patterning. Moreover, the volume of resulting wear tracks after sliding will be measured by this method. The corresponding surface parameters will be explained in more detail in the tribological theory section.

7.3.6. X-ray diffraction (XRD)

The integral microstructural parameters such as the phase, texture and residual stress state were determined by XRD phase analysis measurements using grazing incidence geometry (GIXRD) in order to achieve statistically relevant phase data of a significantly large specimen volume. For this purpose, a seven-axis diffractometer (*Panalytical, X'pert MRD HR*) with a copper x-ray tube ($\lambda = 1.54056 \text{ \AA}$) was used. The texture and residual stress measurements were carried out using a symmetric configuration (*Bragg-Brentano*).

7.3.7. Tribometry

The tribological tests were performed with a nanotribometer using a ball on disk configuration in a linear reciprocating sliding mode (*CSM Instruments*). The tribometer is based on a stiff cantilever, which acts as a frictionless force transducer in both vertical and horizontal directions. The cantilever used for the experiments ST-066 has a normal stiffness of $0.7624 \text{ mN}/\mu\text{m}$ and a tangential stiffness of $1.1447 \text{ mN}/\mu\text{m}$. The static part-

ner is loaded onto the substrate with a precisely known force using piezo-actuation. The normal load and the friction force are determined during the experiment by measuring the deflection of this elastic spring in both horizontal and vertical planes with two high precision fiber optical displacement sensors. Through a PID control, the piezo-actuation maintains the normal load independent of any surface irregularities. The normal force was varied between 1 mN and 100 mN. The linear sliding speed was set to 2 mm/s. The deviation from the nominal normal load was less than 10% related to the reference value in our experiments. The counter body consisted of a typical 100 Cr 6 bearing steel or an Al_2O_3 ball with a diameter ranging between 1.5 mm and 3 mm. After every tribological test, the tribometer balls were cleaned by isopropanol and analysed by WLI with regard to the geometrical size accuracy i.e. possible deviations from the sphericity. Temperature and relative humidity were kept constant at 20 °C and 45% in an environmental chamber. Figure 6.5 shows an overview of the main tribometer components.

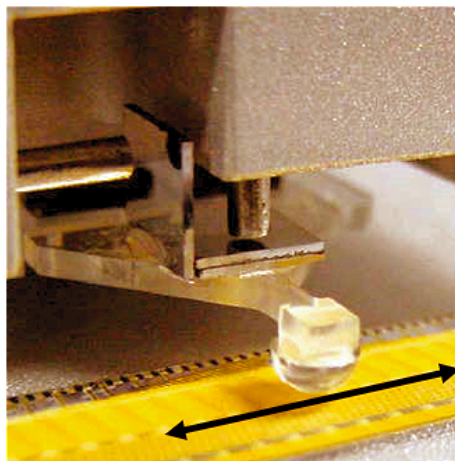


Figure 7.5.: Overview of the main tribometer components.

7.3.8. Nanoindentation

One of the powerful method for determining the mechanical properties of nano- and microstructured materials is the depth-sensing nanoindentation combined with in situ imaging capability, so called nanoindentation scanning probe microscope (NI-SPM). With regard to two aspects, this method offers great advantages over the conventional micro and nanoindentation tests [93]. First, the load and depth of an indentation are continuously monitored and more information dealing with the mechanical behaviour of

7. Experimental methods

materials can be gathered, for example dislocation nucleation, fracture, or phase transformation inside the material. Second, within the SPM function of the instrument it is possible to image the surface, localizing the position of interest, and performing the indentation experiment at the selected position within nanometer accuracy. Here, a TriboIndenter (*Hysitron Inc., Minneapolis, MN*) nanomechanical testing system was used to perform the nanoindentation tests. Within this system the diamond indenter served as both the indenter and the imaging probe. Thereby, it is possible to locate the tailored structures with a nanometre resolution while indenting the substrate. A Berkovich (three-sided pyramidal tip, 142.3°) diamond indenter was used carefully calibrated for its area function on standard material.

8. Results and discussion

8.1. Grain size architectures in metallic thin films

8.1.1. Introduction

Due to an ongoing miniaturisation on device and system levels, mainly driven by the tough competition in the microelectronic industry, thin films are nowadays pervasive in many technical applications, including magnetic storage media, thermal barrier coatings or optics [94][95][96]. A basic understanding of the fundamental aspects during film growth and methods for a subsequent optimisation or tailoring of film microstructure is absolutely essential for improving the physical properties of the as-deposited films. Independent of the deposition technique used (i.e. sputtering or e-beam evaporation), metallic thin films exhibit an amorphous or a polycrystalline microstructure when deposited under typical conditions, such as no or only a moderate substrate heating [97][98]. In the latter case, films are mainly characterised by a logarithmic normal grain size distribution with randomly oriented grains [99]. As far as technical applications are concerned, microstructural randomness leads to highly inhomogeneous and non-optimised device characteristics [100]. Consequently, circumventing the random grain alignment by a laser-interference induced localised recrystallisation for example with specified threshold energies results in a control of nucleation sites and grain orientations. Several techniques for the crystallisation or recrystallisation of amorphous or polycrystalline thin films have been presented so far [99], but due to different limitations, such as the thermal stability of the substrates used [101][102], only few methods are able to fulfill particular requirements. Basically, LIMET enables the formation of periodic patterns having different features with a defined long-range order on the scale of typical microstructures given by the interference periodicity [46]. This technique facilitates various metallurgical processes, such as melting, recrystallisation, recovery and the tailored formation of intermetallic phases in microstructures parallel to the surface,

but also topography effects in metals, ceramics or polymers [103][104][105].

Im et al. have used a sequential laser induced crystallisation process for the microstructural manipulation of silicon for thin film transistors [100]. Moreover, Kelly et al. and Aichmayr et al. studied the applicability of laser interference patterning for semiconductors, such as AlGaAs/GaAs and amorphous silicon films [101][27]. Remarkable advantages of the laser interference principle are that no masks are required, the crystallisation process is induced locally and relatively large areas in the order of cm^2 can be irradiated in a single shot [28][46]. In a narrow processing window, a so called Super Lateral Growth regime (SLG-regime) is observable [100]. The average grain size of the laterally growing grains can reach up to a few micrometre. This regime is influenced by many factors as for instance the energy density, film thickness, periodicity and the substrate properties [100][99]. LIMET permits to locally tune the grain architecture of nanocrystalline thin films from the nano- to the microscale. This means a defined size and orientation of the grains dependent on the applied energy density and film thickness. The exploitation of these two degrees of freedom in the microstructure should lead to a controlled periodic modification of mechanical properties (e.g. hardness).

8.1.2. Microstructural characterisation and modelling of laser-induced grain architectures

At first, the grain morphology and micro-texture of as-deposited gold films were studied by SEM and EBSD. Figure 7.1 shows a histogram plot of the grain size diameter distribution for an e-beam evaporated Au film measured by EBSD. The inserted SEM image depicts the fine grained morphology of the film. The pristine specimen consists of fine grains after the deposition process with a typical grain size ranging between 80 and 160 nm.

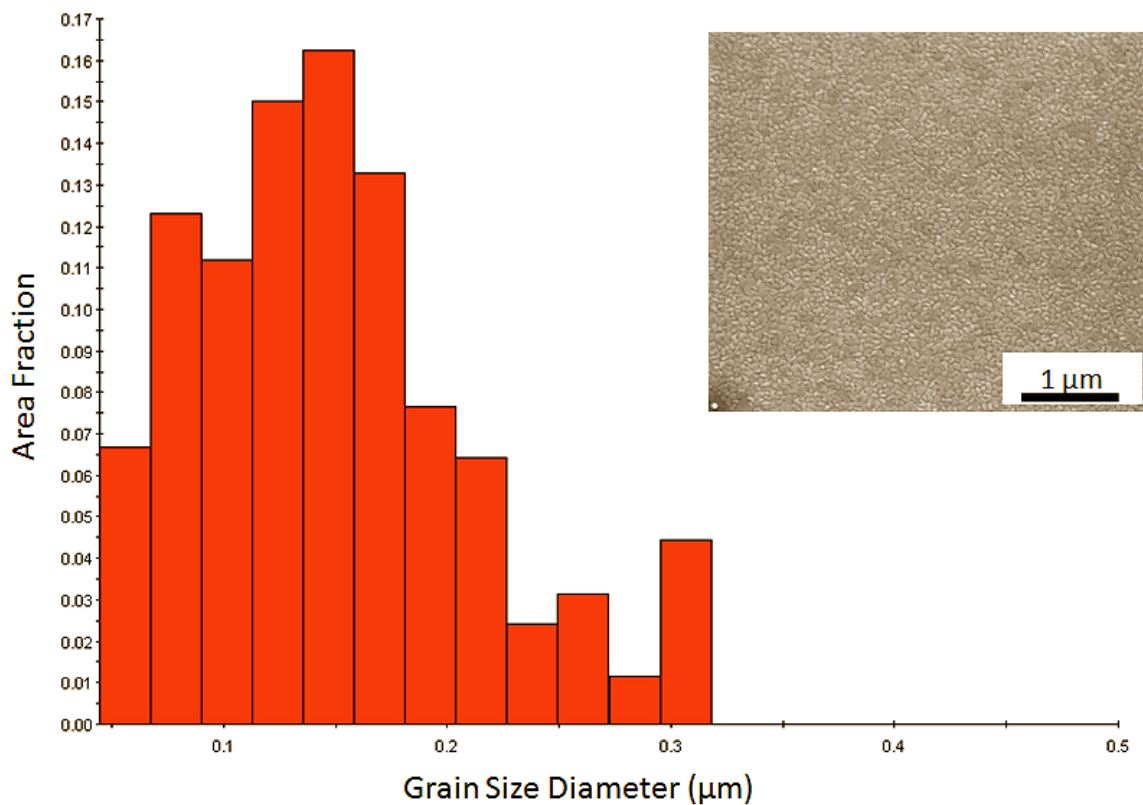


Figure 8.1.: Histogram plot of the grain size diameter distribution of an as-deposited gold thin film by EBSD. The insert represents a SEM image of the film showing the fine grained morphology.

8. Results and discussion

In order to study the effect of film thickness and laser energy density on the microstructure, gold films with two different thicknesses were deposited on Si-wafers by e-beam evaporation and laser irradiated applying three different fluence values. Figure 7.2 shows a series of SEM images for a 690 nm thick gold film (see figures 7.2 a,b and c) with increasing laser fluence and for a 300 nm thick specimen (see figures 7.2 d, e and f) respectively.

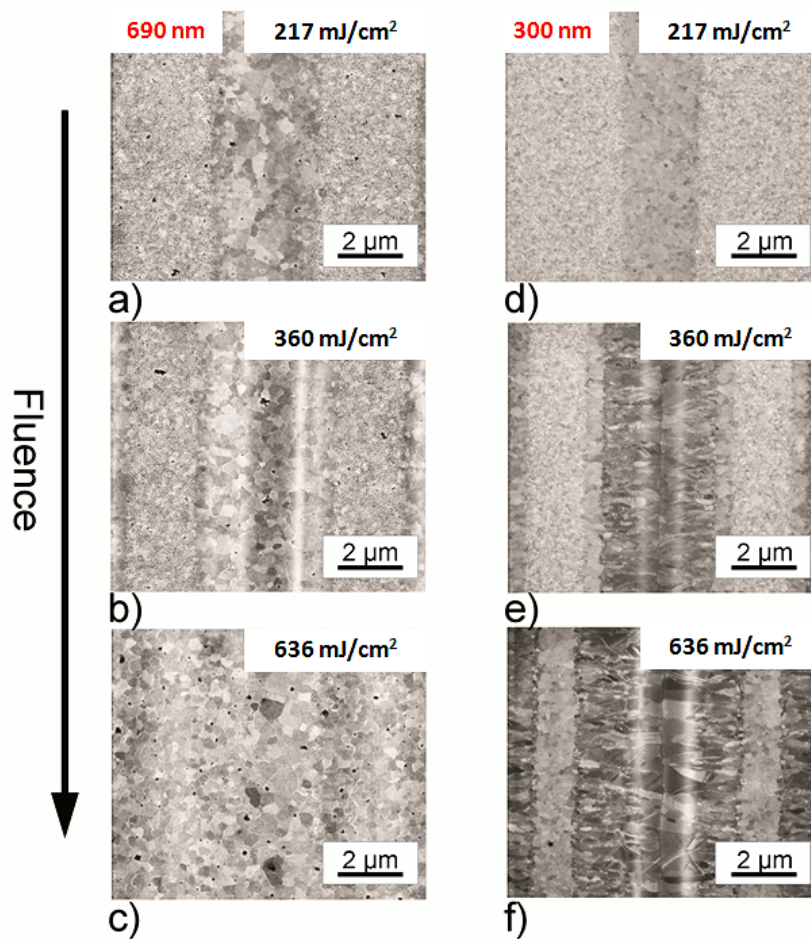


Figure 8.2.: SEM image of thin film morphology as a function of the laser fluence for a 690 nm (a, b and c) and a 300 nm (d, e and f) thick film. The SEM images show a line-like interference pattern typical for two interfering laser beams. Only one laser intensity maximum with the neighboring minima is depicted. The structural periodicity is around $6 \mu\text{m}$.

8. Results and discussion

The centre positions in each micrograph represent the laser intensity maximum and the adjacent areas the laser minima. For low fluence values (figures 7.2 a, d), both films already show a laser-induced grain growth in the positions of maximum intensity. The localised heat input according to the laser intensity distribution is clearly visible. With increasing laser fluence, a more distinct crystallisation zone in the case of the 690 nm thick gold film can be observed (figure 7.2 b). In contrast, the 300 nm sample demonstrates the abovementioned SLG regime (figure 7.2 e). After having exceeded a certain fluence threshold value, laterally growing grains propagating from the not molten areas (laser intensity minima) to the completely molten film regions (laser intensity maxima) appear. The centre-line for the 300 nm thick sample originates from impinging grains which grow from both sides following the temperature gradient [100][99]. The average length of the lateral grains is up to $1.5\ \mu\text{m}$ and the width has a maximum value of approximately $0.4\ \mu\text{m}$ in this case. Varying the energy density, it is possible to adjust the extent of the crystallised area and therefore to tailor the microstructure. Other factors, which strongly influence the width of the crystallised area, are the periodicity, the laser pulse duration, the substrate temperature and the thermal conductivity of the substrate [100]. FIB cross-sections of patterned Au films with a thickness of 300 nm revealed that the laser induced grain growth is not only located at the surface, but throughout its entire thickness (see figure 7.3 a).

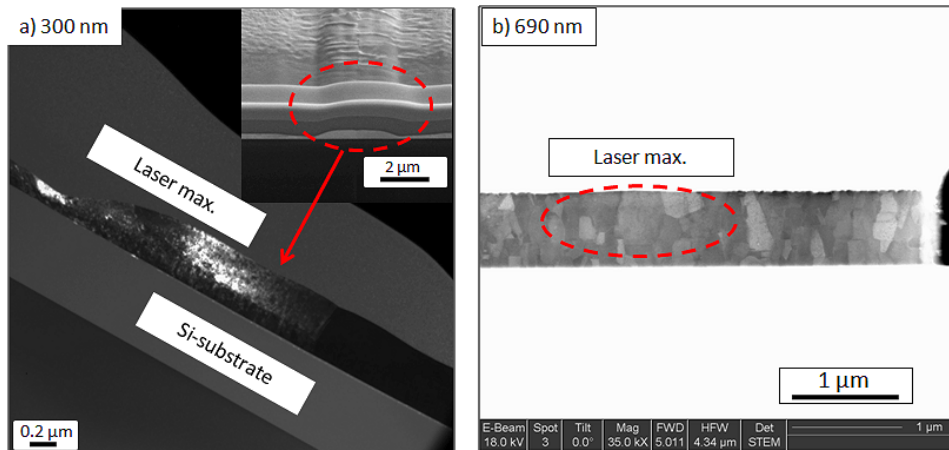


Figure 8.3.: FIB cross-sections of laser patterned Au films with a film thickness of 300 nm (left) and 690 nm (right). The substrate in both cases is silicon.

8. Results and discussion

Here, the laser intensity maximum region is presented with large impinging grains in the centre. The situation is completely different in figure 7.3 (b). For thicker films, the laser irradiated zone is hard to be determined because the topography is strongly reduced and the grain morphology is different to the SLG regime in figure 7.3 (a). The thickness dependent grain morphology and especially the grain orientation were determined by EBSD.

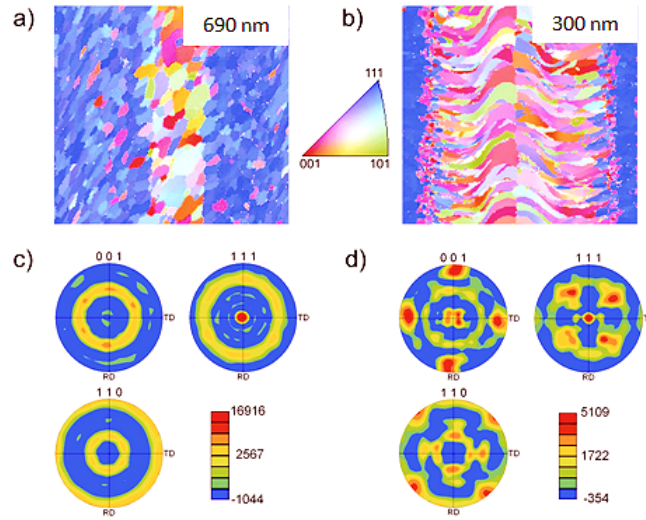


Figure 8.4.: Inverse pole figure maps and corresponding pole figures for the $\langle 001 \rangle$, $\langle 110 \rangle$ and $\langle 111 \rangle$ directions of the 690 nm (a, c) and of the 300 nm thick gold films (b, d) determined by EBSD after laser irradiation. The colour-code is according to the inserted orientation triangle.

Figures 7.4 (a), (b) display the recorded inverse pole figure maps with the orientation triangle and the corresponding pole figures for the $\langle 001 \rangle$, $\langle 110 \rangle$ and $\langle 111 \rangle$ directions are presented for both films (see figures 7.4 c, d). The microstructural morphology as well as the microtexture reveals a strong influence on the film thickness in both cases. The laser fluence for both films was kept constant at about 636 mJ/cm^2 . The predominant blue colour code for the 690 nm thick sample illustrates that the $\langle 111 \rangle$ direction is the preferential one (figure 7.4 c). There is an increased pole density at $\Psi = 0^\circ$ which refers to a $\{111\}$ fibre texture. The ring in the $\{111\}$ pole figure at $\Psi \approx 70^\circ$ is a contribution of other crystallographic equivalent $\{111\}$ planes. By decreasing the film thickness, the texture undergoes a change from the observed $\{111\}$ fibre texture to

a distinct $\{001\}$ cube texture (see figures 7.4 b, d). Instead of one accumulation point at $\Psi = 0^\circ$, four regions of a strong pole density can be found at nearly 90° in the $\{001\}$ pole figure, as illustrated in figure 7.4 (d). The deviation from the $\Psi = 90^\circ$ position probably arises from an alignment error during sample mounting. The inner ring at $\Psi = 54^\circ$ results from $\{111\}$ planes according to the $\{111\}$ fibre texture.

In order to understand the different morphologies and grain orientations, finite-element simulations were performed. A simplified model has already been published elsewhere [102][106][107]. The simulations show the temporal and spatial distribution of the solid-liquid interface during the exposure of the Au-samples to the interfering laser beams (see figure 7.5).

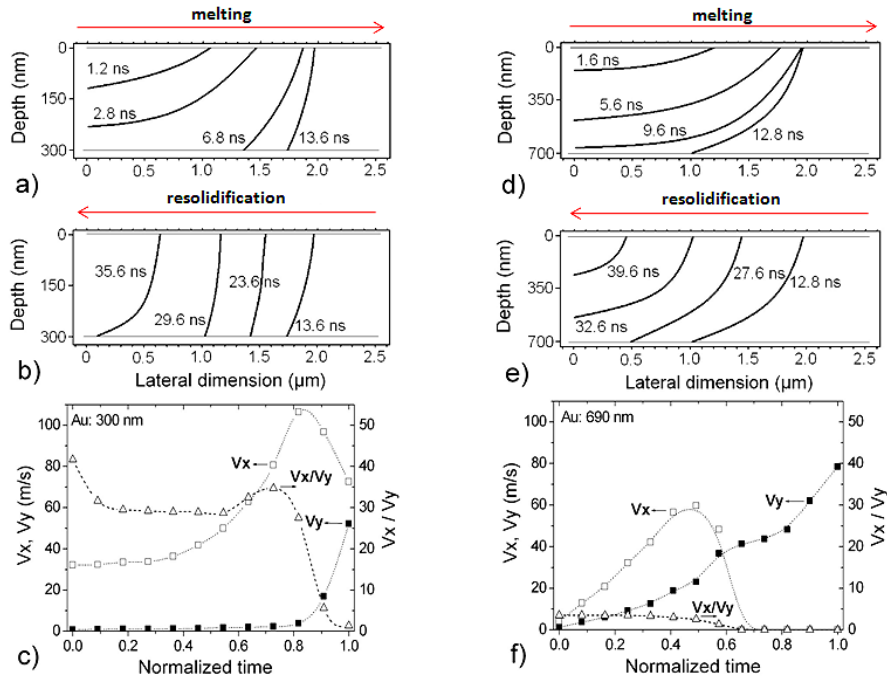


Figure 8.5.: Thermal simulations of 300 nm (a, b and c) and 690 nm (d, e and f) laser irradiated Au-samples. Figures (a) and (b) show the evolution of the solid-liquid interface at the 300 nm sample during melting and resolidification, and figures (d) and (e) for the 690 nm thick film. For both cases, the lateral (v_x) and vertical growth velocities (v_y) as a function of normalised time as well as the ratio between the two velocities is represented in figures (c) and (f).

The simulation is based on the heat diffusion equation and considers thermal properties of the fine grained Au layer representing the as-deposited state and of the microcrystalline material after grain growth. According to Tjong et al. the melting point of gold particles with sizes larger than 10 nm is very similar to the melting point of microcrystalline gold [108]. According to Zhong et al., the same is true for the specific heat of both nano- and microcrystalline phases [109] and the thermal conductivity. Consequently, melting point, specific heat and thermal conductivity of the fine grained material were considered to be equal to those of microcrystalline gold.

Figure 7.5 shows the calculated results on the temperature distribution developing in the 300 and 690 nm thick Au samples when irradiated with a laser fluence of 636 mJ/cm². The results indicate that two distinct types of solidification behavior exist depending on the Au layer thickness. Figures 7.5 (a), (b) show the evolution of the solid-liquid interface of the 300 nm Au sample during melting and resolidification, respectively. The propagation of the solid-liquid interface proceeds mainly in vertical direction during melting. However, when resolidification starts, a strong lateral growth with velocities between 30 and 100 m/s is observed. This is shown in figure 7.5 (c), where both coordinates (x and y) of the resolidification speed (v) are indicated. The normalised time in figure 7.5 (c) and (f) corresponds to the time period for complete resolidification. In contrast, the vertical regrowth velocities (v_y) show values between 1 and 4 m/s, with the exception of the final stage where the vertical velocity abruptly increases up to 50 m/s (see figure 7.4 c).

Comparing the lateral and vertical regrowth velocities, it can be concluded that during the nearly complete time interval the lateral velocities (v_x) are about 30 times higher than those in vertical direction, as shown in figure 7.5 (c). In figures 7.5 (d) and (e), the evolution of the solid-liquid interface during melting and solidification of the 690 nm Au sample is shown. In the melting period (see figure 7.5 d), similar results as obtained with the 300 nm thick Au layer are observed with a dominating vertical propagation direction of the solid-liquid interface. However, during resolidification, the lateral regrowth velocities (v_x) vary from 4 to 62 m/s and the vertical velocities (v_y) increase above average from 4 to 78 m/s (see figure 7.5 f). Due to an almost 20 times higher vertical regrowth velocity the ratio of resolidification speeds decreases to 4. Similar results for thin Si films were obtained by Aichmayr and Gupta [102][107].

Apart from the film thickness influence, the line-spacing of the laser pattern plays an important role with regard to the resulting grain morphology. Figure 7.6 compares the grain morphology of the reference film with two periodicities (2 and 5.6 μm).

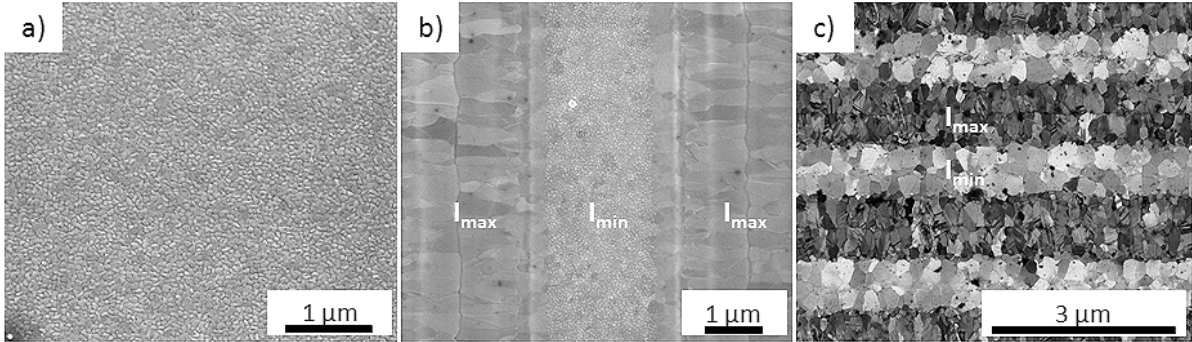


Figure 8.6.: SEM images of a Au reference sample (a), laser crystallised lines with a periodicity of around 5.6 μm (b) and laser-pattern with 2 μm line-spacing (c).

Considering the laser line pattern, the SLG-regime is clearly visible in case of figure 7.6 (b). In the position of minimum intensity, the fine grains in between can still be detected. After having reduced the pattern line-spacing from 5.6 to approximately 2 μm , the grain morphology significantly changes. Considerable grain growth takes place (maximum ranging between 300 and 400 nm) even in the positions of minimum intensity which can be observed in the respective grain size distribution (see figure 7.7).

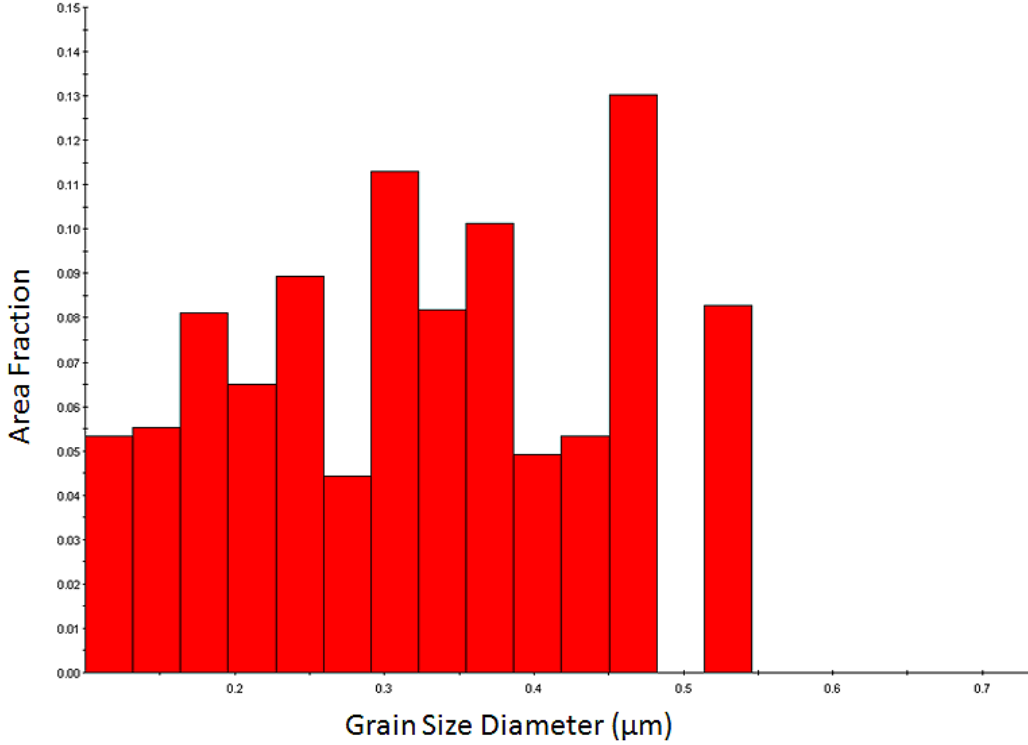


Figure 8.7.: Histogram plot of the grain size diameter distribution for a laser-patterned gold film with a patterning periodicity of around $2\ \mu\text{m}$.

An important parameter in this context is the maximum thermal diffusion depth l_D [48][110].

$$l_D = 2\sqrt{\kappa_{th}\tau} \quad (8.1)$$

where κ_{th} represents the thermal diffusivity and τ the pulse duration of the used laser (here 10 ns). The thermal diffusivity is expressed by:

$$\kappa_{th} = \frac{\lambda_{th}}{\rho \cdot c_p} \quad (8.2)$$

with λ_{th} being the thermal conductivity in (W/mK), ρ the density in (g/cm^3) and c_p the specific heat capacity in (J/kgK).

On the basis of these relations, l_D can be easily calculated for Au. For the calculation, the bulk gold values are chosen because the grain size is ranging between 80 and

160 nm and thus the difference of the values for the thermal conductivity and the specific heat capacity between bulk and fine grained thin film is negligible [109][108][111]. The respective values are: $\lambda_{th} = 317 \text{ W/mK}$, $c_p = 129 \text{ J/KgK}$ and $\rho = 19.32 \text{ g/cm}^3$ [112]. For a pulse duration of 10 ns, the thermal diffusion length l_D is about $2.26 \mu\text{m}$. This is comparable to the selected periodicity of about $2 \mu\text{m}$ and finally explains the complete grain growth even in the positions of minimum laser intensity.

In addition to substantial modifications of the grain morphology, twinning occurs preferably in the laser intensity maxima. Figure 7.8 elucidates this finding regarding a laser cross-pattern.

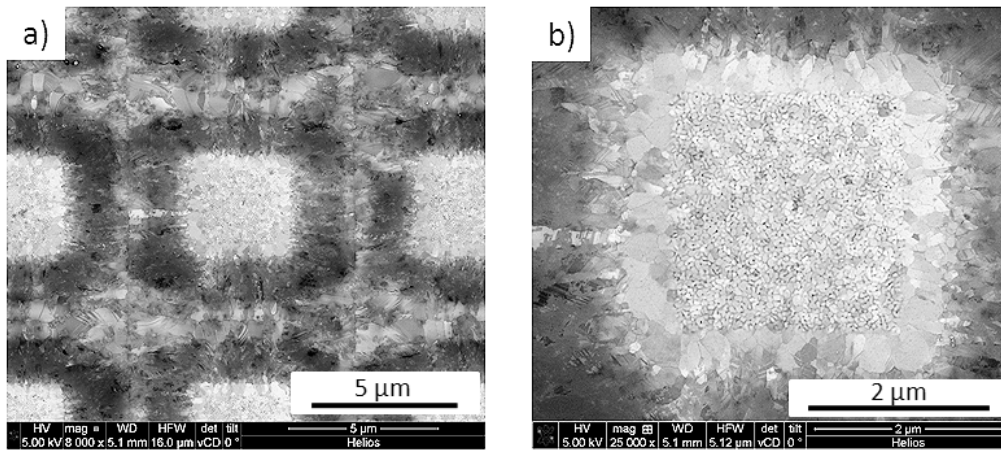


Figure 8.8.: Overview (a) and magnified Insert (b) of laser interference cross-pattern showing twinning in the maxima and overlapping positions.

Gold is a fcc-metal in which twinning is the predominant deformation mechanism. Using a high power Nd:YAG pulsed laser, the specimen surface encounters a relatively high thermal impact with considerable heating and cooling rates and presumably large plastic strain fields at the compressive laser shock front. By now, it is well accepted that twinning in metals can be traced back and finally initiated by pre-existing dislocations splitting into stacking fault structures [113]. In general, metals with a low stacking fault energy tend to accommodate thermal or mechanical stresses by twinning. Table 7.1 gives a brief overview of the typical stacking fault energies of fcc-metals.

8. Results and discussion

Metal	γ_{SFE}^{theory} (mJ/m ²)	γ_{SFE}^{exp} (mJ/m ²)	τ_{twin}^{theory} (MPa)	τ_{twin}^{theory} (MPa)
Pb	49	-	40	19-71
Ag	18	16	65	38-71
Au	33	32	80	85-100
Cu	41	45	120	125-160
Ni	110	125	250	-
Pd	168	180	330	-
Pt	324	322	480	-
Al	120	120	220	-

Table 8.1.: Theoretical and experimental values for stacking fault energies and twinning stresses in fcc-metals [113].

Based upon table 7.1, gold has a relatively low stacking fault energy thus preferring twin formation after thermal or mechanical impact. Depending on the used fluence, only a thin layer might be heated by the laser. Due to a short energy application time, thermal diffusion away from the irradiated region is basically restricted to a few μm [114]. The material may heat up to several thousands of degrees leading to the formation of a plasma which subsequently absorbs the laser energy until the end of the process time. Usually, without confinement, the resulting pressure is in the order of tenths of GPa. If a confined medium is taken into consideration, the peak pressures may exceed 10 GPa [114]. According to previous results from Meyers and Grace et al., it could be shown that the compressive laser shock front may generate defects such as dislocations in the high impact zones [115][116].

An approximation of the laser induced pressure shall be given by **Lindl's equation** describing the conversion of laser power density into pressure:

$$P = 4 \cdot 10^3 \left(\frac{I_{peak}}{\lambda} \right)^{2/3} \quad (8.3)$$

where I_{peak} denotes the laser intensity in 10^{15} W/cm^2 and λ the wavelength in μm [117]. For the used laser, λ is given by 355 nm and $I_{peak} = 1.31 \text{ GW/cm}^2$ which corresponds to the constant fluence of 165 mJ/cm^2 . The resulting shock pressure is approximately 0.97 GPa. As soon as the peak pressure rises above the dynamic yield strength of a material, extensive plastic deformation and thus an increase in the dislocation density

can be expected [114]. According to Thornton and Neugebauer [118][119], the yield strength of Au thin films ranges between 0.19 and 0.21 GPa which is lower than the shock pressure amplitude. Therefore, it can be assumed that the laser patterning leads to a considerable increase in dislocations and also surface residual stresses after the laser process [114].

Kline et al. also achieved super-lateral growth in gold films with a thickness of around 200 nm, thus comparable to the samples used in this thesis, by sequential excimer laser melting [120]. It is reported that the super-lateral grains exhibit significant defect structures typical for rapidly solidified microstructures in fcc-metals [121]. In particular, twin bands or stacking faults were present on $\{111\}$ planes in Au. Dislocation densities were found to be moderate or even high varying from grain to grain. Preliminary estimations refer to $3 \cdot 10^{14} \text{ 1/m}^2$ for line dislocations [120]. This is consistent with values for larger dislocation densities in metallic thin films which are also in the range of 10^{14} 1/m^2 [122].

Extending the previous findings to other metallic thin films, a detailed study of the crystallisation scenario of Pt- and W-thin films, both having significantly different melting points compared to Au, will be presented. Figure 7.9 highlights SEM images of the laser irradiated Au, Pt and W specimens for two different laser fluence regimes. The left (a), (b) and (c) and right (d), (e) and (f) rows denote the low and the high fluence regimes, respectively [30].

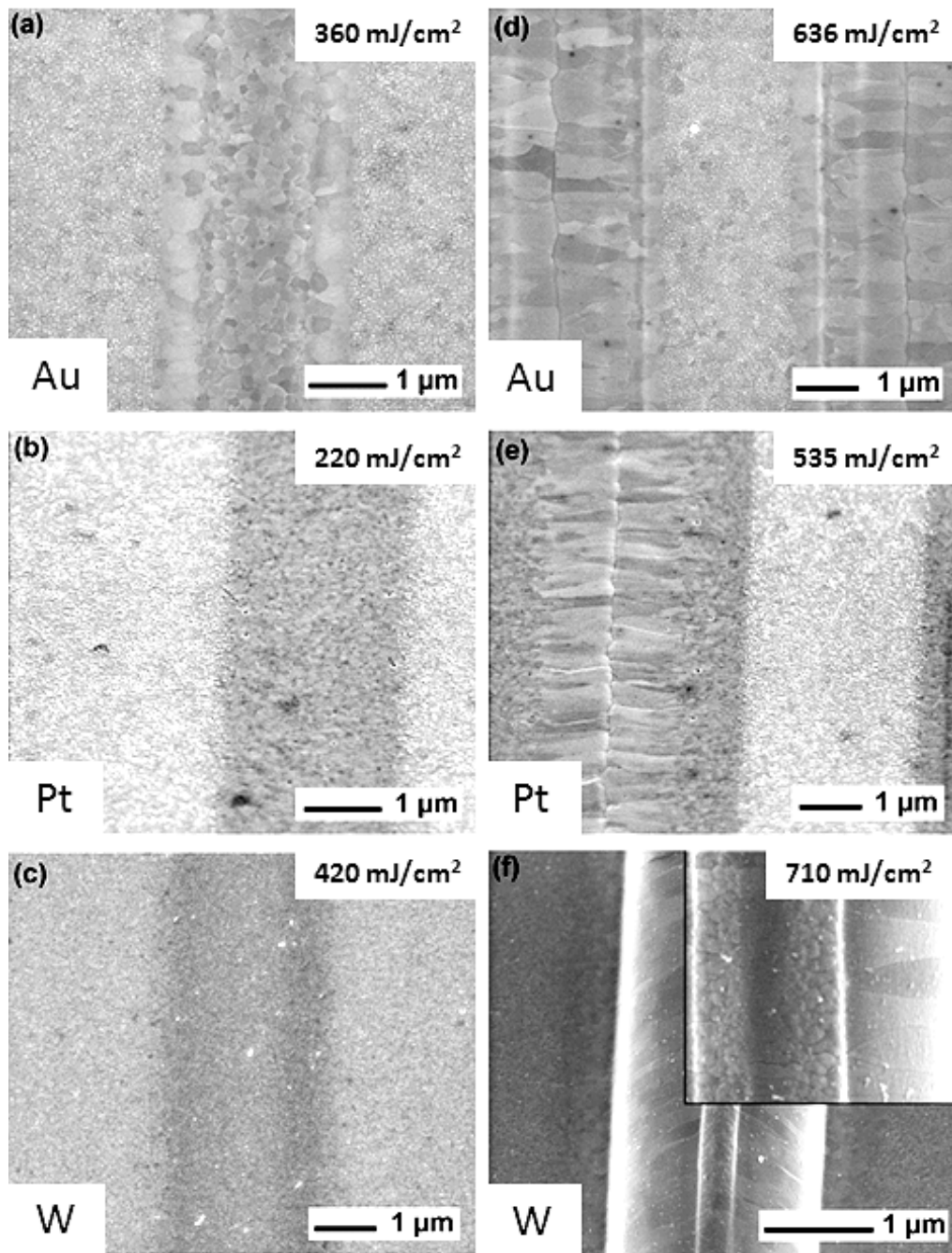


Figure 8.9.: SEM images of irradiated Au, Pt and W 300 nm films at different laser fluences. The left (a, b, and c) and right (d, e, and f) rows denote the low and the high fluence regimes, respectively [30].

All the samples have been irradiated by a single laser pulse and the patterned area per pulse was approximately 4 mm^2 . The laser affected zones correspond to the positions of maximum laser intensity. With the exception of figure 7.9 (d), only one laser maximum is shown in the images. The surrounding areas represent the nearly unaffected laser intensity minimum region with the original film microstructure. Depending on the used energy density and the material, significant differences in the crystallisation behavior of the films can be observed. The results basically indicate three principal energy density regimes: (1) the partial melting of the films by low laser energy densities; (2) the complete melting of the metallic layers for relatively high laser fluence values; (3) and the already discussed SLG scenario located between the partial and the complete melting process.

Figure 7.9 (a) represents the partial melting for a 300 nm thick Au film using a laser fluence of 360 mJ/cm^2 . Cross-sections performed by FIB verified that the film was not molten over the entire thickness.

Although the quenching rates during the laser irradiation can reach values up to 10^{10} K/s [28], the microstructure is neither nanocrystalline nor amorphous in that particular case. During the vertical resolidification process, grains with typical sizes in the range of the film thickness appear. The vertical regrowth is triggered by a thin consistent Au layer remaining in the solid state. A grain coarsening in the laser intensity maximum can be unambiguously identified.

On the other hand, both the Pt (figure 7.9 b) and W films (figure 7.9 c) do not reveal such a distinct grain growth. Especially the W thin films seem to be nearly uninfluenced by the laser treatment. Obviously, the used energy density was not high enough to induce a considerable grain growth compared to gold. This can be mainly attributed to the low melting point of Au ($\approx 1337\text{ K}$) in comparison to Pt ($\approx 2045\text{ K}$) and W ($\approx 3695\text{ K}$) [112].

In contrast, a deviating crystallisation mechanism can be recognised in figures 7.9 (d) to (f). The aforementioned SLG regime appears. In a very narrow processing window, in which the films are nearly completely molten, needle shaped grains grow from the unmolten regions towards the molten laser interference maxima.

A more detailed look at the magnified insert in figure 7.9 (f) for the tungsten film demonstrates that the lateral grains do not proceed to the centre of the laser intensity maximum. Round shaped grains in the middle of this region arise due to the deep supercooling and spontaneous nucleation of the film. A large periodicity or low laser

fluence can facilitate this nucleation. The pattern periodicity in this case was $5\ \mu\text{m}$. In order to avoid spontaneous nucleation, the width of the intensity maxima regions must be narrow enough and the thermal gradient sufficiently high.

Apart from that, the Au and particularly the W films show a strong topography. Generally, a surface tension gradient caused by temperature differences in adjacent areas induces a material flow, as an effect of resulting shear stresses, from the warmer to the cooler regions which is known as the *Marangoni effect* [123]. Accordingly, the resulting shear stresses in lateral-(x) and depth-(y)-direction at the surface can be expressed as [32]:

$$\tau_x = \frac{d\sigma}{dx} = \frac{d\sigma}{dT} \cdot \frac{dT}{dx} \quad (8.4)$$

$$\tau_y = \frac{d\sigma}{dy} = \frac{d\sigma}{dT} \cdot \frac{dT}{dy} \quad (8.5)$$

The gradient $d\sigma/dT$ can be < 0 or > 0 . If $d\sigma/dT < 0$, material flow takes place from the warmer to the cooler regions. In contrast, a positive gradient leads to a pile-up of material in the hot spots [32]. The Marangoni instabilities mainly depend on two time scales: the thermo-capillary and the diffusive time scale [124][125][126]. Thermo-capillary flow leads to the already mentioned material transport from the laser intensity maximum to the intensity minimum. As opposed to this effect, the diffusive mechanism tries to stabilise the film resulting in two competitive processes. It is still not clear which are the main factors influencing or promoting the respective mechanisms. It is supposed that surface active atoms e.g. oxygen or sulphur mainly influence the sign of the surface tension gradient. Due to the fact that the laser irradiation of the samples was performed under ambient conditions, a possible explanation could thus be the presence of oxygen during the laser processing [127]. These adsorbates could also promote the spontaneous nucleation of the film at the central area (figure 7.9 f).

The grain sizes and particularly the micro-texture were determined by EBSD. Figures 7.10 (a) and (b) show the inverse pole figure maps for the Au and Pt samples. The colour-code is related to the inserted orientation triangle. Only one intensity maximum for the Au and Pt films is displayed since the focus of the study is the micro-texture in the SLG-regime. The original fine grained surrounding in the gold sample (figure 7.10 a) clearly demonstrates a $\{111\}$ orientation.

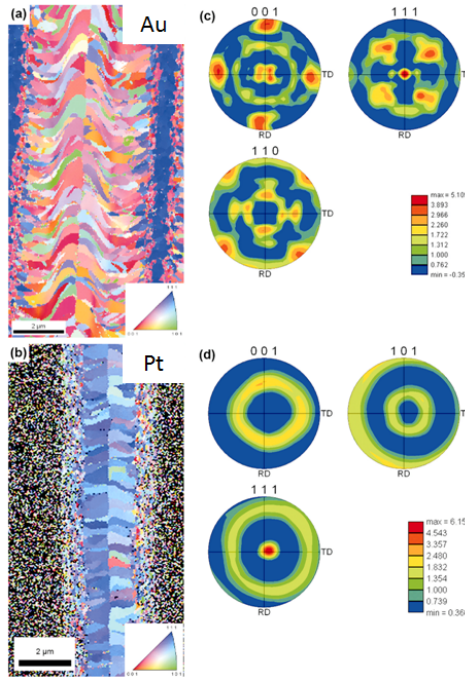


Figure 8.10.: Inverse pole figure maps and corresponding pole figures for the $\langle 001 \rangle$, $\langle 110 \rangle$ and $\langle 111 \rangle$ directions of the 300 nm thick Au (a, c) and Pt thin films (b, d) determined by EBSD. The colour-code corresponds to the inserted orientation triangle.

The inverse pole figure map of the Pt sample shows a different texture (figure 7.10 b). Here, the SLG-zone exhibits a clear $\{111\}$ orientation with a $\{111\}$ fibre texture according to the $\{111\}$ pole figure in figure 7.10 (d). In the as-deposited state, the grain sizes are too small (15–25 nm) for being indexed by EBSD. The lateral resolution limit of the measurement equipment is approximately 30 nm [128]. Obviously, there is a considerable difference between the texture of the Pt and the Au films. A possible explanation for the observed texture could be attributed to the Marangoni forces. Due to the material transport from the laser intensity minimum to the maximum and the resulting topography, this transport process could lead to a tilt of the laterally growing grains. As a consequence, a cube texture would arise from the original $\{111\}$ fibre texture. In the case of Pt, the topography is very slight and the acting Marangoni forces are weak. Therefore, the pristine fibre texture is not significantly changed although a small displacement of the centred accumulation point at $\Psi = 0^\circ$ is clearly visible in the $\{111\}$ pole figure indicating the aforementioned alignment error. Considering the W films, the

necessary Kikuchi signal was too weak finally not allowing for proper indexing. EBSD is a very sensitive surface method with an interaction depth up to 100 nm [129]. Any kind of contamination or deformation layer can result in the disappearance of Kikuchi patterns. Because of the strong topography and a potential oxide layer on top of the W films, an orientation analysis by EBSD was not possible for the abovementioned sample. X-ray diffraction would of course provide texture information but the spatial resolution is quite reduced in comparison to EBSD.

However, the corresponding grain sizes could be evaluated by the linear intercept method. Figures 7.11 (a) and (b) show the grain size distribution for the Au and Pt films measured by EBSD.

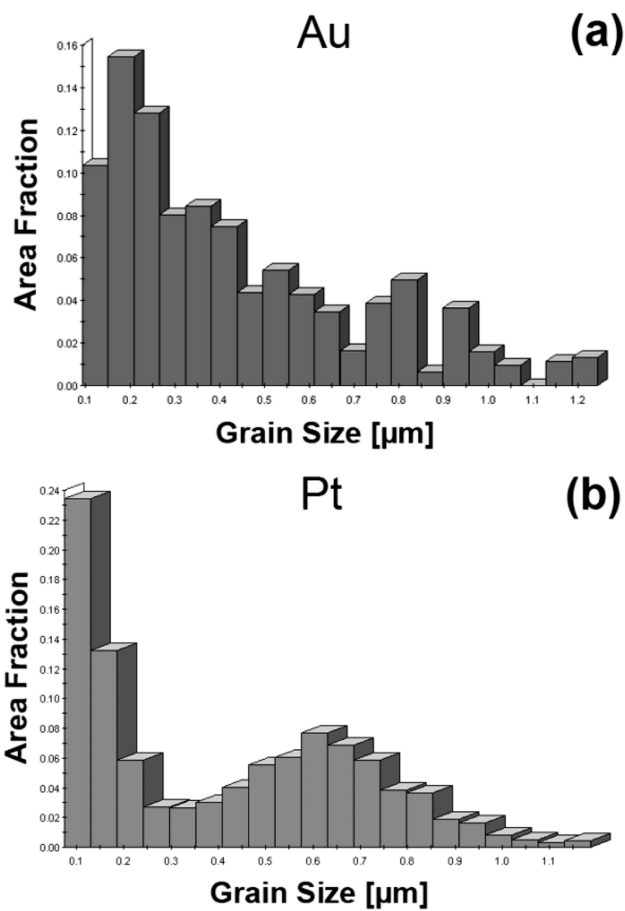


Figure 8.11.: Histogram plot of the grain sizes in laser irradiated Au (a) and Pt samples (b) measured by EBSD.

The histogram plots are directly correlated to figures 7.10 (a) and (b). Looking at the grain size distribution for Au, one peak with a maximum grain size between 100 and 200 nm is clearly visible. Moreover, a smaller peak at around 800 nm can be determined arising from the laterally growing grains. The original grain size in the as-deposited gold films and the laser intensity minimum positions is approximately 100 nm.

In contrast, two different grain size peaks for the Pt films can be well distinguished. The original microstructure is nanocrystalline with very small crystallite sizes only ranging between 15 and 25 nm. Considering the laser intensity maxima, the grain size distribution of the needle-shaped grains exhibits a maximum around 600 nm. Due to the already explained difficulties in measuring the orientation and grain sizes for the W thin films by EBSD, the linear intercept method was applied to calculate the grain sizes in the different crystallisation regions using SEM. Relating to the large-grained area, the grain sizes could be calculated at approximately 563 ± 14 nm. In the centre of the intensity maximum, the globular grains have an average grain size of 57 ± 16 nm. A comparison between the grain sizes of the pristine or nearly unaffected microstructure is hardly possible, because the deposition parameters for the used materials as well as the deposition process for the W films differ significantly. Nevertheless, the resulting grain sizes in the SLG-regime vary between 563 and 800 nm thus being comparable to the other irradiated metallic films.

In addition to experimental studies, further simulations were performed in order to provide insights into the behaviour of the solid-liquid interface (see figure 7.12). Based upon this, it can be clearly observed that the liquid interface of the gold film at a fluence of about 360 mJ/cm^2 was not completely extending to the substrate. The calculated temperatures in figure 7.12 (b) at the interference maxima and minima positions were 2200 and 450 K.

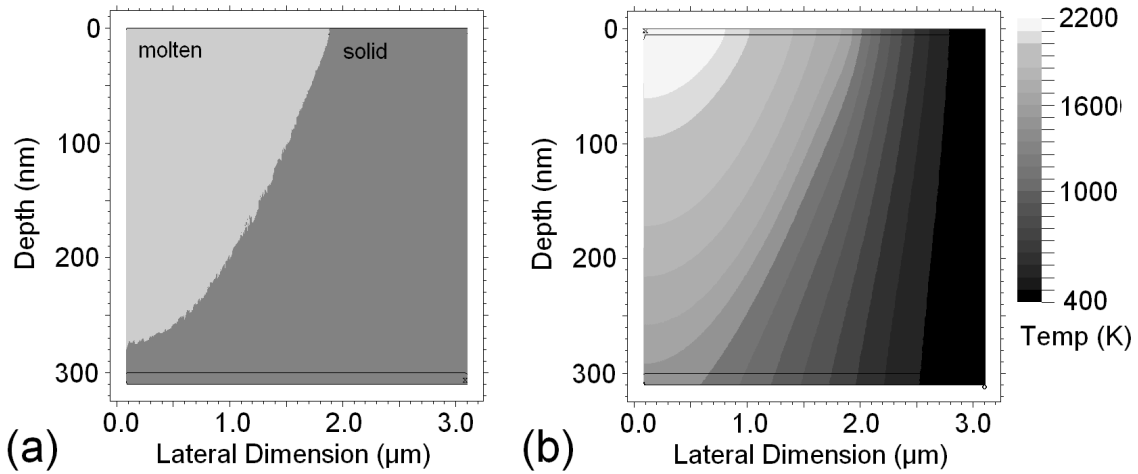


Figure 8.12.: Thermal Simulation of a laser-patterned Au film at a fluence of about 360 mJ/cm^2 . On the left side, the liquid-solid interface during the resolidification is displayed and on the right side, the thermal gradient both through the entire film thickness starting from the center of the intensity maximum.

Furthermore, the temperature distribution for the three studied systems at higher fluences, together with the two-dimensional information about the solid/liquid interface of the metallic layers was simulated.

As can be seen in the figures 7.13 (a), (c) and (e), the temperature gradient is parallel to the film surface which means that the recrystallisation front is perpendicular. Moreover, the adjacent not molten areas act as heterogeneous nucleation sites for the laterally growing grains. These grains are subsequently impinging with one another forming a clear centre-line. The maximum extent over which the grains are able to grow depends strongly on the energy density, the pattern periodicity as well as the substrate temperature [100]. In this particular case, the substrates were not heated. According to the thermal simulations, the temperature difference between interference maxima and minima is about 2400, 1800 and 3000 K for Au, Pt and W at laser fluences of 636, 535 and 710 mJ/cm^2 , respectively (see figures 7.13 b, d and f).

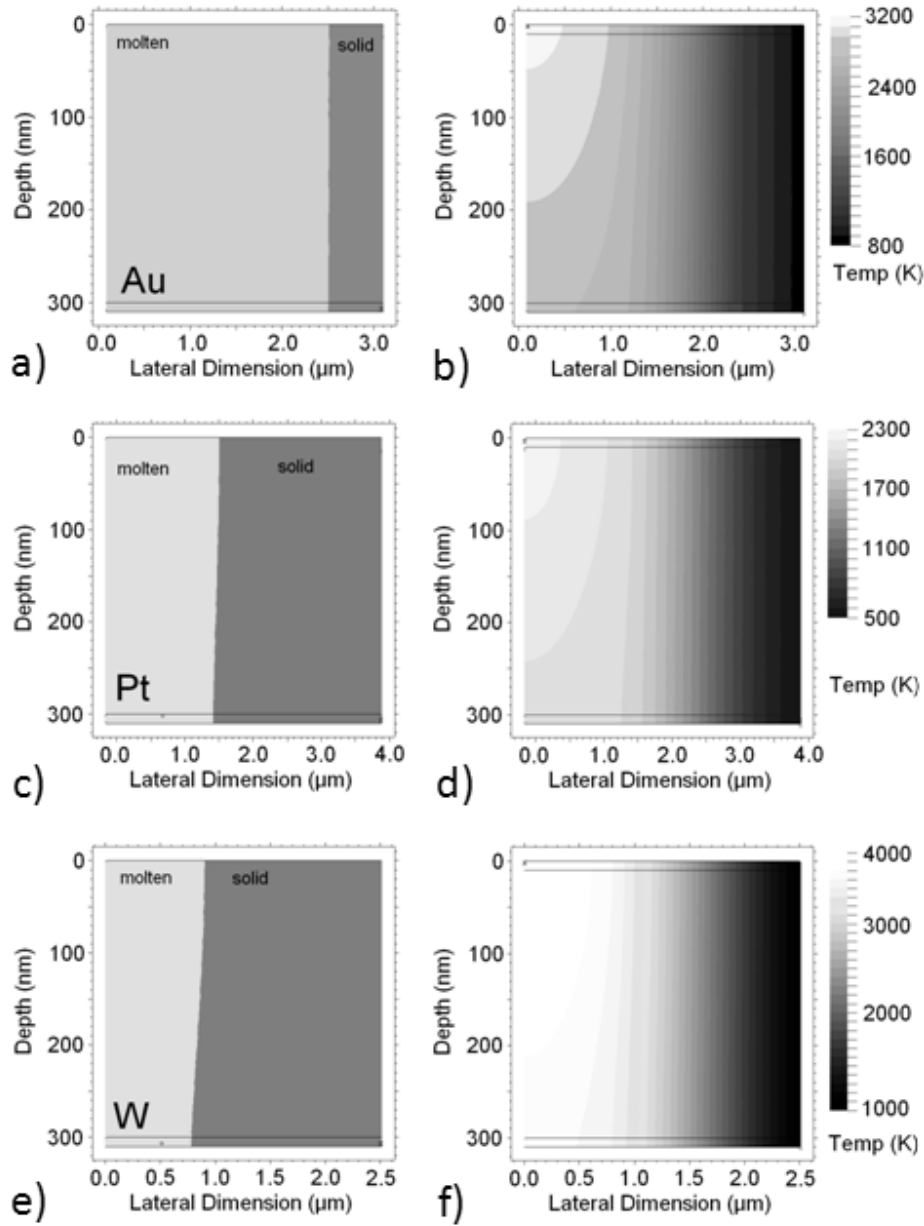


Figure 8.13.: Thermal simulation of the laser-treated Au, Pt and W films. Figures a, c and e show the liquid-solid interface during the resolidification process for the Au, Pt and W samples. The thermal gradient over the cross-section of the film starting from the centre of a laser intensity maximum position is shown in b, d and f for Au, Pt and W films. (a, b) Au: laser fluence 636 mJ/cm^2 , (c, d) Pt: laser fluence 535 mJ/cm^2 , (e, f) W: laser fluence 710 mJ/cm^2 .

8.1.3. Laser processing and topographic analysis of Au thin films

After having studied the possibilities of creating lateral periodic grain size composites in different metallic thin films, it is of particular interest to investigate the tribo-mechanical effectiveness of the microstructural architectures. In this case, the emphasis will be laid on laser patterned Au films and their potential under dry sliding conditions.

Numerous electrical contacts worldwide are exposed to sliding motion. Commonly conductor materials are gold and copper. Very often, electrical contacts are gold plated [130]. This has no bearing on the electrical properties i.e. the electrical resistivity of gold which is indeed higher compared to copper ($\rho_{Cu} = 16.78 \text{ n}\Omega\text{m}$ and $\rho_{Au} = 22.14 \text{ n}\Omega\text{m}$ at 20° C [130]). In fact, gold is primarily used due to its corrosion resistance. Moreover, gold can be easily deformed and deposited (for example by sputtering or evaporation) [131]. A potential drawback of Au is its propensity to adhere which is often compensated by a thin hydrocarbon layer present while exposed to ambient conditions [131].

At first, a brief overview about the experimental procedure with a particular focus on topographic parameters will be presented. Table 7.2 summarises the selected periodicities and pattern geometries:

Labelling	Periodicity (μm)	Pattern
L2	2	Line
L3	3	Line
L5.6	5.6	Line
L6.4	6.4	Line
L8	8	Line
C2	2	Cross
C8	8	Cross
D4	4	Dot

Table 8.2.: Sample labelling, laser periodicity and pattern geometry.

Figure 7.14 shows the three pattern geometries (line-, cross- and dot-like) measured by WLI. Relevant topographic parameters for the subsequent analysis are the Swedish height H , the root mean square roughness r_{ms} , the root mean square slope S_{rms} , the skewness R_{sk} and finally the kurtosis R_{ku} which were determined by WLI and compared

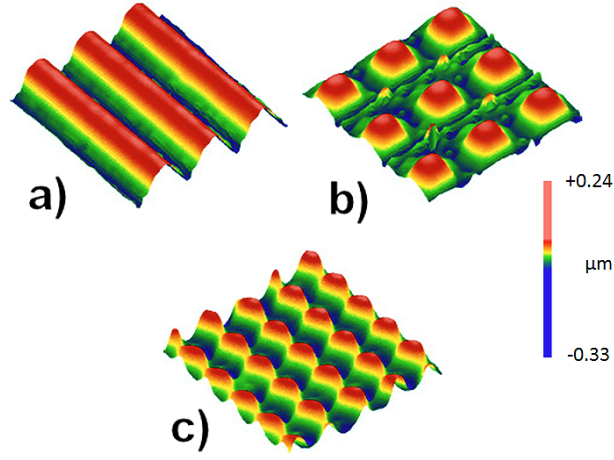


Figure 8.14.: 3-D surface view of line- (a), cross- (b) and dot-like (c) laser pattern recorded by WLI.

to each other.

Table 7.3 outlines the specific parameters for the not-patterned gold reference and the laser irradiated specimens. The averaged values are based upon ten measurements for

Labelling	H (nm)	S_{rms} ($\mu\text{m}/\text{mm}$)	rms (nm)	R_{sk}	R_{ku}
Reference	10 ± 2	103 ± 11	10 ± 1	0.56 ± 0.34	3.27 ± 0.37
L2	202 ± 16	557 ± 26	62 ± 13	-0.15 ± 0.05	2.35 ± 0.20
L3	240 ± 14	542 ± 21	195 ± 26	-0.39 ± 0.16	4.06 ± 0.60
L5.6	236 ± 13	247 ± 13	175 ± 15	-1.47 ± 0.30	3.45 ± 0.31
L6.4	246 ± 36	416 ± 24	85 ± 14	-2.48 ± 0.31	7.99 ± 0.46
L8	93 ± 6	420 ± 18	41 ± 1	-2.76 ± 0.39	1.63 ± 0.33
C2	17 ± 3	14 ± 2	4 ± 1	0.15 ± 0.02	2.35 ± 0.18
C8	76 ± 4	221 ± 16	31 ± 3	-1.64 ± 0.07	1.46 ± 0.06
D4	69 ± 4	40 ± 8	25 ± 6	0.35 ± 0.13	1.53 ± 0.08

Table 8.3.: Surface parameters of reference and laser treated specimens measured by WLI. Here, H denotes the Swedish height, S_{rms} the root mean square slope, rms the root mean square roughness, R_{sk} the skewness and finally R_{ku} the kurtosis.

each pattern geometry. The Swedish height of the line-pattern ranges between 93 and 246 nm. In the case of cross-patterns with a small periodicity, H is much smaller than for other patterns. This might be due to the surface being melted twice, thus levelling

8. Results and discussion

the previous structure height to some extent. In fact, the laser energy density was kept constant at 165 mJ/cm^2 for all samples. But, H is depending on the pattern geometry and selected periodicity which was already discussed in [46]. Interestingly, the skewness R_{sk} , being an indicator for the bearing capability, is most negative for samples L6.4 and L8. While looking at the surface profile plots in figure 7.15 which compare sample L6.4 and L3 for example, it is obvious that the surface profile of L6.4 is more plateau-like which could be beneficial in terms of load supporting.

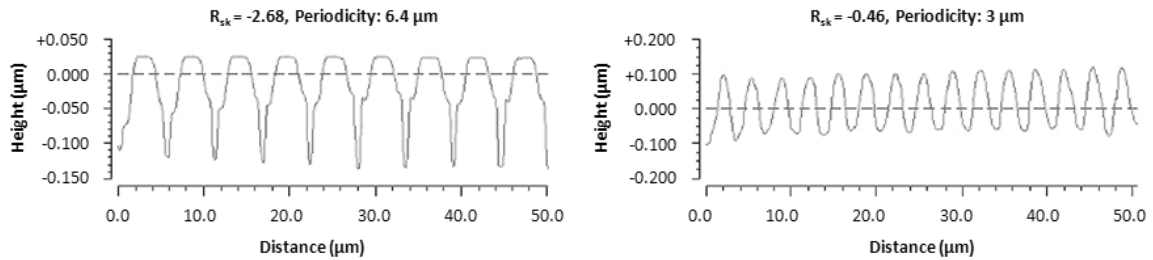


Figure 8.15.: Comparison of two surface profile plots of specimens having a skewness of -2.68 (left) and -0.46 (right). The specimen on the left side shows a more plateau-like surface.

Apart from the reference, only the cross- (C2) and the dot-like pattern (D4) show positive skewness values. But, it is important to note that R_{sk} and R_{ku} are both highly sensitive and may vary significantly along the surface. In the case of R_{sk} , laser patterns with higher periodicities tend to have a more negative skewness thus being less spiky (see samples L6.4, L8 and also C8). Regarding R_{ku} , there seems to be no direct correlation between pattern geometries and lateral feature sizes.

Another interesting feature is the already presented Abbott-Firestone plots. These plots provide geometrical insight regarding the bearing capability of surfaces and might be particularly interesting for the evaluation of surface textures under lubricated sliding. Generally, the cutting depth of a surface height profile is normalised to a maximum cutting depth corresponding to a bearing ratio of 100 %. Consequently, a relative cutting depth is plotted versus the bearing ratio [72]. The following graph comprises the Abbott-Firestone plots of different laser patterns compared to the reference specimen (see figure 7.16).

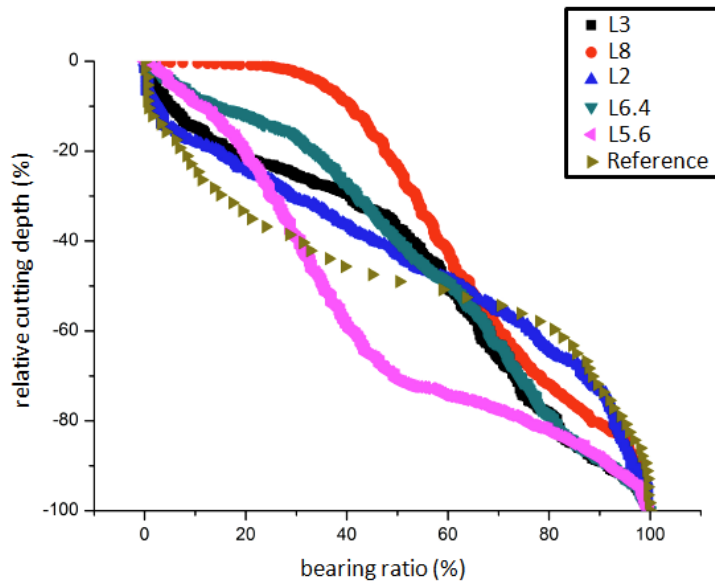


Figure 8.16.: Abbott-Firestone plots of laser-patterned samples vs. reference surface.

Obviously, all the laser patterned samples show a more pronounced decrease depending on the relative cutting depth than the reference. In particular, sample L5.6 and L8 are noticeable. Specimen L8 already has a bearing ratio of nearly 40 % at a relative cutting depth of about 5 %. Thereafter, the respective bearing curve rapidly drops indicating a plateau-like surface with steep flanks. In contrast, sample L5.6 reveals a low bearing ratio even after a large relative cutting depth. In order to understand the presented trend, a closer look at the surface profiles is necessary (see figure 7.17). Indeed, specimen L8 has a clear plateau-like surface with relatively steep flanks. The root mean square slope is according to table 7.3 approximately $420 \mu\text{m}/\text{mm}$. On the other hand, sample L5.6 exhibits a spiky surface. The skewness in this case is only -0.46 whereas R_{sk} for L8 is -2.76 , the most negative of all samples. Comparing all different samples, the abovementioned tendency is obvious.

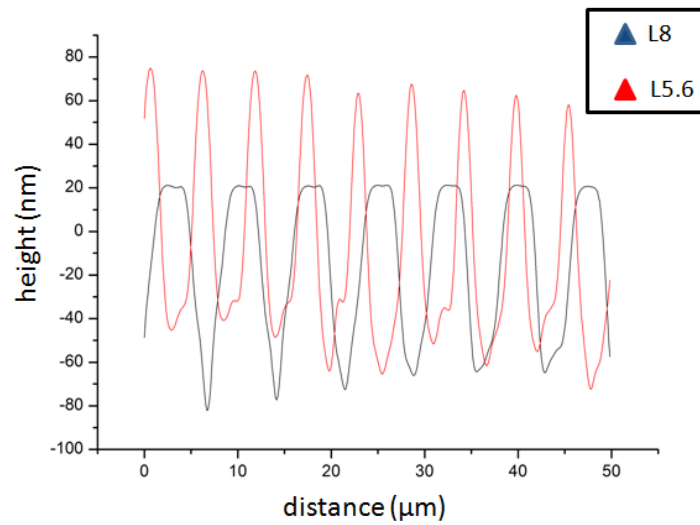


Figure 8.17.: Comparison of surface profiles of samples L5.6 and L8 recorded by WLI.

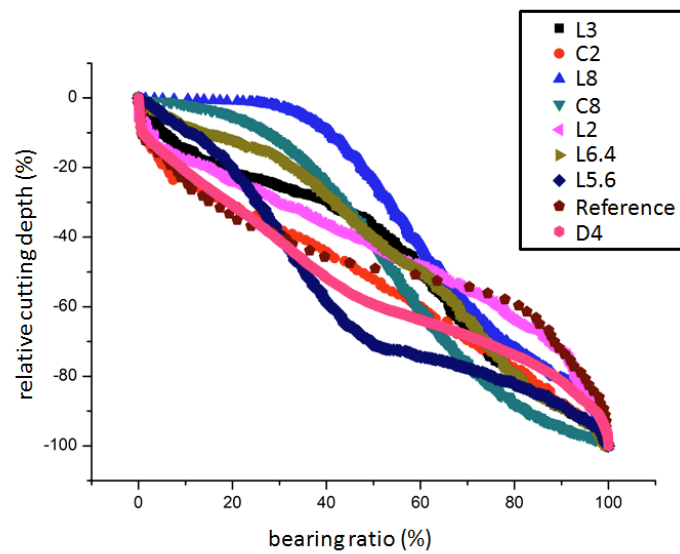


Figure 8.18.: Comparison of Abbott-Firestone plots between laser textured samples and reference.

Figure 7.18 illustrates significant differences between the specimens varying by a bearing ratio of around 50 % at a difference in relative cutting depth of approximately 20 %. Again, specimens having a pronounced negative skewness (L6.4, L8 and C8) initially

show a larger bearing ratio. After running-in, the profile suddenly drops due to relatively steep flanks.

8.1.4. Tribological properties

The tribological tests have been performed by using a ball on disk configuration with an alumina ball under linear reciprocating sliding. Further experimental parameters can be found in table 7.4:

Parameter	Value
Amplitude	0.2 mm
Sliding velocity	0.5 mm/s
Normal force	500 μ N
Laps	100
Acquisition rate	100 Hz
Ball diameter	1.5 mm

Table 8.4.: Tribological measurement parameters.

In this context, linear reciprocating sliding tests were conducted for line- and cross-patterned surfaces under a perpendicular alignment of the laser lines to the sliding direction. Figure 7.19 recapitulates the results of the friction coefficient μ depending on the sliding distance. First of all, there is a clear difference in the frictional behaviour of sample L2 compared to the other samples. The shape of μ versus sliding distance for L2 is characteristic for non-lubricated but also boundary lubricated metals in contact. After having reached a maximum in friction coefficient due to an initial roughness, smoothing may occur leading to a reduction in μ . Moreover, the drop can be also explained by texture softening or low-shear transfer films developing in the contact [132].

In particular texture softening, which was applied by Kuhlmann-Wilsdorf to explain most typical shapes of μ , seems to be interesting and quite realistic [133]. Within this theory, it is supposed that the texture reorientation below the surface may be responsible for the friction reduction. The reorientation process results in a decrease of the effective shear stress in near-surface regions and thus in a reduction of the respective friction force [134]. Previous EBSD results after the very first sliding events revealed a change in micro-texture. The pristine grain orientation within the wear scar changed from a $\langle 111 \rangle$ - to a $\langle 100 \rangle$ -orientation according to the inverse pole figure map. Further differences in the friction curve of L2 compared to the other specimens, apart

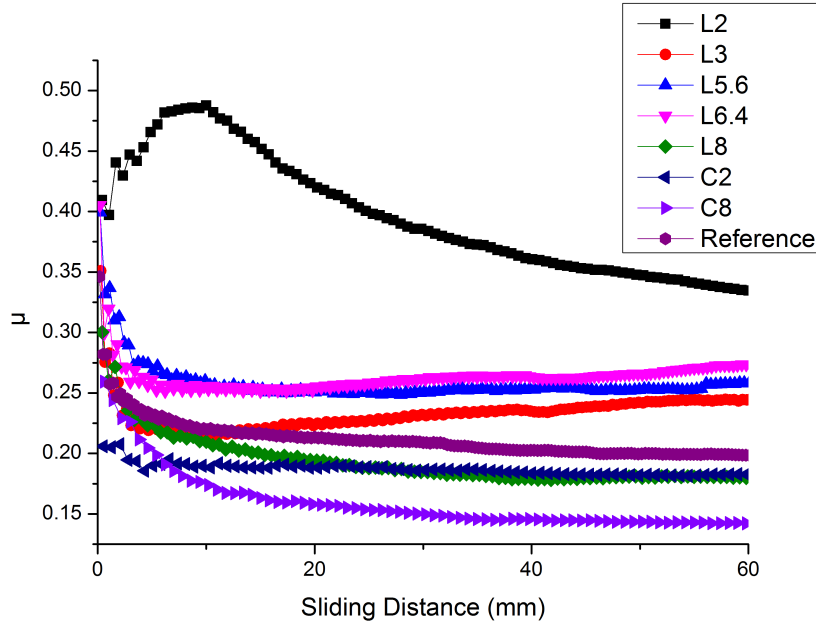


Figure 8.19.: Friction coefficient vs. sliding distance in mm for line- and cross-patterned specimens measured under dry reciprocating sliding conditions and a perpendicular orientation between the laser lines and the sliding direction.

from the general shape, may be attributed to the completely deviating microstructure and a different contact area due to the topographic parameters such as skewness. This seems to be also reasonable for the other samples thus strongly influencing the contact area and finally the coefficient of friction. However, in contrast to L2, all other samples do not show a momentary rise in μ . The coefficient of friction directly drops from different initial values down to a steady-state value which is again characteristic for texture reorientation processes as described by Blau et al. [135]. Once a preferred grain orientation is achieved, having mainly directions of easy shear parallel to deformation-induced shear stresses, a steady-state in μ is accomplished [135].

The not patterned reference sample is located among the structured surfaces. Interestingly, sample C2, having a positive skewness and a large wear volume, illustrates a relatively low initial coefficient of friction which is stable over the sliding distance. The problem is principally based upon the fact that μ is highly system-dependent and influenced by various factors. It is well known that the origins of μ on a fundamental level are difficult to understand [136]. Finally, there is no direct correlation between the

coefficient of friction and the wear behaviour. Two samples may have identical friction coefficients but the wear rates are completely different because the energy of the frictional contact is partitioned in a different way in these two cases [136]. However, the general tendency is demonstrated, especially for samples L2, L8 and C8. A quantitative analysis of the resulting wear scars was performed using the standard method for wear testing with a ball on disk configuration (*ASTM G99*) [137]. Figure 7.20 explains the basic testing principle.

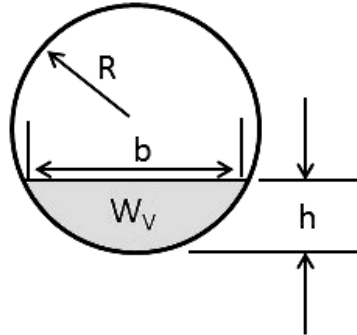


Figure 8.20.: Standard wear testing using a ball on disk configuration according to *ASTM G99*. R denotes the ball radius, b the width of the wear track, h the penetration depth of the counter body and W_V the wear volume [137].

Based upon this model, the wear volume W_V can be calculated by:

$$W_V = \frac{\pi}{6} \cdot h \cdot \left(\frac{3b^2}{4} + h^2 \right) \quad (8.6)$$

with the wear track or penetration depth h which can be determined by:

$$h = R - \sqrt{R^2 - b^2/4} \quad (8.7)$$

Additionally, if $h/R \ll 1$, then W_V may be simplified to:

$$W_V = \frac{\pi \cdot b^4}{64 \cdot R} \quad (8.8)$$

The ball radius is known and the width of the wear tracks is measured by WLI. It is important to note that this testing method is only applicable to the laser line- and cross

patterns and of course to the reference. In the case of dot-patterns, there is no real wear track. Instead, the dots are flattened while rubbing with no resulting track depth. Graph 7.21 represents the measured wear volume for the different line-patterns compared to the reference.

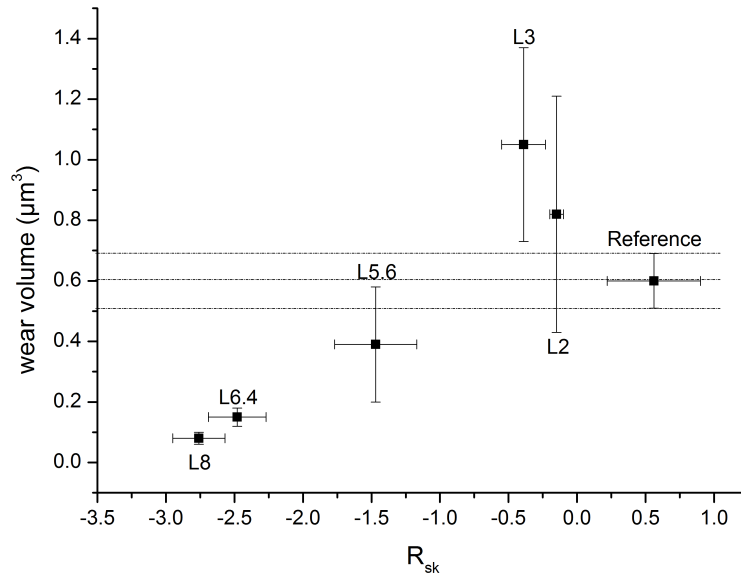


Figure 8.21.: Wear volume in (μm^3) vs. skewness of laser line-patterns compared to the reference.

Except for sample L2, the wear volume rises with increasing skewness. Moreover, some samples have a larger wear volume than the reference. In contrast, specimens L6.4 and L8 lead to a remarkable enhancement. In case of L2 and L3, the error bars are quite large. This is due to the difficulties in determining the depth of the wear tracks. The corresponding wear tracks are very irregular thus complicating the depth measurement. The relatively large wear volume of sample L2 might be attributed to the completely different grain morphology. At a reduced line-spacing, the specimens tend to show grain growth even in the positions of minimum intensity. This is basically explained by a predominant lateral heat flow which was previously shown by calculating the thermal diffusion length.

8. Results and discussion

A comparison of the wear volume between line- and cross-patterns can be found in figure 7.22.

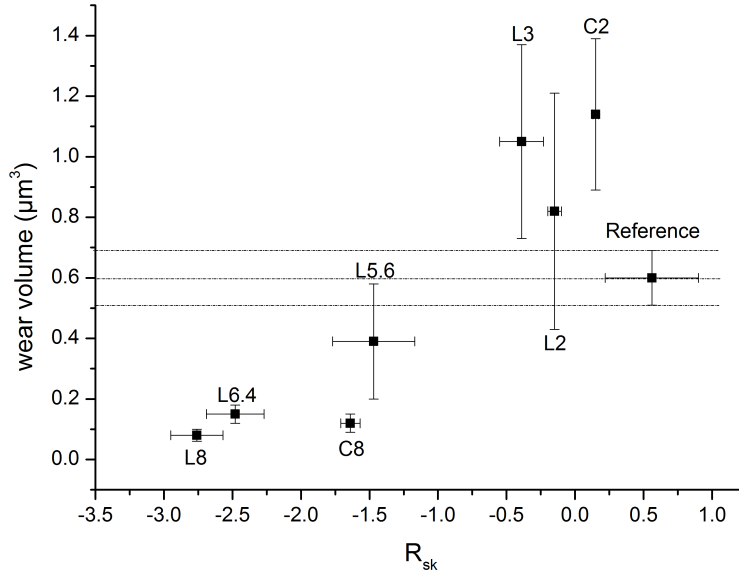


Figure 8.22.: Wear volume vs. skewness of laser line- and cross-patterns compared to the reference.

Here, sample C2 shows a similar trend like L2 both having a line-spacing in the range of the thermal diffusion length. Furthermore, samples C8, L8 and L6.4 are characterised by a low wear volume. Those samples have the most negative skewness values indicating a more plateau-like surface and finally show the best bearing ratio according to the Abbott-Firestone plots. Obviously, there is a direct correlation between the measured topographic parameters such as skewness and the bearing capability. In the following, detailed microstructural and morphological studies of the wear tracks performed by SEM, FIB and EBSD will be presented and discussed with regard to the obtained values for the wear volume W_V . First of all, the evolution of the wear tracks for the reference is shown in figure 7.23.

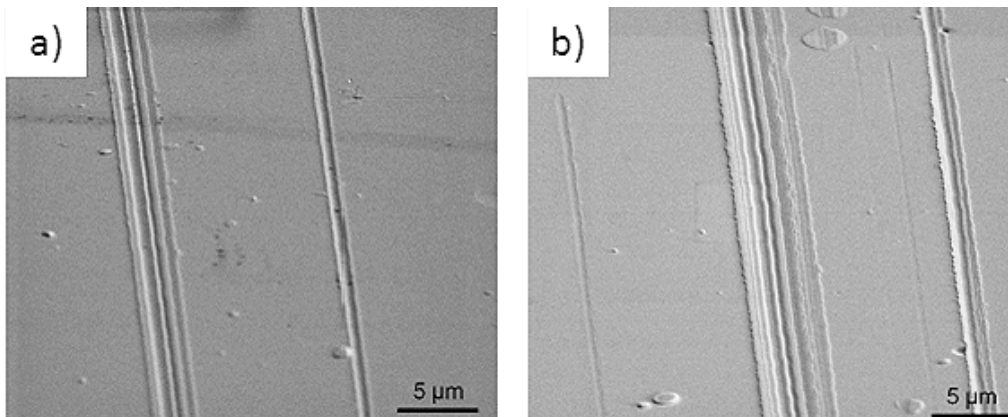


Figure 8.23.: SEM image of a wear scar in a not patterned Au thin film after 1 (a) and 50 sliding cycles (b).

In the beginning, the microstructure is fine-grained (grain size between 80 and 160 nm being typical for the transition nanocrystalline/ultra fine-grained materials.) and has a typical fibre-texture in the as-deposited state [138] (see figure 7.24).

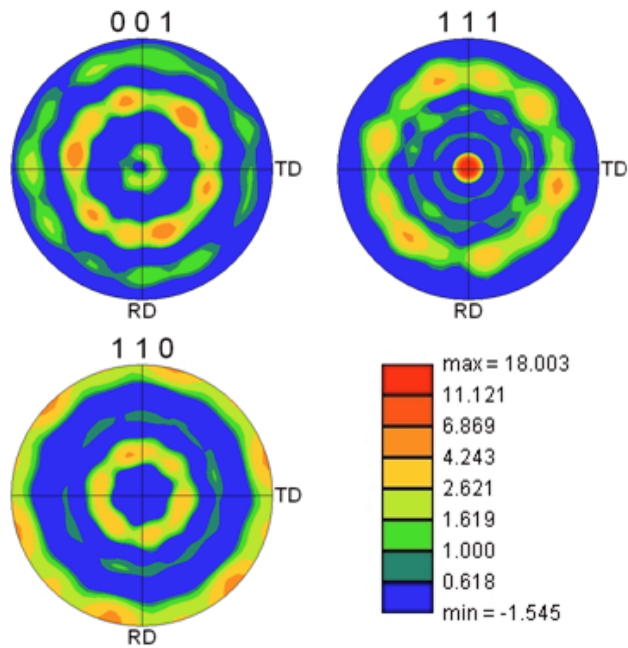


Figure 8.24.: Pole figures of the as-deposited Au thin film for the (001), (110) and (111) lattice planes measured by EBSD.

8. Results and discussion

The original microstructure is modified by the linear sliding process leading to a thermal and mechanical impact. Therefore, the microstructure and micro-texture will be influenced. Figure 7.23 clearly demonstrates that there is no continuous wear scar. Instead, only few interaction paths, with more pronounced primary and a narrower secondary track could be detected even after 50 sliding cycles. Those primary and secondary tracks are the result of the asperity interaction between the ball and the substrate. Looking at a magnified picture of the primary track in figure 7.25, one can identify a considerable grain growth in the interaction zones.

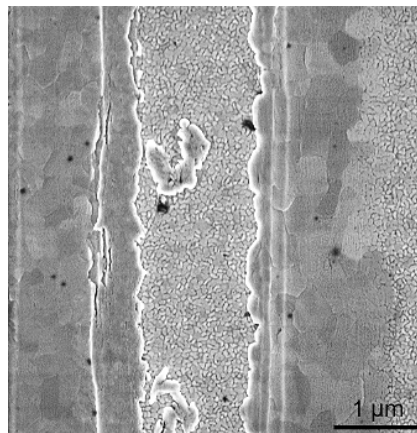


Figure 8.25.: Magnified picture of the primary track in the wear scar of the reference specimen after one sliding cycle.

The grain size distribution in the interaction regions has been determined by EBSD (see figure 7.26).

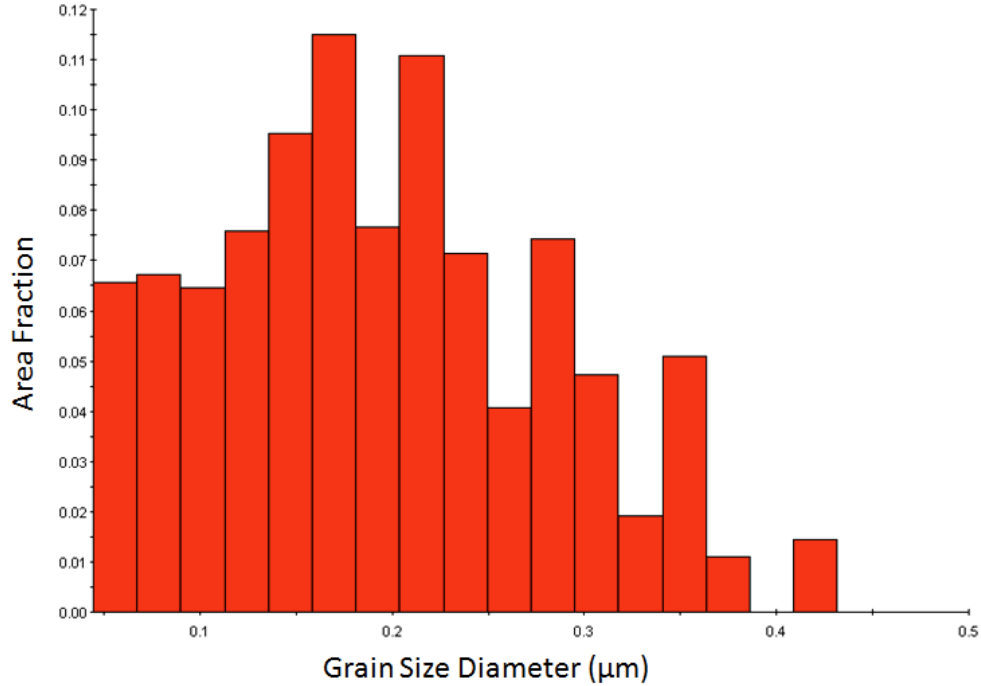


Figure 8.26.: EBSD grain size distribution of the interaction zone in the primary track of the wear scar.

The grain size in the interaction zone of the primary track within the wear scar approximately increased to ≈ 215 nm which is about 50 nm larger compared to the reference.

Apart from grain growth, the micro-texture after the very first sliding event also changed which can be observed in corresponding inverse pole figure maps of the primary track. Figure 7.27 (a) shows the inverse pole figure of the primary track within the wear scar after one sliding cycle. The original grain orientation ($\langle 111 \rangle$ orientation) changed due to the sliding event. Based upon the standard orientation triangle, the colour of each grain corresponds to a distinct orientation. A more detailed look at the inverse pole figure map along the rolling directions discloses that the grains along the track are characterised by a preferred $\langle 100 \rangle$ orientation. For fcc-metals, a suitable Burgers vector is $\langle 110 \rangle$ [139]. Dautzenberg et al. reported about dynamic recrystallisation phenomena which

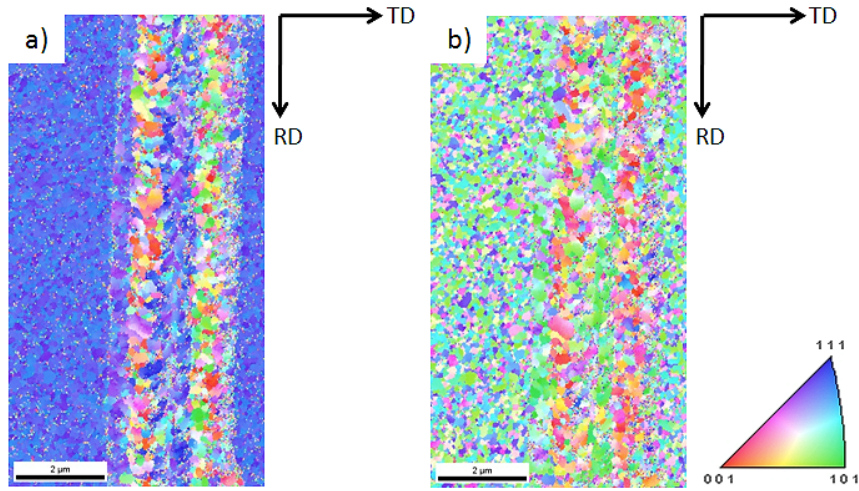


Figure 8.27.: Inverse pole figure map of primary track with corresponding standard orientation triangle. TD denotes transverse- and RD rolling direction. Figure (a) represents the inverse pole figure map along the normal- and (b) along the rolling direction. The step size was set to 30 nm and the confidence index (CI) is 0.15.

play a decisive role in this context [140]. Due to the repeating sliding, the material is heavily deformed. Furthermore, it is known that an additional deformation leads to a decrease in the recrystallisation temperature. This might explain the observed grain growth after few cycles and the texture reorientation. The effect of texture-reorientation was already discussed related to the frictional behaviour. Here, Blau and Kuhlmann-Wilsdorf suggested that the initial drop in the friction coefficient (e.g. for the reference) is influenced by a preferred grain orientation along the deformation-induced effective shear stress [132][133].

Concerning the wear scars in laser line patterns, the pattern seems to be completely worn off after sliding. Figure 7.28 (a) depicts a topographic measurement of a wear scar in a patterned sample with a periodicity of around $6.4 \mu\text{m}$ (L6.4). In figure 7.28 (b), a longitudinal-cut is shown within the wear scar denoted by a black arrow in 7.28 (a).

8. Results and discussion

The laser-induced topography is still visible and the related amplitude spectrum highlights a spatial frequency at $1/160$ mm corresponding to $6.4 \mu\text{m}$ (see figure 7.28 c).

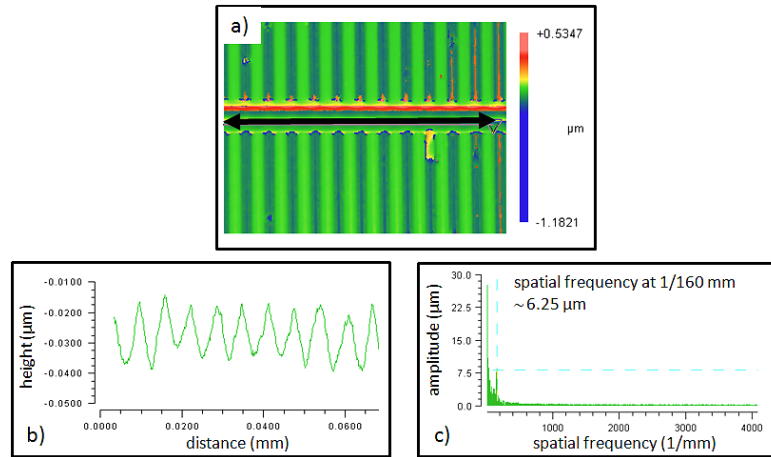


Figure 8.28.: WLI surface plot of a wear scar in a laser line pattern (a). In (b) a longitudinal cut profile is shown for the wear track and (c) is an amplitude spectrum plot depicting a characteristic spatial frequency which corresponds to the pattern line spacing.

A direct comparison between wear tracks in line-, dot- and cross-pattern is presented in figure 7.29.

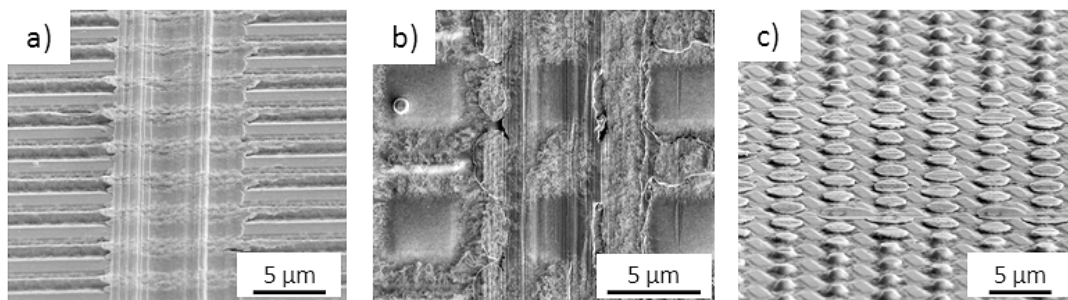


Figure 8.29.: SEM images of worn line- (a), cross- (b) and dot-pattern (c) after 100 cycles.

There are significant differences in the wear track morphology depending on the interference geometry. As already mentioned, in the case of line- and cross-patterns a wear track with a certain width and depth can be found whereas the dot-pattern is subse-

quently shorn off thus increasing the contacting area between the rubbing partners. A magnified SEM picture of the worn dot-pattern with an inverse pole figure map is highlighted in figure 7.30. Figure 7.30 (b) is a combination of a conventional inverse pole

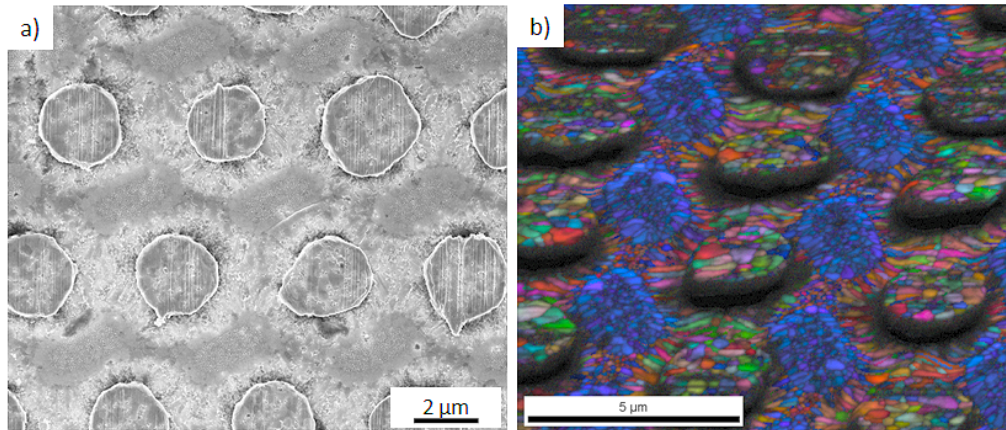


Figure 8.30.: SEM image (a) and inverse pole figure map (b) of worn dot surface. The blue colour coded regions correlate with the original grain structure. The step size was set to 30 nm with a confidence index of 0.15.

figure and an image quality map (IQ map) revealing as a metric the quality of a diffraction pattern. An image quality map is constructed by mapping the IQ value measured for each diffraction pattern obtained during an orientation imaging scan to a gray or colour scale [141]. Darker areas correspond to a reduced backscatter signal. Some parts of the dots are shadowed thus displayed black due to the absence of Kikuchi patterns. The nearly not affected regions can be easily identified with their $\langle 111 \rangle$ -orientation. Within the positions of maximum intensity and sliding contact, no preferable orientation is visible.

Taking the dot-like interference pattern as an example, it is interesting to study the influence of the grain size variation on mechanical properties such as hardness by nanoindentation (*in collaboration with Dr.-Ing. A. Barnoush, group of Prof. Dr. rer. nat. H. Vehoff, Saarland University*). The peak loads of 50, 100 and 200 μN were selected in this range to limit the indentation depth up to 10% of the total film thickness. This ensures that the measurements are neither affected by the geometry of the structured surface nor by the substrate. The loading profiles included five segments: loading to a peak load; holding at the peak load; unloading back to 10% of the peak load; holding at 10% of the peak load; unloading back to zero loads. Separating the thermal drift from

creep in the material was possible by a comparison of the displacement in the two holding load segments. As a result no considerable thermal drift during our measurements was observed. The loading rate for all indents was set to $20 \mu\text{N/s}$. The recorded load-displacement curves for each indent were used to extract the hardness data according to the Oliver-Pharr method [142]. These data are shown in figure 7.31.

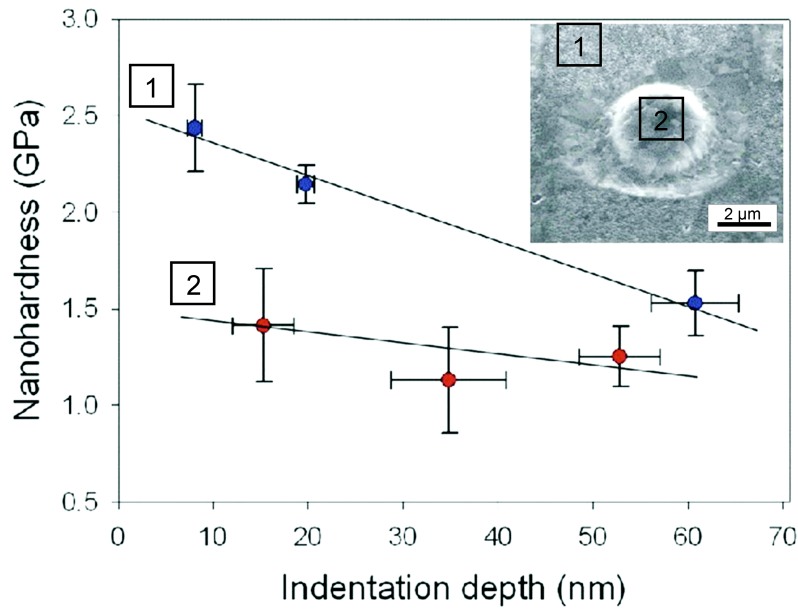


Figure 8.31.: Nanohardness as a function of indentation depth applying three different loads of 50 , 100 and $200 \mu\text{N}$. These results were determined at a 690 nm thick gold sample modified with an interference pattern using three interfering laser beams. The indentations were performed in the laser intensity minima positions and in the laser intensity maxima positions on top of the hemispherical structures.

A strong decrease in the hardness of the laser treated parts due to recrystallisation and grain growth in the irradiated area is visible. The average grain size in the fine-grained area ranges between 80 and 160 nm and in the irradiated region around 300 nm . Due to the Hall-Petch relationship [143][144][145], the hardness in the recrystallised area is reduced. The inserted lines should only emphasise the tendency of the measured hardness and represent no linear fit.

A further question is dealing with the acting wear mechanisms. A very useful parameter for exploring these mechanisms is the cutting efficiency f_{ab} . By means of a typical wear track with the belonging cross-section profile, this parameter will be defined and discussed in more detail.

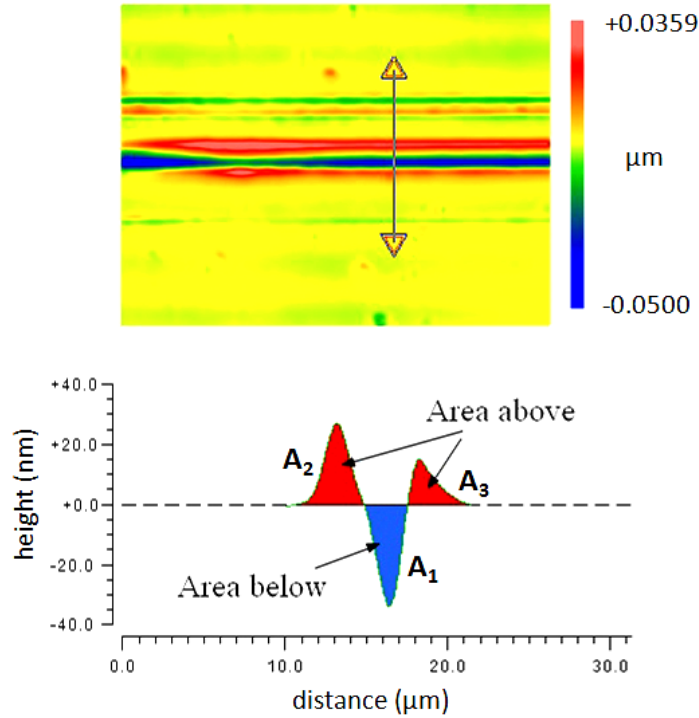


Figure 8.32.: Definition of the cutting efficiency on the basis of a wear track in a not patterned Au film.

According to figure 7.32, the cutting efficiency f_{ab} is defined as follows:

$$f_{ab} = \frac{A_1 - (A_2 + A_3)}{A_1} \quad (8.9)$$

where A_1 denotes the cross-sectional area of the track and $(A_2 + A_3)$ of the rim of the track [146]. If $f_{ab} = 0$, then micro-ploughing is the predominant wear mechanism resulting in mere material displacement without removal. If $f_{ab} = 1$, this means micro-cutting is taking place and material is entirely removed from the track and no lateral ridges are formed. Graph 7.33 presents the cutting efficiency for the different line-patterns compared to the reference.

8. Results and discussion

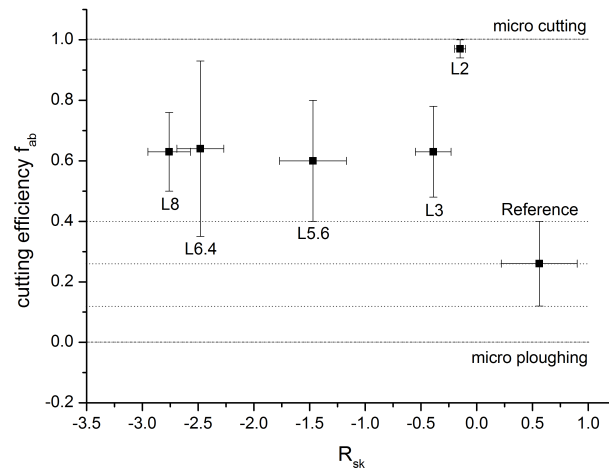


Figure 8.33.: Cutting efficiency for laser line-patterns compared to the reference.

In general, the standard deviations for the specimens are quite high. Due to wear track irregularities, the respective cross sectional areas contributing to the determination of f_{ab} cannot always be unambiguously identified. Nevertheless, specimen L2 has small error bars and the value for f_{ab} is near 1 indicating that micro-cutting is the ruling mechanism. This hypothesis is also supported by the cross-section profile of the track. Figure 7.34 compares the WLI profiles of samples L2 and L8. Obviously, sample L8 is

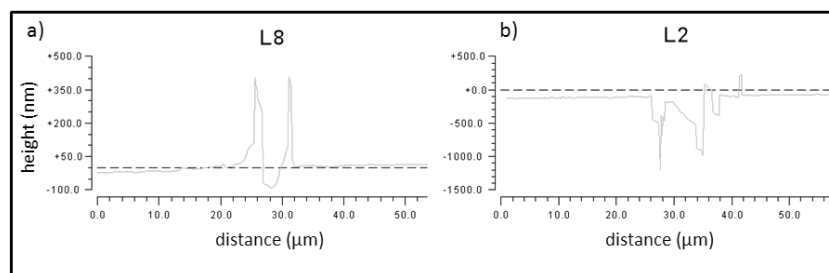


Figure 8.34.: Comparison of cross section profiles.

characterised by lateral ridges being the result of shifted material from the wear track center. In contrast, L2 does not show any rims having a f_{ab} of about 0.97. Although the error bars are in most cases large, this parameter is very useful to get an idea about the apparent wear mechanism. For sample L2 there is a good correlation between the

measured f_{ab} and the corresponding wear profile plot. Concluding, most samples will be subjected to a combination of ploughing and cutting as can be seen in graph 7.33.

8.1.5. Contact modelling

In order to correlate the experimental findings of this section with theoretical considerations, a simple Greenwood-Williamson approach was used to estimate the number of asperities in contact, the contact area and finally the occurring contact pressures for the specimens having line-patterns. As already discussed in the theoretical part of the thesis, the Greenwood-Williamson model allows for the description of a contact between a stochastic surface and a rigid plane. Here, the laser treated substrate corresponds to the modulated surface whereas the ball is considered to be the rigid counter body. This is a legitimate approach because the radius of the ball is much larger than the contact radius. Moreover, the Mohs' hardness of the used alumina ball (3.4) is higher than that of gold (2-2.5)[147]. Therefore, the ball can be regarded as a rigid plane.

Apart from that, it is necessary to know the respective asperity height distribution and the radius. The height distribution can be easily derived from the topographic measurements being equivalent to the rms value. The determination of the asperity radii is more difficult because the WLI does not directly display those values. For that purpose, the measured WLI profiles of the laser patterns are fitted by a sinusoidal function of the type:

$$f(x) = U \cdot \sin\left(\frac{2\pi x}{\lambda}\right) \quad (8.10)$$

where U denotes the amplitude of the selected function (consequently $U/2$ is the structural depth of the laser profiles which will be denoted by d .) and λ the periodicity. Figure 7.35 displays a comparison between a measured profile and the sinusoidal fit function for smaller ($3\ \mu\text{m}$) and larger periodicities ($8\ \mu\text{m}$).

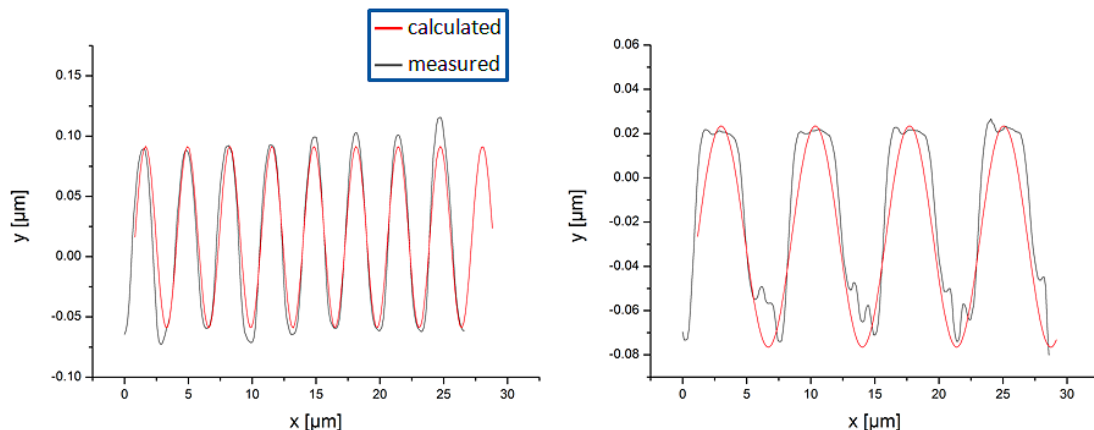


Figure 8.35.: Comparison of measured WLI profiles and the corresponding fit functions for smaller (sample L3) and larger line spacings (Sample L8).

There is a good correlation between the measured and calculated profile for sample L3. In contrast, some errors in fitting may appear for larger line-spacings (sample L8), because the summits of the asperities are more plateau-like thus deviating significantly from the sinusoidal fit function. According to that, the asperity radius will be underestimated to some extent for specimens with larger skewness. The curvature radius $\beta(x_0)$ can be determined by:

$$\beta(x_0) = \left| \frac{(1 + \dot{f}(x_0)^2)^{3/2}}{\ddot{f}(x_0)} \right| \quad (8.11)$$

In order to apply Greenwood's model, there are still two parameters left which are necessary: the separation distance h_0 between the mean plane of the surface and the contacting rigid plane as well as the number of asperities N_0 in the beginning. The distance h_0 in this case is simply the zero line around which the sinusoidal function oscillates, being the amplitude U . As far as the initial number of asperities is concerned, this should be inversely proportional to the used periodicity ($N_0 \propto 1/\lambda$). For a more realistic contact, the initial value shall be multiplied by a factor of 100.

Based on the assumption of N_0 asperities in the beginning, the following analytical expressions for the total number of asperities, the contact area and finally force can be

obtained from equations 4.20, 4.21 and 4.22:

$$N = \frac{N_0 \Phi^*}{\eta} \quad (8.12)$$

$$A = \frac{\pi R N_0 \Phi^*}{\eta^2} \quad (8.13)$$

$$F = \frac{4 E^* N_0 \Phi^* \sqrt{2\pi R}}{3 \eta^{5/2}} \quad (8.14)$$

with the modified distribution function (refer to equation 4.18):

$$\Phi^* = \left(\frac{1}{2\pi (rms)^2} \right)^{1/2} \cdot e^{\left(\frac{d^2}{2(rms)^2} \right)} \quad (8.15)$$

and the parameter η :

$$\eta = \frac{d}{rms} \quad (8.16)$$

The contact pressure is accordingly:

$$p = \frac{4 \sqrt{2} E^*}{3 \sqrt{\pi R \eta}} \quad (8.17)$$

On the basis of these equations, it is possible to plot N, A and p depending on the used laser periodicity and structural depth under purely elastic conditions. It is important to note that the results can only represent a qualitative dependence because some assumptions e.g. the initial number of asperities N_0 were necessary to apply Greenwood's approach. After all, some errors appear by determining the curvature radius for larger line-spacings.

Figure 7.36 demonstrates the total number of asperities as a function of λ and the structural depth d:

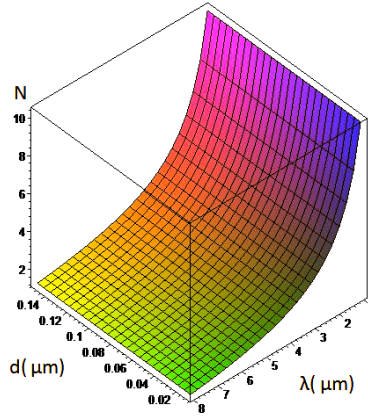


Figure 8.36.: Total number of asperities in contact depending on the periodicity and structural depth.

At first, the number of asperities are of course independent on the structural depth. Yet, as could be expected, there is a clear correlation with the periodicity. The smaller the periodicity, the more asperities are in contact. The total contact area is displayed in figure 7.37. Although the number of asperities increase for smaller periodicities,

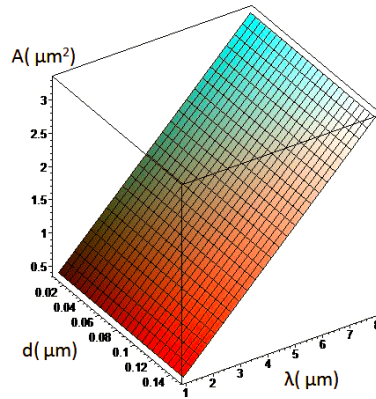


Figure 8.37.: Total contact area in μm^2 as a function of structural depth and periodicity.

the total contact area shows an opposite tendency. This can be traced back to the more negative skewness (more plateau-like summits) for larger periodicities. Finally, the contact pressure p is plotted in figure 7.38.

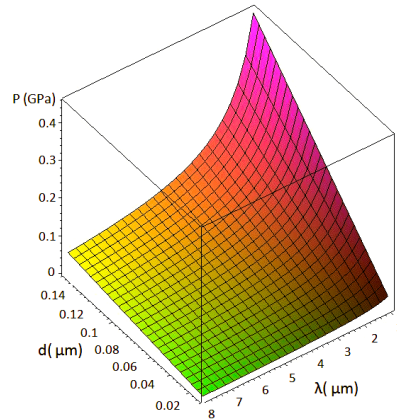


Figure 8.38.: Contact pressure in GPa vs. structural depth and line-spacing.

So far, only elastic conditions have been taken into account. An indicator for the propensity for elastic or plastic deformation within the Greenwood-Williamson theory is given by the plasticity index Ψ (see equation 4.28). The height distribution and the asperity radii are known from above considerations and the hardness for the pristine and laser influenced microstructure was measured by nanoindentation. Therefore, a calculation of Ψ for the different samples is feasible. Graph 7.39 reveals the results of Ψ as a function of R_{sk} .

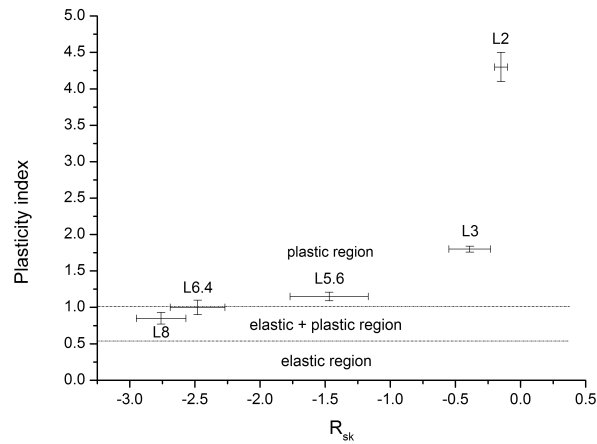


Figure 8.39.: Plasticity index Ψ vs. skewness R_{sk} for different line-patterns.

8. Results and discussion

Interestingly, samples L2 and L3 have relatively high plasticity indices which indicates a large propensity for plastic deformation. This is in good agreement with the measured wear volumes. Additionally, more negative R_{sk} values lead to smaller plasticity indices. Sample L8, having the most negative skewness, is located in the elastic/plastic transition zone.

Summarising, it can be stated that the modelling results based upon a simple Greenwood-Williamson approach are highly consistent with the experimental findings. Indeed, skewness seems to be a suitable parameter to describe the respective laser induced topographies and allows for simple predictions regarding their tribological efficiency.

8.2. Phase composites in TiAl multilayered films

8.2.1. Introduction

Materials can be generally classified with regard to their chemical composition. However, the real material properties are strongly influenced by their microstructure. Hence, it is very important to control the formation of this microstructure including texture, grain sizes, defects and existing phases during material processing. For that purpose, a subsequent heat treatment is often necessary to get the desired properties. Additionally, in many cases it is desirable to have different localised properties as it is well known from composite materials. Hierarchical structures like bones achieve an exceeding performance by the combination of hard and soft structures. In such materials, the arrangement of the components, characterised for example by the structure width, also determines the properties of the composite material which can be calculated with respect to the geometry [148]. In terms of mechanical properties, there are several possibilities to tailor them in a defined way. For instance, grain size architectures can achieve such characteristics thanks to the Hall-Petch effect [30]. An alternative is the combination of high strength materials within a ductile matrix as it is put into effect in bones by calcium phosphate particles within a collagen matrix. In technical systems, hard intermetallic regions in a ductile metal matrix resemble most closely this kind of hard-soft arrangement.

However, there are only a few methods to produce periodic structures in the micrometer range. Selective techniques such as laser writing have the disadvantage of being very time consuming if large areas must be treated. Lithography can handle large areas but many process steps are needed.

TiAl multilayers have been selected for the study of phase composite thin films. Titanium aluminides are very attractive because of their high melting point, low density and good corrosion resistance and the TiAl phase diagram is well described in literature [149][150][151][152]. The local formation of intermetallic phases in the aforementioned metallic multilayer system is induced by laser interference. In order to achieve the maximum composite effect, the reaction in the maximum intensity zones must extend throughout the whole film thickness.

8.2.2. Topographic and microstructural analysis of TiAl multilayer

In a first step, the as-deposited multilayers were studied with regard to their topography and microstructure. Figure 7.40 shows a cross-section after deposition.

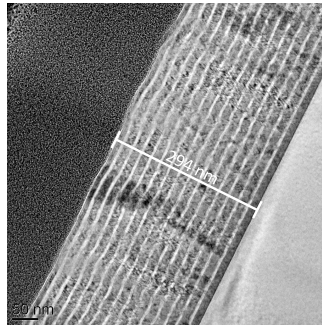


Figure 8.40.: FIB cross-section of an as-deposited 300 nm thick TiAl multilayer. The bright layers correspond to Al and the darker ones to Ti.

The slight difference with the nominal thickness may be explained by uncertainties in the respective sputter rates (Ti: 0.177 nm/s, Al: 0.233 nm/s). An analysis of the topography after magnetron sputtering by WLI reveals a smooth surface with a root mean square roughness of about 1 nm (see figure 7.41).

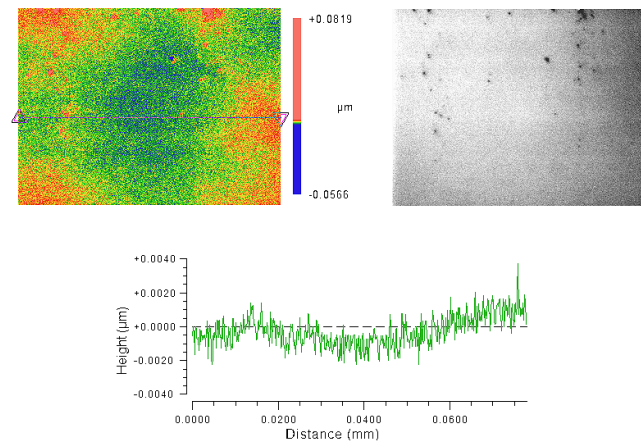


Figure 8.41.: Surface profile (left), intensity map (right) and surface profile cross-section plot (bottom) of the as-deposited TiAl multilayer measured by WLI. The rms value is about 1 nm.

Additionally, grazing incidence X-ray diffraction (*GI-XRD*) was utilised to analyse the phase situation after the magnetron sputtering process. Figure 7.42 shows a diffraction graph of the pristine TiAl multilayer.

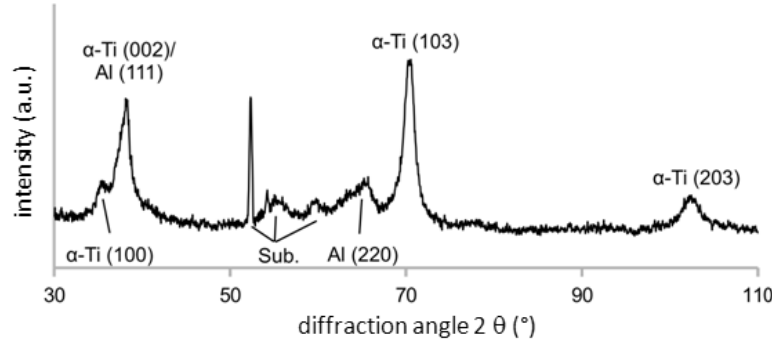


Figure 8.42.: Diffraction pattern of a pristine TiAl multilayer measured by GI-XRD. The peaks of the Si substrate are denoted by Sub. in the diffraction graph.

All the diffraction peaks can be clearly identified and belong to the elemental peaks of Al, α -Ti and the Si substrate. Because of the grazing incidence measurement at an angle $\omega = 1^\circ$, the substrate peaks are slightly shifted. The substrate peak at $2\theta = 56^\circ$ is related to the Si-(311) planes. According to the absorption coefficients of Al and Ti at $\lambda = 0.154$ nm for $\text{CuK}\alpha$ radiation ($\alpha_{\text{Al}} = 135.864 \cdot 10^2$ 1/m, $\alpha_{\text{Ti}} = 912.824 \cdot 10^2$ 1/m [153]), the corresponding information depth can be calculated to be $37 \mu\text{m}$ for Al and $5.45 \mu\text{m}$ for Ti under Bragg-Brentano conditions. Due to the 300 nm total film thickness, a reduction of the information depth is necessary in order to weaken the substrate influence during the measurement. Using GI-XRD, the information depth is determined by the following expression:

$$\tau_{GI} = \frac{\sin(\omega_i) \cdot \sin(2\theta - \omega_i)}{\alpha(\sin(\omega_i) + \sin(2\theta - \omega_i))} \quad (8.18)$$

where α is the absorption coefficient, ω_i the incident angle being 1° and θ the diffraction angle [154]. Based upon this relationship, the respective information depths range from 169-708 nm for Al and 28-116 nm for Ti depending on θ .

Subsequently, TEM foils were prepared by FIB and analysed by transmission electron microscopy.

The selected area diffraction pattern of the as-deposited state is shown in figure 7.43. The pronounced diffraction spots in the SAD pattern are blurred because of nearly over-

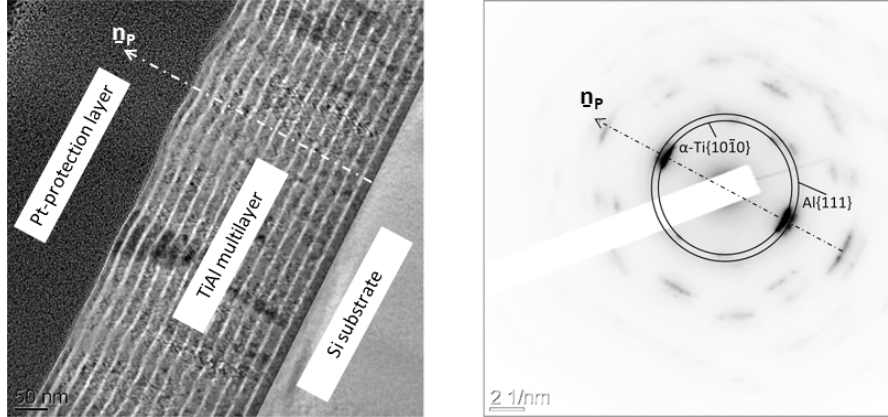


Figure 8.43.: TEM image of as-deposited multilayer (left) and SAD pattern (right). The normal vector of the sample surface is represented by \vec{n}_P .

lapping reflections arising from Al- $\{111\}$ and Ti- $\{0001\}$ planes and due to the waviness of the near-surface layers. Despite that, a fibre-texture with the Ti- $\{0001\}$ and Al- $\{111\}$ planes being parallel to the sample surface can be identified.

During the patterning process of the pristine samples, three general fluence regimes could be determined for TiAl:

- Regime A - low fluence ($< 70 \text{ mJ/cm}^2$): Vanishing topography with very small impact on microstructure.
- Regime B - medium fluence ($70\text{-}220 \text{ mJ/cm}^2$): Resulting topography is very shallow with typical structure depths in the order of 10 nm. Melting and mixing of layers occur.
- Regime C - high fluence ($220\text{-}476 \text{ mJ/cm}^2$): Structure depth significantly increases up to a maximum value of 180 nm with arising secondary maxima; multilayer is partially ablated from the substrate. Laser-induced reaction zone may extend over the entire film thickness.

Figure 7.44 summarises the abovementioned regimes in form of SEM images. As can be seen in the right figure, there are already bubbles inside the multilayer with ablated areas due to the high energy density of about 476 mJ/cm^2 . Concerning the laser pattern

8. Results and discussion

homogeneity, only a line-spacing of $4\ \mu\text{m}$ was feasible in regime C finally being a good compromise. According to the previous simulation results, this periodicity is not located at the limit of lateral diffusivity and is not in the region of maximum temperature which begins at $8\ \mu\text{m}$. Based upon the previous experimental fluence series, two different fluences (170 and $476\ \text{mJ}/\text{cm}^2$) and four different periodicities (2 , 4 , 8 and $12\ \mu\text{m}$) in case of laser line-patterns were finally chosen.

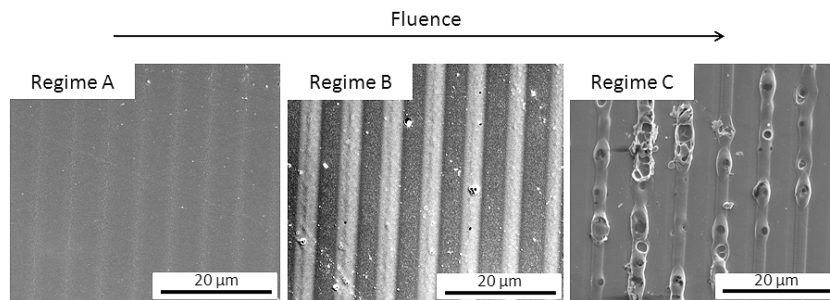


Figure 8.44.: SEM images of different fluence regimes (regime A, B and C) in TiAl at a fixed line-spacing of around $8\ \mu\text{m}$.

In this context, figure 7.45 displays a typical line pattern on a TiAl multilayer specimen with a line spacing of $4\ \mu\text{m}$ at a fluence of $476\ \text{mJ}/\text{cm}^2$ (regime C).

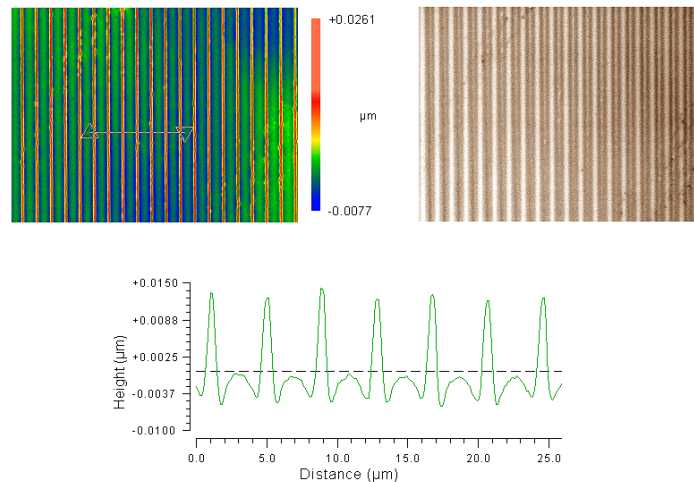


Figure 8.45.: WLI surface map of laser line-pattern on a TiAl multilayer with a line-spacing of $4\ \mu\text{m}$ at a fluence of $476\ \text{mJ}/\text{cm}^2$ (left), intensity plot (right) and corresponding cross-section profile plot (bottom).

8. Results and discussion

The resulting interference pattern is quite homogeneous regarding the line-spacing. Between the primary maxima, some secondary maxima gradually evolve. The structure depth is approximately 10 nm which is very small compared to the line-spacing of 4 μm . Due to the shallow topography, the emphasis is laid more on the microstructure. An important issue within this study is the phase evolution in the TiAl multilayers after laser treatment. In this sense, XRD was carried out for two considerably different fluence regimes namely regime B (170 mJ/cm^2) and regime C (476 mJ/cm^2) (see figure 7.46).

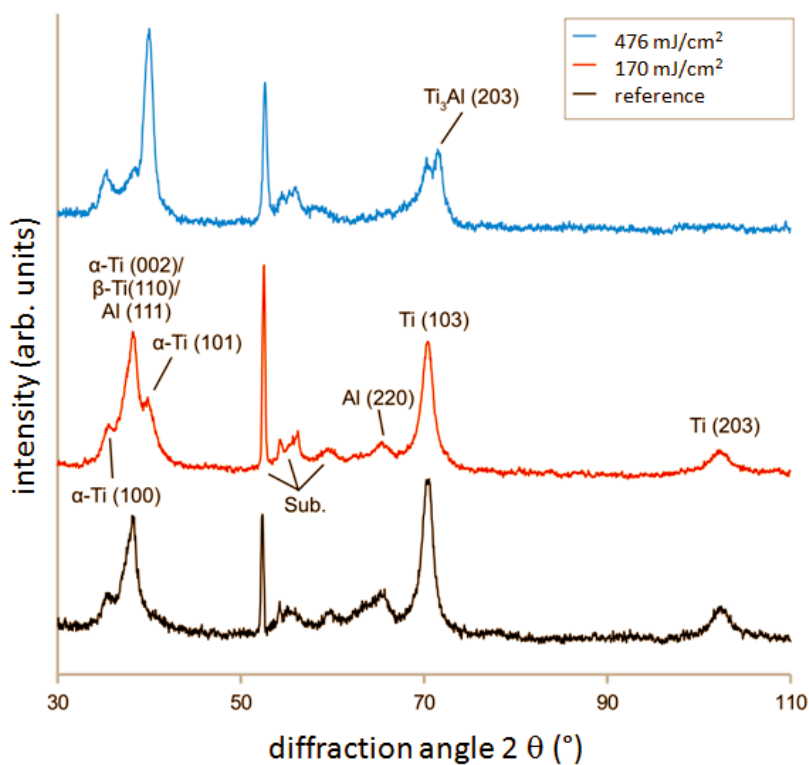


Figure 8.46.: GI-XRD measurement of laser patterned specimens at 170 mJ/cm^2 and 476 mJ/cm^2 compared with the reference.

The direct comparison between regime B and the reference specimen does not reveal considerable differences. At a much higher fluence (regime C), an α -Ti (101) peak is clearly visible. Additionally, a Ti_3Al (203) peak appears. At 38.4°, a reduction of the overlapping peak can be observed.

The unambiguous identification of the phases in this overlapping peak is hindered due to several reflections such as α -Ti (002), Al (111) and β -Ti (110).

Finally, the indexing is further complicated by:

- Peak shifts due to the formation of a solid solution.
- Peak shifts from residual stresses.
- Presence of texture
- Peak broadening due to small grain sizes and a potentially high defect density.

In addition to XRD-measurements, TEM foils were prepared by FIB in order to study the microstructural situation after laser patterning in more detail. For that purpose, samples with a line-spacing of $8\ \mu\text{m}$ irradiated with a fluence of $170\ \text{mJ}/\text{cm}^2$ were used. Figure 7.47 presents such a sample with the related SAD zone axis pattern.

8. Results and discussion

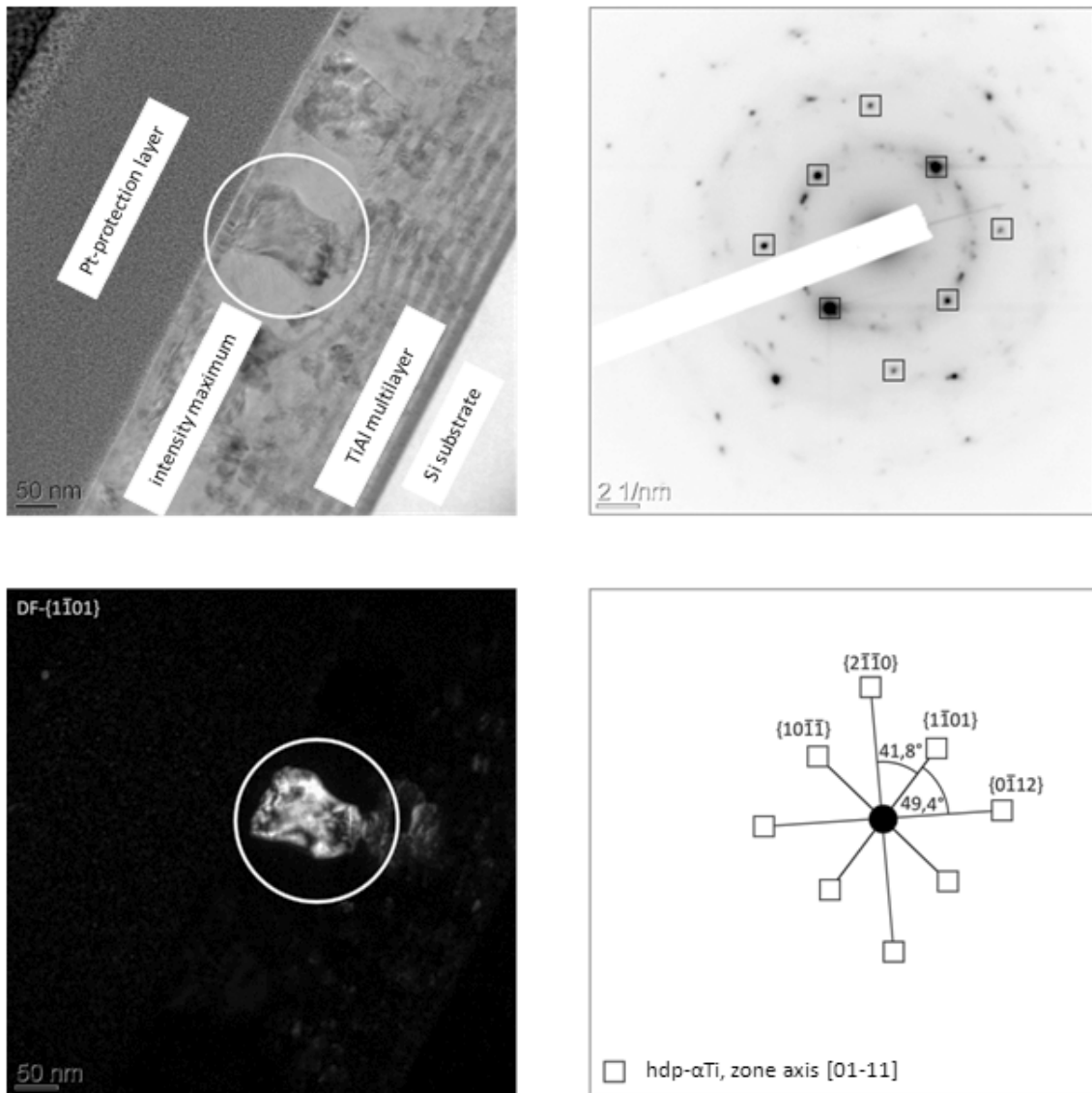


Figure 8.47.: TEM analysis of a laser irradiated multilayer (fluence: 170 mJ/cm^2). The position of maximum laser intensity is displayed (top left). The bottom left image shows a dark field image of the encircled grain. Top right: SAD pattern of zone axis and bottom right represents a schematic drawing of the pattern. The indexing reveals the existence of hdp α -Ti with a $[01-11]$ zone axis.

8. Results and discussion

After laser patterning, the lamellar structure of the multilayer in the top area disappeared, however the reaction does not penetrate the entire film thickness. Some layers are still visible near the substrate. The SAD pattern in the reaction zone indicates the presence of hcp α -Ti. This finding is based on the diffraction of the encircled grain in the top left image of figure 7.47.

In contrast, TEM analysis of an adjacent grain indicates the existence of bcc β -Ti (see figure 7.48).

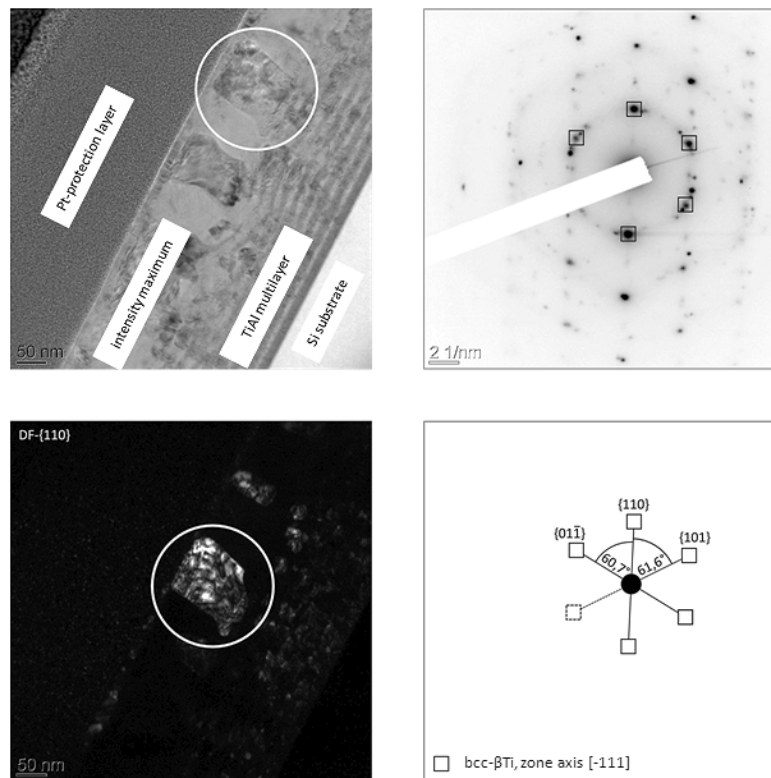


Figure 8.48.: TEM image of a laser-irradiated multilayer (fluence: 170 mJ/cm^2). The position of maximum laser intensity is displayed (top left). The bottom left image shows a dark field image of the encircled grain. Top right: SAD pattern of zone axis and bottom right represents a schematic drawing of the pattern. The indexing reveals the existence of bcc β -Ti with a $[-111]$ zone axis.

Summarising, it can be stated for the given fluence, that there is at first no complete reaction of the multilayer specimen over the entire film thickness and XRD and

TEM-measurements could not prove the formation of intermetallic phases after laser treatment. However, apart from the α -Ti phase, the metastable β -Ti phase could be detected. This may be attributed to the high cooling rates typically being in the range of 10^{10} K/s [29]. It seems reasonable that the β/α -transition is suppressed and the formation of Ti_3Al is kinetically hindered. Furthermore, a very thin layer on top of the sample surface can be seen. The morphology of this layer differs from the reaction zone and the thickness is similar to the original Ti capping layer. Energy dispersive X-ray measurements (EDS) showed the presence of nitrogen in the upper layer which may have its origin in the laser patterning under ambient conditions. Due to nitrogen, the melting temperature of Ti could be increased and therefore, the upper layer would remain solid during the laser process. A more detailed analysis would be necessary to clarify this finding. Nevertheless, this is far beyond the scope of the present thesis.

In order to further demonstrate the effect of laser fluence, some specimens were patterned at 476 mJ/cm^2 having a periodicity of about $4 \mu\text{m}$. The resulting FIB cross-section is shown figure 7.49.

SEM images of the cross-section perpendicular to the line structure reveal a completely

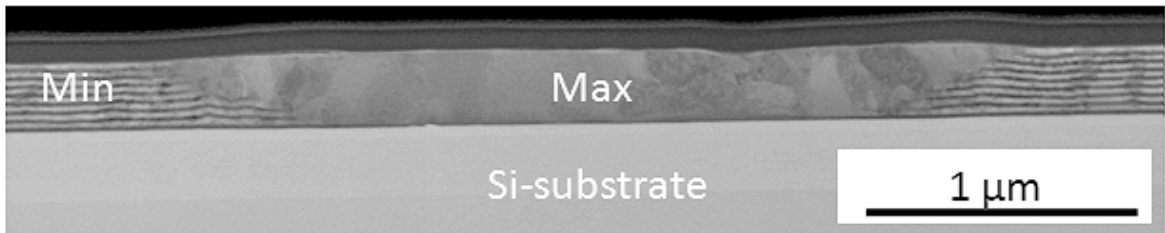


Figure 8.49.: STEM micrograph of a cross-section through the TiAl multilayer after laser patterning at 476 mJ/cm^2 [155].

dissolved layer system at the maximum resulting in a completely modified microstructure. Despite the relatively high fluence, adhesion between the metallic layer and the substrate is still persistent in this section. Finally, the laser-irradiated thin film consists of clearly defined reaction zones which are embedded in the pristine multilayered TiAl matrix. Interestingly, the reaction zone is localised in the intensity maximum and does not extend through the complete film. It is known from literature that multilayer systems can strongly react exothermically leading to a self-propagating reaction front with velocities of up to 17 m/s [156][157]. This self-propagating reaction can be found in several multilayered systems such as TiAl, RuAl and PtAl.

The decisive stored energy density for TiAl is approximately 788 kJ/cm^3 (RuAl: 1000 kJ/cm^3 and PtAl: 1451 kJ/cm^3)[158].

In contrast to the results shown here, most of the research focuses on relatively thick multilayered films in the range of up to $50 \mu\text{m}$ [157] for the total thickness. However, the individual layer thicknesses are comparable to the ones used in the thesis. Furthermore, there are only few reports about the ignition of multilayers with a substrate below. In the most cases, free-standing films are considered. Substrate materials may act as a heat sink thus negatively affecting the self-propagation. In order to start the reaction, a certain reaction volume and a threshold heat input are necessary. In addition, the ignition fluences for the self-propagation with regard to laser-induced processes are above 1 J/cm^2 being higher than the applied fluence in this case [159]. Therefore, it can be concluded that due to the small total film thickness of only 300 nm , the use of a Si substrate (acting as a heat sink) and the selected laser fluence of about 476 mJ/cm^2 are finally not enough to ignite self-propagation reactions.

TEM results prove the presence of intermetallic phases in the regions of maximum intensity, whereas only elemental reflections can be found in the minima (see figure 7.50).

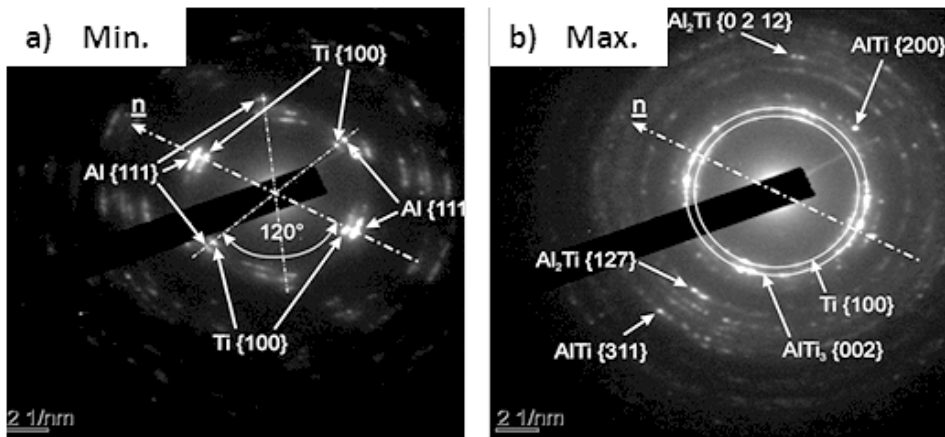


Figure 8.50.: SAD pattern in the locations of minimum (a) and maximum laser intensity (b) at a fluence of 476 mJ/cm^2 . The vector n denotes the surface normal vector.

Obviously, not only one intermetallic phase such as Ti_3Al can be found at the maxima but also TiAl and Al_2Ti . In order to investigate the chemical stoichiometries present in the volume and at the boundaries of the Ti/Al-film, 3-D atom probe tomography

8. Results and discussion

was employed. This technique, yielding highly resolved local information on chemical compositions at the atomic scale, allows for separate analyses of the different laser-treated regions (*courtesy of AMETEK Inc.*).

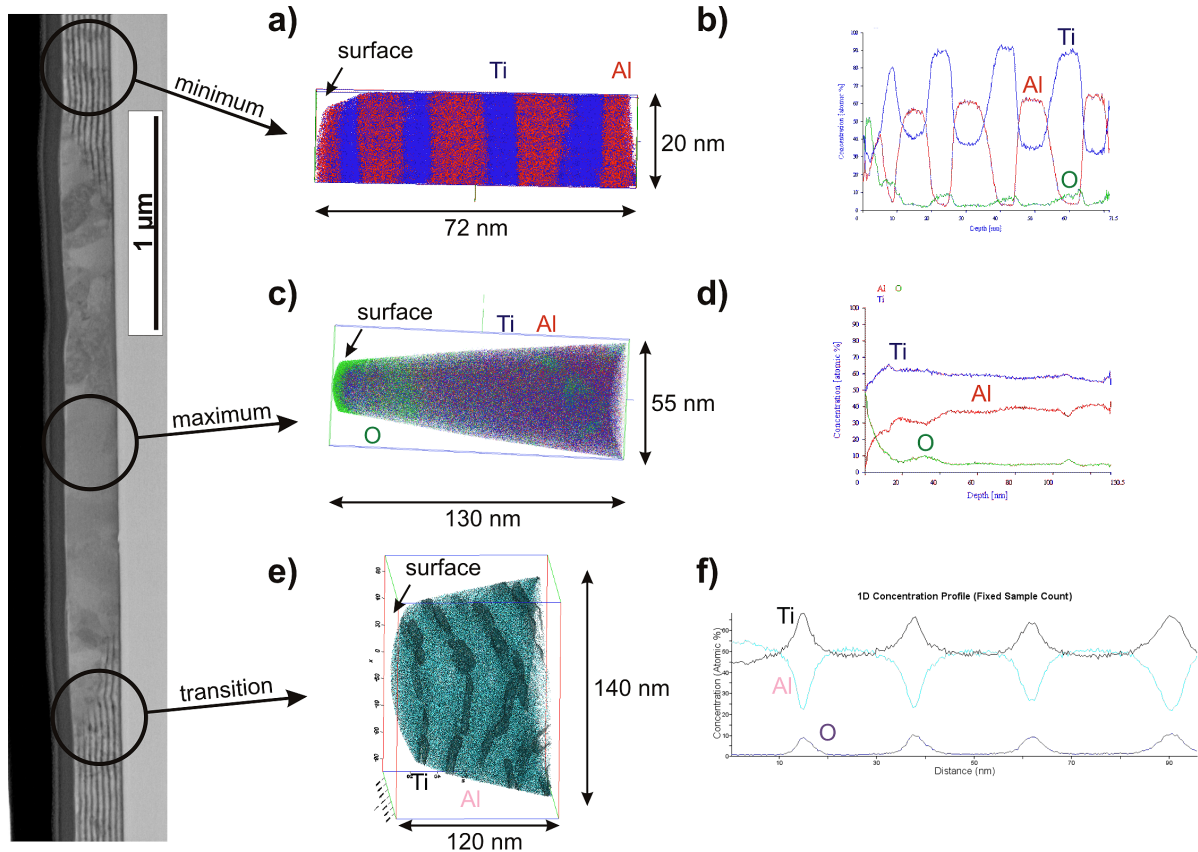


Figure 8.51.: Results of the local chemical analysis in minimum (upper row), maximum (center row) and transition (lower row) zone positions obtained by APT [155].

As the left hand side of figure 7.51 shows, the laser maximum and its vicinity may be subdivided into three regions: the maximum itself, the neighbouring minimum and a transition zone located in between them. Using a FIB-specimen preparation approach closely resembling the procedures of a TEM foil extraction, specimens were taken at the three described locations. By consecutive annular milling steps, tips were shaped until their tip radius reached suitable sizes on the order of 50 nm. Employing a low-kV post-treatment, possibly existing Ga^+ contamination stemming from the ion beam used for extraction and shaping was effectively removed. It was of interest, whether the chemical

information measured by atom probe would support the findings of structural characterisation by TEM. The tomographic data recorded from all sites yielded information up to a depth less than half of the total thickness of the Ti/Al-thin film.

Looking at the results of the minimum region (figures 7.51 a, b), the multilayered microstructure is still visible as in the TEM micrograph of the pristine sample. Analysing the widths of each sublayer at this location, it becomes clear, that the intended thicknesses of 17 nm were not exactly met in both cases, Ti showing approximately 10 nm and Al 15 nm. Moreover, the interfaces between the layers are not smooth from a morphological point of view. From the chemical standpoint, the individual layers are not made of one constituent only: in Ti sublayers an Al content of 4 at.% could be detected, whereas the Ti content in Al sublayers reaches almost 40 at.%. According to the equilibrium phase diagram of this binary system, Al should exist in larger amounts in a solid Ti solution, whereas the solubility of Ti in Al solid solution is almost negligible. However, one should keep in mind, that in the case of thin films, the equilibrium phase diagrams of the bulk situation cannot be completely transferred to a thin film regime [160].

Based on the work of Edelstein et al., the phase formation seems to be controlled more by kinetic aspects of the species with higher diffusivity than by thermodynamic driving forces [161]. Because of Ti being the species in our case, its higher content within Al sublayers can be explained [162]. Additionally, this might explain the different thicknesses of the individual layers: the higher diffusivity of Ti leads to a thinning of the Ti sublayers and correspondingly to a widening of the Al layers already during the sputtering process [163]. Figure 7.51 (b) also depicts the oxygen distribution encountered in the specimen tip. Not surprisingly, the layer close to the former thin film surface (leftmost part of the tomographic representation) contains a substantial amount of oxygen (up to 50 at.%), which decreases in depth. When reaching an Al sublayer, the content reduces to less than 3 at.%, but rises within Ti layers to 8–10 at.%. This is probably due to Ti atoms gettering residual oxygen present in the magnetron PVD chamber during their flight to the substrate.

Another potential contamination source could be the impurities of the Ti target and the sputter gas, in this case Ar [161]. Figures 7.51 (c) and (d) show the results obtained within the interference maximum. Both Ti and Al are homogeneously distributed along the depth axis with 60.5 at.% Ti and 36.9 at.% Al on average corresponding to a Ti:Al ratio between 2:1 and 3:2. As in the case of the minimum, the oxygen content increases to almost 50 at.% close to the surface and drops to approx. 2.5 at.% O deeper down. Look-

ing at depth coordinates 30 nm and 110 nm in 7.51 (d), small increases in the O content up to 10 at.% can be observed, which are also visible in the tomographic representation in 7.51 (c). These might point to a clustering of O even in larger depths which shows the extent of intermixing the chemical species are subjected to during laser processing, when considered together with the Al and Ti distributions. Comparing figure 7.51 (c) with the STEM micrograph in figure 7.49, one is able to deduce, that this atom probe specimen tip has been extracted at the location of a large grain spanning the whole film thickness. The transition zone between the maximum and minimum positions depicted in figures 7.51 (e) and (f) looks different from a morphological and chemical point of view when compared to the two surrounding regions. In the concentration depth profile in 7.51 (f) a layered substructure can be observed, which exhibits two different elemental distributions of Ti:Al equal to 1:1 and 3:1 respectively. The 3D-distribution can be made visible by employing an iso-concentration surface to be plotted during post-processing of the 3D-dataset (dark grey agglomerations in 7.44 e). The boundary of these agglomerations is chosen accordingly to lie at 67 at.% Ti, corresponding to the volume containing the 3:1 ratio to be located inside the surfaces. According to the concentration depth profile, the O content in the very same volume rises to 15 at.% from almost zero outside of it. With regard to the morphology, this type of layer appears to be intersected by the matrix formed of Ti:Al equal to 1:1.

Correspondingly, an interesting question deals with their effect on mechanical properties such as hardness. In this context, nanoindentation experiments were performed in collaboration with the *Department of Materials Science and Methods, Prof. Dr. H. Vehoff*. For the evaluation of the mechanical properties a Tribo Indenter Nanomechanical Testing System (*Hysitron Inc.*) was used to perform the tests. The selected peak loads for the indentation experiments were around 50 μN to limit the indentation depth up to 10% of the total film thickness [142]. For the TiAl multilayer samples, the change in hardness and Youngs modulus is pronounced due to the formation of the different intermetallic phases Al_2Ti and Ti_3Al for example. Figure 7.52 represents a SEM micrograph of the laser-irradiated (fluence: 476 mJ/cm^2) TiAl film.

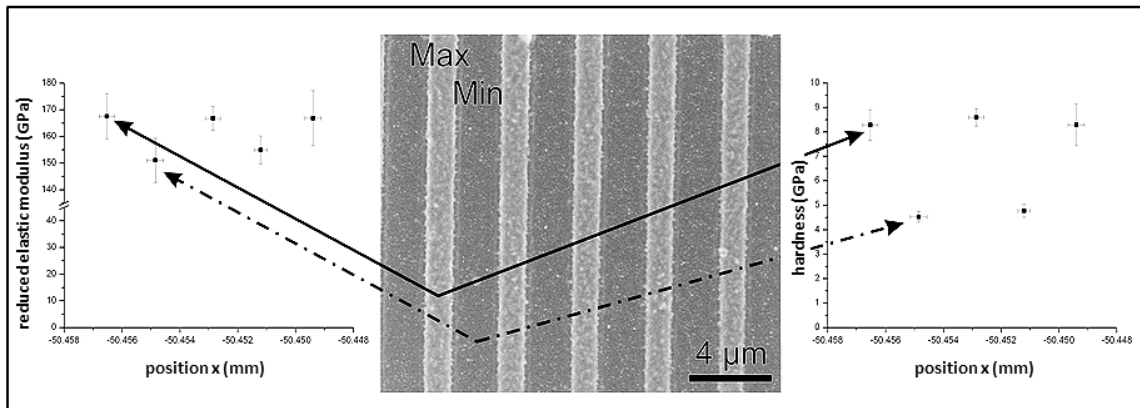


Figure 8.52.: Laser irradiated (476 mJ/cm^2) TiAl sample with a fixed periodicity of $4 \mu\text{m}$. Diagram on the left side shows the reduced elastic modulus for the intensity maxima and minima positions and the right diagram the measured hardness in GPa [164].

The periodicity is around $4 \mu\text{m}$. The diagram on the left shows the reduced Young's modulus for the maxima and minima regions and the right diagram the hardness in GPa. Evidently, the increase in hardness in the intensity maxima positions is up to 47% compared to the contiguous minima positions.

8.2.3. Thermal simulation

For a better understanding of the observed microstructural phenomena after laser patterning, thermal simulations based upon the classical heat diffusion equation were performed. A detailed description of the used software and relevant parameters can be found in the theoretical part of the thesis. It should be mentioned that symmetrical boundary conditions are to be considered thus reducing computing time. At first, it is necessary to determine the maximum depth up to which heat can be absorbed. The so-called skin depth (or optical penetration depth) may be derived from Lambert-Beer's law, and is expressed by the reciprocal absorption coefficient α for Al and Ti [45]. Using the absorption coefficients at 355 nm laser wavelength ($\alpha_{Al} = 1531/\mu\text{m}$ and $\alpha_{Ti} = 71.31/\mu\text{m}$ [112]), the skin depth for Al is approximately 6.6 nm and 14.0 nm for Ti. Most of the laser induced heat is absorbed in the topmost layers.

According to equation 7.1, the thermal diffusion lengths are $l_{D,Al} \approx 2\mu\text{m}$ and $l_{D,Ti} \approx 0.61\mu\text{m}$. The subsequent simulation will be restricted to the first $5\mu\text{m}$. A schematic representation of the used model is illustrated in figure 7.53.

Prior to simulations, the spatial and temporal absorption of the laser radiation is deter-

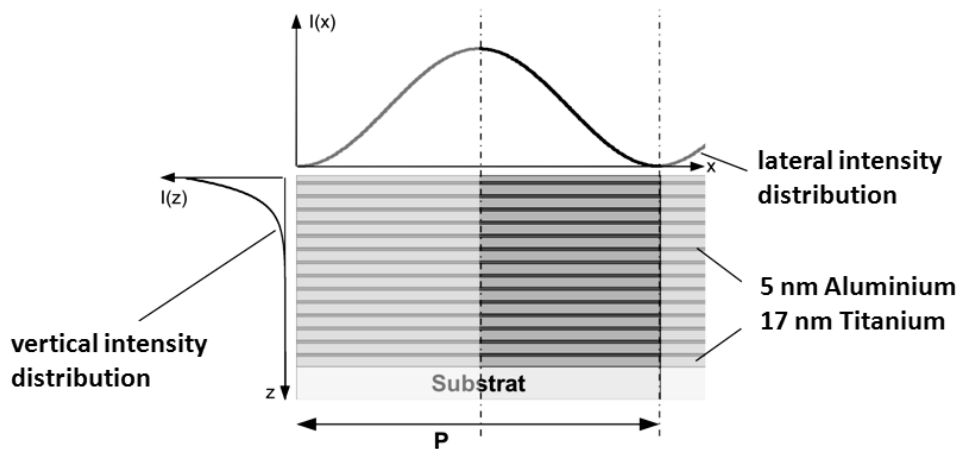


Figure 8.53.: Schematic overview of the model used for thermal simulation. Due to symmetry conditions, only half of the model is considered.

mined analytically. The observed time range is 100 ns. With the exception of the fluence influence on the maximum temperatures ($170\text{ mJ}/\text{cm}^2$ vs. $476\text{ mJ}/\text{cm}^2$), all further results refer to a medium fluence of $170\text{ mJ}/\text{cm}^2$ which was also used for the preliminary results. Figure 7.54 shows the spatial and temporal temperature distribution at a fixed

8. Results and discussion

pattern periodicity of $8\ \mu\text{m}$ and after $t = 33.5\ \text{ns}$ which indicates the moment of maximum laser intensity.

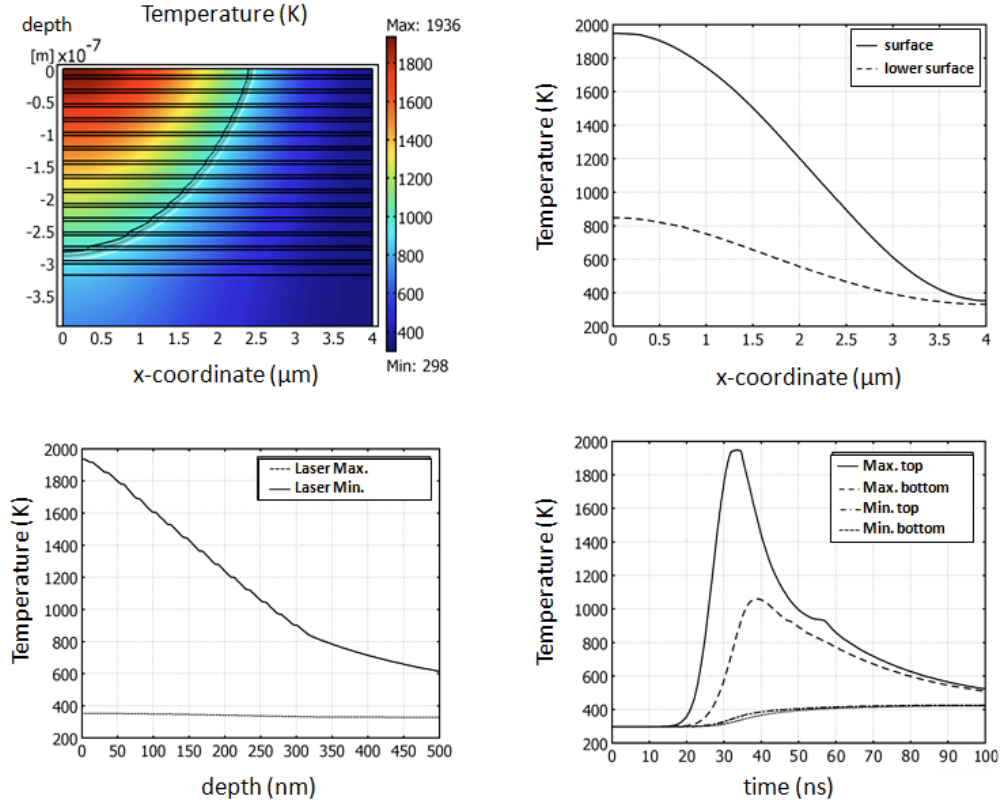


Figure 8.54.: Simulated temperature distribution at a pattern periodicity of $8\ \mu\text{m}$ and a fluence of $170\ \text{mJ}/\text{cm}^2$. Top left: spatial temperature distribution at $t = 33.5\ \text{ns}$. Top right: spatial temperature distribution for cross-sections parallel to the surface. Bottom left: spatial temperature distributions for cross sections being perpendicular to the surface and bottom right: temporal distribution of temperature.

The maximum temperature of $1936\ \text{K}$ is achieved after $33.5\ \text{ns}$ at a fixed laser periodicity of $8\ \mu\text{m}$ in the topmost layer of the maximum (see figure 7.54 bottom right). For the bottom layer, the maximum temperature is reached after $38\ \text{ns}$. Compared with the intensity minimum, it can be pointed out that the temperature only gradually increases thus achieving the maximum after $60\ \text{ns}$. At that time, the temperature difference between the location of maximum and minimum laser intensity is only $200\ \text{K}$. As can be seen in the temperature curve after laser impact, only the lower melting-point component, here Al with a melting point of $934\ \text{K}$ is molten whereas Ti, having a melting point

of 1941 K, remains solid [112]. Furthermore, it can be observed that the temperature in the intensity minimum never exceeds 400 K. Therefore, no significant microstructural influence is expected in those areas for Al and Ti. Figure 7.54 bottom right reveals the latent heat being released. There is a pronounced deviation from the continuous cooling taking place between 900 and 1000 K indicating the solidification point of Al. Some characteristic aspects of the thermal simulation such as maximum achievable temperatures, molten fractions, cooling rates or even melting durations shall be presented in dependence of the pattern line spacing. At first, the maximum achievable temperatures are displayed for the used periodicities.

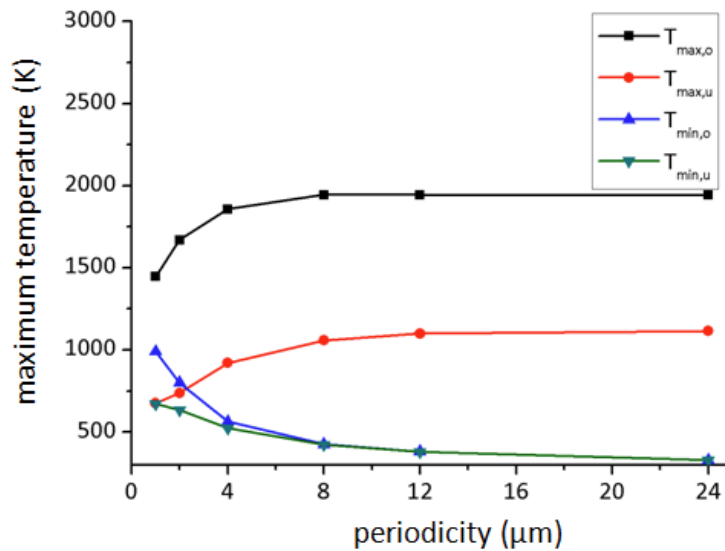


Figure 8.55.: Simulation of the maximum achievable temperatures depending on the pattern line-spacing at a fixed fluence of 170 mJ/cm^2 . $T_{max,o}$, $T_{max,u}$ denote the maximum temperature at the intensity maximum at the surface and at the multilayer-substrate interface and $T_{min,o}$, $T_{min,u}$ at the intensity minimum.

Referring to figure 7.55, the maximum temperature is achieved at $\approx 8 \mu\text{m}$. The periodicities 1 and $24 \mu\text{m}$ have been added in order to see more pronounced potential

thermal effects. The increase is attributed to the fact that for smaller periodicities the heat is directly carried away due to a greater specific area whereas for larger line-spacing the material remains molten for a longer time which can be indentified in figure 7.56.

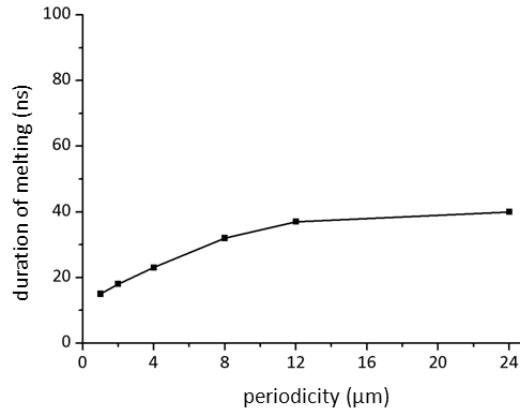


Figure 8.56.: Simulated melt duration as a function of laser periodicities.

The molten fractions are directly correlated with the maximum temperatures and melting durations. Figure 7.57 depicts the molten fractions for aluminium depending on the periodicity at a given fluence of $170 \text{ mJ}/\text{cm}^2$. Titanium is not displayed here because it remains solid during the laser treatment.

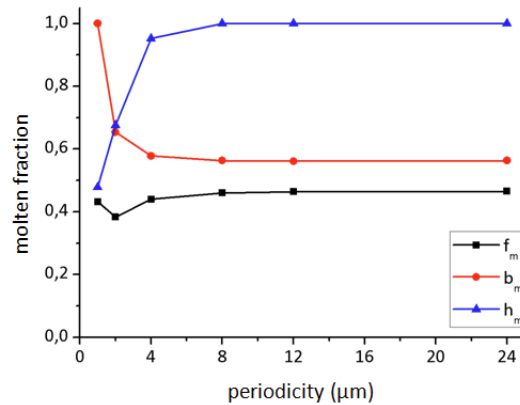


Figure 8.57.: Simulated molten fractions of Al at a fluence of $170 \text{ mJ}/\text{cm}^2$. Here, f_m is the amount of molten Al, b_m the width of the molten region related to the periodicity and h_m the molten depth normalised to the total film thickness.

8. Results and discussion

At a periodicity of around $8\ \mu\text{m}$, the studied parameters f_m , b_m and h_m no longer depend on the line-spacing because the lateral distances for heat diffusion are much larger than in the vertical direction. The width of the molten area increases by decreasing the periodicity, yet the molten depth is reduced. This is due to an enabled lateral heat diffusion. Interestingly, the volume fractions of molten Al merely depend on the used line-spacing. Finally, the cooling rate plays a decisive role in the resulting microstructure (see figure 7.58). In most cases, a high cooling rate leads to a more fine grained microstructure and may complicate diffusion-controlled phase transitions. The time needed for cooling from 1800 to 1000 K was measured to determine the maximum cooling rate.

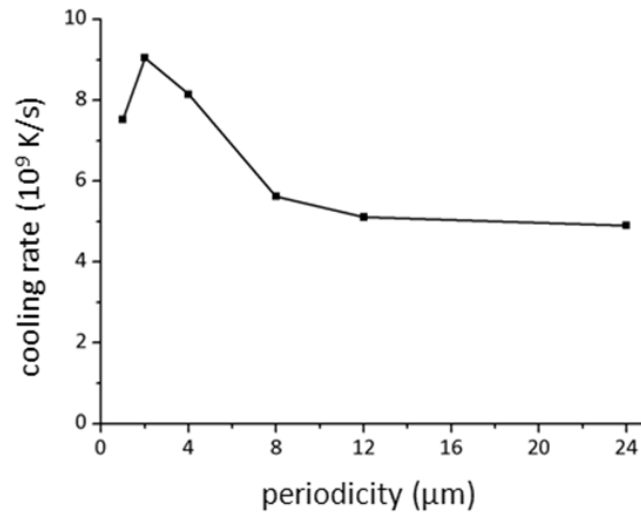


Figure 8.58.: Simulated cooling rate for TiAl after laser treatment at $170\ \text{mJ}/\text{cm}^2$ vs. periodicity.

With the exception of one periodicity ($1\ \mu\text{m}$), the cooling rate decreases with larger periodicities. This can be traced back to higher maximum temperatures and melting durations concerning larger line-spacings. Therefore, the cooling time is longer. The determined cooling rates, typically several $10^9\ \text{K/s}$, are much higher than in the case of other solidification processes. Hence, the formation of metastable phases can be induced. However an argumentation in terms of classical phase diagrams is very difficult due to

the their limitations with respect to equilibrium states and infinitely slow cooling. As could be seen in the TEM results, the β to α -transition is suppressed. The possibility of predicting the phase formation is generally of interest and importance concerning the laser treatment of metallic thin film systems. Bené et al. and Tsaour et al. carried out some pioneering work in this field formulating some basic rules for different thin film systems such as metal-silicon and metal-metal systems [165][166][167].

Bené's rule for metal-metal thin film systems points out that the first phase to nucleate is the one contiguous to the low-temperature eutectic in a binary phase diagram [167]. In the case of TiAl this would be Al_3Ti . According to the subsequent effective heat of formation model by Pretorius et al., the Al_3Ti phase should also form primarily in the Ti/Al system [168]. Based upon this model, the phase with the most negative heat of formation at the effective concentration of the lowest temperature eutectic is formed [168]. Table 7.5 summarises potential phases in the TiAl system with their corresponding negative heats of formation. The most negative ΔH^{eff} can be found for

phase	composition	ΔH^{eff} (kJ/molat.)
Ti_3Al	$\text{Ti}_{0.750}\text{Al}_{0.250}$	-0.67
Ti_2Al	$\text{Ti}_{0.667}\text{Al}_{0.333}$	-1.49
TiAl	$\text{Ti}_{0.500}\text{Al}_{0.500}$	-1.52
TiAl_3	$\text{Ti}_{0.250}\text{Al}_{0.750}$	-2.96

Table 8.5.: Effective heat of formation ΔH^{eff} for titanium aluminides according to Pretorius [168].

TiAl_3 . However, it must be noted that this model is only valid for annealing experiments. In the case of laser interference experiments, the heating and cooling rates are quite high and therefore far away from thermodynamic equilibrium. In this context, the adaption of this model to laser interference is doubtful. Furthermore, the inadequate validity of this model has already been proven for multilayer systems with a significantly reduced single layer thickness [169]. If the layer thickness is small enough (less than 100 nm), TiAl and small amounts of Ti_3Al are formed directly. The formation of additional metastable phases in TiAl multilayer systems was reported by Lucadamo et al. [170]. Due to highly non-equilibrium states, it is important to take these additional phases into account. The variety of possible phases with a similar structure type may lead to some difficulties when identifying them in SAD-patterns. However, the formation of different intermetallic phases in irradiated specimens with a fluence of 476 mJ/cm²

can be confirmed in the electron diffraction patterns. The SAD patterns reveals the existence of mainly Ti_2Al and Ti_3Al . By means of laser interference, a mixture of said intermetallic phases with pure Ti grains is produced.

8.2.4. Tribological properties

The final part of this section deals with the tribological evaluation of the as-patterned TiAl multilayer. First, the Hertzian contact radius and contact pressure has to be calculated for the multilayer. Therefore, it is necessary to calculate the elastic modulus for an equivalent composite. According to the models of Voigt and Reuss, it is possible to approximate the elastic modulus of the composite arrangement [171][172]. Figure 7.59 depicts the schematic representation of the two models.

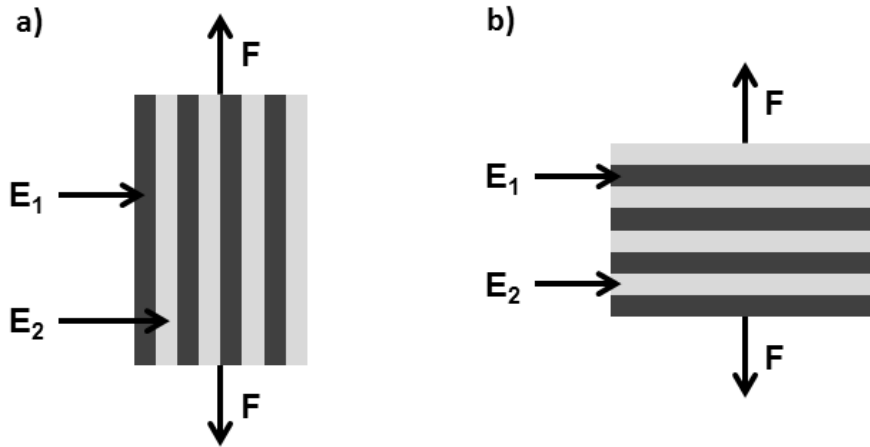


Figure 8.59.: Schematic representation of the Voigt (parallel arrangement) (a) and Reuss model (serial arrangement) (b).

For the given TiAl multilayer system, a serial arrangement according to Reuss may be used as an approximation. Related to this model, every layer carries the same load F . Moreover, the areas are identical and thus are the stresses.

$$\sigma_1 = \sigma_2 = \sigma = \frac{F}{A}. \quad (8.19)$$

Due to the different elastic moduli of the constituents ($E_{Al} = 68 \text{ GPa}$, $E_{Ti} = 116 \text{ GPa}$) and the substrate ($E_{Si} = 130 \text{ GPa}$ for (100)-orientation), the strains are dissimilar thus

leading to:

$$\epsilon_i = \frac{\sigma}{E_i}. \quad (8.20)$$

where E denotes the elastic modulus. Therefore, the effective elastic modulus based upon the model of Reuss can be expressed by:

$$E_{Reuss} = \frac{\sigma}{\epsilon_{total}} = \frac{\sigma d_{total}}{\sum_i \Delta d} = \frac{\sigma d_{total}}{\sum_i \frac{\sigma d_i}{E_i}} = \frac{d_{total}}{\sum_i \frac{d_i}{E_i}} \quad (8.21)$$

with d being the respective film thickness. By building the reciprocal value and inserting the volume fractions f_i of the individual layers, the previous equation can be reformulated to:

$$\frac{1}{E_{Reuss}} = \sum_i \frac{f_i}{E_i}. \quad (8.22)$$

The used multilayer consists of 14 double layers with 5 nm Al and 17 nm Ti, a capping layer of 10 nm Ti and a Si substrate. The corresponding volume fractions are $f_{Ti} = 0.780$ and $f_{Al} = 0.22$. Based upon these values, the effective elastic modulus is calculated at 100 GPa.

Considering the Voigt model, the different strains are equal thus following $\epsilon_1 = \epsilon_2 = \epsilon$. The effective elastic modulus is given by:

$$E_{Voigt} = \sum_i f_i E_i \quad (8.23)$$

However, both models do not account for the Poisson ratios of the constituents. These are calculated on the basis of a linear mixing rule:

$$\nu = \sum_i \frac{\nu_i}{n} \quad (8.24)$$

The Poisson constants for the different materials are $\nu_{Al} = 0.36$, $\nu_{Ti} = 0.34$ and $\nu_{Si} = 0.28$ [173][174]. Using these values, the Hertzian contact radius is $2.03 \mu\text{m}$ and the contact pressure 115 MPa.

After having determined the Hertzian contact radius and pressure, reciprocal sliding tests were performed depending on the pattern line spacing. For each specimen, ten sliding experiments were conducted with 1000 cycles and a stroke length of $300 \mu\text{m}$.

8. Results and discussion

The normal load was set to 1 mN using a 100 Cr6 ball with a radius of 1.5 mm and a rms value of around 3 nm (see figure 7.60). The ball surface was analysed by WLI with regard to geometrical accuracy after every sliding experiment.

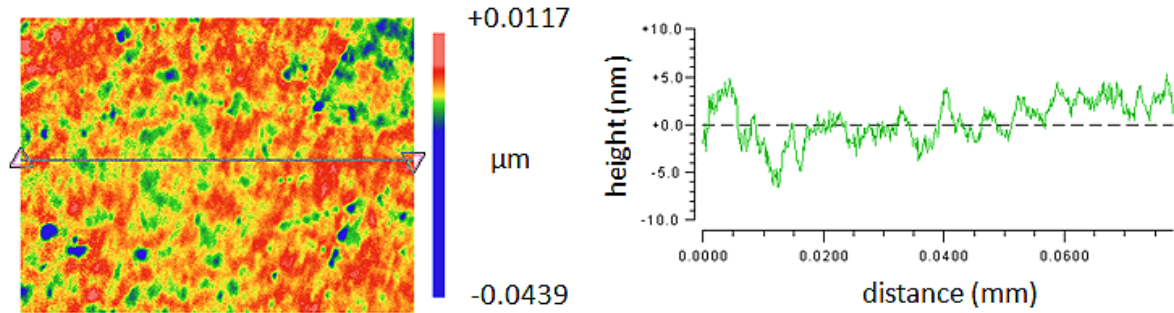


Figure 8.60.: WLI image of the initial ball surface (100 Cr6). Left image shows a surface profile map. The ball curvature was removed by the WLI software (*Metro-Pro*). In the right image, a cross-section profile plot is presented indicating a low roughness.

Figure 7.61 highlights the results of the measurements with a parallel and perpendicular orientation of the slider related to the laser interference lines.

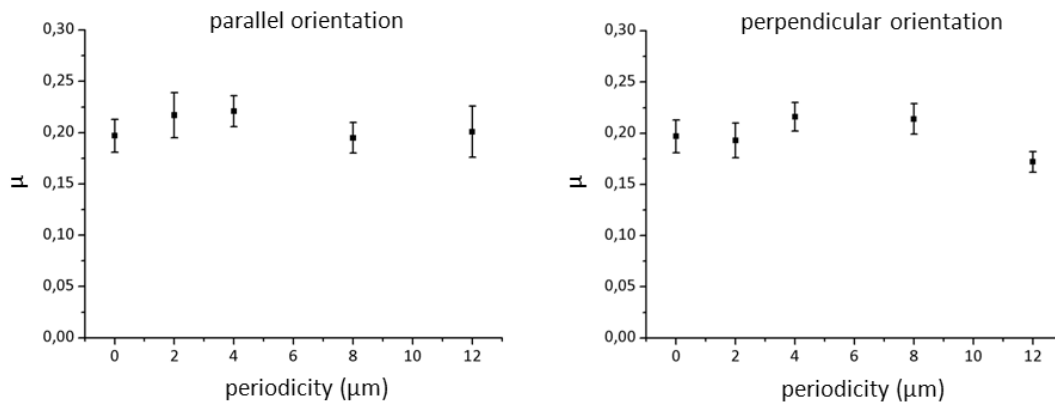


Figure 8.61.: Measured friction coefficient μ vs. laser periodicity in μm with an orientation parallel (left) and perpendicular to the laser interference lines (right). The point 0 μm on the abscissa represents the unpatterned reference sample.

8. Results and discussion

Each data point within the graph is an averaged value of ten individual sliding experiments with the corresponding standard deviation. Obviously, there is no significant difference between the specimens nor regarding the line-spacing neither the orientation. This may be attributed to the nearly vanishing topography after laser patterning which is typically in the range of a few nm.

Apart from measuring the friction coefficient, the resulting wear volume was determined for each sample using *ASTM G99* [137]. The results are shown in figures 7.62 and 7.63 for parallel and perpendicular orientations.

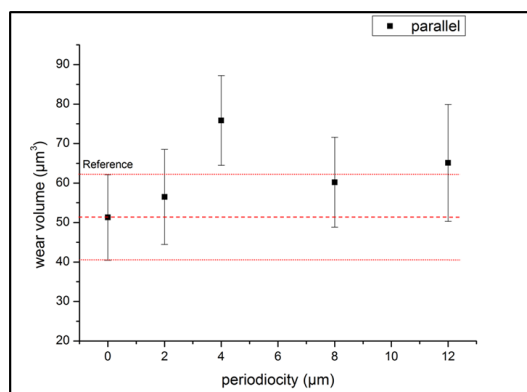


Figure 8.62.: Wear volume vs. periodicity for a parallel orientation between the slider and the laser interference lines measured by WLI.

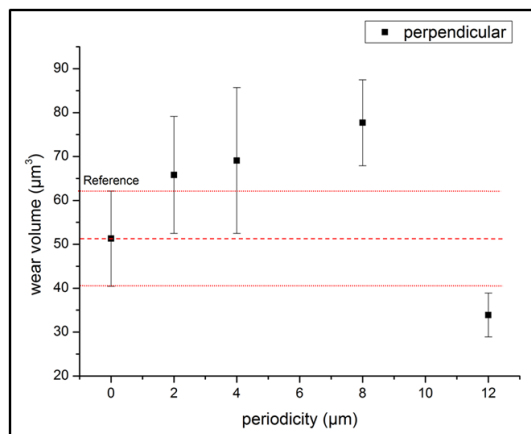


Figure 8.63.: Wear volume vs. periodicity for a perpendicular orientation between the slider and the laser interference lines measured by WLI.

8. Results and discussion

The wear volume data for parallel sliding are scattered around the unpatterned specimen with relatively large error bars. As already explained in section 7.1, the wear tracks are very often irregular thus complicating the determination of the volume. Figure 7.64 highlights an example of a wear scar after parallel sliding.

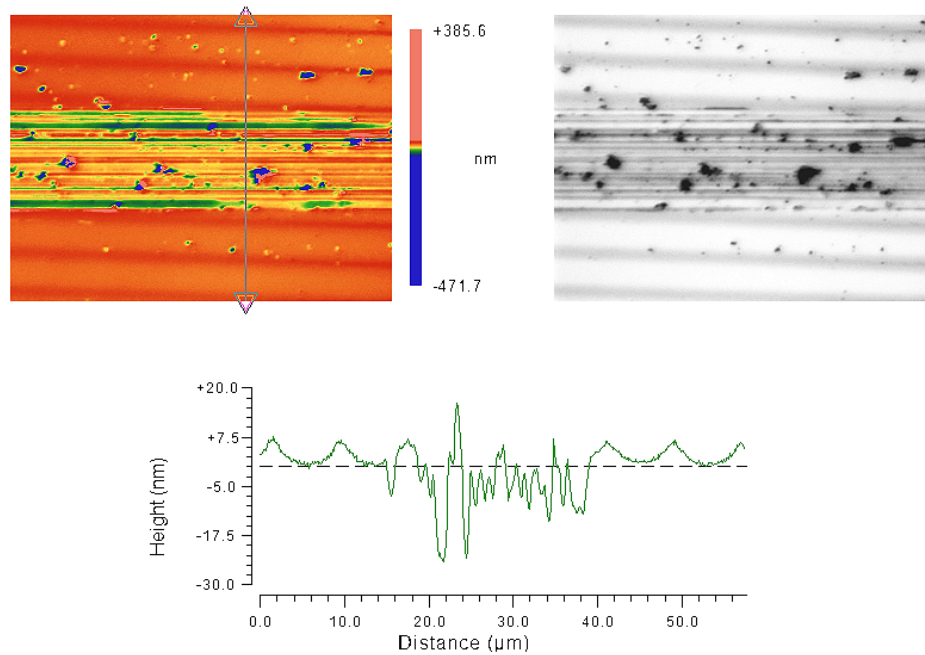


Figure 8.64.: WLI image of a wear scar after parallel sliding. The top left image shows the respective surface intensity map, the top right an intensity map and the bottom the corresponding cross-section profile plot for a patterned sample with a periodicity of around $8 \mu\text{m}$.

Aside some difficulties in defining a suitable reference plane for the determination of the wear volume, the inhomogeneity of the laser spot was also an issue. During the patterning, some fluence peaks can appear leading to height deviations in the final interference pattern.

In the case of parallel sliding, no periodicity dependence can be identified. In contrast, perpendicular sliding conditions demonstrate a reduction of the wear volume for the specimen with a line-spacing of $12 \mu\text{m}$. A closer look at the wear scar reveals, that wear debris is preferentially located in the recessions of the pattern (see figure 7.65).

8. Results and discussion

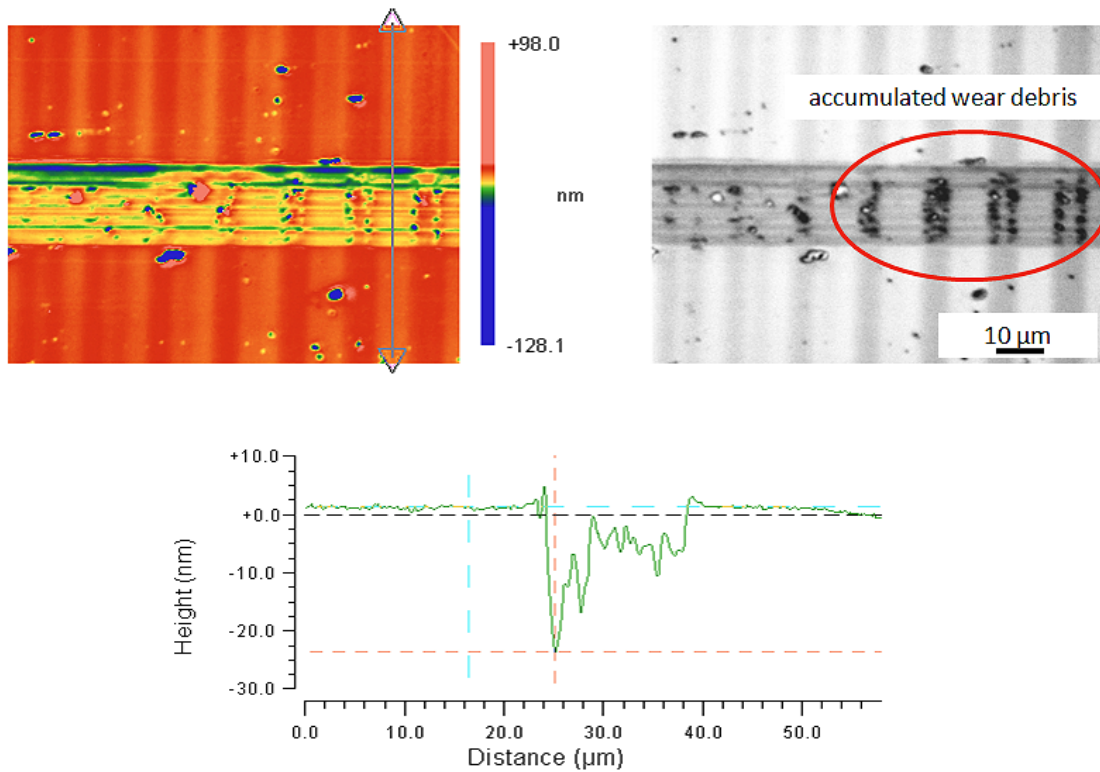


Figure 8.65.: WLI image of a wear scar at a periodicity of $12\ \mu\text{m}$ under perpendicular sliding conditions. The top left image shows surface profile map, the top right the intensity map with indication of accumulated wear debris and the bottom finally the cross-section profile plot.

It is therefore assumed that the abrasive effect is finally minimised resulting in a lower wear volume. A direct comparison between parallel and perpendicular sliding at the aforementioned periodicity of $12\ \mu\text{m}$ shows a significant difference. Under parallel sliding conditions, wear debris is shifted back and forth during the linear reciprocal movement thus always contributing to abrasion in the wear scar. On the other hand, perpendicular sliding ensures an effective trapping of wear debris in respective recessions. In addition to the WLI results and the determination of the wear volume, a TEM foil was prepared out of the wear scar of an unpatterned specimen (figure 7.66).

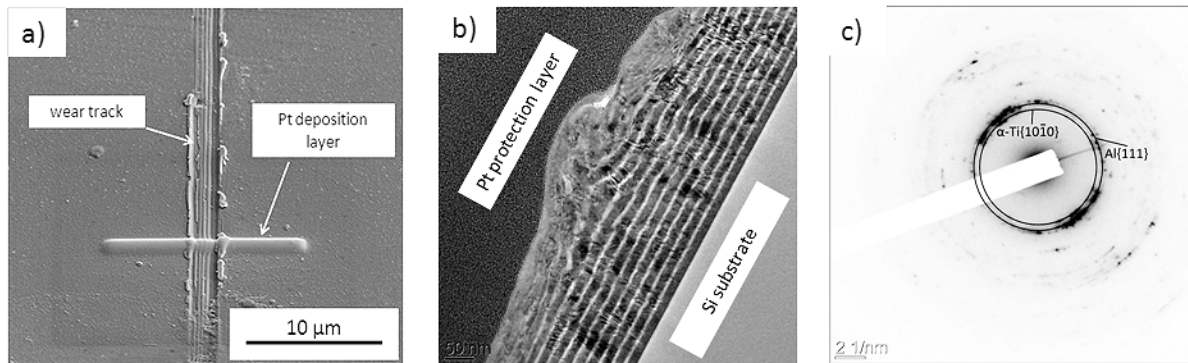


Figure 8.66.: TEM foil preparation in a wear scar of an unpatterned TiAl sample by FIB (a), the corresponding cross-section view (b) and the indexed SAD pattern (c).

Figure 7.66 (b) clearly reveals a strong deformation zone of the upper TiAl layers ranging approximately 50 nm in depth. With increasing distance from the surface, the lamellar multilayer structure appears. The indexed SAD pattern demonstrates that the original fibre texture is nearly vanished due to significant shearing of surface material. However, no additional phases can be identified within the deformation zone.

Basically, XRD and TEM studies have shown that at a given fluence of about 170 mJ/cm^2 , there is no considerable formation of intermetallic phases in the positions of maximum intensity acting as a reinforcement. Instead, a mixture of α - and β -Ti can be identified in those regions. By applying a higher fluence at 476 mJ/cm^2 , different intermetallic phases such as Ti_3Al and TiAl_2 are formed.

Moreover, after having irradiated the specimen surface, the reaction extends over the complete multilayer thickness. Hardness measurements performed by nanoindentation showed an increase in hardness by a factor of two between the maxima and minima.

Considering a specimen with a homogeneous $4 \mu\text{m}$ line-spacing under perpendicular sliding, the wear volume was measured to be $22.5 \mu\text{m}^3 \pm 3.8 \mu\text{m}^3$, which is a 34% reduction with respect to the best results at a fluence of 170 mJ/cm^2 and a periodicity of $12 \mu\text{m}$ having a wear volume of $33.9 \mu\text{m}^3 \pm 4.9 \mu\text{m}^3$.

8.3. Hierarchical surface structures by micro-coining and laser interference

8.3.1. Introduction

It is well known that engine friction loss accounts for 41 % of the total energy produced by a typical automotive engine [175]. With the aim of increasing the resistance to these adverse working conditions, engineered surfaces are necessary to control friction and wear. The performance of tribological systems can be significantly enhanced by tailored surfaces instead of using a perfectly smooth surface finish. However, friction is a multiscale problem and the tailoring of specific surface properties requires methods, capable of reaching structural sizes ranging from sub μm (e.g. wetting and adhesion effects) up to some $100\ \mu\text{m}$ and higher (e.g. lubrication reservoirs for deep-drawing for instance). From hundreds of nm to several μm , LIMET is a versatile technique for many materials. Beyond the lower μm scale, micro-coining can be used for bulk forming or surface structuring in the range of a few hundred μm (*in collaboration with the RWTH Aachen, IBF group of Prof. Dr.-Ing. G. Hirt*).

Usually, a negative form of the desired structure is created on a punch-like tool set and embossed onto the workpiece surface. This process allows fast high quality reproduction of the tool set shape at low cost. Applications include micro heat exchangers or chemical micro reactors. Coining can be applied on one or both sides of the desired part and performed either in cold state or by heating the tool set and/or the coining sample. Earlier research at the institute of metal forming at the RWTH in Aachen focussed on an increasing aspect ratio (height to width) of deterministic channel-like structures with 1-D periodicity. The height and width of those structures were in the range between 100 and $300\ \mu\text{m}$. Achievable aspect ratios were up to 3. Figure 7.67 shows examples of coined channel structures.

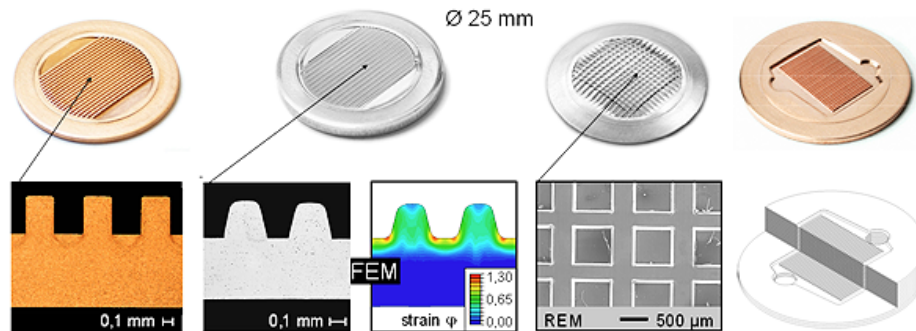


Figure 8.67.: Examples of coined copper and aluminium; cross-sections of different coining structures (left), numerical model of the strain during the coining process (centre), SEM surface detail of a cross-structured aluminium sample, multilayered heat exchanger concept made of stacked coined samples (right)

The form filling of cylindrical cavities in pure aluminium, depending on the diameter, varies between 0.05 and 1.6 mm which was studied by Ike and Plancak [176]. Cavities with diameters in the range of 0.2 to 0.4 mm showed a good and uniform form filling while larger diameters showed peaks in the centre and lower form filling at the borders of the specimen.

In the work of Schubert and Böhm [177], rib and complex structures in the range of 2-20 μm are created in aluminium, steel, copper and brass sheets using dies made of silicon or tool steel. The authors pointed out, that the boundary conditions (e.g. clamping, ejector forces and blank materials properties) influence the coining results.

The idea of hierarchical surface structures consists of combining micro-coining and LIMET. The coined structures, as coarser primary structures in the range of 100 μm , minimise the contact area and may be beneficial in trapping wear debris or as lubricant reservoirs under starved lubrication conditions. The secondary structure in the range of some μm achieved by laser interference can be applied to create different topographies (figure 7.68 a) or to locally modify material properties (figure 7.68 b).

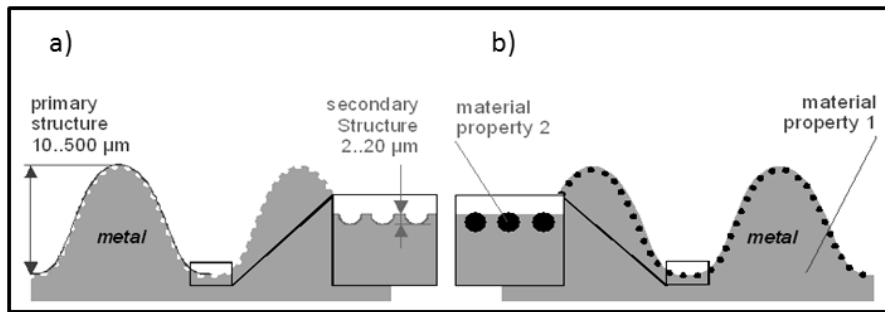


Figure 8.68.: Principle of a secondary LIMET structure used for topographic effects (a) or local influence on material properties such as the hardness of a micro-coined surface (b).

This research was funded by the **Volkswagen Foundation** in the framework of the project (*Integration of Laser Interference Metallurgy and Micro Metal Forming to Functionalize Surfaces*) as a part of this PhD thesis. Only some highlighted results will be presented to show the potential of the process combination.

At first, aluminium bulk samples with a technical purity of 99.5 % were patterned applying two interfering laser beams resulting in a typical ridged pattern. The line-spacing was set to 2, 5, 7 and 8 μm in order to study its influence on the frictional response under linear reciprocating dry sliding. The results were directly compared with numerical studies done by collaboration partners at the Imperial College London (*Tribology group of Prof. Dr. A.V. Olver, Dr. Simon Medina*). For the laser interference experiments, the third harmonic wavelength at 355 nm was used with a fluence of about 1500 mJ/cm² for all the samples. This value was determined in fluence series tests and provided the most homogeneous patterning results. All the samples were irradiated under normal atmospheric conditions in air with one single laser shot.

Thereafter, a combination of micro-coining and LIMET was thus performed. Within the funded project, a superposition of various coining geometries ranging from ridges to cross-hatches as well as honeycomb structures with different laser interference textures (e.g. line-, dot- and cross-pattern) was realised. The resulting morphology and topography were investigated by SEM and WLI. The influence of the micro-coined geometry, especially the flank angle, was studied by finite element simulations and the results were compared to experimental data.

At the institute of metal forming in Aachen, micro-coining was done using 25 mm round plates of aluminium with technical purity. These plates were directly cut off from 1-2 mm thick sheets during the coining process by the upper punch and the lower cutting ring.

The cold coining process was performed on a uniaxial universal press with 400 kN maximum force. The force was applied with a ramp of 5 kN per second. The necessary coining forces for sufficient form filling depend on the desired structures and the hardness of the used materials. A first approximation for 90 to 95 % form filling (coining to tool set height ratio) are normalised pressures (by area and initial flow stress) of 2 to 2.5 for aluminium. After coining, the sample can be ejected by a hydraulic ejecting ring with 25 mm outer diameter that covers the lower punch with 19 mm outer diameter. Typically, single-sided coining occurs on the bottom of the sample, the upper punch is only structured for double-sided sample structuring.

8.3.2. Tribological properties of laser-patterned aluminium surfaces

The tribological tests under dry conditions were performed by a nanotribometer using a ball on disk configuration with a linear reciprocating sliding mode. The temperature and relative humidity were kept constant at 20° C and 45 %. The counter body consisted of a 100 Cr6 steel ball with a diameter of 1.5 mm mounted on a steel cantilever. The normal force was set to 100 mN and the sliding speed to 1 cm/s. The stroke length for all experiments was fixed at 1.5 mm.

First, the tribological behaviour of the laser-patterned Al specimens were studied without micro-coining for line-textures with different spacings under dry sliding. After laser patterning, the surfaces were analysed by WLI regarding topographic parameters. Table 7.6 summarises the main findings.

Periodicity (μm)	H (μm)	rms (nm)	R_{sk}	R_{ku}
Reference	0.030 ± 0.005	8 ± 0.8	-1.44 ± 0.33	3.73 ± 0.79
2	1.58 ± 0.27	547 ± 56.64	0.73 ± 0.16	3.93 ± 0.94
5	1.88 ± 0.34	579 ± 116.77	0.65 ± 0.13	3.35 ± 0.34
7	2.98 ± 0.37	936.5 ± 89.44	0.25 ± 0.09	3.20 ± 0.40
8	2.87 ± 0.36	978.4 ± 76.45	0.53 ± 0.06	3.49 ± 0.24

Table 8.6.: Topographic parameters of laser-patterned Al specimens measured by WLI.

The topographic analysis revealed no significant differences. Skewness values are all positive for laser treated specimens, indicating more spiky surfaces. In addition, the kurtosis is very similar for the listed specimens. The Swedish height and rms rise with increasing line-spacings according to the results of Lasagni et al. [48]. In contrast to the very similar topographic results, experiments under dry sliding with a parallel and a perpendicular orientation to the laser line-textures demonstrate more pronounced differences. Figure 7.69 points out the main results of the tests with the sliding direction parallel to the laser lines.

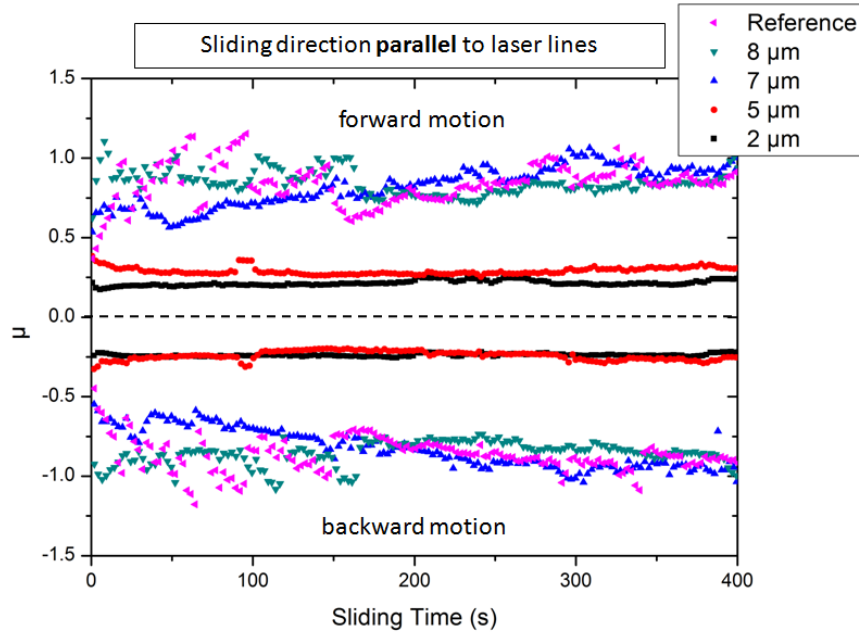


Figure 8.69.: Friction coefficient vs. sliding time for laser-textured Al surfaces. The laser pattern consisted of lines with different spacings. The sliding direction in this case was parallel to the laser lines.

Here, surfaces are separated by different periodicities exhibiting interesting frictional properties. It can be seen that values greater than $7\ \mu\text{m}$ appear to produce friction coefficients which are very similar to those of the not-patterned specimens. Lower values of the line spacing, however, appear to give much lower friction coefficients with less oscillations.

In order to describe this behaviour from the theoretical point of view, half-space simulations were performed on laser textured surfaces in collaboration with the Imperial College London. The simulation is based on a multi-level and multi-integration approach [178]. In this case, the contact between a smooth sphere and a textured plane is represented, with a defined normal load of 100 mN (see figure 7.70). The structured surface is discretised via a finite-element mesh with typically 2048×2048 elements. The results show that with decreasing periodicities, the number of asperities in contact increases from 5 (for $8\ \mu\text{m}$) to 14 (for $2\ \mu\text{m}$), yet the calculated contact area decreases from $55.81\ \mu\text{m}^2$ to $29.48\ \mu\text{m}^2$ (see table 7.7). The colour-code corresponds to a normalised contact pressure. The normalisation is done using the Hertzian contact pressure p_0 . It is

8. Results and discussion

important to note that all surfaces are created from the left hand side (offset reference) and not the centre of the ball. The relative position of the peaks with respect to the centre of the ball varies between cases, explaining the jump from 4 to 5 asperities for 7 to 8 μm .

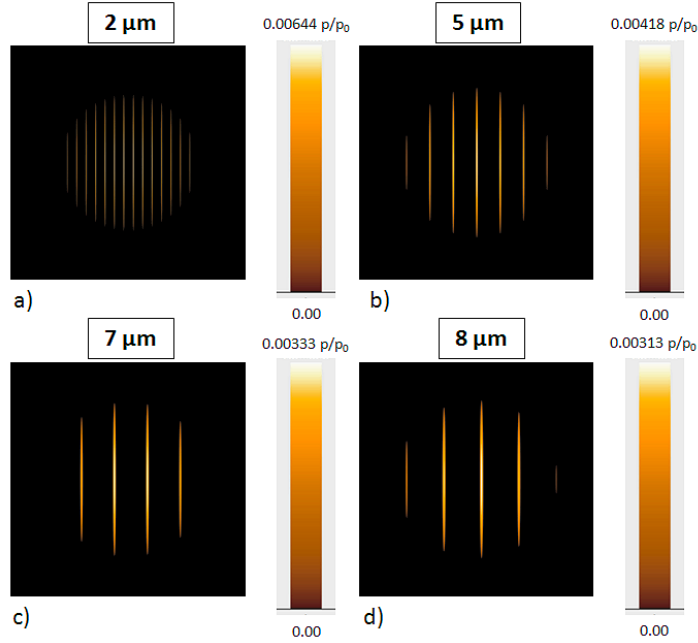


Figure 8.70.: Simulated contact pressure distributions for different periodicities (2, 5, 7 and 8 μm) and number of contacting asperities. The colour-code represents the normalised contact pressure. The normalisation is done using the Hertzian contact pressure p_0 (*in collaboration with Dr. Simon Medina, Imperial College London*).

Periodicity (μm)	2	5	7	8
Normal load (N)	0.1001	0.1000	0.1001	0.1000
Number nodes in contact	49466	74460	84858	93638
Contact area (μm^2)	29.48	44.38	50.58	55.81
Number of asperities	14	7	4	5

Table 8.7.: Summary of modelled results for laser-patterned surfaces (*in collaboration with Dr. Simon Medina, Imperial College London*).

In contrast, the results for perpendicular sliding are completely different (figure 7.71).

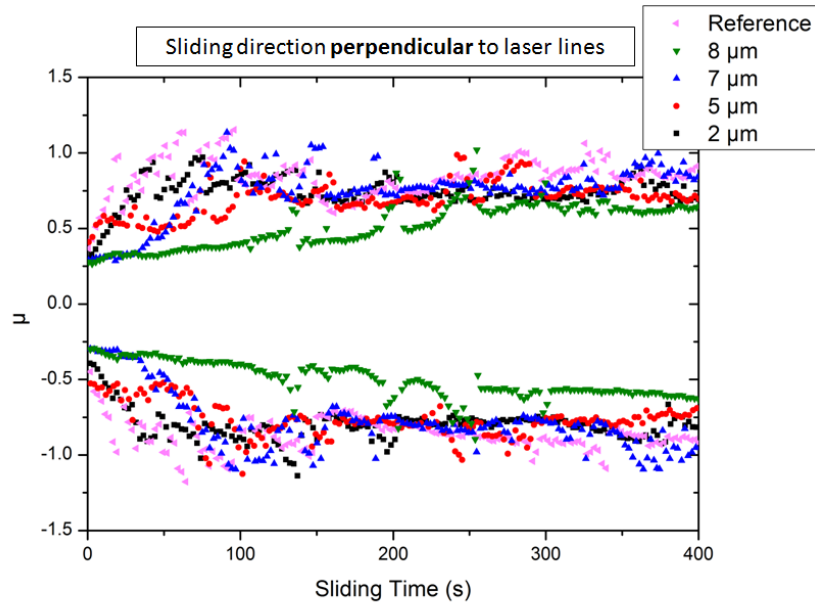


Figure 8.71.: Friction coefficient as a function of sliding time for laser textured aluminium bulk samples with different line-spacings. The measurement direction was perpendicular to the laser lines.

The effect of line-spacing is not very pronounced for a perpendicular alignment (see 2 and 5 μm). The increased corrugation of the surface profile along the direction perpendicular to the ridged texture obviously plays a role in terms of friction force fluctuation. However, the friction coefficient of the reference is in the same range as in parallel orientation. Nearly all samples start from an identical initial value and only the specimen with a periodicity of around 8 μm exhibits a lower coefficient of friction in the beginning, gradually converging to the other friction curves.

8.3.3. Combination of micro-coining and laser interference patterning - the influence of process sequence and coining geometry

After having studied the effects of laser patterning for bulk Al samples under dry sliding, the combination of LIMET and micro-coining was scrutinised in detail.

At first, it was necessary to elucidate the process sequence in order to optimise the combination of both patterning techniques. In the beginning, laser interference patterned aluminium specimens were coined. Due to the already high required forces during the coining process no significant influence of the laser structures on the process could be recognised. Neither the surface hardening caused by the laser patterning process nor the structures themselves had any effect on the resulting form filling at the given forces. In highly deformed areas, such as the flanks of the channel structures, former structures are almost completely destroyed (figure 7.72 a). Those areas are formed under large shear stresses and the additional surface friction increases the effects on the laser structures with low depth. On the top plane and in the lowest part of the channels the laser pattern can withstand the forming process quite well.

This leads to the necessity of designing the forming process with only small shearing in the areas that should be hierarchically structured. Spherical structures, which will be presented further on, fulfil the requirements as they have low deformation on the top plane. The areas close to the top plane which have less deformation due to friction and shear also show good results in this process sequence. Considering the inverted process route (figures 7.72 b, d), the laser structure can be clearly identified on top of the coined structures and in the channels. The structures are homogeneous in both regions .

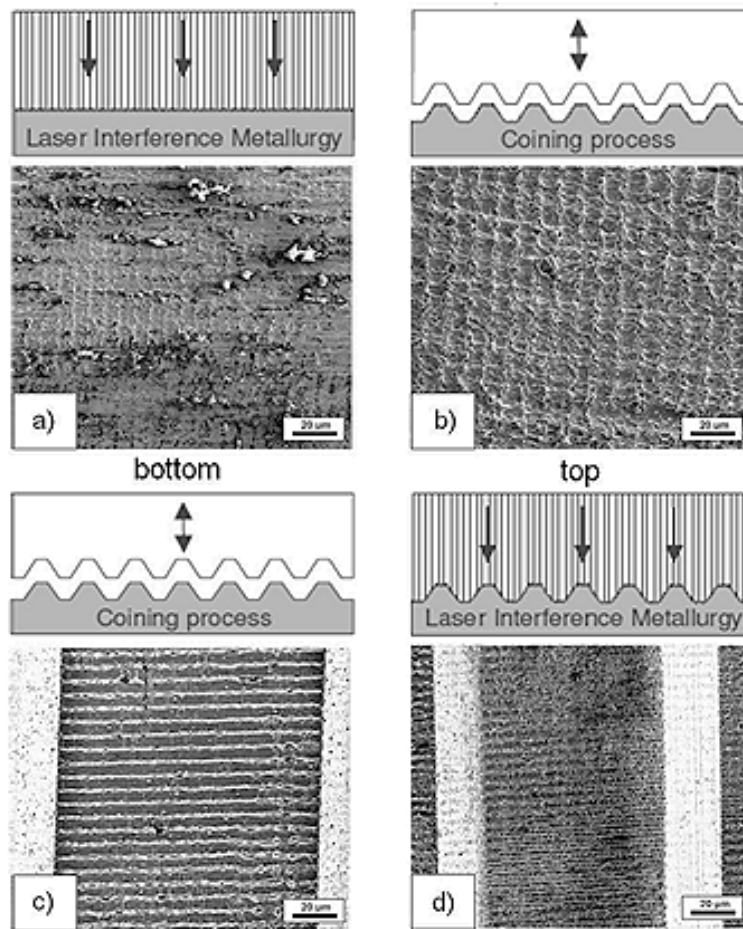


Figure 8.72.: Micro-coining followed by laser interference patterning. SEM images in (a, c) show the bottom and top regions of a laser patterned surface after micro-coining (b, d) of a coined surface after LIMET.

Only the steep flanks of the coining geometry are critical for the subsequent laser process. An increasing flank angle leads to a higher projected area to the normal incident laser beam and thus reduces the laser energy density. The energy density threshold value for aluminium is, according to Lasagni et al., approximately 1500 mJ/cm^2 [48]. Below this value, no significant melting of the aluminium surface occurs. There is a critical angle for which the laser fluence is still sufficient to achieve a homogeneous laser structure even on the flanks. In the considered case, this critical angle was experimentally derived to be about 25° . In order to study the effect of the flank angle on the pattern homogeneity, finite element simulations based on the heat diffusion equation

8. Results and discussion

were performed for 25° (figure 7.73 a) and a typical angle of 45° (figure 7.73 b) for the micro-coined structures [47]

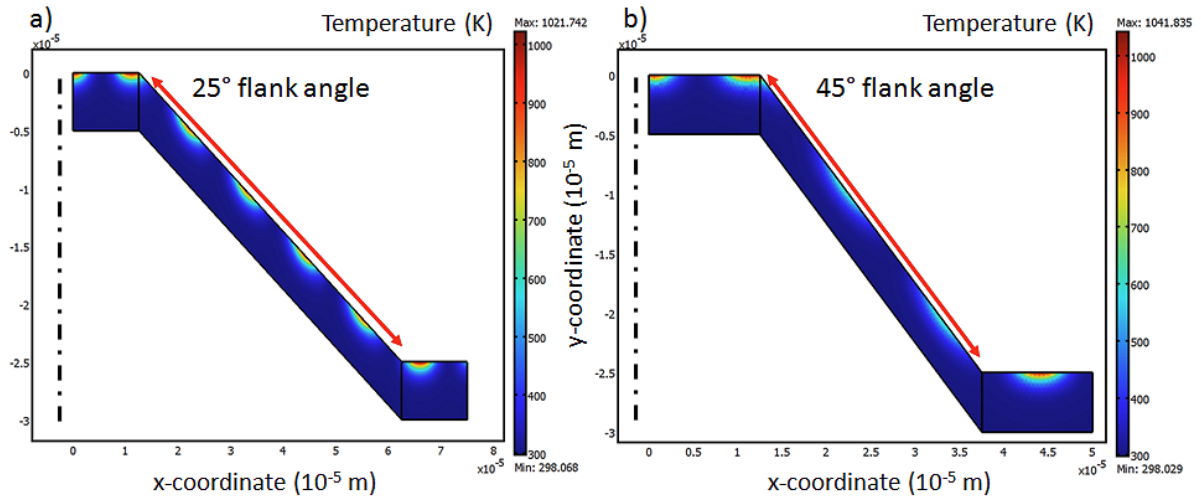


Figure 8.73.: Thermal simulation of the influence of the micro-coined flank angle for 25° (a) and 45° (b) on the subsequent laser patterning. Due to symmetry, only half of the micro-coined structure is presented. The red arrows mark the flank regions for which cross-section temperature profile plots were simulated. The x-scale is different for (a) and (b) thus explaining the apparent similarity of the flank angles in the figure.

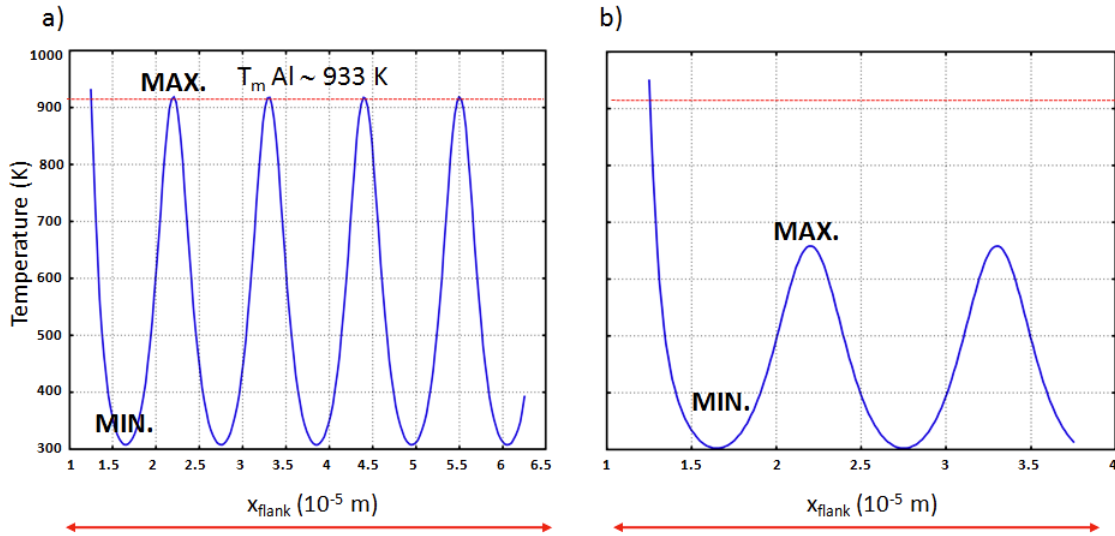


Figure 8.74.: Simulated temperature cross-section profile plots for a flank angle of 25° (a) and 45° (b). The plot was simulated for the flank region of the coining geometry indicated by the red arrows (see figure 7.72).

In figures 7.73 and 7.74, the colour-coded temperature distribution and temperature cross-section plots for the slope region (indicated by the red arrows in figure 7.73) are presented for a flank angle of 45° . Due to symmetry, only half of the micro-coined geometry is displayed in both cases. The maximum temperature in the flank region is about 650 K and thus well below the melting point of aluminium (figure 7.74 b). Because of the increased projected area, the energy density is lower than the necessary threshold. The initial increase in temperature is attributed to the laser interaction zone at the summit, partially extending to the flank area.

In contrast, the maximum temperature for a flank angle of 25° is $\approx 940 \text{ K}$ (figure 7.74 a). Consequently, the aluminium surface starts melting and a homogeneous laser pattern can be observed. The depth of the thermal interaction zone can be estimated to $2 \mu\text{m}$ which is consistent with the thermal diffusion length for aluminium [48].

Based on the findings of the finite-element simulation, micro-coining geometries with circular bumps and more moderate flank angles have been fabricated and subsequently laser-patterned.

8. Results and discussion

A detailed topographic analysis of the patterned surfaces was performed by WLI. Figure 7.75 displays intensity (a, c) and cross-section profile plots (b, d) of micro-coined and hierarchically patterned aluminium surfaces. In figures 7.75 (c) and (d), the superimposed laser line-structures are clearly visible. The used periodicity in this case was around $11\ \mu\text{m}$ with a structural depth of approximately $2\ \mu\text{m}$.

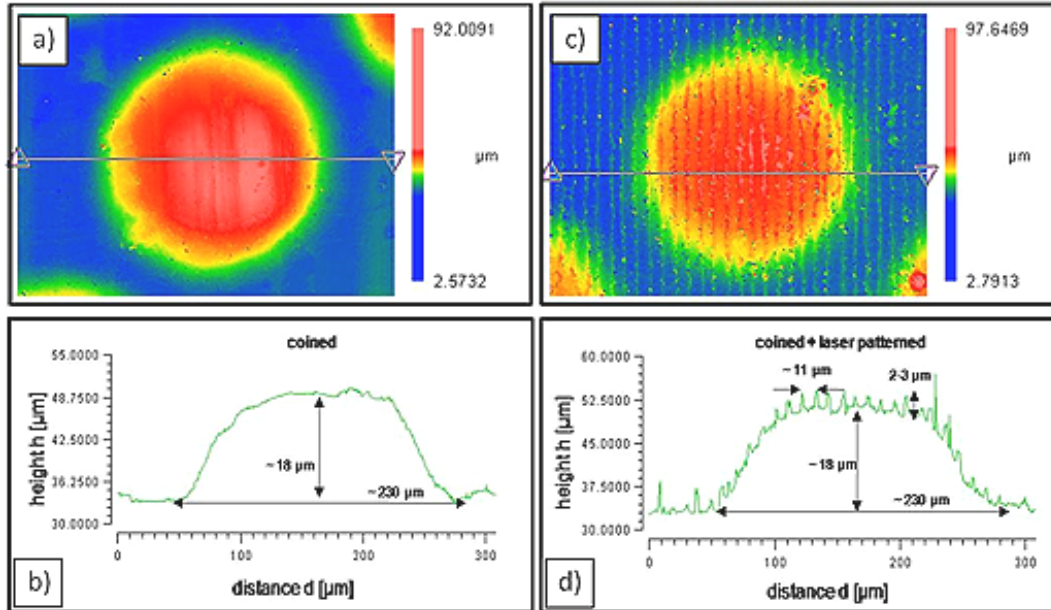


Figure 8.75.: Intensity and cross-section profile plot of a micro-coined (a, b) and a hierarchically patterned aluminium sample surface (c, d) measured by WLI.

During the laser interference process, the material at the positions of maximum laser intensity is molten. In contrast, the adjacent regions of minimum laser intensity are nearly unaffected. This leads to a temperature gradient with a corresponding surface tension gradient thus transferring material from hot to cool regions [30]. The resulting topography is approximately sinusoidal.

Apart from the influences of the process sequence and the coining geometry, the pristine surface roughness plays an important role with regard to the pattern homogeneity. As a rule of thumb, the original surface roughness should be smaller than the respective periodicity. Preliminary polishing of rolled initial material usually fulfills this condition. The rms value for the polished aluminium specimens is approximately $0.21\ \mu\text{m}$. As already discussed in the theoretical part, as long as the ratio between the surface

roughness, here rms, and the wavelength of the incident laser beam is smaller than 1, the initial surface roughness can be neglected [43]. For a used wavelength of 355 nm, this ratio can be calculated to be 0.6. Thus, roughness has no significant effect on reflectivity nor on the patterning process.

Another important factor is the temperature dependence of reflectivity. In the case of aluminium, the reflectivity may drop up to 30 % [31]. The reflectivity at room temperature for the given wavelength is around 0.924 [112]. During melting, R decreases to 0.65 [48]. In order to take the temperature dependence into account, the thermal simulation was modified according to Lasagni et al. by the following equation [48]:

$$R_{Al} = (1.048 - 3.989) \cdot 10^{-4}T \quad (8.25)$$

for $298K < T < T_m$ and for $T \geq T_m$, R is set to be 0.65.

Apart from roughness and temperature influences, the incident angle may also affect R. Most values of R are only listed for normal incidence simplifying the general Fresnel formula. As soon as the incident angle deviates from 90° , the reflectivity is dependent on the angle and the polarisation of the incident beam. Here, the laser source is perpendicularly polarised and equation 3.34 can be applied to calculate R for the two flank angles:

$$R_{perp} = \frac{(n - \cos\theta)^2 + \kappa^2}{(n + \cos\theta)^2 + \kappa^2}. \quad (8.26)$$

The real refractive index n and the extinction coefficient for aluminium at 355 nm are $n = 0.407$ and $k = 4.426$ [112]. Based upon these values, the reflectivity may be calculated for incident angles of 25° and 45° :

$$R_{perp,25} = \frac{(0.407 - \cos 25^\circ)^2 + (4.426)^2}{(0.407 + \cos 25^\circ)^2 + (4.426)^2} = 0.931 \quad (8.27)$$

$$R_{perp,45} = \frac{(0.407 - \cos 45^\circ)^2 + (4.426)^2}{(0.407 + \cos 45^\circ)^2 + (4.426)^2} = 0.945 \quad (8.28)$$

Compared to R at normal incidence and room temperature, the percentaged difference to an incident or flank angle of 25° is only 0.75% and 2.3% for 45° , thus well below 10%.

8. Results and discussion

Finally, SEM images in figure 7.76 highlight the precisely-defined channel (a) and bump structures (c) made by micro-coining and the superimposed laser line-patterns (b, d) which in the case of the aforementioned bumps are uniformly distributed over the entire section.

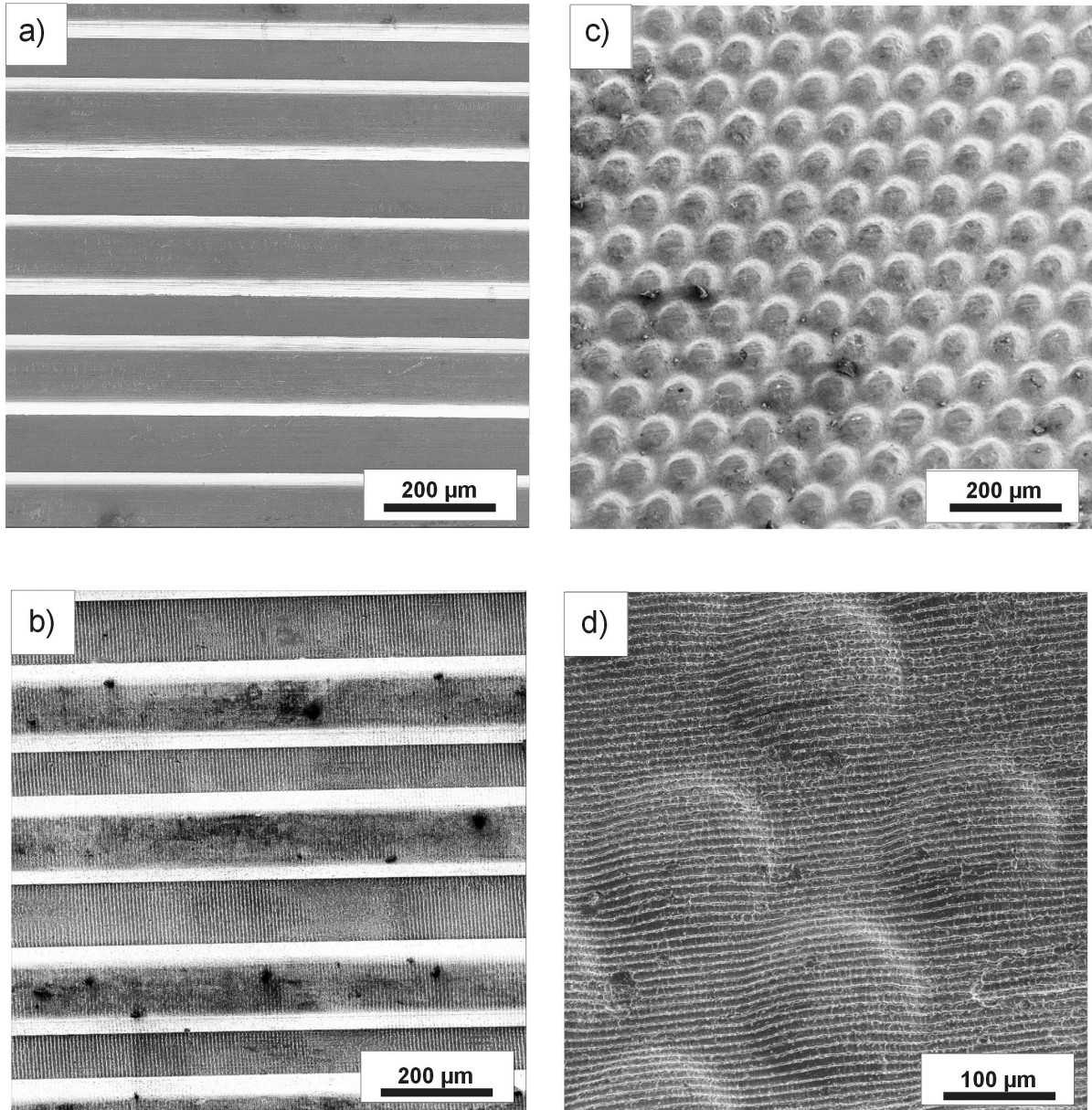


Figure 8.76.: SEM images of micro-coined channels as well as spherical patterns (a, c) and with a superimposed homogeneous laser pattern in (b, d).

8.3.4. Tribological properties of hierarchical surfaces under lubrication

Concluding, tribological tests under lubricated sliding were performed for different surface conditions (polished reference sample, laser interference line-pattern, micro-coined dimples and a sample combining both). A microtribometer was used with a ball on disk setup (Al_2O_3 ball with a diameter of 3 mm) and a normal load of 5 N. The lubricant used for the tribological experiments was a typical engine oil (*Shell Vitrea 100*). Table 7.8 outlines the main properties of the oil.

ρ at 15 °C	ν_k (40 °C)	ν_k (100 °C)	Pour point	Flash point
877 kg/m ³	100 mm ² /s	11.2 mm ² /s	-12°C	225°C

Table 8.8.: Typical physical properties of the used engine oil Shell Vitrea 100. Here, ν_k denotes the kinematic viscosity [179].

In order to obtain a uniform lubricant film on top of the sample surfaces, a defined amount of engine oil of about 350 μl was spread on the surface by spin coating at 80 rps for 30 s. In case of the reference sample, the aluminium surface was metallographically prepared by grinding and polishing with diamond suspensions of up to 1 μm in particle size.

For the laser-patterned specimens, the line-spacing was fixed at 5 μm with a depth of about 1.5 μm . The dimple size of the micro-coined sample was approximately 45 μm with a structure depth of around 13 μm .

The hierarchical surface pattern can be seen according to the schematic drawing in figure 7.77 (a) and the SEM image in figure 7.77 (b). All the patterned aluminium surfaces reveal a considerable improvement of the lubricant lifetime compared to the polished reference sample. Typically, the friction coefficient starts at low values and increases after a certain number of laps, indicating insufficient lubrication. This transition is very sensitive to the used surface pattern. In addition to that, the initial value of the friction coefficient varies with the surface conditions shown here. It can be concluded that the residual oil volume on the sample surface differs for the various patterns. As far as the polished reference sample is concerned, there are no channels or dimples in which the lubricant can be dispersed. Therefore, upon contact a certain amount of oil fills the gap between the sliding bodies, thus lowering the friction coefficient. A patterned surface

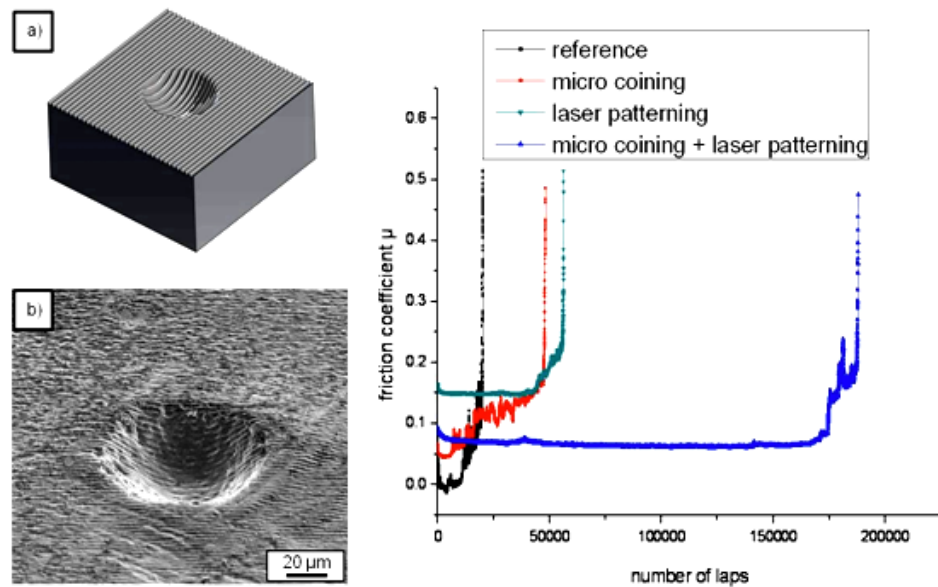


Figure 8.77.: Preliminary tribological test results of different surface conditions under lubricated sliding in a ball on disk setup. Figure 7.76 (a) represents a schematic drawing and (b) SEM pictures of a hierarchically patterned aluminium surface with a micro-coined dimple and a superimposed line-pattern.

with channels or dimples, on the other hand, leads to a reduction of lubricant in direct contact and retains the oil in the so called lubricant reservoirs. As a consequence of the reduced oil film thickness in the contact, the lubrication regime changes from mixed to boundary lubrication according to the well known Stribeck curve with an increasing μ [49]. The largest improvement in lubricant lifetime can be observed for the hierarchically structured surface. In this case, the friction coefficient μ is stable up to 180.000 laps. After that, a sudden increase in μ is visible indicating oil starvation. It is assumed that due to the enlarged surface area, the lubricant reservoir effect is more pronounced. The underlying phenomena associated with different pattern geometries and periodicities are a matter of a current DFG project (*SPP 1551*) which continues the previous project funded by the Volkswagen Foundation.

8.4. Geometrical interlocking

8.4.1. Introduction

In this final chapter of the thesis, a precise topographic design of two sliding steel surfaces by LIMET and the potential to modify frictional properties shall be presented and discussed.

Friction in moving interfaces plays a decisive role in technology, geology and biology. The ability to tune friction by tailoring surface topographies at micron length scales and by changing the relative orientation of crystallites at the atomic scale is well established. Here, both concepts extend to intermediate length scales.

Using two-beam laser interference, line-like patterns with varying periodicities (5, 9 and 18 μm) have been fabricated on stainless steel substrates (1.4301) and on tribometer testing balls made of 100Cr6 with a fluence of 400 mJ/cm^2 at a wavelength of 355 nm. The results highlight the possibility of creating bespoke contacting surface geometries leading to tuneable frictional properties.

8.4.2. Topographic analysis of interlocking surfaces

For the experiments, an austenitic stainless steel (1.4301) was used which is one of the most common steels. It is well known from literature that austenitic stainless steels are widely used for industrial purposes due to their high corrosion resistance and mechanical properties [180].

The lateral dimensions of the nominally flat specimens were 20 x 20 mm^2 . In order to reduce the surface roughness to a minimum, the samples were delivered with a highly polished mirror-like surface finish resulting in a root mean square roughness of approximately 31 nm. The topography was measured using WLI equipped with a 3D imaging surface structure analyser. The tribological tests were performed with a nanotribometer using a ball on disk configuration in a linear reciprocating sliding mode with a stroke length of 0.6 mm. The normal force was set to 1 mN and the linear sliding speed to 2 mm/s. The deviation of the aforementioned normal load was less than 10 % of the reference value in our experiments. The counter body consisted of a typical 100Cr6 bearing steel ball with a diameter of 3 mm. Temperature and relative humidity were kept constant at 20 °C and 45 % \pm 5%.

8. Results and discussion

Figure 7.78 shows a typical line-pattern in the stainless steel substrates with a periodicity of around $9\ \mu\text{m}$.

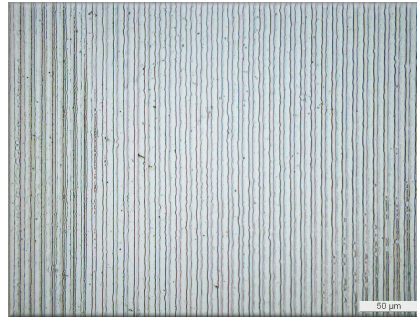


Figure 8.78.: Typical interference line-pattern in a stainless steel substrate [181].

The pattern resulting from two interfering beams is uniformly distributed and largely homogeneous. Some irregularities arise in the lower right corner of the figure and to some extent on the left side, and can be traced back to an inherent inhomogeneity of the laser beam source. Figure 7.79 displays a horizontal intensity cross section of the primary laser beam at 355 nm measured by beam profilometry and the corresponding 2-D intensity profile of the resulting laser spot for two interfering beams.

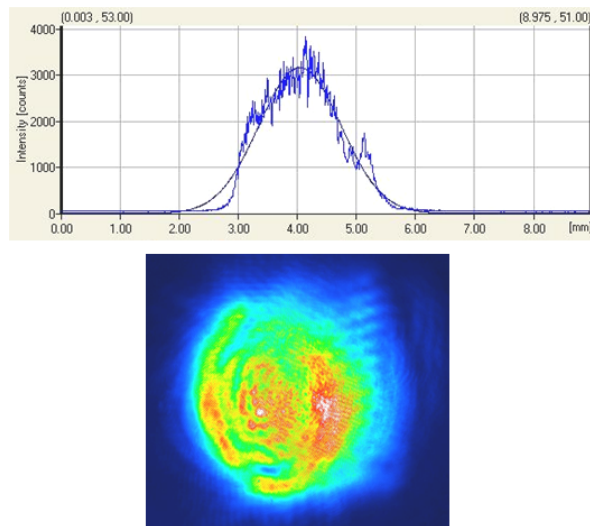


Figure 8.79.: Horizontal intensity cross-section of the primary beam (top) and the corresponding 2-D intensity beam profile for two interfering beams (bottom).

It can be clearly seen that there are some intensity peaks leading to an increased

energy input. Hence, the steel surface in those areas is intensely molten. Due to a temperature gradient between positions of maximum and minimum laser intensity, a surface tension gradient will be the consequence leading to a transfer of molten material away from the hot spots. In addition to optical microscopy, WLI measurements were performed in order to analyse the topography of the resulting pattern on the substrate and ball surface (see figure 7.80).

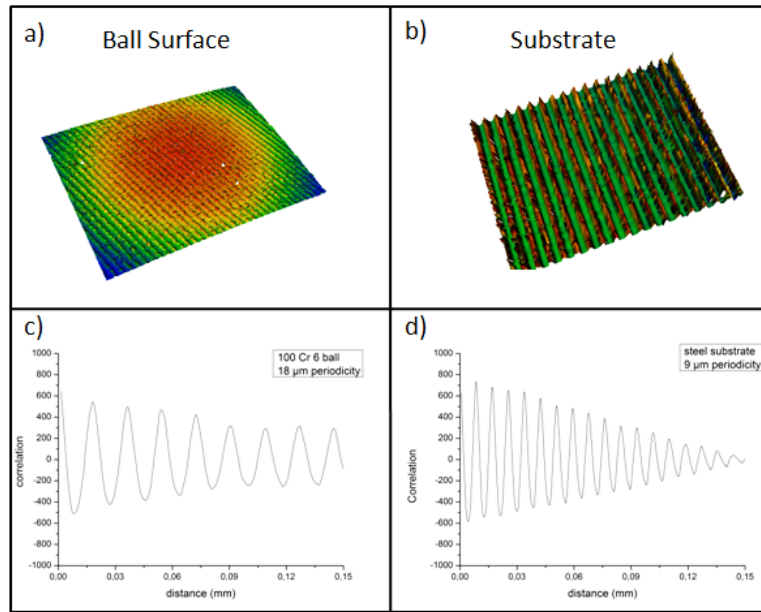


Figure 8.80.: 3-D plots of laser-patterned ball (a) and substrate (b) surface measured by WLI. Figures (c) and (d) show the related autocovariance plots.

Both surfaces show a homogeneous laser interference pattern. Autocovariance plots (see figures 7.80 (c) and (d)) are an indicator of the randomness of a surface. Usually, it is used to determine the periodicity of a surface. For periodic surfaces, the autocovariance plot has a characteristic sinusoidal shape related to the spatial frequencies of the respective surface. In the case of a random surface, the autocovariance function rapidly drops to zero and continues around the zero position. If the autocovariance function oscillates periodically, then the surface will exhibit some dominant spatial frequencies. The first abscissa intersection marks the correlation length. This is the minimum distance along the profile where one point has no relation to the next [69].

For the geometrical interlocking of the two patterned surfaces, the groove and asperity

8. Results and discussion

widths of the contact surfaces are essential. Figure 7.81 shows cross-section plots of a patterned steel substrate and a tribometer ball measured by WLI.

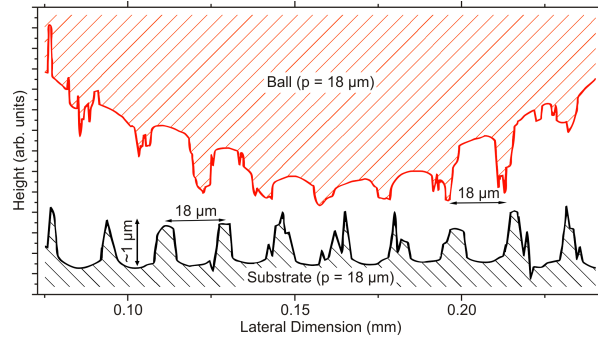


Figure 8.81.: Plots for a patterned steel substrate (black) and a 100 Cr 6 tribometer ball (red) measured by WLI [181].

The laser periodicity in both cases was set to $18 \mu\text{m}$ with a depth of around $1 \mu\text{m}$. The analysed groove widths of the profiles presented in figure 7.81 range from 12 to $14 \mu\text{m}$ in the upper part and 7 to $9 \mu\text{m}$ in the lower part of the structured substrate. In contrast, the asperity widths for both surfaces range between 3 and $10 \mu\text{m}$. Therefore, an interlocking of the structures based upon the topographic analysis is generally possible. Additionally, the line-patterns with varying line-spacing were studied with regard to surface profile parameters and compared to each other.

In particular, the slope roughness S_{rms} , the skewness R_{sk} , the kurtosis R_{ku} and the Swedish height H were determined by WLI. Figure 7.82 depicts the surface profile plots for the three different periodicities. The height deviations for a line-spacing of $5 \mu\text{m}$ are more pronounced than for the other periodicities. When decreasing the periodicity, the lateral thermal flow becomes more important thus setting a lower physical limit which is for most metals similar to the thermal diffusion length. If laser patterns with periodicities in the range of the thermal diffusion length are created, the thermal gradient between the positions of maximum and minimum laser intensity will be reduced. Consequently, the specific metal will be molten in both positions. According to Lasagni et al., the minimum achievable periodicity in stainless steel is about $1.3 \mu\text{m}$ [48]. Table 7.9 highlights the mentioned surface parameters. The rms value of the reference sample is relatively low compared to the laser-patterned surfaces. This is due to the mirror-like surface finish of the specimens. The Swedish height H is maximum for a periodicity of

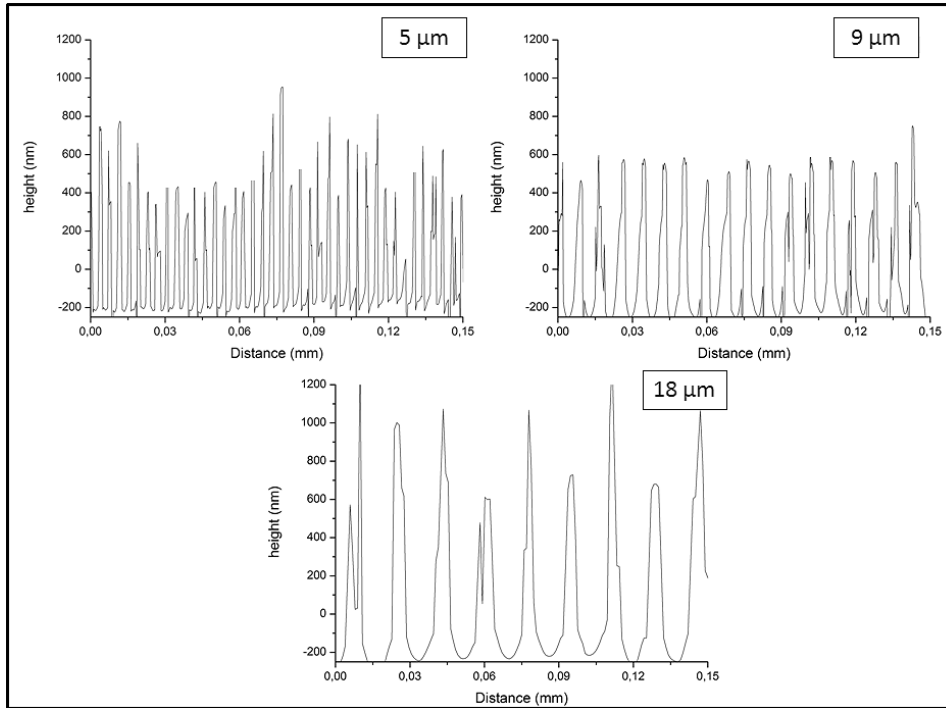


Figure 8.82.: Surface profile plots of laser-patterned steel surfaces measured by WLI. The periodicity of the line patterns was set to be 5, 9 and 18 μm [181].

18 μm being approximately 1.6 μm . There is a direct correlation between the structure depth and the used periodicity, already studied by Lasagni [46]. Usually, the structure depth increases for larger periodicities. This is attributed to the aforementioned thermal gradient which is generally smaller for lower periodicities. Furthermore, the reference specimen has a negative skewness indicating good bearing properties. In contrast, all laser-patterned surfaces show a positive value due to the reduced bearing capability. The highest positive value can be found for the sample with the largest line-spacing. Apart from the reference, the 9 μm pattern has the lowest positive R_{sk} value. A comparison with the corresponding cross-section profile plot reveals a very homogeneous laser-pattern. During the laser induced melting process, the material is shifted away from the intensity maximum towards the minimum positions. In case of larger line-spacings, the distance between the maximum and minimum positions is expanded and so the distance in between cannot be bridged by the molten material. As a consequence, additional topographic maxima may appear with different heights.

Considering the kurtosis, R_{ku} , it is interesting to observe that the 18 μm pattern shows a

Parameter	rms (nm)	S_{rms} ($\mu\text{m}/\text{mm}$)	H (nm)	R_{sk}	R_{ku}
Reference	34 ± 5	26.32 ± 4	94.45 ± 11	-1.50 ± 0.2	3.12 ± 0.8
5 μm	326 ± 12	626.44 ± 57	860 ± 49	0.84 ± 0.03	3.59 ± 0.26
9 μm	305 ± 6	484.89 ± 36	775 ± 11	0.52 ± 0.07	2.38 ± 0.19
18 μm	354 ± 34	218.05 ± 15	1164 ± 107	1.45 ± 0.13	5.30 ± 0.53

Table 8.9.: Surface profile parameters measured by WLI [181].

relatively high value of 5.52, although the 9 μm pattern seems to be more homogeneous according to figure 7.82.

The slope rms, S_{rms} , is listed for the various specimens. This parameter is particularly interesting because it represents the square-root of the second order spectral moment, which can be found in literature as $\sqrt{m_2}$ [19], and is proportional to the real area of contact [77]. As expected for similar structure depths, S_{rms} is highest for the smaller line-spacing.

8.4.3. Tribological properties

In asperity based models and for Persson's theory, a linear relationship between the real contact area and the load can be identified in the limit of small loads [77]:

$$A_c = \Lambda(E^* \sqrt{2m_2})^{-1} F_N \quad (8.29)$$

where Λ represents a numerical factor being $\sqrt{2\pi}$ for multi-asperity contact theories and $\sqrt{8/\pi}$ for Persson's theory, E^* the reduced Young's modulus, $\sqrt{m_2}$ the respective mean square slope and F_N the applied normal force [77].

Assuming a simple Hertzian contact without adhesion, one can roughly estimate the contact area and pressure for the given contact pairs. Strictly speaking, the Hertzian contact model is only valid for flat surfaces without textures. Therefore, the following theoretical considerations are only rough approximations.

The reduced elastic modulus for the steel pair can be determined to be 112.57 GPa. Using the Hertzian contact formula and the respective values for the normal load (1 mN) and the ball radius (1.5 mm), the corresponding contact radius is 2.15 μm coming up to a contact area of 14.56 μm^2 . The maximum Hertzian pressure is 0.16 GPa. This is well below the yield strength of a typical austenitic stainless steel such as 1.4301 at 0.7 GPa [147]. Despite that, wear tracks of the patterned steel surfaces for relative alignments

of 0° and 90° will be presented in the next paragraph revealing that plastic deformation actually takes place. This may be explained by local stress concentrations at the laser-induced asperities. The corresponding area of contact is much smaller and thus the local pressure could easily exceed the yield strength of the material. In addition, a comparison between the Hertzian contact, multi-asperity models and Persson's theory is listed in table 7.10.

Model	Hertz	Multi-Asperity	Persson
Reference	$14.56 \mu m^2$	$0.95 \mu m^2$	$0.59 \mu m^2$
$5 \mu m$	$14.56 \mu m^2$	$0.016 \mu m^2$	$0.04 \mu m^2$
$9 \mu m$	$14.56 \mu m^2$	$0.08 \mu m^2$	$0.05 \mu m^2$
$18 \mu m$	$14.56 \mu m^2$	$0.18 \mu m^2$	$0.12 \mu m^2$

Table 8.10.: Comparison of contact area according to Hertz, multi-asperity based models and Persson's theory for the steel reference and the different laser pattern.

As can be seen, there are large differences between the Hertzian contact and the multi-asperity as well as Persson-based model. The Hertzian approach does not take any surface profile information into account. Because of that, the calculated areas of contact are much smaller than in the Hertzian case. On the other hand, it is important to note, that the study of different wear tracks revealed a larger area of contact which is closer to the results of the Hertzian model. Again, the use of equation 7.29 is based upon several simplifications. In reality, one should also consider the surface parameters of the counter body, which is not the case here. However, the results offer a general idea about the tendency of the contact area for different line-spacings. In this context, the calculated contact area increases with a rising line-spacing which may be traced back to a smaller S_{rms} value (see equation 7.29).

8. Results and discussion

For a better understanding of the tribological kinematics and the relative alignment of the contacting bodies, figures 7.83 (a) and (b) depict a 3-D view of the structured steel sample and the tribometer ball. The sliding velocity was kept constant at 1 mm/s. The labelling $0^\circ/90^\circ$ denotes the angle between the structures and the black arrow indicating the sliding direction in our experiments. In addition, the friction coefficient μ as a function of sliding time for two different periodicities is shown in figures 7.83 (c) and (d).

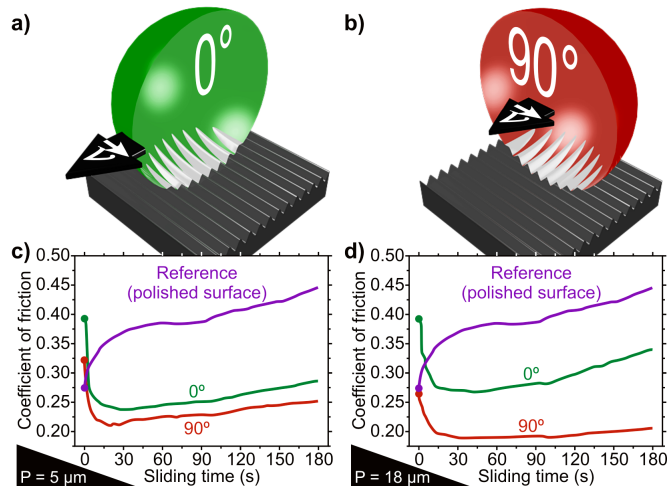


Figure 8.83.: (a) and (b) display a 3-D view of the relative alignment and sliding direction of the patterned contacting surfaces. Insets (c) and (d) show the temporal evolution of μ for different alignments and periodicities. The black arrows indicate the sliding direction [181].

The displayed curves in figures 7.83 (c) and (d) are averaged plots of the friction coefficient of forward and backward strokes. After having exceeded the initial static friction, μ for the polished reference surface is larger than that of the patterned specimens independent of the relative alignment between the rubbing partners. A closer look at the orientation of the surfaces reveals that both results demonstrate a lower μ for a 90° alignment. This is consistent with a structural incompatibility compared to the 0° alignment [57]. Due to the potential geometrical interlocking for 0° , the initial μ is considerably higher ($\mu \approx 0.4$) than the static friction coefficient of the reference ($\mu \approx 0.27$). A closer look at the resulting wear scars for the two different sliding directions ($0^\circ/90^\circ$) is shown in figure 7.84. As expected in the case of 0° alignment, the wear track is more pronounced whereas for an angle of 90° , only distinct contact points can be seen. The

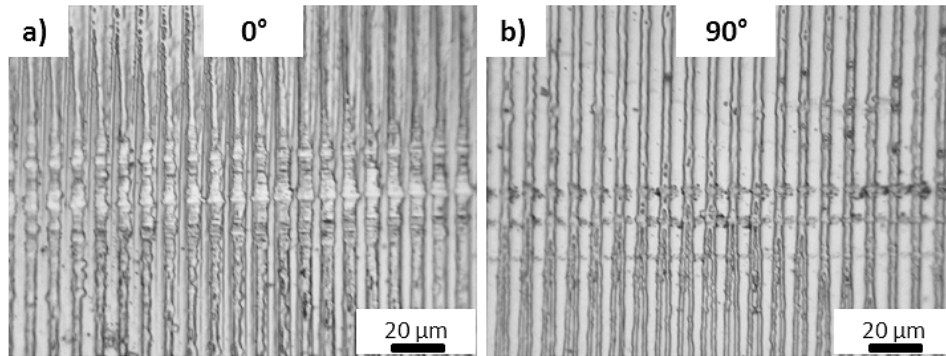


Figure 8.84.: Light microscopic image of wear tracks with a 0° orientation between substrate and ball (a) and 90° (b) [181].

vertical distance of the contact points is equal to the respective periodicity, here $9\ \mu\text{m}$. A comparison of figures (c) and (d) implies a strong effect of the different periodicities. The temporal evolution of μ for the 0° orientation is demonstrated in figure 7.85 for three different line-spacings (5 , 9 and $18\ \mu\text{m}$).

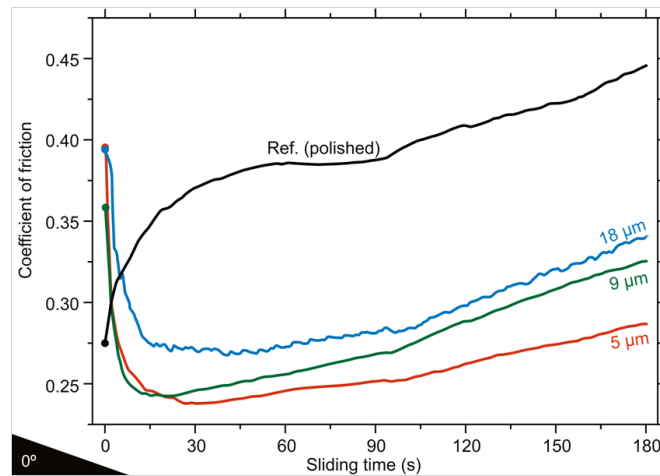


Figure 8.85.: Coefficient of friction over sliding time for three distinct line-spacings at 0° orientation [181].

The coefficients of friction of all the structured specimens are initially higher than the value for the pristine surface. The reference value starts at about 0.27 and increases with sliding time. This increase of μ over the sliding time can be divided into two parts with differing slopes. Focused ion beam cross-sections have revealed the existence of a native oxide layer ($\approx 26\ \text{nm}$) on top of the reference material. It can be expected

that the oxide layer thickness can be modified by the laser treatment. Moreover, during sliding, oxide particles are created and shifted to the reversal points of the slider thus accumulating the particles at the end of the wear track. It is known from literature that the steel-steel friction coefficient is smaller with oxide layers on top (typically 0.27) than without under dry and clean conditions (≈ 0.80) [182]. In contrast, the initial μ for the structured samples is approximately 30 % higher. During the run-in regime, this can be traced back to a larger mean-square slope of the patterned surfaces which is in leading order inversely proportional to the real area of contact [76][77] and to the interlocking at the beginning. Afterwards, μ decreases independent of the used periodicity. On the one hand, this decline after some run-in can be explained by a gradual degradation of the laser patterns and thus an inefficient, hindered interlocking of the contacting bodies. The local properties of the patterned specimens become similar to those of the reference. On the other hand, velocity effects during the linear reciprocating sliding might also contribute to the observed decrease in μ because of the topographic scale and the experimental velocity regime. The subsequent increase is attributed to further flattening of the respective structures causing a larger real contact area which is directly proportional to the frictional force (see figure 7.86).

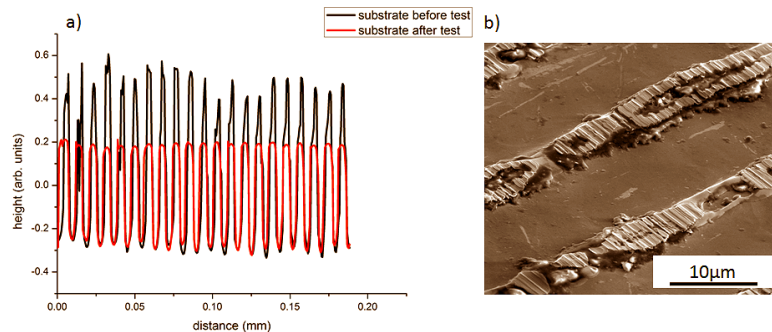


Figure 8.86.: Comparison of a laser-induced surface profile before and after sliding at a 0° orientation measured by WLI in (a). Figure (b) shows a SEM image of the worn surface pattern under a tilt angle of 52° [181].

In figure 7.86, a direct comparison of the laser-induced surface profile is presented before and after sliding. The profile amplitude after sliding is visibly reduced and the profile looks more flattened after the sliding deformation.

The local friction-load relationship then is $\tau_s = \sigma_0 + \alpha_p \sigma_N$, where τ_s and σ_N denote shear

and normal stress, respectively, whereas the system-dependent σ_0 and α_p stand for the offset and the proportionality coefficient [2]. This constitutive relation holds all the way down to the nanometre scale in the presence of lubricants or contaminants with values in the order of 0.1 [56]. This leads to a reduced but not vanishing friction.

8.4.4. Microstructural and mechanical characterisation

The pristine steel surface is shown in figure 7.87.

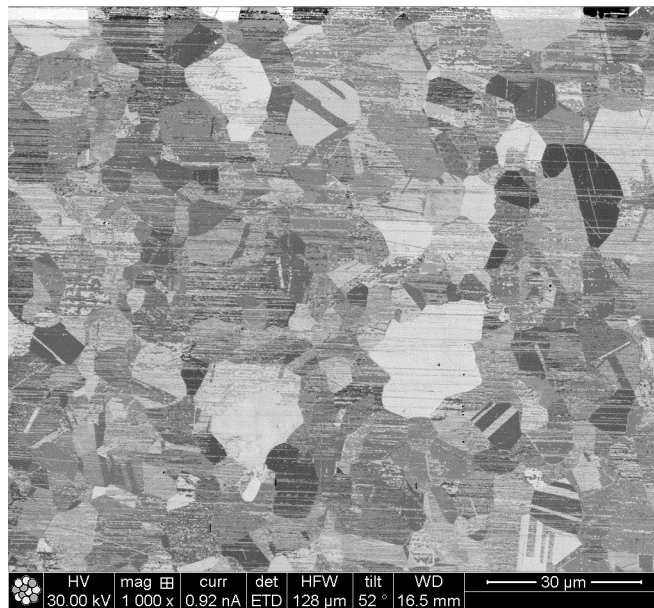


Figure 8.87.: SEM/FIB image of pristine steel surface (1.4301). The image was recorded by means of ion channeling contrast [181].

There are still some polishing artefacts visible. Despite the polishing marks, a coarse-grained microstructure is revealed by using ion channeling contrast. A direct comparison with a laser treated sample surface does not disclose any considerable difference in the positions of maximum laser intensity (see figure 7.88). Due to the relatively coarse grains, the resolidifying microstructure adapts the original one. This can be seen more clearly in a corresponding FIB cross-section (figure 7.89).

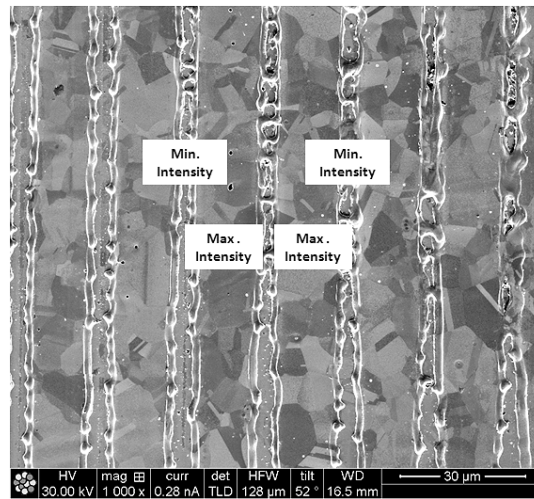


Figure 8.88.: SEM/FIB image of a laser-patterned steel surface [181].

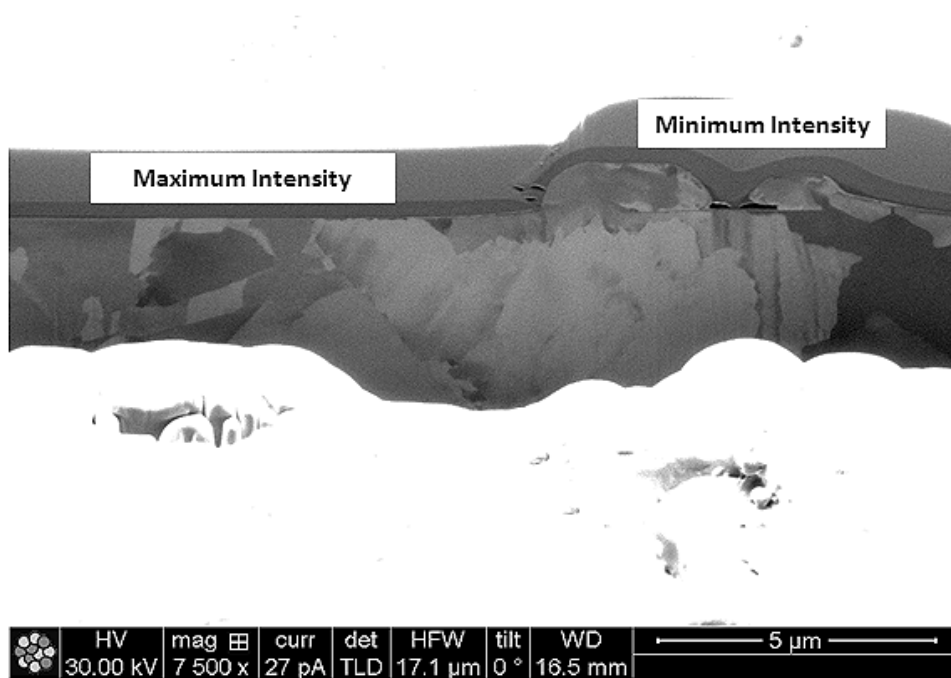


Figure 8.89.: FIB cross-section of a steel surface after laser-patterning [181].

Even in the positions of maximum laser intensity, the grain structure is apparently not affected. Austenitic stainless steels are generally composed of the metastable γ -phase [180]. Thermal simulations were performed for the chosen line-spacings which have not shown any strong difference. Accordingly, the maximum temperature was approximately

8. Results and discussion

1900 K, clearly above the corresponding melting range of the used steel 1.4301 (between 1693 and 1747 K [112]).

Furthermore, nanoindentation experiments (*Group of Prof. Dr. H. Vehoff, Saarland University*) were done measuring the hardness in the positions of maximum laser intensity and in the unpatterned reference regions. A Berkovich (three-sided pyramidal tip, 142.3°) diamond indenter was used, carefully calibrated for its area function on standard material. The loading profile included three segments: loading to a $300\ \mu\text{N}$ peak load within 5 s; holding at the peak load for 15 s; unloading back to zero load in 5 s. No considerable thermal drift during the measurements was observed. The loading rate for all indents was set to $60\ \mu\text{N/s}$. Figure 7.90 shows the results of the hardness measurement for the polished reference and the laser patterned surface. Here, only topographic minima, representing the laser intensity maxima could be indented. Due to the melting process, the laser intensity minima are quite inhomogeneous and too narrow to be indented.

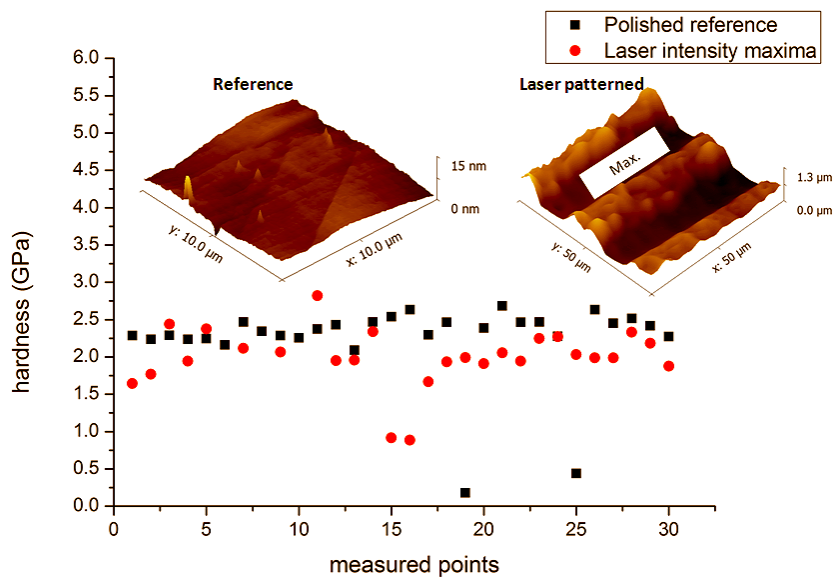


Figure 8.90.: Measured hardness of the reference and laser-patterned specimen surfaces with corresponding 3-D surface plots recorded by a Hysitron tribo-indenter. Only measurement points for the laser intensity maxima positions (topographic minima) are displayed [181].

Despite some scattering, most of the values are similar and thus consistent with the previous SEM images. The average hardness value and standard deviation for the reference is 2.24 ± 0.55 GPa and for the patterned specimen 2.45 ± 0.62 GPa.

Regarding the tribological behaviour of austenitic stainless steels, it can be stated that mechanical deformation very often involves the formation of strain induced ϵ -martensite [180]. According to Hübner et al. the martensitic transformation might occur by shear deformation of the lattice [183]. During sliding, the dislocation density increases and as a consequence, so does the stacking fault density. These steels have a relatively low stacking fault energy of about 18 mJ/cm^2 which is comparable to Ag (see table 7.1) [184]. As already discussed, the stacking fault energy has a significant impact on the mechanical behaviour [185]. Like ϵ -martensite, the formed stacking faults are of hexagonal symmetry and thus finally pile up to form ϵ -martensite [183].

Remarkable work in this field has also been published by Rigney and Hirth. Rigney reported about the occurrence of large plastic strain fields during sliding deformation resulting in a strong rise of dislocations which organise themselves in dislocation cell structures [186]. Typical values for dislocation densities after sliding contact of ductile metals are in the range of 10^{15} 1/m^2 which is consistent with simulation results from Kuhlmann-Wilsdorf [186][187].

Besides the mainly presented topographic analysis, further experimental work is necessary to study the influence of dislocations and stacking faults on the friction behaviour of the used steel. In particular, high resolution techniques such as TEM will be important for the detailed investigation.

In addition, methods sensitive to the surface chemistry e.g. Raman spectroscopy or XPS will be applied to study the observed passivation layer on top of the specimens.

Part III.

Summary and outlook

The presented thesis highlights the possibility of significantly influencing the tribological properties of sliding metallic surfaces by laser interference metallurgy. It could be shown that this technique has a high potential in creating precisely defined topographies and microstructures in thin metallic films and bulk metals. In particular, lateral periodic grain size arrangements and intermetallic phase composites were induced in metallic films.

In addition, a successful combination of two different patterning techniques, micro-coining and laser interference metallurgy, was demonstrated for bulk aluminium and the tribological properties of the as-fabricated specimens studied in detail.

Finally, the geometrical interlocking of patterned steel surfaces was investigated for different pattern alignments and periodicities.

The main findings of the chapter *results and discussion* will be summarised separately for each section.

In section 7.1, the basic idea was the formation of long-range ordered grain size arrangements in Au-, Pt- and W-thin films and to study the effectiveness of laser-patterned Au films under dry sliding conditions.

- The results show that grain size architectures in different metallic films can be produced by laser interference and that the grain growth regime as well as the micro-texture strongly depend on the film thickness, the laser fluence and the used pattern periodicity. Particularly, at higher fluence values at which the films are nearly completely molten, super lateral grain growth with large needle-shaped grains in the positions of maximum laser intensity occurs.

There is a good correlation between the simulation and the experimental results. Differences in temperature up to 3000 K were observed according to the thermal simulations at high laser intensities. In contrast, the simulations at lower laser intensities indicate that the films are only partially molten which can explain the vertical resolidification process. In the case of W, also round-shaped grains appear in the centre of the interference maximum due to a deep supercooling and spontaneous nucleation of the film.

- With respect to the tribological properties, the skewness R_{sk} has proved to be a suitable parameter to describe the laser-induced surface profiles. The more negative the skewness is (surfaces are more plateau-like), the more reduced the resulting wear volume. In this sense, calculated plasticity indices according to the Greenwood-Williamson approach also revealed low values for surfaces with a largely negative skewness which is consistent with experimental results. However, the measured friction coefficients do not show such a clear tendency as a function of skewness. This might be attributed to further microstructural effects which play an important role in the frictional response. It could be seen that periodicities in the range of the thermal diffusion length (for gold approximately $2\ \mu\text{m}$) lead to a complete grain growth after laser patterning even in the positions of minimum laser intensity. Finally, a definite separation of microstructural and topographic contributions in this case is not possible.
- Further simulations based upon the Greenwood-Williamson model elucidated that the number of laser induced asperities are directly related to the selected pattern periodicity. A decreasing periodicity results in a higher number of asperities in the contact. In contrast, the total area of contact parallelly increases with rising periodicity. This can be traced back to the more plateau-like surfaces with negative skewness values. Additionally, as could be expected, the contact pressure increased with a larger aspect ratio of the laser pattern.

Section 7.2 aimed at the study of the formation of intermetallic phase composites in TiAl multilayer and their resulting tribo-mechanical properties.

- Three different laser fluence regimes (A, B and C) could be identified for the laser processing of TiAl multilayer. In regime A at lower fluences ($< 70\ \text{mJ}/\text{cm}^2$), a vanishing topography with very small impact on microstructure is visible. With increasing fluence in regime B ($70\text{-}220\ \text{mJ}/\text{cm}^2$), the resulting topography is very shallow and melting and as well as mixing of layers occur. Finally, regime C is representative for higher fluences ($220\text{-}476\ \text{mJ}/\text{cm}^2$). Here, the structure depth significantly increases up to a maximum value of $180\ \text{nm}$ with the multilayer being partially ablated from the substrate. The laser-induced reaction zone may extend over the entire film thickness. In this context, XRD and TEM verified the formation of the metastable bcc β -Ti phase in regime B. For much higher laser fluences

in regime C, the existence of intermetallic phases in the laser intensity maxima, namely Ti_3Al and Ti_2Al , could be confirmed.

- The formation of these aforementioned intermetallic phases has a significant impact on the mechanical properties such as hardness of the multilayer. Nanoindentation measurements have validated that the hardness in the intensity maxima increases up to a factor of two compared to the nearly unaffected surrounding. Parallely, the reduced elastic modulus varies position-dependent for the maxima and minima regions thus supporting the XRD and TEM results.
- The thermal simulation revealed that the maximum achievable temperatures as well as the melt duration in the intensity maxima during the laser process are highly depending on the corresponding laser periodicity. Up to a periodicity of around $8\ \mu\text{m}$, the temperature and melt duration rise and then saturate.
- The friction coefficient is nearly independent of the used periodicity in the moderate fluence regime B which is attributed to a nearly vanishing topography and only slight microstructural changes.

With respect to the measured wear volume, it can be outlined that there is a strong relationship between the sliding direction and laser line-pattern (parallel or perpendicular to the respective lines). In fluence regime B, only a perpendicular arrangement showed a reduction of the wear volume for a line-spacing of $12\ \mu\text{m}$ compared to the other specimens. It could be demonstrated by WLI that wear debris is effectively trapped in the structural recessions thus avoiding abrasive wear contributions.

Moreover, in fluence regime C, the localised formation of intermetallic phases leads to a further reduction in the wear volume of around 34% for a perpendicular alignment.

Furthermore, in section **7.3** the idea of hierarchically patterned surfaces by a combined processing of micro-coining and laser interference patterning was introduced. At first, the process limits of LIMET with regard to the patterning of bulk aluminium surfaces were studied and tribological experiments under dry sliding performed.

- The results figure out that laser-textured aluminium surfaces also exhibit a pronounced dependence of the friction coefficient on the sliding direction and the used

line-spacing. For a parallel orientation between laser lines and sliding direction, the periodicity dependence is less pronounced because there is nearly no topography change along this direction. In contrast, the friction coefficient is significantly influenced in the perpendicular case. Lower periodicities also result in less oscillating friction curves and finally lower μ -values. This is different to the observations for gold films. It is expected that due to the thin film situation accompanied by a larger surface-to-volume ratio and a completely deviating microstructure compared to the bulk aluminium, this may be responsible for the current findings. The problem is principally based upon the fact that μ is highly system-dependent and influenced by various factors.

According to previous simulation results for laser-patterned Au films, the same tendency for the number of asperities in contact and the total contact area can be found in the case of bulk aluminium.

In addition, the process combination was studied with regard to process sequence, roughness and coining geometry. The following results could be obtained.

- Due to the high required coining forces, the laser-pattern will be completely destroyed if the laser treatment is performed before micro-coining. Therefore, a preliminary micro-coining of the specimens is necessary to achieve homogeneous patterning results.
- The roughness of the reference material and the tool-sets should be smaller than the used line-spacing in order to create well-defined topographies.
- Depending on the respective laser fluence threshold of the used materials, there exists a critical flank angle of the coined surfaces for which the flanks can be homogeneously laser-patterned. In the case of aluminium, this critical flank angle was determined theoretically and experimentally to be 25° .
- Finally, the hierarchically-patterned aluminium surfaces were tested under oil lubrication and compared to the different reference situations (unpatterned, laser-treated and only micro-coined). The results highlight the beneficial effects of the hierarchical structure regarding the lubrication lifetime in the contact which is strongly enhanced by a factor of approximately 14 in comparison to the unpatterned reference.

In the last section of the thesis 7.4, the geometrical interlocking of two laser-patterned austenitic stainless steel surfaces and the consequences on the tribological behaviour were investigated.

- In a good agreement with the previous results, μ is again mainly influenced by the orientation of the two-patterned surfaces ($0^\circ/90^\circ$) to each other and the chosen line-spacing which was kept constant for both contacting bodies at 5, 9 and 18 μm .
- As expected, the friction coefficient is higher for a parallel alignment between the two line-pattern of the sliding partners due to geometrical interlocking compared to the 90° orientation with only partial interacting points.
- Moreover, μ follows the same trend as in the case of the aluminium bulk surfaces. Higher periodicities lead to higher values of μ because of larger contacting areas. This is also consistent with the measured values of the slope rms, S_{rms} , which is inversely proportional to the real area of contact. Patterned surfaces with larger periodicities have smaller S_{rms} -values and thus an enhanced contact area.

Part IV.

Appendix

Bibliography

- [1] A. KHAMLIHI. *International Journal of Physical Sciences*, 3:065–070, 2008.
- [2] F.P. BOWDEN AND D. TABOR. *Nature*, 15:197–199, 1942.
- [3] M. URBAKH, J. KLAFTER, D. GOURDON AND J. ISRAELACHVILI. *Nature*, 430:525, 2004.
- [4] I.F. SANTOS. *Tribology Transactions*, 38:700–706, 1995.
- [5] C. SUBRAMANIAN AND K.N. STRAFFORD. *Wear*, 165:85–95, 1993.
- [6] A.A. VOEVODIN AND J.S. ZABINSKI. *Thin Solid Films*, 370:223–231, 2000.
- [7] K. HOLMBERG, A. MATTHEWS AND H. RONKAINEN. *Tribology International*, 31:107–120, 1998.
- [8] A. ERDEMIR. *Tribology International*, 38:249–256, 2005.
- [9] I. ETSION. *Transactions of the ASME*, 127:248–253, 2005.
- [10] U. PETTERSSON: *Surfaces Designed for High and Low Friction*. PhD Thesis, Uppsala University Sweden, 2005.
- [11] D.B. HAMILTON, J.A. WALOWIT AND C.M. ALLEN. *ASME Journal of Basic Engineering*, 88:177–185, 1966.
- [12] N.P. SUH, M. MOSLEH AND P.S. HOWARD. *Wear*, 175:151–158, 1994.
- [13] A. VOLCHOK, G. HALPERIN AND I. ETSION. *Wear*, 253:509–515, 2002.
- [14] I. ETSION. *Tribology Letters*, 17:733–737, 2004.

Bibliography

- [15] X. WANG, W. LIU, F. ZHOU AND D. ZHU. *Tribology International*, 42:1118–1123, 2009.
- [16] H. L. COSTA AND I.M. HUTCHINGS. *Tribology International*, 40:1227–1238, 2007.
- [17] M. WAKUDA. *Wear*, 254:356–363, 2003.
- [18] P. ANDERSSON, J. KOSKINEN, S. VARJUS, Y. GERBIG, H. HAEFKE, S. GEORGIU, B. ZHMUD AND W. BUSS. *Wear*, 262:369–379.
- [19] T. NANBU. *Tribology Letters*, 29:241–252, 2008.
- [20] R.B. SIRIPURAM AND L.S. STEPHENS. *Journal of Tribology*, 126:527–534, 2004.
- [21] H. ISHIHARA, H. YAMAGAMI, T. SUMIYA, T. OKUDERA, M. INADA AND A. TERADA. *Wear*, 172:65–72, 1994.
- [22] R. RANJAN, D.N. LAMBETH, M. TROMEL, P. GOGLIA AND Y. LI. *Journal of Applied Physics*, 69:5745–5747, 1991.
- [23] L. RAPOPORT, A. MOSHKOVICH, V. PERFILYEV, I. LAPSKER, G. HALPERIN, Y. ITOVICH AND I. ETSION. *Surface and Coatings Technology*, 202:3332–3340, 2008.
- [24] M. NOSONOVSKY AND B. BHUSHAN. *Materials Science and Engineering Reports*, 58:162–193, 2007.
- [25] S.K. CHILAMAKURI AND B. BHUSHAN. *Tribological Transactions*, 40:303–311, 1997.
- [26] A. BORGHI, E. GUALTIERI, D. MARCHETTO, L. MORETTI AND S. VALERI. *Wear*, 265:1046–1051, 2008.
- [27] M.K. KELLY. *Physica Status Solidi (a)*, 166:651–657, 1998.
- [28] F. MÜCKLICH, A. LASAGNI AND C. DANIEL. *International Journal of Materials Research*, 97:1337–1344, 2006.
- [29] C. DANIEL AND F. MÜCKLICH. *Applied Surface Science*, 242:140, 2005.
- [30] C. GACHOT. *Applied Surface Science*, 255:5626, 2009.

- [31] W.M. STEEN: *Laser Material Processing*. Springer, London Limited, 2003.
- [32] H. HÜGEL AND T. GRAF: *Laser in der Fertigung*. Vieweg + Teubner, Wiesbaden, 2009.
- [33] F. KLOCKE AND W. KÖNIG: *Fertigungsverfahren-Abtragen, Generieren und Lasermaterialbearbeitung*. Springer Verlag, Berlin Heidelberg, 2007.
- [34] SPECTRA PHYSICS: *Laser Description Manual Quanta Ray Pro 290*, 2006.
- [35] M. MALDOVAN AND E.L. THOMAS: *Periodic Materials and Interference Lithography*. Wiley-VCH, Weinheim, 2009.
- [36] M. DRESSEL AND G. GRÜNER: *Electrodynamics of Solids*. Cambridge University Press, Cambridge, UK, 2002.
- [37] M. VON ALLMEN: *Laser-Beam Interactions with Materials*. Springer, Berlin, Germany, 1995.
- [38] P. DRUDE. *Annalen der Physik*, 1:566–613, 1900.
- [39] G.A. BOLOSHIN. *Opt. Spectry USSR*, 18:423, 1965.
- [40] K. UJIHARA. *Journal of Applied Physics*, 43:2376–2383, 1972.
- [41] R. FRANZ AND G. WIEDEMANN. *Annalen der Physik*, 165:497–531, 1853.
- [42] CH. KITTEL: *Einführung in die Festkörperphysik*. Oldenbourg Verlag, München-Wien, 2002.
- [43] L.K. ANG, Y.Y. LAU, R.M. GILGENBACH AND H.L. SPINDLER. *Applied Physics Letters*, 70:696–698, 1997.
- [44] M. BORN AND E. WOLF: *Principles of Optics*. Cambridge University Press, Cambridge UK, 1999.
- [45] E. HECHT: *Optik*. Oldenbourg, München, 2009.
- [46] A.F. LASAGNI: *Advanced design of periodical structures by laser interference metallurgy in the micro/nano scale on macroscopic areas*. PhD Thesis, Saarland University, Saarbrücken, Germany, 2006.

- [47] F.P. INCOPRERA AND D.P. DE WITT: *Fundamentals of heat and mass transfer 3rd Edition*. John Wiley and Sons, New York, 1990.
- [48] A. LASAGNI, M.D´ALESSANDRIA, R. GIOVANELLI AND F. MÜCKLICH. *Applied Surface Science*, 254:930–936, 2007.
- [49] H. SPIKES: *Tribology Notes*. Imperial College London UK, 2011.
- [50] D. TABOR. *Proceedings of the Royal Society of London*, A251:378–393, 1959.
- [51] M.H. MÜSER. *Physical Review B*, 84:125419, 2011.
- [52] L. PRANDTL. *Reine Angewandte Mathematik*, 8:85, 1928.
- [53] D. DOWSON: *History of Tribology*. Longman, New York, 1979.
- [54] M. HIRANO, K. SHINJO, R. KANEKO AND Y. MURATA. *Physical Review Letters*, 67:2642–2645, 1991.
- [55] M. HIRANO. *Wear*, 254:932–940, 2003.
- [56] G. HE, M.O. ROBBINS AND M.H. MÜSER. *Science*, 284:1650, 1999.
- [57] M.H. MÜSER. *Physik Journal*, 2:43–48, 2003.
- [58] U. TARTAGLINO, V.N. SAMOILOV AND B.N.J. PERSSON. *Journal of Physics Condensed Matter*, 18:4143–4160, 2006.
- [59] M. DIENWIEBEL, N. PRADEEP, G.S. VERHOEVEN, H.W. ZANDBERGEN AND J.W.M. FRENKEN. *Surface Science*, 576:197–211, 2005.
- [60] J. SONDDHAUSS, H. FUCHS AND A. SCHIRMEISEN. *Tribology Letters*, 42:319–324, 2011.
- [61] M.H. MÜSER. *Europhysics Letters*, 66:97–103, 2004.
- [62] W. WANG, H. CHEN, Y. HU AND H. WANG. *Tribology International*, 39:522–527, 2006.
- [63] D. ZHU. *Tribology Transactions*, 46:44–48, 2003.

Bibliography

- [64] R.S. SAYLES AND T.R. THOMAS. *International Journal of Production Research*, 14:641–655, 1976.
- [65] D.J. WHITEHOUSE: *Handbook of surface metrology*. Institute of Physics Publishing, Bristol, 1994.
- [66] ASM METALS HANDBOOK: *Friction, Lubrication and Wear Technology*. ASM International, USA, 1992.
- [67] M. WIELAND, P. HÄNGGI, W. HOTZ, M. TEXTOR, B.A. KELLER AND N.D. SPENCER. *Wear*, 237:231–252, 2000.
- [68] R.S. SAYLES AND T.R. THOMAS. *Nature*, 271:431–434, 1978.
- [69] ZYGO CORPORATION: *MetroPro Reference Guide*. Connecticut, USA, 2006.
- [70] E.S. GADELMAWLA, M.M. KOURA, T.M.A. MAKSOD, I.M. ELEWA AND H.H. SOLIMAN. *Journal of Materials Processing Technology*, 123:133–145, 2002.
- [71] G. NIEMANN: *Maschinenelemente Band 1: Konstruktion und Berechnung von Verbindungen, Lagern und Wellen*. Springer Verlag, Berlin Heidelberg, 2005.
- [72] E.J. ABBOTT AND F.A. FIRESTONE. *Mechanical Engineering*, 55:569–572, 1933.
- [73] M. BIGERELLE AND A. IOST. *Tribology International*, 40:1319–1334, 2007.
- [74] D. NOWELL. *Strain*, 46:213–214, 2010.
- [75] J.A. GREENWOOD AND J.B.P. WILLIAMSON. *Proceedings of the Royal Society of London*, A295:300–319, 1966.
- [76] B.N.J. PERSSON. *Journal of Chemical Physics*, 115:3840, 2001.
- [77] G. CARBONE AND F. BOTTIGLIONE. *Journal of the Mechanics and Physics of Solids*, 56:2555–2572, 2008.
- [78] J.I. MCCOOL. *Wear*, 107:37–60, 1986.
- [79] P.R. NAYAK. *Journal of Lubrication Technologies*, 93:398–407, 1971.
- [80] J.A. GREENWOOD. *Wear*, 261:191–200, 2006.

Bibliography

- [81] R.W. CARPICK, D.F. OGLETREE AND M. SALMERON. *Journal of Colloid and Interphase Science*, 211:395–400, 1999.
- [82] J.A. GREENWOOD. *Proceedings of the Royal Society of London A*, 453:1277, 1997.
- [83] D. MAUGIS. *Journal of Colloid Interface Science*, 150:243, 1992.
- [84] V.L. POPOV: *Kontaktmechanik und Reibung*. Springer, Berlin Heidelberg, 2011.
- [85] H. HERTZ. *Reine Angewandte Mathematik*, 92:156, 1882.
- [86] D. TABOR: *The hardness of metals*. Oxford University Press, Oxford, UK, 1951.
- [87] L. DETERS: *Konstruktionselemente des Maschinenbaus*. Springer Verlag, Springer Verlag Berlin Heidelberg, 2008.
- [88] H. CZICHOS AND K.H. HABIG: *Tribologie-Handbuch*. Vieweg und Sohn Verlag, Wiesbaden, 2003.
- [89] J.A. VENABLES AND C.J. HARLAND. *Philosophical Magazine*, 27:1193, 1973.
- [90] D.J. DINGLEY, M. LONGDEN, M. WEINBREN AND J. ALDERMAN. *Scanning Microscopy*, 1:451, 1987.
- [91] P. DE GROOT AND L. DECK. *Journal of Modern Optics*, 42:389–401, 1995.
- [92] K.G. LARKIN. *Journal of the Optical Society of America A*, 13:832–843, 1996.
- [93] P. NAGY, B. VERÖ, G. PÁLINKÁSA AND E. KÁLMÁN. *Materials Science Forum*, 414-415:297–304, 2003.
- [94] D. FLYNN AND M. DESMULLIEZ. *Journal of Physics: Conference Series*, 34:112–117, 2006.
- [95] P.A. LISSBERGER. *Reports on Progress in Physics*, 33:197–268, 1970.
- [96] A.G. EVANS, M.Y. HE AND J.W. HUTCHINSON. *Progress in Materials Science*, 46:249–271, 2001.
- [97] U. SCHMID AND H. SEIDEL. *Thin Solid Films*, 516:898–906, 2008.

Bibliography

- [98] U. SCHMID AND H. SEIDEL. *Journal of Vacuum Science and Technology*, A24:6, 2006.
- [99] R.B. BERGMANN, J. KÖHLER, R. DASSOW, C. ZACZEK AND J.H. WERNER. *Physica Status Solidi (a)*, 166:587–602, 1998.
- [100] J.S. IM, M.A. COWDER, R.S. SPOSILI, J.P. LEONARD, H.J. KIM, J.H. YOON, V.V. GUPTA, H. JIN SONG AND H.S. CHO. *Physica Status Solidi (a)*, 166:603–617, 1998.
- [101] G. AICHMAYR, D. TOET, M. MULATO, P.V. SANTOS, A. SPANGENBERG, S. CHRISTIANSEN, M. ALBRECHT AND H.P. STRUNK. *Physica Status Solidi (a)*, 166:659–666, 1998.
- [102] G. AICHMAYR. *Journal of Applied Physics*, 85:4010–4023, 1999.
- [103] F. MÜCKLICH, A. LASAGNI AND C. DANIEL. *Intermetallics*, 13:437–442, 2005.
- [104] A. LASAGNI, M. NEJATI, R. CLASEN AND F. MÜCKLICH. *Advanced Engineering Materials*, 8:580–584, 2006.
- [105] F. YU, F. MÜCKLICH, P. LI, H. SHEN, S. MATHUR, C.M. LEHR AND U. BAKOWSKY. *Biomacromolecules*, 6:1160–1167, 2005.
- [106] A. LASAGNI AND F. MÜCKLICH. *Journal of Materials Processing Technology*, 209:202–209, 2009.
- [107] V.V. GUPTA, H. SIN JONG AND J.S. IM. *Applied Physics Letters*, 71:99–101, 1997.
- [108] S.C. TJONG AND H. CHEN. *Materials Science and Engineering R*, 45:1–88, 2004.
- [109] Z. ZHONG AND X. WANG. *Journal of Applied Physics*, 100:044310, 2006.
- [110] G. GOTTSTEIN: *Physikalische Grundlagen der Materialkunde*. Springer Verlag, Berlin Heidelberg, 2007.
- [111] B. FENG, Z. LI AND X. ZHANG. *Journal of Physics D: Applied Physics*, 42:055311, 2009.

Bibliography

- [112] W.M. HAYNES AND D.R. LYDE: *Handbook of Chemistry and Physics*. CRC Press, CRC Press, Taylor and Francis Group, Boca Raton, 2010.
- [113] S. KIBEY, J.B. LIU, D.D. JOHNSON AND H. SEHITOGLU. *Acta Materialia*, 55:6843–6851, 2007.
- [114] A.H. CLAUER, J.H. HOLBROOK AND B.P. FAIRAND: *Effects of Laser Induced Shock Waves*. Plenum Publishing Corporation, New York, 1981.
- [115] M.A. MEYERS, F. GREGORI, B.K. KAD, M.S. SCHNEIDER, D.H. KALANTAR, B.A. REMINGTON, G. RAVICHANDRAN, T. BOEHLY AND J.S. WARK. *Acta Materialia*, 51:1211–1228, 2003.
- [116] F.I. GRACE. *Journal of Applied Physics*, 40:2649–2657, 1969.
- [117] J. LINDL. *Physics of Plasmas*, 2:3933–3982, 1995.
- [118] C.A. NEUGEBAUER. *Journal of Applied Physics*, 31:1096–1101, 1960.
- [119] J.A. THORNTON AND D.W. HOFFMAN. *Thin Solid Films*, 171:5–31, 1989.
- [120] J.E. KLINE AND J.P. LEONARD. *Applied Physics Letters*, 86:201902, 2005.
- [121] D. LI AND D.M. HERLACH. *Journal of Crystal Growth*, 160:59, 1996.
- [122] B. VON BLANCKENHAGEN, E. ARZT AND P. GUMBSCH. *Acta Materialia*, 52:773–784, 2004.
- [123] E. SAIZ AND A.P. TOMSIA. *Nature Materials*, 3:903–909, 2004.
- [124] M.G. VELARDE: *Interfacial Phenomena and the Marangoni Effect*. Springer Verlag, Berlin Heidelberg, 2002.
- [125] P. COLINET: *Nonlinear Dynamics of Surface-Tension-Driven Benard Convection*. John Wiley and Sons, New York, 2001.
- [126] S.J. VAN HOOK, M.F. SCHATZ, J.B. SWIFT, W.D. MCCORMICK AND H.L. SWINNEY. *Journal of Fluid Mechanics*, 345:45–78, 1997.
- [127] V.Y. BALANDIN, D. OTTE AND O. BOSTANJOGLO. *Journal of Applied Physics*, 78:2037–2044, 1995.

- [128] R. CATRIN, A. LASAGNI, C. GACHOT, U. SCHMID AND F. MÜCKLICH. *Advanced Engineering Materials*, 10:5, 2008.
- [129] A.KOBLISCHKA-VENEVA, C. GACHOT, P. LEIBENGUTH AND F. MÜCKLICH. *Journal of Magnetism and Magnetic Materials*, 316:431–434, 2007.
- [130] J. BARRIGA. *Tribology International*, 40:1526–1530, 2007.
- [131] S.P. PATTON AND J.S. ZABINSKI. *Tribology Letters*, 18:215–229, 2005.
- [132] P.J. BLAU. *Tribology International*, 38:1007–1012, 2005.
- [133] D. KUHLMANN-WILSDORF: *Dislocation concepts in friction and wear in D.A. Rigney (Ed.), Fundamentals of Friction and Wear of Materials*. ASM, Metal Park Ohio, 1980.
- [134] Z.N. FARHAT. *Wear*, 250:401–408, 2001.
- [135] P.J. BLAU. *Wear*, 71:29–43, 1981.
- [136] P.J. BLAU. *Tribology International*, 34:585–591, 2001.
- [137] ASME: *Wear volume equations, appendix 1*. Wear Control Handbook, 1980.
- [138] L.SPIESS, R. SCHWARZER, H. BEHNKEN AND G. TEICHERT: *Moderne Röntgenbeugung*. Teubner Verlag, Wiesbaden, 2005.
- [139] J. RÖSLER, H. HARDERS AND M. BÄKER: *Mechanisches Verhalten der Werkstoffe*. Teubner Verlag, Wiesbaden, 2003.
- [140] J.H. DAUTZENBERG. *Wear*, 60:401–411, 1980.
- [141] S.I. WRIGHT AND M.M. NOWELL. *Microscopy and Microanalysis*, 12:72–84, 2006.
- [142] W.C. OLIVER AND G.M. PHARR. *Journal of Materials Research*, 7:1564–1583, 1992.
- [143] K.S. KUMAR, H. VAN SWYGENHOVEN AND S. SURESH. *Acta Materialia*, 51:5743–5774, 2003.

Bibliography

- [144] E. ARZT. *Acta Materialia*, 46:5611–5626, 1998.
- [145] B. YANG AND H. VEHOFF. *Acta Materialia*, 55:849–856, 2007.
- [146] R. VILAR AND R. COLACO. *Surface and Coatings Technology*, 203:2878–2885, 2009.
- [147] M. MERKEL AND K.H. THOMAS: *Taschenbuch der Werkstoffe*. Fachbuchverlag Leipzig im Carl Hanser Verlag, Carl Hanser Verlag München Wien, 2003.
- [148] I. JÄGER AND P. FRATZL. *Biophysical Journal*, 79:1737, 2000.
- [149] R.K. SHIUE, S.K. WU AND S.Y. CHEN. *Intermetallics*, 12:929, 2004.
- [150] X.K. WU, D. HU AND M.H. LORETTO. *Journal of Materials Science*, 39:3935, 2004.
- [151] W.J. ZHANG, B.V. REDDY AND S.C. DEEVI. *Scripta Materialia*, 45:645, 2001.
- [152] O.N. SENKOV, M.D. UCHIC, S. MENON AND D.B. MIRACLE. *Scripta Materialia*, 46:187, 2002.
- [153] B.D. CULLITY AND S.R. STOCK: *X-Ray Diffraction*. Prentice Hall, New Jersey, 2001.
- [154] U. WELZEL, J. LIGOT, P. LAMPARTER, A.C. VERMEULEN AND E.J. MITTEMEIJER. *Journal of Applied Crystallography*, 38:1–29, 2005.
- [155] E. DETEMPLE, P. LEIBENGUTH, C. GACHOT AND F. MÜCKLICH. *Thin Solid Films*, 519:736–741, 2010.
- [156] L. WANG, B. HE AND X.H. JIANG. *Combustion Science and Technology*, 182:1000–1008, 2010.
- [157] A.S. ROGACHEV ET AL. *Combustion, Explosion, and Shock Waves*, 40:166–171, 2004.
- [158] K. WOLL: *Festkörper-und selbst fortschreitende Reaktionen in Multilagen zur RuAl-Dünnschichtsynthese*. PhD Thesis, Saarland University, Saarbrücken, Germany, 2012.

Bibliography

- [159] Y.N. PICARD, D.P. ADAMS, J.A. PALMER AND S.M. YALISOVE. *Applied Physics Letters*, 88:144102, 2006.
- [160] H.T.G. HENTZELL, B. ANDERSSON AND S.E. KARLSSON. *Acta Metallurgica*, 31:1131, 1983.
- [161] A.S. EDELSTEIN, R.K. EVERETT, G.Y. RICHARDSON, S.B. QADRI, J.C. FOLEY AND J.H. PEREPEZKO. *Journal of Applied Physics*, 76:7850, 1994.
- [162] J.G. LUO AND V.G. ACOFF. *Welding Journal*, 79:239, 2000.
- [163] A. MOTAYED, R. BATHE, M.C. WOOD, O.S. DIOUF, R.D. VISPUTE AND S.N. MOHAMMAD. *Journal of Applied Physics*, 93:1087, 2003.
- [164] C. GACHOT, P. LEIBENGUTH AND F. MÜCKLICH: *Friction, Wear and Wear Protection-Tribological properties of laser interference induced microstructural architectures in metallic systems*. A. Fischer and K. Bobzin, Wiley-VCH, 2009.
- [165] R.M. WALSER AND R.W. BENÉ. *Applied Physics Letters*, 28:624, 1976.
- [166] B.Y. TSAUR, S.S. LAU, J.W. MAYER AND M.A. NICOLET. *Applied Physics Letters*, 38:922, 1981.
- [167] R.W. BENÉ. *Applied Physics Letters*, 41:529, 1982.
- [168] R. PRETORIUS, A.M. VREDENBERG AND F.W. SARIS. *Journal of Applied Physics*, 70:3636–3646, 1991.
- [169] A.S. RAMOS AND M.T. VIERA. *Surface and Coatings Technology*, 200:326, 2005.
- [170] G. LUCADAMO, K. BARNAK, C.LAVOIE, C. CABRAL AND C. MICHAELSEN. *Journal of Applied Physics*, 91:9575, 2002.
- [171] W. VOIGT: *Lehrbuch der Kristallphysik*. B.G. Teubner, Leipzig, 1910.
- [172] A. REUSS. *Zeitschrift für Angewandte Mathematik und Mechanik*, 9:49, 1929.
- [173] M.F. ASHBY AND D.R.H. JONES: *Engineering Materials I*. Butterworth Heinemann, Oxford, 1996.

Bibliography

- [174] R.W. HERTZBERG: *Deformation and Fracture Mechanics of Engineering Materials*. John Wiley, New York, 1996.
- [175] M. NAKADA. *Tribology International*, 27:1, 1994.
- [176] H. IKE AND M. PLANCAK. *Advanced Technology of Plasticity*, II:907–912, 1999.
- [177] A. SCHUBERT, J. BÖHM AND T. BURKHARDT. *Werkstattechnik*, 90:479–483, 2000.
- [178] S. MEDINA, D. DINI AND A.V. OLVER. *Proceedings of the STLE/ASME International Joint Tribology Conference*, 2008.
- [179] SHELL COMPANY: *Shell Vitrea Oils*. <http://www.epc.shell.com>. last access 16.06.2012.
- [180] J. TALONEN, P. NENONEN, G. PAPE AND H. HÄNNINEN. *Metallurgical and Materials Transactions A*, 36A:421–432, 2005.
- [181] C. GACHOT, A. ROSENKRANZ, L. REINERT, E. RAMOS-MOORE, N. SOUZA, M.H. MÜSER AND F. MÜCKLICH. *Tribology Letters*, pages 1–10, 2012.
- [182] W.E. CAMPBELL: *Proceedings of M.I.T.* MIT Press, Cambridge, 1940,.
- [183] W. HÜBNER. *Tribology International*, 34:231–236, 2001.
- [184] R.E. SCHRAMM AND R.P. REED. *Metallurgical and Materials Transactions A*, 6A:1345–1351, 1975.
- [185] H.G. FELLER AND B. GAO. *Wear*, 132:1–7, 1989.
- [186] D.A. RIGNEY. *Materials Research Innovations*, 1:231–234, 1998.
- [187] D. KUHLMANN-WILSDORF. *Materials Science and Engineering*, 39:231–245, 1979.

List of Figures

4.1. Schematic description of an effective interaction cross section σ_{lu} regarding absorption of light.	21
4.2. Schematic summary of absorption, spontaneous and stimulated emission according to [33].	22
4.3. A typical four-level laser transition scheme [34]	24
4.4. Energy level diagram for a Nd:YAG solid state laser [34]	25
4.5. Frequency dependence of the dielectric function ϵ_D , the refractive index n , the absorption coefficient α and the reflectivity R [37].	31
4.6. Wavelength dependence of the reflectance R and the absorption coefficient α for gold and aluminium thin films [37].	32
4.7. Reflectivity versus temperature for different metallic surfaces [40].	33
4.8. Representation of surface roughness by rectangular shaped wells with height h and width w [43].	34
4.9. Cumulative absorption coefficient versus surface roughness h_0/w_0 for two different wavelengths on a solid aluminium surface [43].	35
4.10. Reflectivity of steel as a function of incidence angle and beam polarisation [31].	36
4.11. Superposition of two harmonic waves having the same amplitude but different frequencies. The resulting wave is a beat [45].	40
4.12. Beam configuration and calculated intensity distribution (top), white light interferometry measurements (middle) and scanning electron micrographs (bottom) of the corresponding laser patterns on different material surfaces [46].	42
5.1. Model of the real area of contact shown for two contacting asperities. A_1 and A_2 define the respective contact areas [49].	45

List of Figures

5.2. Schematic representation of the one-dimensional Prandtl-Tomlinson model for elastic instabilities [51].	46
5.3. Illustration of an instability in the Prandtl-Tomlinson model [51].	47
5.4. One-dimensional friction model. In (a) friction is not zero and in (b) friction is reduced to zero. The arrows denote the directions of the resulting forces [55].	48
5.5. Frictional force as a function of twist angle between two mating mica surfaces for different surface temperatures and relative water vapor pressures [54].	50
5.6. Average friction force as a function of the rotation angle of a graphite specimen around an axis perpendicular to the surface. The plot fitting the data points is based on a simulation of a Tomlinson model for graphite [59].	51
5.7. Schematic overview of the measuring set up. A titanium sphere with fixed radius is mounted to a tip. Patterned silicon surfaces fabricated by FIB are used with different groove widths [60].	52
5.8. Geometrical deviations of technical surfaces composed of roughness values on different scales [66].	53
5.9. Definition of the root mean square roughness value (rms) of a given cross-section profile plot within a sampling length L_s [69].	54
5.10. Definition of the Swedish height H of a cross section profile [69].	54
5.11. Calculation of the bearing length t_b of a profile [70].	55
5.12. Surface profile and resulting Abbott-Firestone plot with the belonging Abbott parameters [71].	55
5.13. Definition of skewness (R_{sk}) for more peaked surfaces (top) having a positive value and bearing surfaces (bottom) with a negative R_{sk} value. The ADF for the two cases is shown on the right [70].	57
5.14. Definition of the kurtosis (R_{ku}) and distinction between leptokurtotic surfaces [70].	57
5.15. Schematic overview of a Hertzian point contact with the respective dimensions and the maximum Hertzian contact pressure p_0 [49].	61
5.16. Schematic figure of the point contact and the resulting vertical displacement $w(r)$ [49].	62

List of Figures

5.17. Simplified model of a rough surface composed of spherical asperities with the same curvature radius and height.	63
5.18. Model of a stochastic surface according to Greenwood and Williamson [75] [84].	64
5.19. Contact and average contact area as functions of the dimensionless variable ξ_0 [84].	65
6.1. Schematic Stribeck curve with linear (left) and logarithmic abscissa (right) [49].	70
6.2. Representation of the different friction regimes according to the Stribeck curve [87].	71
7.1. Schematic drawing of the interference set up. The scanning electron micrograph shows a typical interference line-pattern made on stainless steel.	74
7.2. General scheme for TEM foil preparation using FIB. Insets a) and b) show the coarse milling step with the nearly released foil. In c) the transfer of the foil to the TEM grid by the micromanipulator is displayed. Finally, d) shows the fixed foil at the TEM copper grid.	76
7.3. Schematic overview of a typical EBSD measuring system consisting of sample holder, fluorescence screen and CCD camera (left picture) and the technical realisation in the SEM (right picture)	78
7.4. Optical system for scanning white light interferometry [91].	79
7.5. Overview of the main tribometer components.	81
8.1. Histogram plot of the grain size diameter distribution of an as-deposited gold thin film by EBSD. The insert represents a SEM image of the film showing the fine grained morphology.	85
8.2. SEM image of thin film morphology as a function of the laser fluence for a 690 nm (a, b and c) and a 300 nm (d, e and f) thick film. The SEM images show a line-like interference pattern typical for two interfering laser beams. Only one laser intensity maximum with the neighboring minima is depicted. The structural periodicity is around $6 \mu\text{m}$	86
8.3. FIB cross-sections of laser patterned Au films with a film thickness of 300 nm (left) and 690 nm (right). The substrate in both cases is silicon. . . .	87

List of Figures

8.4. Inverse pole figure maps and corresponding pole figures for the $\langle 001 \rangle$, $\langle 110 \rangle$ and $\langle 111 \rangle$ directions of the 690 nm (a, c) and of the 300 nm thick gold films (b, d) determined by EBSD after laser irradiation. The colour-code is according to the inserted orientation triangle.	88
8.5. Thermal simulations of 300 nm (a, b and c) and 690 nm (d, e and f) laser irradiated Au-samples. Figures (a) and (b) show the evolution of the solid-liquid interface at the 300 nm sample during melting and resolidification, and figures (d) and (e) for the 690 nm thick film. For both cases, the lateral (v_x) and vertical growth velocities (v_y) as a function of normalised time as well as the ratio between the two velocities is represented in figures (c) and (f).	89
8.6. SEM images of a Au reference sample (a), laser crystallised lines with a periodicity of around $5.6 \mu\text{m}$ (b) and laser-pattern with $2 \mu\text{m}$ line-spacing (c).	91
8.7. Histogram plot of the grain size diameter distribution for a laser-patterned gold film with a patterning periodicity of around $2 \mu\text{m}$	92
8.8. Overview (a) and magnified Insert (b) of laser interference cross-pattern showing twinning in the maxima and overlapping positions.	93
8.9. SEM images of irradiated Au, Pt and W 300 nm films at different laser fluences. The left (a, b, and c) and right (d, e, and f) rows denote the low and the high fluence regimes, respectively [30].	96
8.10. Inverse pole figure maps and corresponding pole figures for the $\langle 001 \rangle$, $\langle 110 \rangle$ and $\langle 111 \rangle$ directions of the 300 nm thick Au (a, c) and Pt thin films (b, d) determined by EBSD. The colour-code corresponds to the inserted orientation triangle.	99
8.11. Histogram plot of the grain sizes in laser irradiated Au (a) and Pt samples (b) measured by EBSD.	100
8.12. Thermal Simulation of a laser-patterned Au film at a fluence of about 360 mJ/cm^2 . On the left side, the liquid-solid interface during the resolidification is displayed and on the right side, the thermal gradient both through the entire film thickness starting from the center of the intensity maximum.	102

List of Figures

8.13. Thermal simulation of the laser-treated Au, Pt and W films. Figures a, c and e show the liquid-solid interface during the resolidification process for the Au, Pt and W samples. The thermal gradient over the cross-section of the film starting from the centre of a laser intensity maximum position is shown in b, d and f for Au, Pt and W films. (a, b) Au: laser fluence 636 mJ/cm^2 , (c, d) Pt: laser fluence 535 mJ/cm^2 , (e, f) W: laser fluence 710 mJ/cm^2	103
8.14. 3-D surface view of line- (a), cross- (b) and dot-like (c) laser pattern recorded by WLI.	105
8.15. Comparison of two surface profile plots of specimens having a skewness of -2.68 (left) and -0.46 (right). The specimen on the left side shows a more plateau-like surface.	106
8.16. Abbott-Firestone plots of laser-patterned samples vs. reference surface. .	107
8.17. Comparison of surface profiles of samples L5.6 and L8 recorded by WLI.	108
8.18. Comparison of Abbott-Firestone plots between laser textured samples and reference.	108
8.19. Friction coefficient vs. sliding distance in mm for line- and cross-patterned specimens measured under dry reciprocating sliding conditions and a perpendicular orientation between the laser lines and the sliding direction. .	110
8.20. Standard wear testing using a ball on disk configuration according to <i>ASTM G99</i> . R denotes the ball radius, b the width of the wear track, h the penetration depth of the counter body and W_V the wear volume [137].	111
8.21. Wear volume in (μm^3) vs. skewness of laser line-patterns compared to the reference.	112
8.22. Wear volume vs. skewness of laser line- and cross-patterns compared to the reference.	113
8.23. SEM image of a wear scar in a not patterned Au thin film after 1 (a) and 50 sliding cycles (b).	114
8.24. Pole figures of the as-deposited Au thin film for the (001), (110) and (111) lattice planes measured by EBSD.	114
8.25. Magnified picture of the primary track in the wear scar of the reference specimen after one sliding cycle.	115
8.26. EBSD grain size distribution of the interaction zone in the primary track of the wear scar.	116

List of Figures

8.27. Inverse pole figure map of primary track with corresponding standard orientation triangle. TD denotes transverse- and RD rolling direction. Figure (a) represents the inverse pole figure map along the normal- and (b) along the rolling direction. The step size was set to 30 nm and the confidence index (CI) is 0.15.	117
8.28. WLI surface plot of a wear scar in a laser line pattern (a). In (b) a longitudinal cut profile is shown for the wear track and (c) is an amplitude spectrum plot depicting a characteristic spatial frequency which corresponds to the pattern line spacing.	118
8.29. SEM images of worn line- (a), cross- (b) and dot-pattern (c) after 100 cycles.	118
8.30. SEM image (a) and inverse pole figure map (b) of worn dot surface. The blue colour coded regions correlate with the original grain structure. The step size was set to 30 nm with a confidence index of 0.15.	119
8.31. Nanohardness as a function of indentation depth applying three different loads of 50, 100 and 200 μN . These results were determined at a 690 nm thick gold sample modified with an interference pattern using three interfering laser beams. The indentations were performed in the laser intensity minima positions and in the laser intensity maxima positions on top of the hemispherical structures.	120
8.32. Definition of the cutting efficiency on the basis of a wear track in a not patterned Au film.	121
8.33. Cutting efficiency for laser line-patterns compared to the reference.	122
8.34. Comparison of cross section profiles.	122
8.35. Comparison of measured WLI profiles and the corresponding fit functions for smaller (sample L3) and larger line spacings (Sample L8).	124
8.36. Total number of asperities in contact depending on the periodicity and structural depth.	126
8.37. Total contact area in μm^2 as a function of structural depth and periodicity.	126
8.38. Contact pressure in GPa vs. structural depth and line-spacing.	127
8.39. Plasticity index Ψ vs. skewness R_{sk} for different line-patterns.	127
8.40. FIB cross-section of an as-deposited 300 nm thick TiAl multilayer. The bright layers correspond to Al and the darker ones to Ti.	130

List of Figures

8.41. Surface profile (left), intensity map (right) and surface profile cross-section plot (bottom) of the as-deposited TiAl multilayer measured by WLI. The rms value is about 1 nm.	130
8.42. Diffraction pattern of a pristine TiAl multilayer measured by GI-XRD. The peaks of the Si substrate are denoted by Sub. in the diffraction graph.	131
8.43. TEM image of as-deposited multilayer (left) and SAD pattern (right). The normal vector of the sample surface is represented by \vec{n}_P	132
8.44. SEM images of different fluence regimes (regime A, B and C) in TiAl at a fixed line-spacing of around $8\ \mu\text{m}$	133
8.45. WLI surface map of laser line-pattern on a TiAl multilayer with a line-spacing of $4\ \mu\text{m}$ at a fluence of $476\ \text{mJ}/\text{cm}^2$ (left), intensity plot (right) and corresponding cross-section profile plot (bottom).	133
8.46. GI-XRD measurement of laser patterned specimens at $170\ \text{mJ}/\text{cm}^2$ and $476\ \text{mJ}/\text{cm}^2$ compared with the reference.	134
8.47. TEM analysis of a laser irradiated multilayer (fluence: $170\ \text{mJ}/\text{cm}^2$). The position of maximum laser intensity is displayed (top left). The bottom left image shows a dark field image of the encircled grain. Top right: SAD pattern of zone axis and bottom right represents a schematic drawing of the pattern. The indexing reveals the existence of hcp α -Ti with a [01-11] zone axis.	136
8.48. TEM image of a laser-irradiated multilayer (fluence: $170\ \text{mJ}/\text{cm}^2$). The position of maximum laser intensity is displayed (top left). The bottom left image shows a dark field image of the encircled grain. Top right: SAD pattern of zone axis and bottom right represents a schematic drawing of the pattern. The indexing reveals the existence of bcc β -Ti with a [-111] zone axis.	137
8.49. STEM micrograph of a cross-section through the TiAl multilayer after laser patterning at $476\ \text{mJ}/\text{cm}^2$ [155].	138
8.50. SAD pattern in the locations of minimum (a) and maximum laser intensity (b) at a fluence of $476\ \text{mJ}/\text{cm}^2$. The vector \mathbf{n} denotes the surface normal vector.	139
8.51. Results of the local chemical analysis in minimum (upper row), maximum (center row) and transition (lower row) zone positions obtained by APT [155].	140

8.52. Laser irradiated (476 mJ/cm^2) TiAl sample with a fixed periodicity of $4 \mu\text{m}$. Diagram on the left side shows the reduced elastic modulus for the intensity maxima and minima positions and the right diagram the measured hardness in GPa [164].	143
8.53. Schematic overview of the model used for thermal simulation. Due to symmetry conditions, only half of the model is considered.	144
8.54. Simulated temperature distribution at a pattern periodicity of $8 \mu\text{m}$ and a fluence of 170 mJ/cm^2 . Top left: spatial temperature distribution at $t = 33.5 \text{ ns}$. Top right: spatial temperature distribution for cross-sections parallel to the surface. Bottom left: spatial temperature distributions for cross sections being perpendicular to the surface and bottom right: temporal distribution of temperature.	145
8.55. Simulation of the maximum achievable temperatures depending on the pattern line-spacing at a fixed fluence of 170 mJ/cm^2 . $T_{max,o}$, $T_{max,u}$ denote the maximum temperature at the intensity maximum at the surface and at the multilayer-substrate interface and $T_{min,o}$, $T_{min,u}$ at the intensity minimum.	146
8.56. Simulated melt duration as a function of laser periodicities.	147
8.57. Simulated molten fractions of Al at a fluence of 170 mJ/cm^2 . Here, f_m is the amount of molten Al, b_m the width of the molten region related to the periodicity and h_m the molten depth normalised to the total film thickness.	147
8.58. Simulated cooling rate for TiAl after laser treatment at 170 mJ/cm^2 vs. periodicity.	148
8.59. Schematic representation of the Voigt (parallel arrangement) (a) and Reuss model (serial arrangement) (b).	150
8.60. WLI image of the initial ball surface (100 Cr6). Left image shows a surface profile map. The ball curvature was removed by the WLI software (<i>MetroPro</i>). In the right image, a cross-section profile plot is presented indicating a low roughness.	152
8.61. Measured friction coefficient μ vs. laser periodicity in μm with an orientation parallel (left) and perpendicular to the laser interference lines (right). The point $0 \mu\text{m}$ on the abscissa represents the unpatterned reference sample.	152

List of Figures

8.62. Wear volume vs. periodicity for a parallel orientation between the slider and the laser interference lines measured by WLI.	153
8.63. Wear volume vs. periodicity for a perpendicular orientation between the slider and the laser interference lines measured by WLI.	153
8.64. WLI image of a wear scar after parallel sliding. The top left image shows the respective surface intensity map, the top right an intensity map and the bottom the corresponding cross-section profile plot for a patterned sample with a periodicity of around $8\ \mu\text{m}$	154
8.65. WLI image of a wear scar at a periodicity of $12\ \mu\text{m}$ under perpendicular sliding conditions. The top left image shows surface profile map, the top right the intensity map with indication of accumulated wear debris and the bottom finally the cross-section profile plot.	155
8.66. TEM foil preparation in a wear scar of an unpatterned TiAl sample by FIB (a), the corresponding cross-section view (b) and the indexed SAD pattern (c).	156
8.67. Examples of coined copper and aluminium; cross-sections of different coining structures (left), numerical model of the strain during the coining process (centre), SEM surface detail of a cross-structured aluminium sample, multilayered heat exchanger concept made of stacked coined samples (right)	158
8.68. Principle of a secondary LIMET structure used for topographic effects (a) or local influence on material properties such as the hardness of a micro-coined surface (b).	159
8.69. Friction coefficient vs. sliding time for laser-textured Al surfaces. The laser pattern consisted of lines with different spacings. The sliding direction in this case was parallel to the laser lines.	162
8.70. Simulated contact pressure distributions for different periodicities (2, 5, 7 and $8\ \mu\text{m}$) and number of contacting asperities. The colour-code represents the normalised contact pressure. The normalisation is done using the Hertzian contact pressure p_0 (<i>in collaboration with Dr. Simon Medina, Imperial College London</i>).	163
8.71. Friction coefficient as a function of sliding time for laser textured aluminium bulk samples with different line-spacings. The measurement direction was perpendicular to the laser lines.	164

8.72. Micro-coining followed by laser interference patterning. SEM images in (a, c) show the bottom and top regions of a laser patterned surface after micro-coining (b, d) of a coined surface after LIMET.	166
8.73. Thermal simulation of the influence of the micro-coined flank angle for 25° (a) and 45° (b) on the subsequent laser patterning. Due to symmetry, only half of the micro-coined structure is presented. The red arrows mark the flank regions for which cross-section temperature profile plots were simulated. The x-scale is different for (a) and (b) thus explaining the apparent similarity of the flank angles in the figure.	167
8.74. Simulated temperature cross-section profile plots for a flank angle of 25° (a) and 45° (b). The plot was simulated for the flank region of the coining geometry indicated by the red arrows (see figure 7.72).	168
8.75. Intensity and cross-section profile plot of a micro-coined (a, b) and a hierarchically patterned aluminium sample surface (c, d) measured by WLI.	169
8.76. SEM images of micro-coined channels as well as spherical patterns (a, c) and with a superimposed homogeneous laser pattern in (b, d).	171
8.77. Preliminary tribological test results of different surface conditions under lubricated sliding in a ball on disk setup. Figure 7.76 (a) represents a schematic drawing and (b) SEM pictures of a hierarchically patterned aluminium surface with a micro-coined dimple and a superimposed line-pattern.	173
8.78. Typical interference line-pattern in a stainless steel substrate [181]. . . .	175
8.79. Horizontal intensity cross-section of the primary beam (top) and the corresponding 2-D intensity beam profile for two interfering beams (bottom).	175
8.80. 3-D plots of laser-patterned ball (a) and substrate (b) surface measured by WLI. Figures (c) and (d) show the related autocovariance plots. . . .	176
8.81. Plots for a patterned steel substrate (black) and a 100 Cr 6 tribometer ball (red) measured by WLI [181].	177
8.82. Surface profile plots of laser-patterned steel surfaces measured by WLI. The periodicity of the line patterns was set to be 5, 9 and 18 μm [181]. .	178
8.83. (a) and (b) display a 3-D view of the relative alignment and sliding direction of the patterned contacting surfaces. Insets (c) and (d) show the temporal evolution of μ for different alignments and periodicities. The black arrows indicate the sliding direction [181].	181

List of Figures

8.84. Light microscopic image of wear tracks with a 0° orientation between substrate and ball (a) and 90° (b) [181].	182
8.85. Coefficient of friction over sliding time for three distinct line-spacings at 0° orientation [181].	182
8.86. Comparison of a laser-induced surface profile before and after sliding at a 0° orientation measured by WLI in (a). Figure (b) shows a SEM image of the worn surface pattern under a tilt angle of 52° [181].	183
8.87. SEM/FIB image of pristine steel surface (1.4301). The image was recorded by means of ion channeling contrast [181].	184
8.88. SEM/FIB image of a laser-patterned steel surface [181].	185
8.89. FIB cross-section of a steel surface after laser-patterning [181].	185
8.90. Measured hardness of the reference and laser-patterned specimen surfaces with corresponding 3-D surface plots recorded by a Hysitron tribo-indenter. Only measurement points for the laser intensity maxima positions (topographic minima) are displayed [181].	186